Noninvasive Ambient Pressure Estimation using Ultrasound Contrast Agents

– Invoking Subharmonics for Cardiac and Hepatic Applications

A Thesis

Submitted to the Faculty

of

Drexel University

by

Jaydev K Dave

in partial fulfillment of the

requirements for the degree

of

Doctor of Philosophy

July 2012

Dedications

To Mom, Avani *N* Dad for their unwavering Support, Inspiration and unconditional love.

Jay

Acknowledgements

This runs into 2 pages for obvious reasons!!!

There are no words that can *justly* express my gratitude towards Dr. Flemming Forsberg. Entrusting me a project of potentially high caliber after my M.S. Thesis Defense in May 2008 embodies one such attribute of his! On a professional (and personal) note, I do acknowledge his support and encouragement towards keeping me focused throughout the past 5 years. Discussions with Dr. Forsberg have always been fruitful for me (may not be for him!). Working in a hospital setting, I appreciate his "patience" in dealing with my idiosyncrasies – but I should partly acknowledge 'massively multiplayer online role-playing game' for that as well. Finally at times, I was in line of the "Danish liquorice", but was somehow able to escape the full wrath! Christine, Mark and Anya, thanks for providing some humorous and memorable and motivating encounters over the 5 years - remember he chose to spend his 50th birthday with us, away from home. To Dr. Forsberg, I owe and shall owe my accomplishments.

At the same time, I do acknowledge my Ph.D. committee members, specifically, Dr. Peter Lewin (whose probing and encouragement were always admired), Dr. Margaret Wheatley (whose emails were a constant source of encouragement), Dr. Fred Allen (with whom my interactions at Drexel began since September 2006; and who most likely stayed awake in "anticipation" of my Ph.D proposal) and Dr. Daniel Brown (who was accommodating to my questions, meetings and emails in spite of his clinical duties). I also extend my acknowledgements to Dr. Joel Raichlen who guided me through much of the cardiac work done in this thesis – I do very well remember his first reactions on seeing cardiac pressure waveforms obtained from the subharmonic data!

Much of this work would not have been possible without the constant support that I have received from a very dynamic team in the lab – Valgerður Halldórsdóttir (Valla), John Eisenbrey, Priscilla Machado, Anush Sridharan, Khoa Nguyen, Andrew Marshall, Manasi Dahibawkar and Lauren Rosenblum: you all have always been a source of inspiration. Valla has specifically assisted me in data acquisition for most of the experiments since some *in vitro* and *in vivo* work required at

least 2 people to operate the ultrasound scanner, run LabVIEW and at the same time log the experiment parameters and acquisition runs. I would also like to thank Dr. Ji-Bin Liu, Daniel Merton, Maureen E. McDonald and Joseph Altemus, who shouldered responsibilities for most part of the canine experiments. This work may not have been finished if it were not for Dr. Barry Goldberg – his frequent visits confirmed that everyone were working in the lab; and thanks to his supply of food and water that we survived in the lab till late night.

Thanks to Dr. Forsberg, that I attended many conferences throughout these 5 years and had quite motivating/memorable encounters with Drs. Ken Hoyt, Kai Thomenius, Anne Hall, and with Anna Solace, Reshu Saini, Kris Dickie and Laurent Pelissier – thanks all. I would also like to thank Suhyun Park, Scott Dianis, Carl Chalek, Kirk Wallace and Feng Lin from GE Healthcare and Corina Leung from Ultrasonix for their technical assistance. A note of thanks extends to the unknown reviewers who provided valuable feedback and critique for publications that resulted from this work.

Also, for the kind nature of Dr. Eric Gingold who has always supported my dual role as a Physicist and as a Research Assistant – I would like to thank him for bestowing his trust in my work. Our department head, Dr. Vijay Rao has been a source of inspiration through encouraging emails and by recognizing the importance of this work. Our department administrator, Victor Sarro has extended assistance when required – thanks! Also, conversations with Andrea Frangos and Dr. Parker, statistics related or not, were educational. I would also like to thank Dr. Whaley (who offered me my first faculty appointment), Raja Gali (responsible for my caffeine intake) and Dr. Gardiner (in neighboring office – who sat and slept through the choice of my loud music while chewing through data).

None of this would have been possible without the financial support in the form of grants from the American Heart Association, the National Institutes of Health and the US Army Medical Research and Material Command (Appendix 11) – hopefully part of this work reciprocates your trust.

Friends and family, in India and the USA, I can only admire all your support and I consider myself lucky for the same.

Mom, Avani and Dad, to whom I dedicate this thesis, I want to THANK them only for their patience, support, love, encouragement, assistance, guidance, trust…; basically for everything!

Table of Contents

Dedications ii

Acknowledgements iii

List of Tables x

List of Figures xii

List of Abbreviations xv

Abstract xvii

1. INTRODUCTION 1
   - 1.1 An Overview 1
   - 1.2 Thesis Objective(s) 3

2. BACKGROUND AND LITERATURE REVIEW 11
   - 2.1 Cardiac Pressure Monitoring 11
     - 2.1.1 Need for Cardiac Pressure Monitoring 11
     - 2.1.2 Need for Noninvasive Cardiac Pressure Monitoring 15
     - 2.1.3 Noninvasive Techniques for Cardiac Pressure Monitoring 15
   - 2.2 Portal Vein (PV) Pressure Monitoring 19
     - 2.2.1 Need for PV Pressure Monitoring 20
     - 2.2.2 Need for Noninvasive PV Pressure Monitoring 21
     - 2.2.3 Noninvasive Techniques for PV Pressure Monitoring 23
   - 2.3 Ultrasound and Ultrasound Contrast Agents (UCAs) 27
     - 2.3.1 Ultrasound 27
     - 2.3.2 Ultrasound Contrast Agents (UCAs) 31
       - 2.3.2.1 Modeling of Un-Encapsulated and Encapsulated Microbubbles 32
       - 2.3.2.2 Properties of Microbubbles based UCAs 36
       - 2.3.2.3 UCAs – Status Update & Safety 38
       - 2.3.2.4 Contrast Specific Ultrasound Imaging Modes and Applications 40
   - 2.4 UCAs as Ambient Pressure Sensors 42
   - 2.5 Subharmonic Aided Pressure Estimation (SHAPE) with UCAs 46

3. MATERIALS AND METHODS 49

3.1 Materials 49

3.1.1 Selection of UCA for Dynamic *In Vitro* Studies and *In Vivo* Studies 49

3.1.2 Selection of Ultrasound Scanner for SHAPE 51

3.2 Methods 53

3.2.1 Dynamic *In Vitro* Studies 53

3.2.1.1 Incident Acoustic Output (IAO) Measurements for Sonix RP Scanner with the PA4-2 Array 53

3.2.1.2 Experimental Setup 54

3.2.1.3 Data Acquisition, Processing and Statistical Analyses 58

3.2.2 *In Vivo* Cardiac SHAPE Studies 66

3.2.2.1 Animal Preparation 66

3.2.2.2 Evaluating Feasibility of Noninvasive *In Vivo* SHAPE 67

3.2.2.3 Developing a Technique to Obtain Clinically Relevant Left Ventricle (LV) Pressures using SHAPE 70

3.2.2.4 Developing a Technique to Obtain Clinically Relevant Right Ventricle (RV) Pressures using SHAPE 73

3.2.3 *In Vivo* Portal Hypertension (PH) SHAPE Studies 78

3.2.3.1 IAO Measurements for Logiq 9 Scanner with the 4C Array 78

3.2.3.3 Selection of PH Models 79

3.2.3.3 Animal Preparation 80

3.2.3.4 Implementation of PH Models 83

3.2.3.5 Efficacy of SHAPE to Investigate PH (PH Study 1) 86

3.2.3.6 Validation of Automated IAO Optimization Algorithm (Implemented on Logiq 9 Scanner; PH Study 2) 94

4. RESULTS AND DISCUSSIONS 104

4.1 Dynamic *In Vitro* Studies 104

4.1.1 Acoustic Output Measurements for Sonix RP scanner with the PA4-2 Array 104

4.1.2 Identifying Most Sensitive IAO Level for Dynamic *In Vitro* SHAPE 105

4.1.3 Ability of SHAPE to Estimate Ambient Pressures 107

4.1.4 Confirmation of Variation of Subharmonic Signals as a Function of Ambient Pressures 110

4.1.5 Developing “Best” Processing Technique for SHAPE 111
 4.1.5.1 Comparing Processing Techniques 111
 4.1.5.2 SHAPE with “Best” Processing Technique 116
4.1.6 Discussion Based on *In Vitro* Experiments 117
4.1.7 Summary Based on *In Vitro* Experiments 121
4.2 Cardiac SHAPE Studies 122
4.2.1 Determination of Optimum IAO Levels for Cardiac SHAPE Studies 122
4.2.2 Feasibility of Noninvasive *In Vivo* SHAPE 125
4.2.3 Efficacy of SHAPE for Clinically Relevant LV Pressures 128
 4.2.3.1 Optimum IAO levels for SHAPE 128
 4.2.3.2 Calculation of Calibration Factor (mmHg/dB) in the Aorta 129
 4.2.3.3 Obtaining LV Pressure Profiles in Canines 130
 4.2.3.4 Comparison of SHAPE LV Pressures with Catheter Pressures 132
 4.2.3.5 Discussion for Cardiac SHAPE - LV 134
4.2.4 Efficacy of SHAPE for Clinically Relevant RV Pressures 135
 4.2.4.1 Optimum IAO levels for SHAPE 135
 4.2.4.2 Calculation of Calibration Factor (mmHg/dB) in the Aorta 136
 4.2.4.3 Obtaining RV Pressure Profiles in Canines 138
 4.2.4.4 Comparison of SHAPE RV Pressures with Catheter Pressures 139
 4.2.4.5 Discussion for Cardiac SHAPE - RV 141
4.2.5 Discussion Based on *In Vivo* Cardiac SHAPE Studies 142
4.2.6 Summary Based on *In Vivo* Cardiac SHAPE Studies 143
4.3 PH SHAPE Studies 144
4.3.1 Verification of PH Models In Canines 144
 4.3.1.1 PH Induction in Canines 144
 4.3.1.2 Inferior Vena Cava (IVC) and PV Data 146
 4.3.1.3 Statistical Analyses for Comparing Parameters Before and After Inducing PH 150
 4.3.1.4 Discussion 152
4.3.2 Efficacy of SHAPE to Investigate PH (Study 1) 155
 4.3.2.1 Induced PH in Canines 155

4.3.2.2 Subharmonic Amplitude as a Function of Number of Transmit Cycles and IAO Levels 156
4.3.2.3 Comparison of 3 and 4 Transmit Cycles for SHAPE Based PH Tracking 159
4.3.2.4 Comparison of 20 % and 40 % IAO Levels with 4 Transmit Cycles for SHAPE Based PH Tracking 162
4.3.2.5 Discussion based on PH Study 1 168
4.3.3 Efficacy of SHAPE to Investigate PH (Study 2) 171
4.3.3.1 Induced PH in Canines 171
4.3.3.2 Analyses of IAO Optimization Function 171
4.3.3.3 SHAPE's Performance for PV pressures and PH Tracking 173
4.3.3.4 Discussion based on PH Study 2 179
4.3.4 Discussion Based on PH SHAPE Studies 179
4.3.5 Summary Based on PH SHAPE Studies 181
4.4 General Discussion Based on SHAPE Studies 183
4.4.1 Cross Platform Compatibility 183
4.4.2 Specific Aims and Hypotheses 183
4.4.3 Sensitivity of Sonazoid and other UCAs for SHAPE 184
4.4.4 Algorithm for Future SHAPE Applications 187
5. CONCLUSIONS AND FUTURE RECOMMENDATIONS 189
5.1 Conclusions and Contributions to Science 189
5.2 Future Recommendations 192
LIST OF REFERENCES 194
Appendix 1: Detailed List of Equipment and Materials Used 213
Appendix 2: Use of Vertebrate Animals in the Experiments 218
Appendix 3: Detailed Operating Procedures 222
Appendix 4: Matlab Functions Developed for Processing 227
Appendix 5: Canines Used for Cardiac SHAPE Studies 232
Appendix 6: Equipment Setup and Matlab Functions Specific to Logiq 9 Scanner 233
Appendix 7: Canines Used for PH SHAPE studies 239
Appendix 8: List of Statistical Tests Used 241
Appendix 9: List of Key Personnel 243

Appendix 10: List of Software Used 245
Appendix 11: Grants 247
Appendix 12: List of Professional Contributions 248
Appendix 13: Ambigram for SHAPE 253
VITA 254

List of Tables

Table 2.1: Currently available UCAs..38

Table 3.1: UCAs investigated for SHAPE *in vitro* 49

Table 3.2: Behavior of different UCAs when ambient pressure was varied in the range from 0 to 186 mmHg...50

Table 3.3: Data acquisition parameters for the *in vitro* SHAPE studies..........................57

Table 3.4: Data acquisition parameters for cardiac SHAPE studies................................77

Table 3.5: Data acquisition parameters for PH Study (study 1) 93

Table 3.6: Data acquisition parameters for PH Study (study 2) 101

Table 4.1: Variation in subharmonic signal amplitude as a function of IAO levels......106

Table 4.2: Comparing SHAPE and catheter pressure after regression analyses............127

Table 4.3: Optimum IAO levels obtained from the aortic and the LV data 129

Table 4.4: Calibration factor calculations from the aorta for LV pressure estimation ..130

Table 4.5: LV pressure measurements with aortic calibration factors...........................133

Table 4.6: LV pressure measurement without aortic calibration factors 133

Table 4.7: Paired comparisons of SHAPE in LV and the manometer pressures for all canines...134

Table 4.8: Optimum IAO levels obtained from the aortic and the RV data 136

Table 4.9: Calibration factor calculations from the aorta for RV pressure estimation ..137

Table 4.10: RV pressure measurements with aortic calibration factors 140

Table 4.11: Paired comparisons of SHAPE in RV and the manometer pressures for all canines...141

Table 4.12: PH Induction in canines using the Gelfoam technique...............................145

Table 4.13: PH Induction in canines using the A-V shunt technique............................146

Table 4.14: Parameters obtained from the canines before and after inducing PH from the PV and from the IVC 148

Table 4.15: Comparing baseline and PH parameters in the PV 151

Table 4.16: PV pressures from canines used in PH study 1 156

Table 4.17: Pearson's correlation coefficient (r) between the change in subharmonic signal and change in PV pressures 162

Table 4.18: Pearson's correlation coefficient (r) between absolute subharmonic signal amplitudes and absolute PV pressures 164

Table 4.19: Paired t-test results when comparing subharmonic signal amplitudes obtained at baseline and PH conditions with 4 transmit cycles 165

Table 4.20: Predicting PV pressures and comparing with true pressures 166

Table 4.21: Comparing errors between manometer pressures and SHAPE results using cross-validation approach 167

Table 4.22: Sensitivity, specificity and accuracy for detecting moderate through severe PH 168

Table 4.23: PV pressures from canines used in PH Study 2 171

Table 4.24: Pearson's correlation coefficient (r) between subharmonic signals and PV pressures 174

Table 4.25: Paired t-test results when comparing subharmonic signal amplitudes obtained at baseline and PH conditions 178

Table 4.26: Sensitivity of Sonazoid to ambient pressure changes 184

Table A5.1: List of canines used for cardiac SHAPE studies 232

Table A7.1: List of canines used for PH SHAPE studies before the optimized IAO control algorithm was implemented on the Logiq 9 scanner 239

Table A7.2: List of canines used for PH SHAPE studies after the optimized IAO control algorithm was implemented on the Logiq 9 scanner 240

List of Figures

Figure 2.1: Experimental setup for first *in vivo* SHAPE experiments 47

Figure 2.2: Data acquisition for first *in vivo* SHAPE experiments 47

Figure 3.1: *In vitro* experimental setup for dynamic SHAPE studies 54

Figure 3.2: Process of extracting the time-variant subharmonic signal for ambient pressure tracking 60

Figure 3.3: Extraction techniques for subharmonic amplitudes 64

Figure 3.4: Frequency response for Daubechies second-order low-pass and high-pass filter coefficients 64

Figure 3.5: Grayscale ultrasound images of the LV before Sonazoid infusion and after Sonazoid infusion 68

Figure 3.6: Snapshot of the data acquisition during *in vivo* cardiac SHAPE studies 68

Figure 3.7: Sample data acquired from a PW Doppler gate 69

Figure 3.8: Ultrasound RF data acquired from the PW Doppler gate from the RV 75

Figure 3.9: Summary of experimental approach for *in vivo* cardiac SHAPE studies..........76

Figure 3.10: A color Doppler image depicting flow in the IVC...81

Figure 3.11: Animal preparation for PH studies...82

Figure 3.12: Implementation of the A-V shunt model..84

Figure 3.13: Experimental setup for PH study 1 86

Figure 3.14: Snapshot showing the setup to acquire the data 88

Figure 3.15: Images confirming the present of the pressure catheter in the PV and showing the surgical inlet for inducing PH..88

Figure 3.16: RF data acquisition mode on Logiq 9 scanner 89

Figure 3.17: MIP subharmonic image 91

Figure 3.18: Experimental setup for PH study 2 95

Figure 3.19: The dual grayscale and pulse inversion subharmonic imaging modes 97

Figure 3.20: Flowchart of the incident acoustic output (IAO) optimization function.........98

Figure 3.21: Summary of experimental approach for *in vivo* PH SHAPE studies 102

Figure 4.1: Variation in subharmonic signal amplitude as a function of IAO levels 105

Figure 4.2: *In vitro* SHAPE results..109

Figure 4.3: *In vitro* SHAPE with IAO levels that resulted in possible bubble destruction .110

Figure 4.4: Processing of the subharmonic data using median filtering.............................112

Figure 4.5: Processing of the subharmonic data using wavelet technique 113

Figure 4.6: Comparing RMSEs obtained with different processing techniques.................114

Figure 4.7: Comparing SHAPE results with catheter pressures 116

Figure 4.8: Selection of optimum IAO level for SHAPE 124

Figure 4.9: SHAPE results for LV pressures obtained from canine 1 125

Figure 4.10: SHAPE results for LV pressures obtained from canine 2 126

Figure 4.11: SHAPE results in the LV 131

Figure 4.12: SHAPE results in the RV 138

Figure 4.13: IVC and PV pressure waveforms 147

Figure 4.14: PV pressures before and after inducing PH 149

Figure 4.15: Pulsatility index before and after inducing PH 149

Figure 4.16: Diameter before and after inducing PH...150

Figure 4.17: Boxplot of subharmonic signal amplitudes obtained with different transmit parameters...158

Figure 4.18: MIP subharmonic images of the data obtained from ROI 159

Figure 4.19: PV pressure changes vs. subharmonic signal amplitude changes for 3 transmit cycles 160

Figure 4.20: PV pressure changes vs. subharmonic signal amplitude changes for 4 transmit cycles 161

Figure 4.21: Absolute PV pressures vs. absolute subharmonic signal amplitude acquired for 4 transmit cycles....164

Figure 4.22: Output of the IAO optimization function....172

Figure 4.23: Representation of the subharmonic signal at varying IAO levels used in the optimization function....173

Figure 4.24: PV pressures vs. subharmonic signal amplitudes....175

Figure 4.25: Proposed flow chart for selection of optimum IAO levels for *in vivo* SHAPE....188

List of Abbreviations

ACCORD: Action to Control Cardiovascular Risk in Diabetes

ANOVA: Analysis of Variance

A-V shunt: Arterial-Venous (A-V) Shunt

BMI: Body Mass Index

BNP: B-type Natriuretic Peptide

BP: Blood Pressure

CEUS: Contrast Enhanced Ultrasound

DICOM: Digital Imaging and Communications in Medicine

EFSUMB: European Federation of Societies for Ultrasound in Medicine and Biology

FDA: Food and Drug Administration

FFT: Fast Fourier Transform

HCC: Hepatocellular Cancer

HVPG: Hepatic Venous Pressure Gradient

IAO: Incident Acoustic Output

IVC: Inferior Vena Cava

LSM: Liver Stiffness Measurement

LV: Left Ventricle/Ventricular

LVD$_{min}$: Minimum LV Diastolic Pressure

LVEDP: LV End Diastolic Pressure

LVPSP: LV Peak Systolic Pressure

MELD: Model for End-stage Liver Disease

MLVDP: Mean LV Diastolic Pressure

MI: Mechanical Index

MIP: Maximum Intensity Projection

MRI: Magnetic Resonance Imaging

PCWP: Pulmonary Capillary Wedge Pressure

PH: Portal Hypertension

PV: Portal Vein

PW: Pulse Wave

RA: Right Atrium/Atrial

RF: Radiofrequency

RMSE: Root Mean Square Error

ROI: Region of Interest

ROI_{PV}: Region of Interest with the PV

RP: Rayleigh-Plesset (as in RP equation)

RV: Right Ventricle/Ventricular

RVD_{min}: Minimum RV Diastolic Pressure

RVSP: RV Systolic Pressure

SHAPE: Subharmonic Aided Pressure Estimation

SH_{All_Frames}: Subharmonic Amplitudes from Mean Signal of All Frames

SH_{MIP}: Subharmonic Amplitudes from MIP image

TDI: Tissue Doppler Imaging

UCA: Ultrasound Contrast Agent

Abstract

Noninvasive Ambient Pressure Estimation using Ultrasound Contrast Agents
– Invoking Subharmonics for Cardiac and Hepatic Applications

Jaydev Dave
Flemming Forsberg, PhD and Peter Lewin, PhD

Ultrasound contrast agents (UCAs) are encapsulated microbubbles that provide a source for acoustic impedance mismatch with the blood, due to difference in compressibility between the gas contained within these microbubbles and the blood. When insonified by an ultrasound beam, these UCAs act as nonlinear scatterers and enhance the echoes of the incident pulse, resulting in scattering of the incident ultrasound beam and emission of fundamental (f_0), subharmonic ($f_0/2$), harmonic ($n*f_0$; $n\in$ N) and ultraharmonic ($((2n-1)/2)*f_0$; $n\in$ N & $n > 1$) components in the echo response.

A promising approach to monitor *in vivo* pressures revolves around the fact that the ultrasound transmit and receive parameters can be selected to induce an ambient pressure amplitude dependent subharmonic signal. This subharmonic signal may be used to estimate ambient pressure amplitude; such technique of estimating ambient pressure amplitude is referred to as subharmonic aided pressure estimation or SHAPE. This project develops and evaluates the feasibility of SHAPE to noninvasively monitor cardiac and hepatic pressures (using commercially available ultrasound scanners and UCAs) because invasive catheter based pressure measurements are used currently for these applications.

Invasive catheter based pressure measurements pose risk of introducing infection while the catheter is guided towards the region of interest in the body through a percutaneous incision, pose risk of death due to structural or mechanical failure of the

catheter (which has also triggered product recalls by the USA Food and Drug Administration) and may potentially modulate the pressures that are being measured. Also, catheterization procedures require fluoroscopic guidance to advance the catheter to the site of pressure measurements and such catheterization procedures are not performed in all clinical centers. Thus, a noninvasive technique to obtain ambient pressure values without the catheterization process is clinically helpful.

While an intravenous injection is required to inject the UCAs into the body, this procedure is considered noninvasive as per the definition provided by the Center for Medicare and Medicaid Services; invasive procedures include surgical procedures as well as catheterization procedures while minor procedures such as drawing blood (which requires a similar approach as injecting UCAs) are considered noninvasive.

In vitro results showed that the standard error between catheter pressures and SHAPE results is below 10 mmHg with a correlation coefficient value of above 0.9 – this experimental error of 10 mmHg is less than the errors associated with other techniques utilizing UCAs for ambient pressure estimation. *In vivo* results proved the feasibility of SHAPE to noninvasively estimate clinically relevant left and right ventricular (LV and RV) pressures. The maximum error in estimating the LV and RV systolic and diastolic pressures was 3.5 mmHg. Thus, the SHAPE technique may be useful for systolic and diastolic pressure estimation given that the standard recommendations require the errors for these pressure measurements to be within 5 mmHg. The ability of SHAPE to identify induced portal hypertension (PH) was also proved. The changes in the SHAPE data correlated significantly ($p < 0.05$) with the changes in the portal vein (PV) pressures and the absolute amplitudes of the subharmonic signal also correlated with absolute PV pressures.

The SHAPE technique provides the ability to noninvasively obtain *in vivo* pressures. This technique is applicable not only for critically ill patients, but also for screening symptomatic patients and potentially for other clinical pressure monitoring applications, as well.

1. INTRODUCTION

1.1 An Overview

Ultrasound contrast agents (UCAs) are microbubbles that contain a gas core encapsulated within a shell (for stabilization) and have mean diameters less than 5 µm so that they can traverse the entire vasculature (1). Subharmonic aided pressure estimation (SHAPE) is a technique that involves utilizing subharmonic signals (signals at half the transmit frequency) exclusive to UCAs for ambient pressure estimation (2, 3) *in vitro* and *in vivo*. The concept of SHAPE revolves around the fact that the ultrasound-transmit parameters (e.g., transmit frequency, incident acoustic output (IAO), number of transmit cycles, etc.) can all be tailored to induce ambient pressure dependent subharmonic signals from the UCAs (2, 3). Therefore, the long-term goal of this project is to develop and evaluate the feasibility of SHAPE to noninvasively monitor *in vivo* pressures. Specifically, in this thesis, the clinical focus will be towards assessing the feasibility of SHAPE for measuring cardiac and hepatic pressures – both clinical applications utilizing invasive catheterizations for pressure monitoring as a standard approach (4, 5).

Invasive catheter based pressure measurements pose risk of introducing infection while the catheter is guided towards the region of interest in the body through a percutaneous incision, pose risk of death due to structural or mechanical failure of the catheter (which has also triggered product recalls by the USA Food and Drug Administration (FDA)) and may potentially modulate the pressures that are required to be measured (4, 6-13). Also, catheterization procedures require fluoroscopic guidance to advance the catheter to the site of pressure measurements and such catheterization procedures are not performed in all clinical centers (14, 15). Thus, a noninvasive technique to obtain ambient pressure values without the catheterization process will be clinically helpful. An intravenous injection of UCAs is considered noninvasive as per the definition provided by the Center for Medicare and Medicaid Services (16); invasive procedures include surgical procedures as well as catheterization procedures while minor procedures such as drawing blood (which requires a similar approach as injecting UCAs) are considered noninvasive.

Previously, other *in vitro* techniques to utilize UCAs for pressure monitoring have yielded errors in the range of 10 to 50 mmHg which is clinically unacceptable (17-21), because the recommendations for using a technique for systolic and diastolic pressure assessments require the errors to be within 5 mmHg (at least for 50 % of the recordings) (22). An initial proof-of-concept SHAPE study with an invasive approach yielded a maximum standard error of 5.4 mmHg corresponding to a root mean square error (RMSE) of about 27 % in the aorta of canines (23). Thus, the work in this thesis will evaluate if the SHAPE technique has translational potential for noninvasive *in vivo* pressure estimation.

If the SHAPE technique can be successfully implemented and tested, then the technique will reduce the number of invasive catheterizations and the associated risks as well as costs for cardiac and hepatic pressure monitoring. Also, this SHAPE approach will have the potential to improve patient management by providing absolute pressures and replacing the existing auxiliary pressure estimates/indices (5, 14, 24-38) which are mostly applicable in specific subsets of clinical pathologies for the aforementioned clinical applications. As microbubble-based UCAs are already approved in the United

States for Left Ventricle (LV) opacification and due to promising clinical applications based on UCAs to assess severity of portal hypertension (PH) (39), the SHAPE approach will enhance the utility of the administered contrast agent. Finally, this innovation will provide the ability to noninvasively obtain *in vivo* pressures not only for critically ill patients, but also for screening symptomatic patients and potentially for other clinical pressure monitoring applications as well, such as interstitial fluid pressure measurements in tumors, pressure measurements in renal vasculature, etc.

1.2 Thesis Objective(s)

A practical and clinically feasible SHAPE approach to determine ambient pressures using UCAs will be developed and investigated *in vitro*. Then, refinement of this technique will be used to assess the feasibility of noninvasive cardiac and hepatic pressure monitoring in canines. For all purposes the ambient pressures around the UCAs both *in vitro* and *in vivo* will be monitored using a calibrated solid state pressure catheter as a reference standard. The specific aims and hypotheses for this thesis are now presented.

Specific Aim 1**: To develop and evaluate the feasibility of SHAPE *in vitro*.**

All previous attempts to harness the capability of the UCAs for measuring ambient pressures have lacked a clear translational potential, because these investigations used in-built (specifically-built) hardware platforms, or specifically engineered UCAs, or an equipment setup that is not feasible for clinical use. Such bench top approaches are required for verifying the initial hypothesis (e.g., in (3)), but the concepts and techniques need to be implemented on commercially available platforms for translation into clinical use. *Specific Aim 1* was designed, primarily, to address this goal - commercially available ultrasound scanners and UCAs will be selected and used. A suite of signal processing techniques will be developed for SHAPE applications (based on the ultrasound data format made available by the manufacturers).

Eventually, *in vivo* pressure monitoring using SHAPE may require obtaining temporal waveforms of pressure fluctuations. Thus, the functionality and reproducibility of SHAPE algorithm for tracking dynamic pressures *in vitro* will be investigated. Previous attempts to utilize UCAs for *in vitro* ambient pressure estimation have yielded errors above 10 mmHg (17-21) – this specifies the upper limit on errors for *Hypothesis 1*.

Hypothesis 1: Standard error between catheter pressures and SHAPE results will be below 10 mmHg with an $r^2 > 0.75$ for continuous runs of at least 4 seconds.

Specific Aim 2: **To develop and evaluate the feasibility of using SHAPE for tracking and measuring clinically relevant left ventricle (LV) and right ventricle (RV) pressures noninvasively in canines.**

Here, the SHAPE technique developed under *Specific Aim 1* will be tested to monitor cardiac pressures in canines. The approach will be noninvasive i.e., all ultrasound scanning for SHAPE will be performed with closed chest cavity; unlike previous attempts (23). More specifically, the potential of SHAPE to track clinically relevant LV and RV systolic and diastolic pressures will be investigated. For cardiac SHAPE, this will serve as a pilot study for noninvasive testing of SHAPE and thus, no a priori power analysis will be performed. Data from five canines will be used to test this proof-of-concept and evaluate the following hypotheses:

Hypothesis 2: SHAPE data will correlate with catheter pressures with an $r^2 > 0.75$.

Hypothesis 3: SHAPE results in the LV and RV will be in agreement with catheter pressures and show a maximum error of less than 10 %.

The criteria of 10 % maximum error was selected because the trend in pressure fluctuations in addition to the absolute pressure values is also desirable. Thus, if all the errors associated with the SHAPE technique show either positive or negative errors then the trend analysis will be useful to monitor pressure fluctuations as well, which are also clinically useful, in addition to the absolute pressure values[1].

---

[1] Personal communication with Joel S. Raichlen, MD, FACC (joel.raichlen@astrazeneca.com)

In order to test *Hypothesis 3* and to obtain absolute values of LV and RV systolic and diastolic pressures, a calibration factor in mmHg/dB will be calculated using least square regression analyses based on the aortic data (utilizing both subharmonic data and pressure values). This calibration factor will be applied to the subharmonic data from the LV of the individual canines to determine clinically relevant LV systolic and diastolic pressures which include the mean LV diastolic pressure (MLVDP), minimum LV diastolic pressure (LVD_{min}), LV end diastolic pressure (LVEDP) and LV peak systolic pressure (LVPSP) (40). The LV pressure estimates will also be obtained with the mean calibration factor determined from all the canines. This supplementary test will provide verification of a sub-hypothesis i.e., can a single calibration factor be used across all canines/clinical cases? Next, for the RV, the calibration factor obtained from the aorta will be used with the right atrial (RA) pressures (that can be obtained noninvasively) and the subharmonic data from the RV to obtain specific RV pressures, namely, minimum RV diastolic pressure (RVD_{min}), RV systolic pressure (RVSP) and the RV relaxation rate i.e., peak isovolumic –dp/dt values (40). These LV and RV pressure values obtained with the SHAPE technique will be compared to the reference pressures obtained using a Millar pressure catheter using two tailed paired t-tests. Two tailed paired t-tests will be used because it is not known (a-priori) if the pressures estimated with the SHAPE technique will be above or below the pressures obtained using the Millar pressure catheter.

***Specific Aim 3*: To develop and evaluate the feasibility of SHAPE to investigate portal hypertension (PH) in canines and the implementation of the SHAPE approach on a commercial scanner for future clinical evaluation.**

The normal portal vein (PV) pressures in humans range from 6 to 12 mmHg (5, 41, 42). Portal hypertension (PH) is defined as absolute increases in PV pressures over the normal range or if the pressure gradient between the PV and the hepatic vein or the inferior vena cava (IVC) exceeds 5 mmHg (43). The clinical complications associated with PH manifest only after severe liver dysfunction or cirrhosis develop and are accompanied by relatively high mortality rates (20 to 70 % mortality within 2 years); thus identifying nascent PH is clinically beneficial.

In *Specific Aim 3*, the efficacy of the SHAPE technique for monitoring PV pressures and distinguishing baseline and induced PH states will be investigated. Once again a canine model will be used. Twenty-two canines will be used to develop SHAPE processing technique and to evaluate the feasibility and application of SHAPE to identify PH in canines; with 3 repetitions in each canine, the data obtained will have sufficient power (i.e., > 0.8) to detect the relationship of decrease in the subharmonic signals with an increase in PV pressures if a large effect (r > 0.5) genuinely exists (44). Portal hypertension will be induced under low flow and high flow conditions in the PV. A different ultrasound scanner as compared to the one used in *Specific Aim 2* will be used to establish that the SHAPE application is independent of any specific hardware platform and that the concept of SHAPE can readily be implemented on other ultrasound scanners as well by incorporating the processing techniques developed for SHAPE on the other scanners. Finally, the SHAPE approach developed will be ported on to an ultrasound scanner and the implementation of this approach will be verified explicitly in a group of canines wherein PH will be induced using either the low- or the high- flow PH model. The selection of a particular model to establish acute low- or high- flow conditions in the PV will be based on data published in literature and the observations made by a radiologist, an ultrasonographer, and a certified veterinary technician present during the experiments. No explicit measurements to quantify flow will be performed in this work so as to maintain the patency and the accessibility of the PV for acquiring ultrasound data for SHAPE.

Hypothesis 4: SHAPE results will be able to identify induced PH (PV pressures above 10 - 12 mmHg) under both low flow and high flow conditions.

Hypothesis 5: The changes in subharmonic signals obtained for SHAPE will correlate significantly with changes in PV pressures ($p < 0.05$; baseline vs. PH).

Hypothesis 6: SHAPE data will correlate with catheter pressures with an $r^2 > 0.75$.

To test *Hypotheses 4-6*, linear regression analysis will be conducted to establish the relationship between subharmonic data and the pressure catheter data and also the changes in the subharmonic data due to induced PH. Two tailed paired t-test will be used to identify significant changes (p-values < 0.05) in the subharmonic amplitude before and after inducing PH. To evaluate the robustness of the results, a cross-validation study will be performed to estimate the errors obtained with the SHAPE technique. For the cross-validation study, data from one canine under baseline and PH will be eliminated and, a linear model between subharmonic amplitude and the PV pressures will be obtained using data from the remaining canines. Then, based on this linear model the PV pressures at baseline and at PH condition will be calculated for the canine not included in the linear model and compared to the pressure catheter data. Also based on the pressures obtained with this cross-validation approach, the sensitivity, specificity and the accuracy of identifying PH in these canines will be calculated.

Note, for *Specific Aims 1-3* (*Hypotheses 1-6*), all statistical analyses will be performed using IBM SPSS Statistics (IBM Corporation, Armonk, NY) licensed by the Drexel University. Also, for *Specific Aims 2 and 3*, all canine experiments will be conducted as per specific guidelines by the American Veterinary Medical Association to alleviate animal discomfort and ensure compliance with the Institutional Animal Care and Use Committee. Before clinical evaluation of the efficacy and accuracy of the SHAPE technique, *in vivo* verification in canines (*Specific Aims 2 and 3*) is warranted. Canines have been selected for these studies, because smaller animals, such as rabbits, have blood vessels too small to catheterize and because some species, such as swine, may have marked pulmonary hypertension during contrast microbubble experiments (45). The initial proof-of-concept *in vivo* study was also performed in canines (23). Also the team at Thomas Jefferson University has had extensive experience in UCA studies in canines.

Chapter 2 highlights the clinical need for measuring *in vivo* pressures, specifically for cardiac and hepatic applications. Chapter 3 then presents the materials and methods espoused to address *Specific Aims 1-3*. Chapter 4 presents the results and the discussions in light of the relevant published literature. Chapter 5 summarizes the conclusions of this work with some future recommendations. Additional material is included in the Appendices placed towards the end of the thesis.

2. BACKGROUND AND LITERATURE REVIEW

This chapter explains the clinical need for monitoring central cardiac pressures and PV pressures noninvasively, as well as provides a current review of the techniques that are being used to obtain these pressures. Then, an overview of the UCAs is provided along with the rationale for potential use of the UCAs as ambient hydrostatic pressure sensors.

2.1 Cardiac Pressure Monitoring

2.1.1 Need for Cardiac Pressure Monitoring

Cardiovascular diseases are ranked as the top cause of mortality responsible for 25.4 % of the total deaths in the United States (46). A recent update from the American Heart Association predicts mortality of about 2,200 Americans per day attributable to cardiovascular diseases – equivalent to 1 death every 39 seconds (47). Also, worldwide cardiovascular diseases are the dominant cause of mortality (48). High blood pressure (BP; systolic BP $\geq$ 140 mmHg and/or diastolic BP $\geq$ 90 mmHg) is prevalent in about 92 % of American adults suffering from cardiovascular diseases (47). Monitoring peripheral BP during routine clinical assessment with a cuff sphygmomanometer at the brachial artery is common. Unfortunately, this peripheral BP measurement does not reveal information about systolic and diastolic pressures in the cardiac chambers (49, 50), which tend to be more useful for screening, diagnosing and monitoring therapeutic outcomes in cardiac patients as is explained in this section below.

Pressure measurements within the chambers of the heart provide essential information for the assessment and management of patients in cardiogenic shock or other circulatory compromise. The assessment of intra-cardiac pressures is of particular use in determining the contribution of heart failure in complex clinical situations such as sepsis, acute renal failure or acute coronary syndrome, and for the assessment of efficacy of treatment (51). Direct measurement of intra-cardiac pressures plays a role in the evaluation of the patient with dyspnea and concomitant pulmonary and cardiac disease, and patients with heart failure with preserved LV systolic function also benefit from accurate quantification of LVEDP, for diagnosis, intervention and prognosis. Central BP measurements in the LV and RV for the systolic and diastolic phases are of use to the clinician.

The central cardiac BP and hemodynamics may be a better indicator than peripheral BP of the target organ damage due to the increased BP - specifically to the heart, the brain and the kidney (50). Furthermore, a study involving 2,073 participants showed that different drugs affect the central BP and the peripheral BP differently (52). That study revealed that amlodipine and/or perindopril treated subjects showed a significant reduction in the central systolic BP (4.3 mmHg; 95 % CI: 3.3 to 5.4; $p < 0.0001$) and the central aortic pulse pressure (3.0 mmHg; 95 % CI: 2.1-3.9; $p < 0.0001$), while their peripheral systolic BP remained relatively constant (0.7 mmHg; 95 % CI: -0.4 to 1.7; $p = 0.2$) as compared to subjects treated with atenolol and/or diuretic regimen. Thus, monitoring drug effects may benefit from the knowledge of central cardiac pressures. A meta-analysis conducted to review the effect of different antihypertensive treatments with heart failure as clinical end-point, showed that treatments with diuretics was the best, followed by angiotensin converting enzyme inhibitors, angiotensin-II receptor blockers, calcium channel blockers and beta blockers (53). The performance of alpha blockers was poor with respect to placebo (53). However, with a different clinical end-point such as stroke, the performance of calcium channel blockers was found to be superior (54). This disparity arises from the fact that control in BP arising from different treatment regimens, can have different impact based on the observed clinical end-point. On the other hand, no change in primary outcome observed in the ACCORD (Action to Control Cardiovascular Risk in Diabetes) trial for patients treated with intense systolic BP reduction strategy (< 120 mmHg) as compared to control patients (55), suggests that knowing ventricular diastolic filling pressures may play a crucial role in prognosis. Thus knowing changes in peripheral and central BP (both systolic and diastolic) is worthwhile for treatment monitoring.

Additionally, knowledge of LV filling pressure is extremely important in the diagnosis and treatment of severe cardiac decompensation[2] while the “left-sided pressure estimation has remained an elusive goal of noninvasive cardiac imaging” (56). Also, systolic and diastolic heart failure (left-sided or right-sided or both), which are responsible for over 1 million hospitalizations annually, frequently requires hemodynamic monitoring (4, 47, 57). The hemodynamic pressures at the level of the heart are also required in cardiac transplantation work-up (4). Additionally, moderate to severe episodes of biopsy negative rejections following heart transplantations are accompanied by changes in the intra-cardiac pressures, which may require cardiac pressure monitoring (58).

---

[2] Personal communication with Joel S. Raichlen, MD, FACC (joel.raichlen@astrazeneca.com)

Further, the RV has limited ability to cope with abnormal hemodynamic loading and chronic pressure loading before severe RV dysfunction or RV failure occurs (33). Since various cardiac abnormalities affect RV functionality (59), obtaining and measuring RV pressures is clinically relevant and necessary. The RV dysfunction is a presage for inferior prognosis in patients with ischemic and idiopathic dilated cardiomyopathy, acute myocardial infarction, myocarditis and predicts survival in advanced congestive heart failure cases (60). The RV output is extremely sensitive to changes in the afterload (33) and the histological changes (in myocardial density) associated with RV pressure overload states are more pronounced compared to the volume overload states (61, 62). This implies that early determination and treatment of RV pressure overload may circumvent structural changes which may otherwise occur due to overpressures. High RVSPs (above 35 mmHg) also portend decreased survival in cardiac resynchronization therapy patients (63). An impairment in RV relaxation, identified by monitoring RV filling pressure difference, is marked by a reduced RV driving force (64) – the mean peak RV filling pressure difference was 1 mmHg in patients with dilated cardiomyopathy as compared to 1.4 mmHg in age-matched controls and 2.3 mmHg in young healthy volunteers. Thus, measuring the RV filling pressures may help identify RV diastolic dysfunction. Finally if the pressure waveforms are obtained from the cardiac chambers then they can be used to monitor wave reflection, ventricular relaxation and cardiac index in patients (65, 66).

In summary, obtaining central cardiac pressures in the LV and the RV is clinically beneficial and important.

2.1.2 Need for Noninvasive Cardiac Pressure Monitoring

The techniques used to obtain the central BP can be broadly classified as invasive or noninvasive. Invasive techniques include fluid filled catheters and micro-tip pressure transducers (49). These catheterization techniques can provide accurate absolute pressure values (4), but they require frequent calibration with changes in the patient's position (49). More importantly, the invasive approach is expensive and is accompanied by a risk of introducing infection. Consequently the merits of invasive catheterization procedures are, therefore, debated vigorously, which underscores the need for alternative noninvasive and reliable methods to obtain the central pressure values (4, 6-12). Whereas one study in a cohort of 5,051 patients showed that the catheterization process did not result in increased mortality or days in hospital but also did not confer any clinical benefit (12), another study with 5,735 patients revealed that increased mortality, cost and length of hospital stay were all associated with the catheterization process (6). The inherent distortion in the pressure introduced by the catheter cannot be neglected either. Also safety issues related to the mechanical, structural or functional failure of these catheters have triggered the USA FDA initiated recalls for the affected catheter models – the latest one being in March, 2011 (13); such safety issues indicate the need for accurate and reliable noninvasive pressure measurement techniques.

2.1.3 Noninvasive Techniques for Cardiac Pressure Monitoring

Currently used noninvasive techniques to monitor the central BP include applanation tonometry, plethysmography and ultrasound-based techniques (49). Briefly, applanation tonometry (based on deformation force calculations) is limited due to the preferred locations for this technique – the radial or the carotid artery (49). The waveform from the radial artery requires calibration (dependent on individual patients) to indicate central pressures, while the application at the carotids may activate baroreceptors and inherently suffers from a lack of posterior bony structure (49). Another limitation of this technique is its sensitivity to motion artifacts (49). Plethysmography techniques (to measure changes in blood volume content) have been shown to be more accurate revealing changes in the BP and pressure derived parameters like pulse amplitude variations as compared to indicating the absolute pressure values (49).

An ultrasound based technique for tracking pressure monitors the changes in the BP modulated distensibility of the arteries (67). These changes may be used to indirectly provide a rough estimate of the underlying BP. A more commonly used ultrasound technique to assess the pressure gradients in the chambers of the heart is based on Doppler echocardiography - measuring the blood velocity and then use a modified form of the Bernoulli equation (change in pressure ~ $4xV^2$; V: velocity; assuming negligible flow acceleration effects, negligible viscous friction losses and very low proximal flow velocities relative to the distal flow velocities across the orifice i.e., the heart valves) (49). Noninvasive pressure determinations have been made using Doppler estimates of transvalvular pressure gradients. Estimates of pulmonary artery systolic pressures are generated by combining RV–RA pressure gradients obtained by Doppler, with estimates of RA pressure (56, 68). The estimation of LV diastolic pressures can be approached using measurements of pressure differences in or around the left heart. In the presence of aortic insufficiency, the Doppler gradient across the aortic valve can be combined with the diastolic blood pressure, to provide an estimate of LV diastolic pressure[3]. In the absence of aortic valvular disease, LV diastolic pressures could be estimated from knowledge of the difference in LV systolic and diastolic pressure, combined with the systolic blood pressure[4]. But the pressures obtained using the Doppler methods have been documented to be unreliable and not reproducible (69, 70).

Another study aimed to measure local pressures in “large” arteries (2.5 cm diameter based on *in vitro* phantom setup) by using ultrasound and a pulse-wave velocity approach showed a precision of 1.5 mmHg (71). Unfortunately these results are immature, again, due to idealized *in vitro* conditions that do not mimic *in vivo* situations (e.g., flow tube had uniform mechanical properties, depth of scan was 2 cm, maximum monitoring time was limited to 3.8 seconds, only pulse wave (PW) velocities less than 0.8 m/s would yield accurate results, perpendicular insonification requirement and errors that would be introduced for noncircular areas in the vessel or nonuniform tissue properties) and thus, future *in vivo* work to measure pressures in the cardiac chambers appears to be doubtful (71). The inability of these noninvasive methods to accurately yield systolic and diastolic LV and RV pressures has paved way for the cardiovascular community to embrace auxiliary or indirect estimates/indices for assessing functional changes associated with overpressures.

Several Doppler indices have been proposed for predicting LV filling pressures and function, however there is no single index that has gained widespread clinical use (24, 26, 28, 35, 37, 38), particularly due to proven efficacy only in certain subsets of

---

3 Personal communication with Joel S. Raichlen, MD, FACC (joel.raichlen@astrazeneca.com)

4 Personal communication with Joel S. Raichlen, MD, FACC (joel.raichlen@astrazeneca.com)

clinical pathologies. For example, the ratio of isovolumetric relaxation time to the time interval between the E wave (mitral inflow velocity on conventional Doppler) and the Ea wave (annular early diastolic velocity) can track pulmonary capillary wedge pressures (PCWP), however only in patients with mitral valve disease (26). Also, LV systolic function evaluated using the instantaneous ejection intra-ventricular pressure difference correlated ($r > 0.85$) with the peak of dP/dT corrected for end-diastolic volume and with the peak elastance (37, 58). Still, this Doppler derived index was used to characterize LV systolic performance and would not be expected to reflect diastolic dysfunction in patients with normal systolic function. Another technique, to quantify LV pressures is based on tissue Doppler imaging (TDI). Tissue Doppler imaging utilizes the high amplitude Doppler signals from the relatively slower moving myocardial tissue (compared to the blood flow within the LV) (29). Mitral inflow velocity and mitral annular movement from TDI may yield accurate left atrial pressures, which could be combined with transmitral pressure gradients to permit estimation of LV filling pressures (29, 56). The TDI techniques provide a rough assessment of whether or not LVEDP exceeds 15 mmHg (30), but a more specific measurement (i.e., absolute pressure values) would clearly be of great benefit to the clinician. Another study compared TDI and B-type natriuretic peptide (BNP; obtained from venous blood samples) in 50 patients to estimate LV filling pressures (27). This study found that BNP detected PCWP greater than 15 mmHg in patients without cardiac disease whereas the TDI echocardiography index (E/Ea) detected this increase in patients with cardiac disease, again exemplifying the deterrent to a widespread application of any particular index to gauge all cardiac pressures. Given the results from the above 2 studies, currently a resolution of 15 mmHg may be the best capability of techniques based on TDI (27, 30).

For the RV, calculation of ejection fraction has been a primary echocardiographic measurement to evaluate the systolic function. This ejection fraction can be measured noninvasively and accurately only by cardiac magnetic resonance imaging (MRI), which is expensive and may not be available in all clinical centers let alone in the clinician's office (33). Instead the 2D echocardiographic size measurements from the apical four-chambered view are used; these measurements obviously do not correlate with 3D volumes but are still used because the 3D echocardiographic assessments await standardization before clinical acceptance is possible (33, 34).

Thus, there is a clinical need to obtain LV and RV pressures. There are shortcomings of currently available techniques and indices to delineate these pressures. Swan-Ganz catheter (balloon flotation catheter requiring invasive access to vasculature) is therefore an accepted "gold" standard to assess cardiac hemodynamics (including pressures) and to classify patient populations into subsets for therapy and monitoring (4).

2.2 Portal Vein (PV) Pressure Monitoring

Anatomically, the superior mesenteric vein (from the small intestine, sometimes also the inferior mesenteric vein)[5] and the splenic vein (from the spleen) unite to form the PV that supplies 2/3rd of the total hepatic blood flow (72). Under normal conditions, the hepatopetal blood flow in the PV is about 700-1200 ml/min at 15-18 cm/s and it supplies about 50 % of the oxygen consumed by the liver (43, 72). The normal PV pressures range from 6 to 12 mmHg (5, 41, 42). Portal hypertension (PH) is defined as absolute increases in PV pressures over the normal range or if the pressure gradient between the PV and the hepatic vein or the IVC exceeds 5 mmHg (43).

---

[5] Personal communication with Daniel B. Brown, MD (Daniel.Brown@jefferson.edu)

2.2.1 Need for PV Pressure Monitoring

Hepatic cirrhosis is characterized by a prolonged pre-clinical phase (with stealthy disease progression) and then a short clinical phase wherein the symptoms manifest and are mostly fatal (73). Clearly an early identification of cirrhotic liver may mitigate fatalities. The transition from pre-clinical to clinical phase for the cirrhotic liver is marked by PH i.e., elevated pressures in the PV (73).

Chronic liver diseases also lead to PH, but nonetheless cirrhosis (mostly alcohol induced) accounts for over 90 % of the PH cases in the developed world (43). Pathophysiologically, an increase in intrahepatic vascular resistance due to architectural distortion of the liver (by fibrosis and increased sinusoidal tone) followed by an hyperdynamic circulatory state with increased plasma volume causing an increase in PV inflow contribute to PH states (73, 74). These factors contribute to an increase in the pressure gradient between the PV and the IVC as per the modified form of Ohm’s law for fluid flow (75),

$$\Delta P = Q \; x \; R \qquad \text{Equation 2.1}$$

where, ‘ΔP’ represents change in pressure, ‘Q’ and ‘R’ represent flow and resistance.

Etiologically, the origin of PH may be pre-, intra- or post- hepatic (43).

Common complications associated with PH are ascites, encephalopathy and variceal bleeding, but still the natural history of PH and its complications remain to be understood (15). For example, the formation and the rate of development of esophageal varices followed by fatal bleeding episodes vary based on the nature of liver dysfunction, cause of cirrhosis (alcoholic or viral induced); the development rate exceeds the formation of a new varix and the rupture ultimately occurs after the pressures in dilated mucosal veins exceed an unknown threshold dependent on hemodynamics and vessel wall properties (73, 76-78). The mortality associated with these common complications is also high e.g., patients with ascites have 50 % two year mortality, which deteriorates to 70 % one year mortality for infections with ascites and variceal bleeding episodes carry up to 20 % risk of death even after endoscopic evaluation/intervention (42, 74, 79). Altogether, clinical manifestations of PH occur only after severe liver dysfunction or cirrhosis have developed and, thus, early identification of PH is crucial for decreasing the associated morbidity and mortality (41, 80).

2.2.2 Need for Noninvasive PV Pressure Monitoring

For directly accessing the PV to measure PV pressures, one of the following approaches is required: percutaneous transhepatic catheterization, needle puncture of umbilical vein, laparotomy, needle puncture of intra-hepatic portal branch or endoscopic-ultrasound guided PV catheterization. All of these processes are very invasive and are no longer performed. Instead, an indirect measure of PH, the hepatic venous pressure gradient (HVPG), is the clinical standard (5). HVPG is calculated as the difference between the wedged/occluded and free hepatic venous pressure (5). HVPG measurement involves introducing a pressure catheter in the hepatic vein for free and occluded pressure measurements mostly performed along with a transjugular liver biopsy (15). PH is considered 'moderate' for HVPG ranging from 5 - 10 mmHg, 'clinically significant' for HVPG ranging from 10 - 12 mmHg and then 'severe' for HVPG above 12 mmHg. The complications associated with PH develop when HVPG is in the range of 10-12 mmHg and the mortality associated with severe PH is very high (> 20 %), whereas risks associated with moderate PH are low. Thus, identifying nascent PH is clinically imperative. Moreover, the value of HVPG measurements in the management of hepatocellular cancer (HCC), which is a common and deadly complication of cirrhosis, has been demonstrated (81). For example, the HVPG predicts hepatic decompensation following hepatic resection of HCC (82). The value of the HVPG has been demonstrated beyond the scenario of variceal bleeding and its prevention. The sinusoidal pressure has been found to correlate with the degree of injury in cirrhosis seen on liver biopsy (83), and with progressive fibrosis due to recurrent hepatitis C after liver transplantation (84). In non-transplant patients, hemodynamic assessments have been performed and a correlation between HVPG and sustained virological response has been shown (85).

Noninvasive technique(s) to measure the HVPG or the PV pressures directly may be of clinical value, as the clinically accepted HVPG measurements are still fairly invasive, are relatively expensive, require radiographic/fluoroscopic guidance to guide the pressure catheter and are not performed in all centers (14). A noninvasive technique may also promote screening patients suspected of having compensated liver diseases to gauge PV pressures or progression of cirrhosis.

2.2.3 Noninvasive Techniques for PV Pressure Monitoring

Some noninvasive techniques are being developed to detect PH (moderate or clinically significant or severe) or to indicate HVPG or to detect cirrhosis. A technique to measure liver tissue stiffness using the Fibroscan apparatus (Echosens, Paris, France) (86) was evaluated as a predictor for severe PH (36). This technique relies on the principle that the induced shear wave velocity is proportional to the liver stiffness measurements (LSMs) and that liver stiffness increases with cirrhosis and/or fibrosis. The study revealed that the correlation coefficient (r^2) between LSMs and HVPG dropped from 0.61 for all patients to 0.17 for patients only with severe hypertension (36). This implies patient monitoring post severe PH is compromised with LSMs (or LSM is independent of fibrotic or cirrhotic liver stiffness after severe PH). This may be a major limitation of the LSM technique for monitoring improvement in clinical management of PH patients given that monitoring reduction in HVPG by greater than 20 % for severe PH, significantly reduces bleeding risks and mortality (87). Also, patient recruitment was biased based on body-mass-index (BMI) – only patients with BMI less than 35 were included as above this range the LSM reproducibility is sub-optimal (36). Similarly, the applicability of this technique in patients with nonalcoholic fatty liver disease may be questionable due to over- or under-estimation of stiffness because of high BMI. While LSMs may be used to select patients with large esophageal varices and subsequent endoscopic follow-up (36), LSMs are prohibited for patients with ascites (because fluid buildup will restrict shear wave propagation and consequently, shear wave velocity measurements).

Another study attempted to quantify splenic stiffness in assessment of PH using MRI (14). The hypothesis driving that study was that esophageal varices developed due to PH may result in splenomegaly ultimately resulting in a modification of spleen stiffness. The group observed a strong correlation ($r^2 = 0.75$) between liver and spleen stiffness, however no correlation was performed between spleen stiffness and HVPG (which was the original objective of the study i.e., to assess PH and its severity) (14). Even if that goal is met and high correlation values are observed in subsequent studies, the use of MRI restricts a number of patient types (e.g., with metallic implants, defibrillators, etc.). Other noninvasive tests such as measurement of cardiac output, circulation hemodynamics, baroreflector sensitivity may provide information about PH, due to the associated hyperdynamic circulatory state (or hyperkinetic syndrome, (15)). In this regard a recent study showed that the heart rate, cardiac index and baroreceptor sensitivity weakly correlated with HVPG measurements (r^2 ranging from 0.28 to 0.48); also the optimal cut-offs need to be defined for predicting clinically significant PH (87). Some other biomarkers that may potentially be useful for assessing cirrhotic PH include serum endothelin levels or endothelial cell count (88, 89), but these need to be validated before they can be used widely along with HVPG. Child–Pugh scores and/or MELD (model for end-stage liver disease) scores were initially used to predict mortality associated with liver diseases and are based on biochemical markers including serum bilirubin, creatinine and albumin, prothrombin time and international normalized ratio, and presence of ascites or hepatic encephalopathy (90). However the Child-Pugh scores have relied on empirical evidence and give equal weight to all sub-components (thus correlated components can amplify the score), whereas the MELD scores lack clearly defined values for categorizing cirrhotic patients (90). Also, these scores are not useful in quantifying PV pressures.

The use of ultrasound to assess several indirect measures predicting PH like PV diameter and flow, hepatic artery and vein flow, subjective evaluation of liver morphology, splenic size, portosystemic collateral and ascites has also been studied (43). Unfortunately PV diameter and flow patterns vary even in PH states, due to differential development of portosystemic shunts and collateral circulation in patients (43, 91). Similarly, other ultrasound based estimators also provide an indirect assessment of HVPG, which in turn is an indirect measure of PV pressures or PH. Another study, analyzed Doppler ultrasound waveforms of the hepatic vein to monitor PV pressures indirectly (25). It was concluded that monophasic or biphasic Doppler waveforms were observed with patients suffering from PH. A triphasic Doppler ultrasound waveform was observed for normal PV pressures. It was also shown that the biphasic waveforms transformed to triphasic (6/8 patients) and the monophasic waveforms transformed to biphasic (7/11 patients) and triphasic (4/11 patients), indicating reduction in the PV pressure, following administration of Terlipressin (a vasoconstrictor for the mesentric artery). A major limitation of this study is the lack of quantitative assessment of reduction in the PV pressures. Further the inter-observer variability was tested with n = 2. Also, the role of treatment agents may have different effects on the Doppler waveforms of the hepatic vein, thereby restricting the usefulness of this technique (25). In a subsequent study, a quantitative parameter called the damping index (ratio of minimum to maximum hepatofugal flow velocities) was compared with HVPG and also evaluated to track changes in HVPG after propranolol administration (used for decreasing hypertension) (31). This damping index showed a weak correlation with HVPG (r^2 = 0.42) and changes in HVPG after drug administration also weakly correlated with changes in damping index (r^2 = 0.47). However, an increase in HVPG (in 2 patients) after drug administration showed a corresponding increase in the damping index in only 1 patient, while no changes in HVPG were also marked by changes in damping index (31). This reveals that tracking changes in damping index for analyzing changes in HVPG (and hence in severity of PH) after treatment may be limited. Also Doppler measurements are known to be operator dependent and all patients in this study were scanned by a single individual, thus repeatability of these measurements with respect to inter-operator dependency needs to be established. Another study added the damping index ratio (calculated at expiration and inspiration) and also the corresponding damping index difference to assess severity of PH (32). These parameters may be indicative of decompensated liver cirrhosis (in patients with higher damping index and damping index ratio, and lower damping index difference) but the efficacy of these parameters for tracking temporal progression of nascent PH to clinically significant and severe levels needs to be validated (32). The safety of an approach combining endoscopy and PV pressure measurements was proved in a live porcine model, however no simultaneous pressure measurements were obtained from other techniques to validate this method (92).

The current requirement by the interventional community for screening, diagnosis, monitoring and prognosis of chronic liver diseases or cirrhosis is a noninvasive, accurate and reliable method to estimate HVPG or PV pressures (15). Such a method will permit repeated PV pressure measurements and thereby, limit the number of endoscopies performed (especially for screening populations or for patients without clinical signs of PH) (15).

Overall, there is a need to obtain *in vivo* pressures noninvasively, at least for cardiac and hepatic applications as the standard clinical approaches rely on invasive catheter based measurements.

2.3 Ultrasound and Ultrasound Contrast Agents (UCAs)

An overview of some of the basic ultrasound concepts is provided specifically in sub-section 2.3.1 for review. An overview of UCAs with the intent of elucidating the mechanism for subharmonic signal generation in the echo response of the UCAs is also provided because the subharmonic signals are used for SHAPE.

2.3.1 Ultrasound

Ultrasound refers to sound waves of frequencies exceeding the range of human hearing (93, 94). Medical ultrasound imaging refers to transmission of sound waves (longitudinal waves comprising of compressions and rarefactions) through a body and production of "echo" images based on the reflected components of these sound waves (93, 94). As sound waves travel through the body, they undergo either reflection, refraction or absorption. Reflection is dependent upon the acoustic impedance (in Rayls) defined by equation 2.2 and the angle of incidence (93, 94),

$$Z = \rho \; x \; v \qquad \text{Equation 2.2}$$

where, ‘Z’ is the acoustic impedance in Rayls, ‘ρ’ is the density of the medium ‘g/cm^3’ and ‘v’ is the velocity of sound in the medium in ‘cm/s’. More specifically, for perpendicular incidence of sound waves on a smooth boundary separating two media with different acoustic impedances, the amount of reflected intensity component ‘R’ of the beam may be calculated as,

$$R = (\frac{Z_1 - Z_2}{Z_1 + Z_2})^2 \qquad \text{Equation 2.3}$$

where, Z_1 and Z_2 are the acoustic impedances of the two media (94).

Consequently, the transmitted intensity component (T) can be calculated as (94),

$$T = 1 - R = \frac{4Z_1Z_2}{(Z_1 + Z_2)^2} \qquad \text{Equation 2.4}$$

An ultrasound transducer converts electrical energy into mechanical energy based on piezoelectricity, thereby creating sound waves that are propagated through the body and the received echoes i.e., mechanical energy is reconverted to electrical energy, which is then used for image formation (95). The ultrasound beam can be broadly classified into a Fresnel zone or the divergent Fraunhofer zone extending beyond the Fresnel zone; the length of the Fresnel zone being dependent on the diameter of the ultrasound transducer and the wavelength of the ultrasound, as given by,

$$Fresnel\ Zone = \frac{D^2}{4\lambda} \qquad \text{Equation 2.5}$$

where, ‘D’ is the diameter of the transducer and ‘λ’ is the ultrasound wavelength (94). Thus by decreasing the ultrasound wavelength, the length of Fresnel zone (non-divergent beam) may be increased; however, a decrease in wavelength is associated with a corresponding increase in the frequency because the speed of sound in a given medium is essentially constant, given by,

$$v = \lambda \, x \, f \qquad \text{Equation 2.6}$$

where, ‘λ’ is the ultrasound wavelength and ‘f’ is the frequency.

The attenuation offered to the ultrasound beam is directly proportional to frequency,

$$Attenuation\ (\mathrm{f}) \sim f^{n} \qquad \text{Equation 2.7}$$

where, ‘f’ represents the frequency and ‘n’ is about 1.1 for soft tissue.

The axial resolution for an ultrasound beam is,

$$Axial\ Resolution = \frac{n\lambda}{2} \qquad \text{Equation 2.8}$$

where, ‘nλ’ represents the spatial pulse length.

Thus, from equations 2.7 and 2.8, it can be seen that a relatively better axial resolution requires a decrease in the ultrasound wavelength (or an increase in ultrasound frequency), but an increase in ultrasound frequency leads to increased attenuation of the ultrasound beam. This necessitates a compromise between the axial resolution of the given ultrasound beam and the depth of penetration. For diagnostic ultrasound imaging, the frequency spans a range from 1 MHz to 18 MHz depending on the clinical applications, whereas specific transducers permitting even higher frequency operations for certain clinical applications utilizing catheter based ultrasound transducers (e.g., intravascular ultrasound) are available (96). For the frequency range of 1 MHz to 18 MHz, the wavelength varies from about 1.5 mm to 0.09 mm, assuming the speed of sound in soft tissue to be 1540 m/s and based on equation 2.6; thus the corresponding axial resolution also varies depending on the number of transmit cycles constituting a given transmit pulse as per equation 2.8. A detailed overview of ultrasound transducers and basic ultrasound scanning modes is not provided in this section because it has been summarized elsewhere[6] (93-95).

The field of diagnostic ultrasound has graduated progressively through single element transducers used in mid-1970s to transducer array based systems, and currently research is being focused on hand held ultrasound systems and real-time 3D/4D imaging (96). This rapid growth of diagnostic ultrasound is also evident from the annual instruments sales cumulating to greater than $4 billion[7]. Also, based on Medicare data it was shown that from 1993 to 2001, the utilization rate of ultrasound examinations increased by about 25 % amongst radiologists, 87 % amongst cardiologists and 43 % amongst other physicians (97). Amongst the cardiologists, a vast majority of the ultrasound examinations were echocardiograms (97). The number of non-cardiac ultrasound examinations has also increased by about 21 % from 2004 through 2009 for the Medicare population (98). Likewise, the total number of emergency department ultrasound examinations in the Medicare population has increased by as much as 164.5 % over the time frame from 1993 through 2001 (99). Although these data (97-99) are based on a specific subset of the American population, a general growth trend in the utilization of ultrasound examinations may be surmised, especially because of the advantages offered by ultrasound over other imaging modalities. The chief advantages include portability, low-cost and real-time imaging. The premier advantage of ultrasound over x-ray based modalities is the non-ionizing nature of ultrasound unlike x-rays where ionization events may pose stochastic risks (e.g., cancer) or deterministic risks (e.g., skin injury) to the patient. The other imaging modalities like fluoroscopy, computed tomography, MRI, etc., have benefitted from utilizing contrast agents for diagnosis, prognosis and therapy especially for vascular anomalies. A similar development in utilizing contrast agents with ultrasound has also occurred (1, 96).

---

[6] Masters Thesis: Novel automated motion compenasation algorithm for producing cumulative maximum intensity images from subharmonic ultrasound imaging of breast lesions (pages: 4-10) – May be accessed from the Drexel University Archives at: http://idea.library.drexel.edu/bitstream/1860/2918/1/Dave_Jaydev.pdf (last verified: May 20, 2012; 22:00)

[7] Ultrasonic Imaging Systems: From Principles to Implementation – A Short Course at the 2011 IEEE Ultrasonics Symposium presented by Kai E. Thomenius, PhD.

The next section introduces UCAs and their basic properties with specific focus on the ambient pressure sensitivity of UCAs, providing a connecting link between the clinical need to obtain *in vivo* pressures and the potential of the UCAs to act as ambient pressure sensors.

2.3.2 Ultrasound Contrast Agents (UCAs)

The field of ultrasound contrast imaging began with a personal communication between Joyner C. Jr. and Gramiak R. in 1968; agitated saline was used with echocardiography and the origin of enhanced echoes in the received signal was attributed to microbubbles in the agitated saline (100, 101). Considering microbubbles with air, the acoustic reflection or scattering from these bubbles for a perpendicular incident beam may be calculated using equation 2.3, and Z_{air} = 0.0004 Rayls and Z_{blood} = 1.61 Rayls (94), as,

$$R = (\frac{0.0004 - 1.61}{0.0004 + 1.61})^2$$

$$R = 0.999 \ or \ 99.9 \ \%$$

Thus, in presence of microbubbles (air/blood or air/tissue interface) more than 99 % of the incident ultrasound beam is reflected or scattered.

In the sub-sections that follow, details about modeling the behavior of microbubbles (both, free or un-encapsulated and encapsulated microbubbles) when subjected to time varying acoustic pressure excitation and the properties of the microbubbles-based UCA are presented before providing a current update on the use of available UCAs and a motivation for using these UCAs as ambient pressure sensors - this forms the background for the work presented in this thesis.

2.3.2.1 Modeling of Un-Encapsulated and Encapsulated Microbubbles

Modern UCAs are encapsulated microbubbles that vary in the chemical composition of the gas contained within the shell and, the encapsulating shell developed to prevent bubble coalescence and breakup under normal conditions. Before studying the behavior of the encapsulated microbubbles, a brief overview of the dynamics of un-encapsulated microbubbles is provided here. Note, that several publications (1, 102, 103) have provided substantial information on the modeling of the microbubbles and in this section the excerpts based on the review of these publications and of other models to predict behavior of microbubbles are given.

In an attempt to study the high pressures developed during the collapse of bubbles, specifically when the collapse is against a rigid obstacle[8], Lord Rayleigh presented the mathematical approach for investigating bubble collapse in an incompressible liquid, which led to one of the basic equation describing bubble dynamics (104),

---

[8] A study, probably undertaken to present an alternate theoretical approach explaining the erosion/surface damage for the propeller blades of the ships used by the Royal Navy, around World War I (Wilson M, Physics Today, September-2010 issue, Pg. 17) and because it was earlier demonstrated by S. Cook that the associated pressures may be greater than 1 GPa (Rayleigh L. Philosophical Magazine Series 6. 1917;34(200):94-8)

$$\rho\left(\frac{3}{2}\dot{R}^2 + R\ddot{R}\right) = P(R) - P_\infty(t) \qquad \text{Equation 2.9}$$

where, ‘ρ’ represents the liquid density, ‘R, R, and R’, represents the instantaneous bubble radius and the velocity and acceleration associated with the bubble boundary motion, ‘P(R)’ is the pressure in the liquid at the bubble boundary and ‘P_∞(t)’ represents the pressure in the liquid at very large distance from the bubble.

The equation 2.9 was not explicitly mentioned in the study (104) - but using the equations of kinetic energy imparted to the liquid due to the bubble boundary motion and the corresponding work done this equation is realized. Also, the effects of surface tension and liquid viscosity were not considered. Therefore, a modified form of equation 2.9, including these effects was presented (105),

$$\left(\frac{3}{2}\dot{R}^2 + R\ddot{R}\right) = Pi(t) - \frac{2\sigma}{R} - \frac{4\mu}{R}\dot{R} - P_\infty(t) \qquad \text{Equation 2.10}$$

where, ‘σ’ represents the surface tension and ‘μ’ represents the coefficient of liquid viscosity. This equation is termed as a generalized Rayleigh-Plesset (RP) equation for bubble dynamics. The significance of the RP equation lies in its solution, which yields the instantaneous bubble wall motion ‘R(t)’; this motion results in an “emitted” (or scattered or reflected) acoustic wave which is a function of the distance from the bubble ‘r’ and time ‘t’, given by,

$$P_s(r,t) = \frac{\rho R}{r}(2\dot{R}^2 + R\ddot{R}) \qquad \text{Equation 2.11}$$

Thus, in simulations, after providing an excitation signal to the bubble, the resulting acoustic wave due to the bubble oscillations may be obtained and may be used to predict the frequency components in the received signal; this information may be then used for designing transmit sequences or specific scanning modes on an ultrasound scanner.

Strasberg showed that the volume pulsations associated with gas bubbles in a liquid could generate pressure waves (106, 107). These volume pulsations i.e., small changes in the radius ($R(t) << R_o$; $R(t)$ instantaneous radius; R_o equilibrium radius) of the gas bubbles, occur due to the changes in the pressure on the bubbles, irrespective of their shape (106, 107). Strasberg also showed that the sound pressure radiated by the gas bubbles could deviate from linearity and exhibit nonlinear oscillations i.e., higher harmonics of the pulsation frequency, when the bubbles are insonated by an external sinusoidally varying pressure (107). Apart from the nonlinear oscillations of higher harmonic frequencies, Neppiras confirmed experimentally the presence of the subharmonic signals from the insonated bubbles in liquids (108). Further, Eller and Flynn calculated the threshold acoustic pressure for subharmonic generation and showed that the minimum pressure value for subharmonic generation occurs when the driving frequency of the external pressure is twice the linear resonance frequency of the bubble (109). Thus, after excitation the response of a microbubble may contain components above and below the frequency of the excitation, and may span a range from the subharmonics to higher harmonics.

Empirically the presence of subharmonics and higher harmonics generated by modern UCAs have also been confirmed (1, 103). These UCAs differ from free bubbles because of an encapsulating shell preserving the gas core as the UCAs traverse the vasculature. Consequently, to better understand the dynamics of encapsulated microbubbles several equations that represent modifications of the RP equation, specifically to include the effect of the encapsulating shell, have been presented in the literature (102, 103). In the following paragraph the models using different approaches for modelling the shell encapsulation have been reviewed with the motivation of providing an accurate encapsulation model that can explain the subharmonic emissions.

The shell encapsulation has been modeled as a viscoelastic solid (110), as an incompressible solid elastic material (111), and as a material with viscous and elastic properties (112) – and RP-type equations were derived for each model. However, the above models required assumptions of isotropy and homoegeneity for the shell (assumed to have finite thickness). Because these assumptions may not be accurate, a different approach to model the shell with an infinitesimal thickness and express the interactions at the boundary with Newtonian interface rheology has been developed (113). The model was validated in the linear regime using experimental data and by comparison with another model (112); the model also predicted the nonlinear behavior specifically the subharmonic response. However, the value for interfacial tension was an order of magnitude higher as compared to the air-water interface tension value of about 0.07 N/m. This cannot be a correct result as the interfactial tension should have been lower relative to the air-water interface because of the surfactants. Susequently, another approach was adopted to model the encapsulation using a non-Newtonian interface rheology including an elasticity component (114) absent in the Newtonian interface rheology model (113). The calculated interfacial tension values were, as expected, about 70 % below the air-water interfacial tension values. However, this model did not predict the subharmonic emissions as well as the Newtonian interface rheology model (113) and (112) – the problem was ascribed to the use of a constant elasticity parameter value. Another model for shell encapsulation was presented based on a ‘buckling’ shell radius, shell compressibilty and maximum interfacial tension value corresponding to the rupture of the

UCAs (115). This model predicted the compression only behavior of the bubbles at acoustic pressures below 150 kPa (115). Two different approaches were adopted to model the encapsulation similar to the non-Newtonian interface rheology model (114), but with either a quadratic elasticity model or a exponential elasticity model (contrary to the linear elasticity model with thresholds based on change in bubble area as used in (115)). Both these models were capable of predicting the subharmonic response from the UCAs, specifically the appearance of a threshold value for IAOs, below which no subharmonic response was present and above which the subharmonic response from the UCA matched the experimental values – note, that this nature of threshold dependent subharmonic emissions was demonstrated by Eller and Flynn for un-encapsulated bubbles (109).

2.3.2.2 Properties of Microbubbles based UCAs

Resonance Frequency: The resonance frequency of an air bubble in water may be roughly estimated using (116),

$$f_o x\ R_o = 3.3 \qquad \text{Equation 2.12}$$

where, ‘f_o’ and ‘R_o’ are the resonance frequency in MHz and the bubble radius in μm, respectively. Another common approximation used to identify the resonance frequency of a bubble neglecting the surface tension and assuming adiabatic conditions is (116),

$$f_o = \frac{1}{2\pi R}\sqrt{\frac{3\kappa P_o}{\rho}} \qquad \text{Equation 2.13}$$

where, ‘P_o’ and ‘ρ’ represent the fluid pressure and density, ‘R’ represents the bubble radius and ‘κ’ is the polytropic gas exponent.

For specific models of encapsulation, the equation for the resonance frequency of the bubble will vary according to the model parameters, but, in general, the resonance frequency of the encapsulated bubble will be greater than the un-encapsulated bubble of the same size (110), mainly due to the damping provided by the encapsulation.

Scattering Cross-section: The scattering cross-section for a small scatterer (small: product of wavenumber 'k' and the radius 'r' of the scatterer is less than 1) is given by (1),

$$\sigma = \frac{4\pi}{9}\, k^4\, r^6\, [\frac{(K_s - K)^2}{K^2} + \frac{1}{3}\, (\frac{3(\rho_s - \rho)}{2\rho_s + \rho})^2] \qquad \text{Equation 2.14}$$

where, 'K' and 'ρ' represent compressibility and the density of the fluid/medium and 'K_s' and 'ρ_s' represent similar quantities for the scatterer. This equation indicates that the scattering cross section depends on the differences in compressibility and the density between the scatterer and the surrounding medium, and is sensitive to the frequency (dependency of the fourth power) and to the radius of the scatterer (dependency of the sixth power). The microbubbles act as good scatterers and enhance the backscattered signals compared to the surrounding fluid i.e., blood (*in vivo*) because of the difference between the compressibility and the density of the gas contained within these microbubbles and the blood; the effect of difference in compressibility is greater because of the squared term in the bracket in equation 2.14. Thus, UCAs are encapsulated microbubbles that provide a source for an acoustic impedance mismatch with the blood, due to difference in compressibility between the gas contained within these microbubbles and the blood (1).

Stability: Modern UCAs consist of a gas core encapsulated in a shell because free bubbles will dissolve within milliseconds after introduction in the vasculature. Also,

$$Diffusivity\ \alpha\ \frac{Solubility}{\sqrt{Molecular\ Weight}} \qquad \text{Equation 2.15}$$

Thus, changing the gas core to contain gases with high molecular weight and low solubility like SF_6 and C_4F_{10} is valuable so that the UCAs are stable for relatively longer durations permitting diagnostic imaging.

Size: The UCAs should have size small enough to pass through the capillaries. The capillaries on average have about a diameter of 7 µm (117) and this represents an upper limit on the size of the UCAs for clinical use. Most commercially available UCAs have mean diameters below 5 µm.

2.3.2.3 UCAs – Status Update & Safety

A summary of currently available UCAs is presented in Table 2.1.

Table 2.1: Currently available UCAs

UCA	Manufacturer	Gas Core	Shell	Approval for clinical use in
Definity®	Lantheus Medical Imaging	C_3F_8	Phospholipids	Canada, USA*
Optison™	GE Healthcare	C_3F_8	Human Albumin	EU, USA*
Sonazoid™	GE Healthcare	C_4F_{10}	Lipids	Japan, S. Korea
SonoVue®	Bracco Diagnostics	SF_6	Phospholipids	EU, China, South America

*: Approved for LV opacification studies

As seen in Table 2.1, in the USA, the FDA approved clinical use of UCAs is restricted to the study of the LV. Optison and Definity received approval for clinical use in the USA in 1997 and in 2001, respectively. The safety concerns over the clinical use of UCAs in the USA arose after 4 deaths following Definity administration which led the FDA to announce a 'black-box' warning for the use of UCAs (118). However as reviewed in (118), these 4 deaths occurred in patients with severe cardiac anomalies and the deaths may presumably be due to "pseudocomplications" i.e, death attributable to either the procedure (Definity administration) or due to the progression of underlying disease states. Main et al further state that even if the deaths were directly due to Definity administration, then, given over 2 million Definity administrations worldwide, the risk of death due to Definity administration will be 1:500,000 – considerably less than the risk of death or myocardial infraction following exercise treadmill testing (1:2500; commonly referred to as stress testing) (118).[9] Further description of events between the FDA and the physicians citing the safety and clinical use and benefits of UCAs is summarized elsewhere (119), finally leading to downgrading of the 'black-box' warning. An in-depth review of the usage and safety profile of UCAs, with prime focus on Definity, has also been provided (120). The limitation of the use of UCAs in the USA is in stark contrast with the recently published update on the guidelines of the European Federation of Societies for Ultrasound in Medicine and Biology (EFSUMB) for contrast enhanced ultrasound (CEUS) in pediatric and adult populations (121). Sonazoid is currently approved for diagnosis in patients with liver lesions in Japan and South Korea

---

[9] In the USA, the average probability of being struck by lightning is 1-in-280,000 (http://www.lightningsafety.com/nlsi_pls/probability.html) or of death due to lightning strike is 1-in-83930 (http://www.livescience.com/3780-odds-dying.html) – these represent far greater risk as compared to deaths due to Definity administration.

(122). The safety of the use of Sonazoid for clinical applications has also been established (123); Sonazoid is not yet approved for clinical use in the USA. [The work presented in this thesis is based on the use of Sonazoid, but may be extended to the other UCAs as well – this is discussed in Chapter 4].

2.3.2.4 Contrast Specific Ultrasound Imaging Modes and Applications

Due to the recent advancements in the field of ultrasound imaging and UCAs (such as the production of stable encapsulated microbubbles and their capability to traverse the entire vasculature) several contrast specific non-linear imaging modes have been developed to increase the sensitivity and specificity of CEUS, e.g., (1, 124-129). Acting as nonlinear scatterers the microbubbles enhance the echoes of the incident pulse, resulting in scattering of the incident ultrasound beam and emission of fundamental (f_0), subharmonic ($f_0/2$), harmonic ($n*f_0$; $n\in$ N) and ultraharmonic ($((2n-1)/2)*f_0$; $n\in$ N & $n > 1$) components in the scattered beam profile (1). A brief overview of the principles and modes for CEUS imaging is provided here (1):

Fundamental B-Mode Imaging: In this mode, the fundamental signal, at the insonation frequency, is used from the received beam profile. The backscattered signals from the microbubbles are relatively stronger than the surrounding tissues and this enables localization and visualization of the vasculature in the imaging plane.

Harmonic B-Mode Imaging: In this mode, the higher harmonics specifically the second harmonic signals are used for image formation. Since the backscattered energy at the harmonic components of the insonation frequency is relatively greater for the microbubbles compared to the tissue, an improved contrast ratio is obtained relative to the fundamental B-mode imaging.

Harmonic Power Doppler Imaging: As in harmonic B-mode imaging, the signals received at twice the insonation frequency are used. However, compared to conventional power Doppler imaging, the susceptibility of motion-induced artifacts is reduced because contrast agent signals are utilized to display the blood flow.

Subharmonic Imaging: In this imaging mode, the signals at half the transmit frequency are used for image formation. An advantage of this mode is that the subharmonic signals are exclusive to microbubbles and thus, provide an exclusive view of the vasculature, much like digital subtraction angiography. A limitation is the lack of tissue landmarks, but this can be addressed with a split screen setup as recently published (130).

Pulse Inversion Imaging: In this mode, two pulses with 180° phase difference are transmitted and the received echoes are summed. The linear echoes from tissues cancel out, while the even nonlinear echoes mostly from the microbubbles increase the contrast seen in the ultrasound images.

Power Modulation Imaging: Another mode exploiting the nonlinear response of microbubbles to different types of pulses is the power modulation imaging mode. In this mode two pulses with different amplitudes (power) are transmitted and the received signals are weighted appropriately before being subtracted to isolate and enhance the depiction of nonlinear signals mostly arising from the microbubbles.

Destruction Replenishment Imaging: In this mode a transmit pulse with high mechanical index (MI; but less than the maximum permissible limit of 1.9) is used to destroy the microbubbles in the imaging plane, and then the slow replenishment of the vasculature (anatomy) in the scanned plane is captured by the inflow of microbubbles using low MI pulses. This assists in defining the vasculature (tortuous, etc.), estimating the blood flow (in ml/min), perfusion (in ml/min/g), etc. and may aid in diagnosis.

The above list is not totally exhaustive of the techniques used by different manufacturers. Here, an insight into the use of nonlinear components of the backscattered signals from the microbubbles to create contrast specific imaging modes is provided.

2.4 UCAs as Ambient Pressure Sensors

The nonlinear signals from UCAs have been used in clinical imaging applications, both in harmonic and subharmonic scanning modes with specifically tailored pulse sequences varying amongst ultrasound manufacturers. In addition to the imaging applications, various techniques to estimate ambient pressures using UCAs have been proposed (2, 3, 17-21). Broadly, these may be classified into two types, techniques proposed based on experiments conducted with un-encapsulated (or free) microbubbles

(18-21) and those based on experiments conducted with encapsulated microbubbles (2, 3, 17).

Fairbank and Scully proposed measuring the ambient pressure based on the shift in resonance frequency of small bubbles (diameter 20 µm to 40 µm). They proposed that ambient pressure changes would manifest as changes in bubble volume ultimately leading to a change in resonant frequency (18). Their technique suffered from non-uniformity in bubble sizes. This resulted in broad-band scattered spectrum at the receive transducer, which did not show the predicted resonance shift with an increase in ambient pressure and prevented accurate tracking of ambient pressure changes (18). To circumvent the problem of non-uniform bubble sizes, Hök proposed to utilize single bubble echo amplitude as a measure of ambient pressure (19). However the technique is limited in application to areas containing non-flowing clear fluid (not applicable in heart and blood vessels). Also the localization of a single air bubble *in vivo* would require precisely controlled ultrasound scanning parameters. More importantly Hök's experiment conducted under "ideal" conditions resulted in an error of approximately 30 % (75 mmHg true pressure; 99 mmHg derived pressure); clearly not clinically acceptable. Based on a principle similar to Fairbank and Scully for measuring the ambient pressure based on changes in the size of the bubbles, Shankar et al. utilized a dual frequency technique for calculating these size changes more accurately and thereby obtain the ambient pressure profile (21). However their technique achieved a resolution of only 10-15 mmHg at best (measured vs. observed; (21)). Miwa patented a technique to mark the onset of cavitation as a function of ambient pressure (20), but no *in vivo* experiments were reported. Bouakaz et al proposed a technique to measure the dissolution time of free microbubbles following the rupture of encapsulated microbubbles (17). However, the technique proposed by Bouakaz et al could only detect pressure changes of about 50 mmHg (17). A simulation study utilizing the disappearance time of the gas bubbles along with the appearance of the subharmonic signal and its gradual decay (as the bubble shrinks) for ambient pressure estimation showed that using this technique ambient overpressures in the range of 11 mmHg may be measureable (131). However, these simulations revealed that such low errors would require gas bubbles with diameters of the order of 14 µm (131), considerably greater than the average diameters of the capillaries (7 µm) (117). Also no follow-up experimental evaluations using this approach have been documented. Overall these techniques yield errors ranging from 10-50 mmHg, which is clinically unacceptable because the recommendations for using a technique for systolic and diastolic pressure assessments require the errors to be within 5 mmHg (at least for 50 % of the recordings) (22).

A different technique to determine changes in the ambient pressure based on subharmonic emissions from microbubbles called subharmonic aided pressure estimation or SHAPE has also been proposed (2, 3). The subharmonic signal generation as a function of IAO, may be characterized into 3 stages – occurrence, growth and saturation; this observation has also been characterized in the models published in the literature (2, 3, 113, 114, 132, 133). In the occurrence stage, the subharmonic signal amplitude is probably too low to be detected above the noise level. In the saturation stage, the subharmonic signal is the highest (amongst the 3 stages of the subharmonic signals) mostly due to strong subharmonic emissions by the collapsing bubbles. The concept of SHAPE revolves around the subharmonic signal emissions in the intermediate stage i.e., the growth stage. In this stage, the subharmonic amplitude decreases linearly (in dB; $r^2 \geq 0.96$) with an increase in ambient pressure over a range of 0 to 186 mmHg (3); note that this range covers blood pressures encountered clinically in most situations. Thus, subharmonic emissions from microbubbles in the growth stage can be calibrated to provide the ambient overpressures.

Recently other groups have also explored SHAPE applications *in vitro*, but either with the use of in-house ultrasound transducers/systems, single element transducers or custom-made contrast bubbles (131, 134-141). An inherent limitation in these studies is the lack of consideration of the flow dynamics encountered *in vivo*, and also the use of such "in-house platforms," which delays the clinical evaluation and, ultimately, acceptance (due to prerequisite safety studies and lack of availability). Another recently proposed technique showed (theoretically) that the shift in subharmonic optimal driving frequency may be attributable to changes in ambient pressure, and thus this shift may be useful to indicate ambient pressures (142). In this technique, simulations with single bubble model and with bubbles having a size distribution typically encountered in a UCA vial were used, with the characteristics of SonoVue microbubbles. The subharmonic optimal driving frequency was defined as the driving (insonation) frequency that elicited a maximum subharmonic signal amplitude (142). Consequently such an approach requires the transducer to sweep through a range of the transmit frequencies in order to determine the optimal driving frequency. Since this would require transmitting a number of interrogating pulses at different transmit frequencies, a real time *in vivo* application may be challenging, given that the ambient pressures *in vivo* i.e., blood pressure varies considerably within a cardiac cycle that lasts about 0.83 s (assuming 72 beats per minute). The authors suggest using calibrations with *in vitro* experiments to relate the shift measured *in vivo* to the ambient pressures (142) – and these interesting results shall be awaited. The two simulations of LV pressures provided in the results by the authors were for a SonoVue microbubble with diameter 1.6 µm and a group of SonoVue microbubbles with mean diameter of 0.8 µm and a standard deviation of 0.2 µm following a Gaussian distribution, and the errors in reporting maximum LV pressure were within 3 mmHg (142). Again the implications of these results may require scrutiny especially when *in vitro* and *in vivo* experiments are conducted, given that 80 % of the echogenicity from SonoVue microbubbles is provided by bubbles ranging from 3 to 9 µm in diameter (143).

Thus, in the next section, the concept of SHAPE is revisited with the specific purpose of providing motivation for the work presented in this thesis.

2.5 Subharmonic Aided Pressure Estimation (SHAPE) with UCAs

It was demonstrated that subharmonic signal amplitude shows a sigmoidal relationship with IAO and in the growth phase the subharmonic signal amplitude becomes dependent on the ambient pressures (2, 3). Thus, growth phase subharmonic emissions may be used to estimate ambient pressures i.e., SHAPE may be feasible with growth phase subharmonics. After the initial *in vitro* results (3), the first *in vivo* application of SHAPE was investigated (23). The experimental setup used for that study is shown in Figs. 2.1 and 2.2[10].

---

[10] Courtesy Dr. Forsberg.

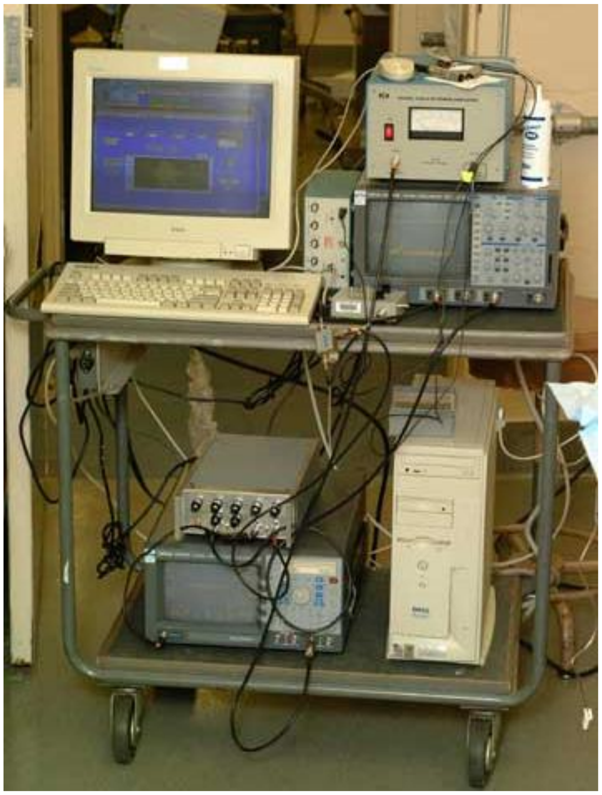

Figure 2.1: Experimental setup for first *in vivo* SHAPE experiments

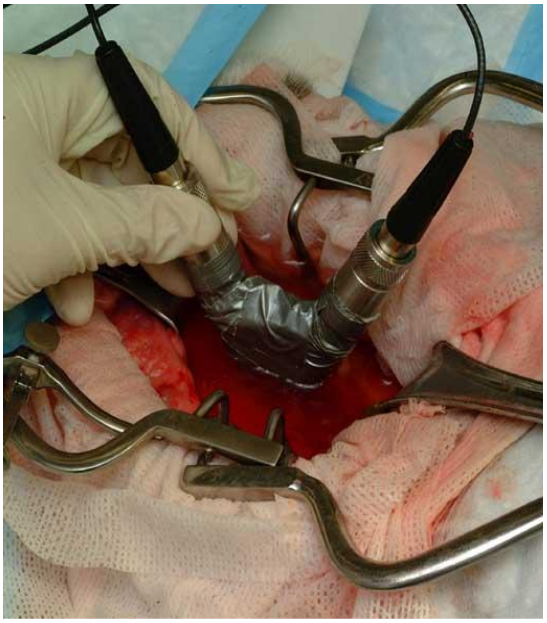

Figure 2.2: Data acquisition for first *in vivo* SHAPE experiments

The experiments were conducted with an invasive approach to access the aorta. A mid-line abdominal incision was created and 2 single element transducers (one for transmit and the other for receive) were used. The results from the study were promising because a maximum standard error of 5.4 mmHg was obtained with SHAPE relative to simultaneous pressures recorded by a Millar pressure catheter (23). Since single element transducers were used there was no simultaneous imaging performed, which is a severe limitation given that *in human* measurements need to be conducted noninvasively. This experimental setup was plagued by other acquisition problems (employing 2 single element transducers held together with duct tape – see Fig. 2.2), which is also not clinically acceptable.

Hence, while several methods have been proposed over the last 4 decades to track *in vivo* pressures using microbubbles, none of these techniques have been translated into clinical use, either due to high errors (greater than 10 mmHg) *in vitro* and/or due to experimental setups lacking clinical feasibility. The objective of the work presented in this thesis was to develop and evaluate the feasibility of SHAPE to noninvasively monitor cardiac and PV pressures using a commercially available ultrasound scanner and an existing UCA, mitigating problems associated with previous experimental techniques.

The next chapter (Chapter 3) presents the materials and the methods espoused for the *in vitro* studies and, cardiac and hepatic *in vivo* studies and the results with discussions are presented in Chapter 4.

3. MATERIALS AND METHODS

3.1 Materials

3.1.1 Selection of UCA for Dynamic *In Vitro* Studies and *In Vivo* Studies

Preliminary studies for SHAPE applications were undertaken with different UCAs. The UCAs investigated for SHAPE are listed with their key properties in Table 3.1.

Table 3.1: UCAs investigated for SHAPE *in vitro*

UCA	Manufacturer	Gas Core	Shell	Mean Diameter (μm)	f_o^* (MHz)
†Definity®	Lantheus Medical Imaging	C_3F_8	Phospholipids	1.1-3.3	2.7
Levovist®	Schering, AG	Air	Galactose / Palmitic Acid	2.0-4.0	2
†Optison™	GE Healthcare	C_3F_8	Human Albumin	2.0-4.5	2
Sonazoid™	GE Healthcare	C_4F_{10}	Lipids	2.4-3.5‡	4.4
ZFX	Zhifuxian, Xinqiao Hospital	C_4F_{10}	Lipids	2.0-4.0	3

*: resonance frequency; †: Approved for LV opacification studies in the USA; ‡: median diameter

Note, that these UCAs were investigated, because other experimental agents like the one used in Ref. (137) were not accessible. The results showed that over a static pressure increase from 0 to 186 mmHg (almost the clinical BP range), the maximum linear decrease in subharmonic signal occurred for Sonazoid (3, 144) – see Table 3.2 below (sorted in descending order based on subharmonic reduction). Note, that the highest sensitivity of Sonazoid was also confirmed by a parameter study in which the subharmonic reduction of Levovist and Sonazoid were compared (135) – Sonazoid showed relatively higher ambient pressure sensitivity. Thus, Sonazoid was selected as the UCA for developing and evaluating the SHAPE algorithm in a dynamic *in vitro* setup (pressures continually varying with time) and for subsequent *in vivo* studies.

Table 3.2: Behavior of different UCAs when ambient pressure was varied in the range from 0 to 186 mmHg

	Subharmonic reduction (dB) (n= 3)	Linear Regression (r^2)
Sonazoid	13.3 ± 0.19	0.99
ZFX	12.2 ± 0.17	0.97
Definity	11.0 ± 0.26	0.98
Optison	10.1 ± 0.18	0.97
Levovist	9.6 ± 0.23	0.98

Sonazoid microbubbles consist of perfluorobutane gas encapsulated in a membrane of hydrogenated egg phosphatidyl serine and have the capability of withstanding ambient pressure as high as 300 mmHg (145). The clinical safety profile for Sonazoid has been established (123) and it has already been approved for diagnosis in patients with liver lesions outside the USA (122). Sonazoid is provided as a powder for reconstitution before injection. After addition of 2 ml of sterile water and gentle shaking by hand, the product is easily reconstituted and produces a homogenous dispersion of microbubbles with a concentration of 10 μl of microbubbles/ml (in this form the agent is stable for four hours at room temperature).

3.1.2 Selection of Ultrasound Scanner for SHAPE

Two ultrasound scanners were selected, the Sonix RP (Ultrasonix, Richmond, BC, Canada) and the GE Logiq 9 (GE Healthcare, Milwaukee, WI). The Sonix RP scanner was selected because it provided full access and control of the imaging data. The Sonix RP platform permitted access to the radiofrequency (RF) data and enabled new imaging modes like pulse inversion to be configured (146). The RF data refers to the data after conversion of mechanical energy (backscattered signals) back to the electrical signals by the transducer – this RF data may be pre-beamformed, post-beamformed, filtered or unfiltered. Thus, for the dynamic *in vitro* studies and the cardiac studies in canines the Sonix RP scanner was used. To prove that the concept of SHAPE may be implemented on multiple hardware platforms, in the next phase of study - to identify PH for hepatic applications, a GE Logiq 9 scanner was selected. A research contract with

GE Global Research permitted access to the RF data after modification of the operating software.

An additional consideration after the selection of the ultrasound scanner was the choice of transmit frequency, which governs the selection of the ultrasound transducers (probes) for the respective ultrasound scanners. In preliminary studies in static tank experiments (144), the subharmonic reduction of Sonazoid over an ambient pressure variation of 0 to 186 mmHg was investigated as a function of transmit frequency. The optimum transmit frequency for SHAPE with Sonazoid was 2.5 MHz which implies that the theoretical subharmonic receive frequency would be 1.25 MHz. Based on this selected transmit frequency (2.5 MHz), on the *in vivo* application to be investigated (cardiac and hepatic) and on the available transducers with the respective ultrasound scanners, a PA4-2 phased array was selected for the Sonix RP scanner for *in vitro* and *in vivo* cardiac studies and a curvi-linear array 4C probe was selected for the Logiq 9 scanner for *in vivo* hepatic studies. The modifications of the Sonix RP scanner and the Logiq 9 scanner were performed and tested in conjunction with the respective manufacturer's research support team personnel ensuring adequate representations of transmit and receive signals at 2.5 MHz and 1.25 MHz, respectively.

Additionally a detailed list of equipment including the auxiliary equipment with model and serial numbers (where applicable) is provided in Appendix 1.

3.2 Methods

This section is divided into three sub-sections, namely, dynamic *in vitro* studies, cardiac *in vivo* studies and then hepatic *in vivo* studies. For each sub-section the experimental setup, data processing and statistical tests used are explained. The data processing were performed offline in Matlab (The Mathworks, Inc., Natick, MA), unless explicitly stated. An explicit mention of the 'Use of Vertebrate Animals in Experiments' is provided in Appendix 2.

3.2.1 Dynamic *In Vitro* Studies

3.2.1.1 Incident Acoustic Output (IAO) Measurements for Sonix RP Scanner with the PA4-2 Array

The subharmonic emissions from the UCAs may be in the occurrence stage, the growth stage, or the saturation stage (3) – this depends on the IAO; about 100-200 kPa for the occurrence stage, 300-600 kPa for the growth stage and higher IAO levels for the saturation (or bubble destruction) stage. The growth phase subharmonic emissions are sensitive to ambient pressures (3). Thus, it is necessary to select the IAO levels that elicit growth phase subharmonic emissions. For dynamic *in vitro* studies and *in vivo* studies it is not feasible to obtain the accurate IAO levels at the site of the microbubbles, because this would require inserting a hydrophone in the lumen of the vessel (in the Doppler flow phantom) or in the heart or the liver for the *in vivo* studies. However, it is important to have an estimate of the IAO levels given the need for growth phase subharmonic emissions to measure ambient pressures. At the same time, most manufacturers encode the acoustic output of the scanner – for the Sonix RP, the acoustic output is encoded as -2 dB levels with 0 dB representing the maximum acoustic output. The acoustic output spans a range from -32 dB to 0 dB. Consequently, the IAO levels corresponding to these encoded dB levels were measured using a standard water bath approach.

The incident acoustic pressures at the focus of the transducer were measured using a calibrated 0.2 mm needle hydrophone (Precision Acoustics, Dorchester, Dorset, UK; sensitivity of 57.1 mV/MPa at 2.5 MHz). The focal point was determined by finding the point of maximum acoustic pressure using a semi-automated electronic x-y-z-positioning system. The measurements at each encoded dB level were performed in triplicate.

3.2.1.2 Experimental Setup

A schematic of the experimental setup is shown in Fig. 3.1.

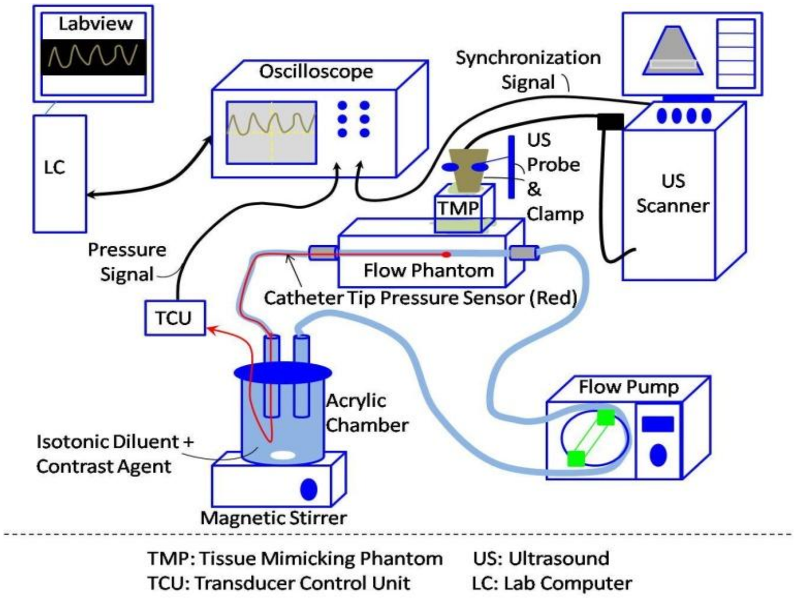
Labview
Oscilloscope
Synchronization Signal
LC
US Probe & Clamp
US Scanner
TMP
Pressure Signal
Flow Phantom
Catheter Tip Pressure Sensor (Red)
TCU
Acrylic Chamber
Flow Pump
Isotonic Diluent + Contrast Agent
Magnetic Stirrer
TMP: Tissue Mimicking Phantom
US: Ultrasound
TCU: Transducer Control Unit
LC: Lab Computer

Figure 3.1: *In vitro* experimental setup for dynamic SHAPE studies

Closed-Loop Flow System: A closed-loop flow system was implemented using an acrylic water bath (4071.5 cm^3), a Sarns S10K II Blood Pump (Sarns Inc., Ann Arbor, MI; operated at 650 ml/min), a Doppler flow phantom (ATS Laboratories, Inc., Bridgeport, CT) and flexible PVC tubes (8 mm inner diameter). The ambient pressures in the flow system were controlled using the blood pump and the revolutions per minute on the blood pump was set to achieve ambient pressures varying from 0 to 120 mmHg. A dose of 0.2 ml reconstituted Sonazoid microbubbles (approximately equivalent to 1.6 µl microspheres with volume median diameter of about 2.6 µm (145)) was mixed with 750 ml of isotonic diluent (Val Tech Diagnostics Inc., Pittsburgh, PA) in the acrylic water bath (temperature 25 °C). A magnetic stirrer was used to ensure uniform mixing. A tissue-mimicking phantom (L ×W × H: 15 × 9.5 × 8 cm^3; ATS Laboratories Inc.) was coupled to the Doppler flow phantom with acoustic gel. This tissue mimicking phantom was used, because the depth of the vessel within the Doppler flow phantom was only 1.5 to 2 cm, and thus, would not simulate the depth encountered *in vivo* in cardiac and hepatic applications. A 5 French solid-state curved tip pressure catheter (SPR 350, Millar Instruments Inc., Houston, TX) was inserted into the flow phantom through the acrylic water bath. The pressure catheter was connected to a control unit (TCB 500, Millar Instruments) and the output of the control unit was connected to an oscilloscope (9350 AM, LeCroy, Chestnut Ridge, NY) providing the reference standard for these experiments i.e., the ambient pressure values in the flow phantom. The pressure catheter was calibrated to have an error band of ± 1.5 mmHg at zero pressure and adjusted using the manufacturer's specification to indicate the absolute pressure values.

Ultrasound Scanner Configuration: A Sonix RP scanner with a PA4–2 phased array transducer (Ultrasonix Medical Corp., Richmond, BC, Canada) was operated in the Research mode. The Sonix RP scanner was configured to perform in pulse-inversion imaging mode, transmitting 2-cycle pulses at a 2.5 MHz center frequency (-6 dB bandwidth: 1.3 MHz). In pulse-inversion mode, 2 pulses with a 180° phase difference are transmitted and the received echoes are summed, enhancing the even nonlinear signals while canceling out the linear signals and odd harmonics. In this study, the pulse-inversion technique was selected to enhance the nonlinear signals from the Sonazoid microbubbles, specifically the nonlinear subharmonic signal. The pulse inversion imaging mode caused the frame rate (for simultaneous imaging; on the Sonix RP scanner) to be reduced to nearly half in the B/PW mode compared to grayscale B-mode imaging alone. However, the temporal resolution of the signal acquired for tracking ambient pressure depends on the pulse repetition frequency (PRF) corresponding to the PW mode and is, therefore, not markedly affected. A pulsed Doppler gate size of 1.5 mm placed within the lumen of the vessel was used to acquire unprocessed accumulated pulse data. The unprocessed RF data was post-beamformed and accessed before envelope modulation of the RF signal.

Synchronization Setup: A synchronization pulse, obtained from the 'Print' output on the Sonix RP scanner, was used to trigger the oscilloscope during active data capture. The oscilloscope was configured to acquire the pressure catheter data on a lab computer via a GPIB interface (driver version 2.7.0.49152) through LabVIEW (version 8.0, National Instruments Corp., Austin, TX). The PRF was set to the maximum possible value of 3.3

kHz (limited by the depth of penetration i.e., 9.5 cm in this setup) to achieve maximum temporal resolution.

A summary of data acquisition parameters for the *in vitro* experiment setup is provided in Table 3.3. The IAO levels were varied across the range as indicated in Table 3.3 to identify the IAO level that would elicit subharmonic emissions from Sonazoid in the growth phase i.e., the ambient pressure sensitive phase. Additionally, specific details including configuration and operating procedures are given in Appendix 3.

Table 3.3: Data acquisition parameters for the *in vitro* SHAPE studies

Scanner; probe:	Sonix RP; PA4-2
Scanning mode:	Pulse inversion imaging; 2 transmit cycles
$f_{transmit}$; $f_{receive}$:	2.5 MHz; 1.25 MHz
Contrast agent; Administration:	Sonazoid; 0.2 ml reconstituted microbubbles with 750 ml isotonic diluent
Synchronous pressure monitoring:	5F solid state catheter tip manometer
IAO:	-8 dB to 0 dB (0 dB maximum output; 76 kPa to 897.04 kPa_{pk-pk}; mechanical index < 0.38)
Pulse repetition frequency:	3.3 kHz
Vessel depth(s) in flow phantom:	9.5 cm with external tissue mimicking phantom and 1.5 cm without the tissue mimicking phantom
Scanned region:	Vessel lumen (4 mm diameter)
Gate size (PW Doppler):	1.5 mm
Acquisitions:	5 second runs (n = 3 to 5 per IAO level)

3.2.1.3 Data Acquisition, Processing and Statistical Analyses

Part-I Goal: To identify most sensitive IAO level for SHAPE

Data Acquisition-I: Five IAO levels corresponding to -8 dB, -6 dB, -4 dB, -2 dB and 0 dB were selected because the range of these IAO levels varied from 76 to 897 $kPa_{pk\text{-}pk}$ i.e., these encoded levels spanned a range of IAO levels that are most likely to elicit growth phase subharmonic emissions. For each IAO level, the data from the ultrasound PW gate were acquired over 5 s in synchrony with the pressure catheter – these measurements were repeated in triplicate. Based on the PRF of 3.3 kHz, data from about 16500 pulses (from each experimental run) were obtained.

Data Processing-I: The data from each pulse were converted to the Fourier domain. The subharmonic signal was extracted as the mean signal in a 0.2 MHz (16 %) bandwidth around the subharmonic frequency (1.25 MHz) i.e., signals from 1.15 to 1.35 MHz for each pulse data. Then the resulting subharmonic amplitude time variation signal was noise filtered using a median filter of order 500. This technique was selected because it was analogous to our previous approach (147). The median filter was selected, because it eliminates transient high-frequency noise (probably due to multiple scattering, etc.) and extracts the underlying slow-frequency amplitude variations; in this case, the underlying subharmonic signal that may be used for ambient pressure estimation. This process is illustrated in Fig. 3.2 and was repeated for all data sets acquired at the selected IAO levels. Since the data acquisition was performed at varying IAO levels, there is a possibility of more than one IAO level eliciting growth phase subharmonics. Consequently there is a need to identify the IAO level that elicits the growth phase subharmonic emissions that are most sensitive to ambient pressures. Thus, the range of subharmonic signals for each pulse contour (i.e., maximum – minimum subharmonic amplitude) were extracted, averaged over all pulse contours at a given IAO level and compared.

Statistical Analyses-I: To determine the most sensitive IAO level for ambient pressure tracking in this experimental setup, the changes (i.e., the range) of subharmonic amplitude were compared using a one-way analysis of variance (ANOVA) with Bonferroni corrections for multiple comparisons (148). *P*-values less than 0.05 were considered significant. The ANOVA tests and the Bonferroni corrections for multiple comparisons were used because subharmonic amplitude ranges obtained at five IAO levels were to be compared and for comparing these different mean values the ANOVA technique in conjunction with the Bonferroni corrections will maintain the probability of making type I error to 5 % (i.e., a *p*-value of 0.05).

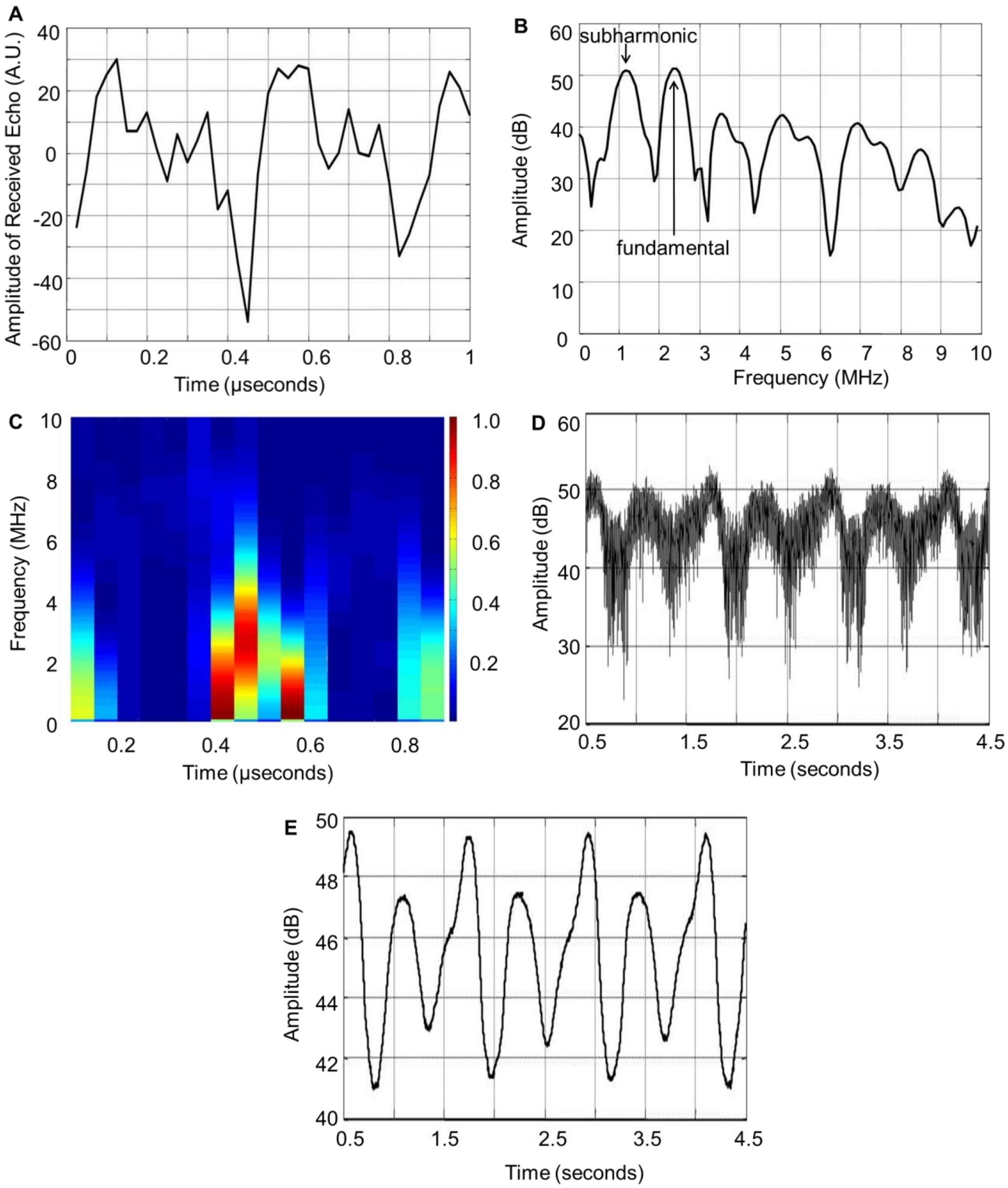

Figure 3.2: Process of extracting the time-variant subharmonic signal for ambient pressure tracking. The signal obtained from the pulse Doppler gate (A) is shown along with the Fourier Domain representation (B) and the short-time Fourier transformation (C). The subharmonic signal obtained from all the pulses acquired during the acquisition (D) was processed using a median filter of order 500 to remove high frequency noise (E).

Part-II Goal: To investigate the ability of SHAPE to estimate ambient pressures

Data Acquisition, Processing and Statistical Analyses-II: In the next phase of experiments, the data were acquired at the IAO level that elicited subharmonic emissions most sensitive to ambient pressure variations. The data sets (synchronous pressure catheter data and the PW data) were acquired as 5 s runs and also as a long 20 s run consisting of at least 20 cycles of pressure changes. The processing approach was as adopted in *Data Processing-I.* Least squares linear regression analysis was used to assess the ability of the processed subharmonic data (in dB) to predict the ambient pressure values (in mmHg). Also in order to verify that the variations in the subharmonic signal were not solely due to the variations in the concentration of Sonazoid microbubbles (due to the pulsatile flow), the fundamental and the second harmonic signals were also extracted and studied. If the fundamental and/or the second harmonic signals also showed a similar variation as compared to the subharmonic signals, then the efficacy of SHAPE would be questionable.

Part-III Goal: To confirm the variation of subharmonic signals as a function of ambient pressures

Data Acquisition, Processing and Statistical Analyses-III: This part of the experimentation was developed for cross-validation of the subharmonic emissions. The tissue mimicking phantom from Fig. 3.1 was removed and it was hypothesized that the IAO level used in *Part-II* should induce collapse of the microbubbles (due to the removal of 8 cm of attenuation; the tissue mimicking material attenuation was 0.5 dB/cm/MHz). Due to the collapse of the microbubbles, the resulting subharmonic signals may not be able to predict the subharmonic emissions, and the resulting pressure waveforms obtained from the subharmonic data may be distorted. The processing approach and statistical analyses were as adopted in *Part-II*.

Part-IV Goal: To develop "best" processing technique for in vivo SHAPE studies

Data Acquisition-IV: The experimental setup was as shown in Fig. 3.1 and, pressure catheter data and RF data were acquired at the most sensitive IAO level used for *Part-II*. The data were acquired as 5 s runs and the acquisitions were repeated 5 times.

Data Processing-IV: When the accumulated data from the PW gate after pulse inversion was inspected in the Fourier domain, shifts in peak subharmonic amplitudes from the expected subharmonic frequency of 1.25 MHz were noted (Fig. 3.3A). These shifts may occur due to transient variations in the concentration and the size of microbubbles probably due to the variable/pulsatile flow and the problem may be aggravated *in vivo* due to processes like phagocytosis (149) affecting microbubbles' concentration or due to the combined frequency response of the ultrasound transducer and system. Overall there was a need to compensate for such shifts in the subharmonic peak frequency before the subharmonic data were used for ambient pressure estimation.

Four different techniques were used to extract the subharmonic signal amplitude from each accumulated pulse data (after pulse inversion) – average subharmonic amplitude in a 0.5 MHz bandwidth about the theoretical subharmonic frequency (Fig. 3.3B) representing a relatively wide bandwidth (40 %) signal, average subharmonic amplitude in a 0.2 MHz bandwidth about the theoretical subharmonic frequency (Fig. 3.3C) representing a relatively narrow bandwidth (16 %) signal, parabolic fit to capture the subharmonic peak in a 0.5 MHz bandwidth about the theoretical subharmonic frequency (Fig. 3.3D) and the exact signal amplitude at the theoretical subharmonic frequency (Fig 3.3A). A parabolic fitting technique was used to locate the expected subharmonic peak within this range. In *Part-I*, an extraction bandwidth of 0.2 MHz was used. The extracted subharmonic amplitudes were filtered using two techniques to eliminate the high frequency noise. A median filter with varying order from 50 to 500 (specifically, 50, 100, 250, 325 and 500; representing a time integral of 15 ms to 151 ms) was implemented. Note, that in *Part-I*, a median filter with order 500 was used. Another filtering approach was based on wavelets. An 8-stage subband decomposition using Daubechies second-order low-pass and high-pass filter coefficients was employed to isolate the time-varying subharmonic signal within a frequency band of 0 to 6.5 Hz corresponding to 0 to 360 beats per minute (i.e., encompassing a wide range of cardiac arrhythmias from bradycardia to tachycardia that may be encountered clinically). The frequency response of the Daubechies filter coefficients is shown in Fig. 3.4. Daubechies second-order low-pass and high-pass filter coefficients were chosen because they are compactly supported orthonormal wavelets useful for data analysis (150, 151).

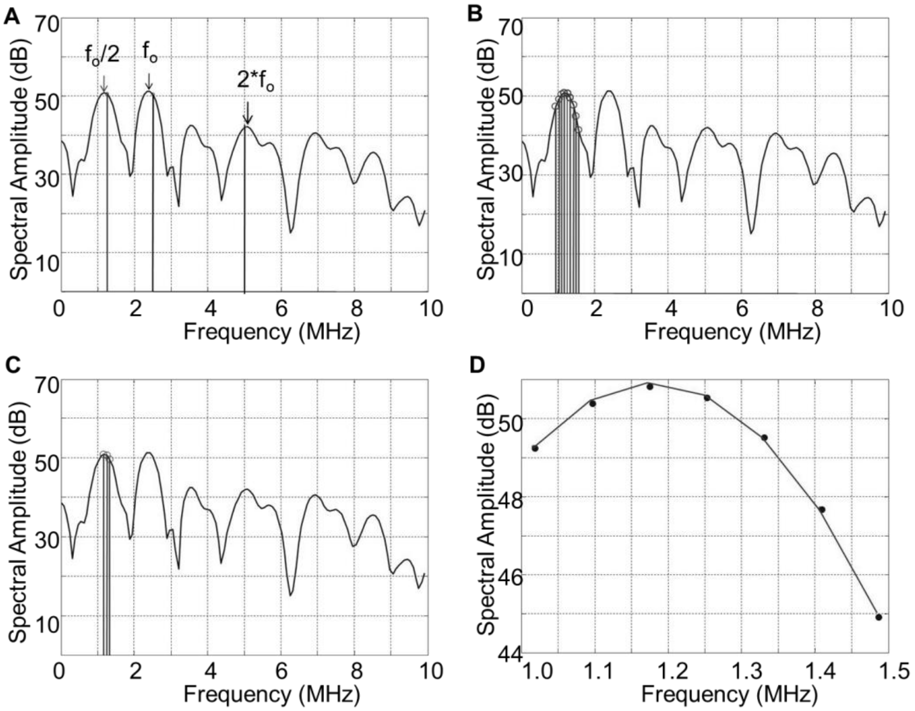

Figure 3.3: Extraction techniques for subharmonic amplitudes. (A) A frequency shift in the received spectrum between the theoretical (bars) subharmonic (1.25 MHz), fundamental (2.5 MHz) and second harmonic (5 MHz) peaks and the actual signal peaks (arrows). Average subharmonic amplitude extraction (bars) in 0.5 MHz (B) and in 0.2 MHz (C) bandwidth about the subharmonic frequency. (D) Extraction of the peak value in a 0.5 MHz bandwidth around the theoretical subharmonic frequency after performing a parabolic fit (solid).

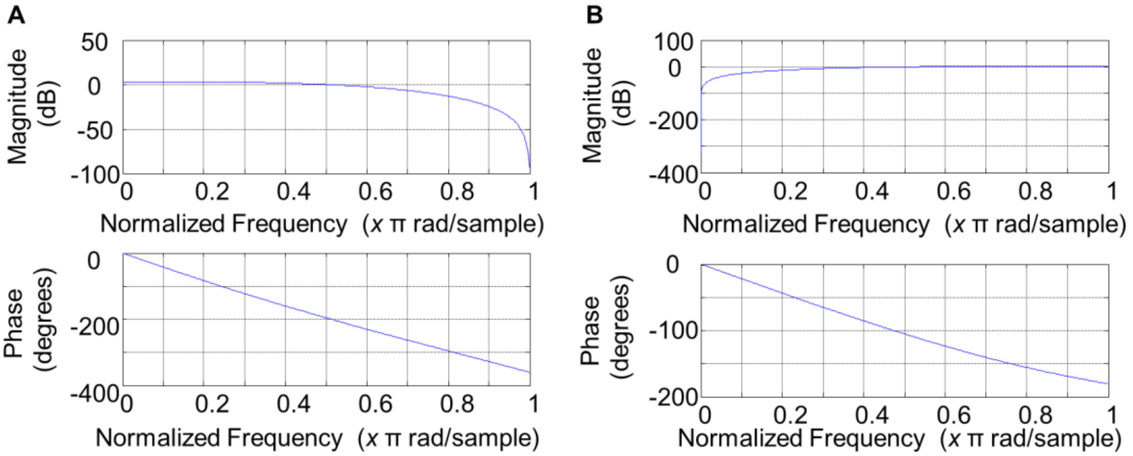

Figure 3.4: Frequency response for Daubechies second-order low-pass (A) and high-pass filter coefficients (B).

Statistical Analyses-IV: A least-squares linear regression analysis was initially conducted to determine the slope (mmHg/dB), the correlation coefficient and the RMSE generated from predicting the pressure values (in mmHg) using the filtered subharmonic signal (in dB) relative to the reference standard (the pressure catheter). A repeated measures ANOVA was used to compare the four extraction techniques and the median filtering approach with five filter orders, and the combination of four extraction techniques with the wavelet based approach to identify the combined technique with the smallest RMSE – thereby providing the best representation of the ambient pressure fluctuations. The post-hoc comparisons were performed using t-tests with Bonferroni corrections for multiple comparisons (148). *P*-values less than 0.05 were considered significant.

The Matlab functions and subroutines created for processing the data are presented in Appendix 4.

3.2.2 *In Vivo* Cardiac SHAPE Studies

The study was approved by the Institutional Animal Care and Use Committee of Thomas Jefferson University and conducted in accordance with the recommendations of the Panel on Euthanasia of the American Veterinary Medical Association. The cardiac SHAPE studies were divided into three separate studies: in 2 canines the efficacy of obtaining subharmonic signals for SHAPE was evaluated, then in 4 canines a technique to obtain clinically relevant LV pressures was investigated and lastly, in 5 canines a technique to obtain clinically relevant RV pressures was investigated. The animal preparation for these studies were similar and thus, the next section summarizes the common steps in the three studies. Following the 'Animal Preparation' section, the specific motivation for each study and data acquisition, processing and statistical analyses steps are presented.

3.2.2.1 Animal Preparation

Initially, an intravenous injection of Propofol (Abbott Laboratories, Chicago, IL; dose of 7 ml/kg) was used as the anesthetic. The canines were placed in supine position on the operating table. During the course of the experiments, the animals were intubated and anesthesia maintained with 0.5 to 2 % Isoflurane (Iso-thesia; Abbott Laboratories, Chicago, IL) via an endotracheal tube. Also a warming blanket was used to maintain normal body temperature. An 18-gauge catheter was placed in a forelimb vein for infusion of Sonazoid microbubbles (GE Healthcare, Oslo, Norway) at a concentration of 0.015 μl/kg/min. This concentration was selected based on previous study (23). A 5F solid state micromanometer tipped catheter (SPR 350, Millar Instruments, Inc., Houston, TX) was used as the reference standard and was introduced at the site for pressure measurements under ultrasound guidance. The pressures signals were recorded on an oscilloscope and digitized and captured on the computer using LabVIEW. A synchronization signal between the Sonix RP scanner and the oscilloscope enabled simultaneous acquisition of the pressure catheter data and the RF data on the Sonix RP. The Sonix RP scanner was operated with the PA4-2 probe and configured for pulse inversion imaging with 2 transmit pulses. At the end of the experiments the canines were sacrificed by an intravenous injection of Beuthanasia (0.25 mg/kg).

3.2.2.2 Evaluating Feasibility of Noninvasive In Vivo SHAPE

The motivation for this study was to evaluate the feasibility of obtaining subharmonic signals that would be sensitive to pressures in the LV, noninvasively. To the best of our knowledge, this documents the first-ever study of noninvasive SHAPE and thus, 2 canines were studied for the feasibility of the approach.

Data Acquisition: The ultrasound guided pressure catheter was positioned in the LV. After confirmation of the pressure catheter in the LV (Fig. 3.5A), the infusion of Sonazoid microbubbles was started. After confirmation of the presence of Sonazoid microbubbles in the LV the data acquisition began (Fig. 3.5B). The PW gate was positioned in the LV close to the location of the pressure catheter. The IAO levels on the Sonix RP scanner were varied from -8 dB to 0 dB (to compensate for attenuation differences between canines) and the data were acquired in triplicate as 5 s runs. A representative of snapshot of equipment setup is shown in Fig. 3.6.

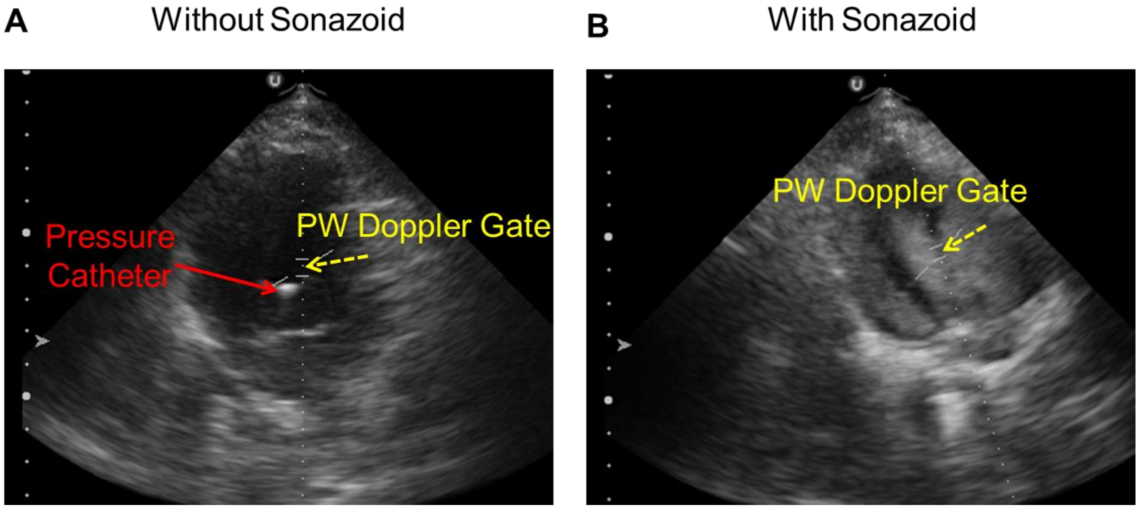
A
Without Sonazoid
B
With Sonazoid
Pressure Catheter
PW Doppler Gate
PW Doppler Gate

Figure 3.5: Grayscale ultrasound images of the LV before Sonazoid infusion (A) and after Sonazoid infusion (B). The pressure catheter and the PW Doppler gate to acquire RF data are indicated.

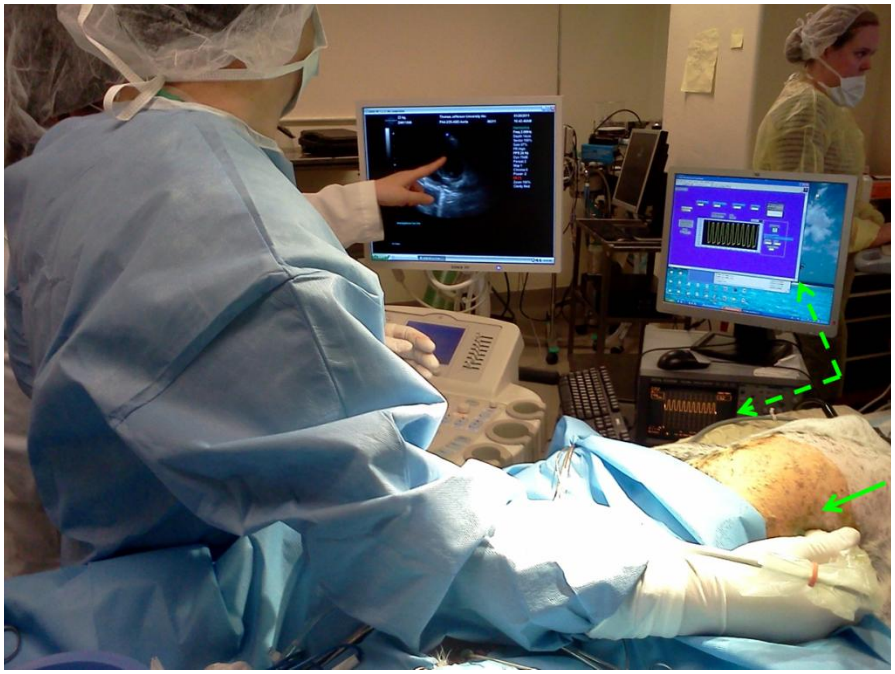

Figure 3.6: Snapshot of the data acquisition during *in vivo* cardiac SHAPE studies. Note, that the ultrasound scanning is done noninvasively (solid green arrow) – in stark contrast with an earlier approach (cf., Fig. 2.2). The dotted green arrows indicate the pressure in the LV as viewed on the oscilloscope and simultaneously being captured on a lab computer via LabVIEW.

Data Processing: The subharmonic data were extracted as the mean signal in a 0.2 MHz bandwidth around the theoretical subharmonic frequency of 1.25 MHz (Fig. 3.7).

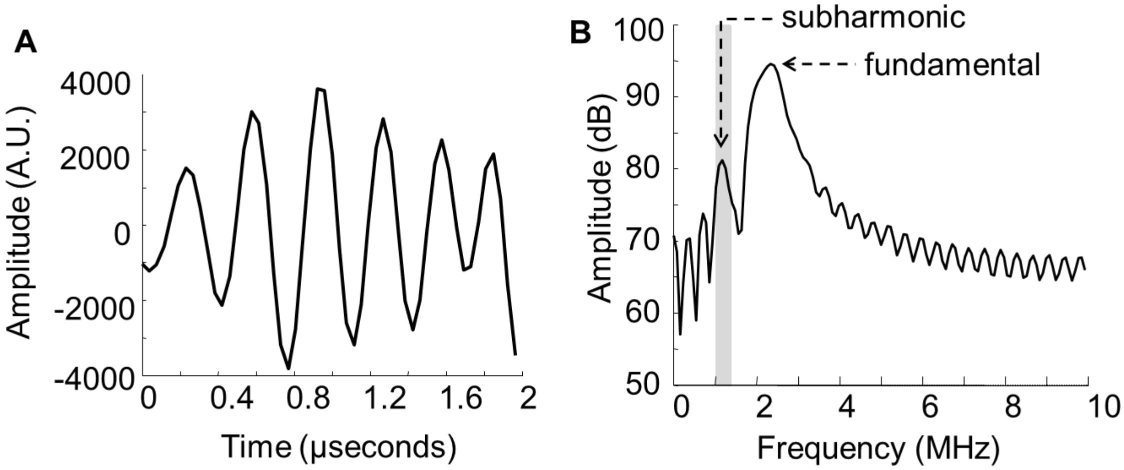

Figure 3.7: Sample data acquired from a PW Doppler gate. Data acquired from a single pulse (A) using the PW Doppler gate and the corresponding frequency domain representation (B). The shaded region in (B) indicates the bandwidth used for subharmonic amplitude extraction.

The resulting subharmonic signals were median filtered. This process was performed for all the runs acquired at every IAO level.

Statistical Analyses: The IAO levels eliciting most LV pressure sensitive subharmonic emissions were identified in each canine after performing one way ANOVA and post-hoc comparisons using Bonferroni corrections (148). In order to evaluate the feasibility of SHAPE, a linear regression analyses was performed using the pressure catheter values and the subharmonic data acquired at the most sensitive IAO level.

3.2.2.3 Developing a Technique to Obtain Clinically Relevant Left Ventricle (LV) Pressures using SHAPE

This study with 4 canines was undertaken because in the previous study (*Section 3.2.2.2*), the LV pressure values were used in conjunction with the subharmonic data obtained from the LV for regression analyses. While the results there would elucidate the relationship between the subharmonic data and the ambient pressure values, the approach is not suitable to obtain unknown *in vivo* pressures. Thus an approach needed to be developed for utilizing the subharmonic data from the LV to indicate LV pressures without using the LV pressure values obtained using the pressure catheter. Thus, in contrast to the previous study (*Section 3.2.2.2*), in this section the study was geared towards obtaining the "blind" LV pressures from the subharmonic data and then comparing the values to the reference LV pressures obtained with the pressure catheter.

Data Acquisition: The data acquisition involved two steps. First, the ultrasound guided pressure catheter was introduced into the aorta. The PW gate for RF data acquisition (accumulated or post pulse inversion) was placed in the aorta. After confirmation of the pressure catheter in the aorta based on grayscale ultrasound images, Sonazoid infusion was initiated. Once the presence of Sonazoid microbubbles in the aorta was confirmed data were acquired. The IAO levels on the Sonix RP scanner were varied from -8 dB to 0 dB, and the synchronous RF data and pressure catheter data were acquired; in triplicate at each IAO level.

For the second part, the Sonazoid infusion was stopped. The pressure catheter was advanced into the LV. The confirmation of the pressure catheter in the LV was obtained from grayscale ultrasound images and by studying the shape of the pressure profile measured. The PW gate for RF data acquisition (accumulated or post pulse inversion) was placed in the LV. Sonazoid infusion was resumed and the presence of Sonazoid microbubbles in the LV was again confirmed with ultrasound. Then, the IAO levels on the Sonix RP scanner were varied from -8 dB to 0 dB, and the synchronous RF data and pressure catheter data were acquired; in triplicate at each IAO level.

Data Processing: The following steps were repeated for data acquired from the aorta and the LV. The RF data for each accumulated pulse were transformed to the Fourier domain, and the subharmonic signal amplitude in dB was extracted as the average signal in a bandwidth ranging from 1 to 1.5 MHz (40 %). These data were processed using a median filter to eliminate noise spikes. The range of the subharmonic signal (i.e., maximum minus minimum subharmonic amplitude) was compared from each pulse contour (after eliminating noisy pulses) for each IAO level. The IAO level with maximum stable subharmonic signal range (at each location – aorta and LV) was selected for pressure estimation in each canine. Note, that a stable range was required because at higher IAO levels, the subharmonic range may be maximum due to the collapse of the microbubbles (saturation stage) but may not be stable; growth stage subharmonic emissions were shown to be ambient pressure sensitive (3).

Based on the subharmonic data and the pressure catheter data from the aorta, a calibration factor was calculated in (mmHg/dB) by dividing the systemic pulse pressure values and the selected subharmonic range. This calibration factor with the peak systemic pulse pressures, was applied to the subharmonic data from the LV to obtain LV pressure contours. From the resulting LV pressure contours the MLVDP, LVD_{min}, LVEDP and LVPSP were obtained and compared with the pressure catheter values.

In two canines (canines 1 and 2), the data were acquired from the aorta and the LV, while in two other canines (canines 3 and 4) the data were only acquired from the LV. This experimental design was used to evaluate a sub-hypothesis that a single calibration factor could be used across all canines or clinical cases – if this hypothesis is true, then, in future, only the data from the LV would be required. Also, such an approach would simulate a real clinical scenario, wherein a patient whose LV pressures were to be determined, is not a part of the patient-group that led to the formation of the calibration factor (statistically equivalent to a cross-validation study which involves using a data set (canines 3 and 4) independent of the data set (canines 1 and 2) used to obtain the model (i.e., calibration factor in this case). Thus, in 2 canines (canines 1 and 2) the LV pressure estimates were obtained using the calibration factors from the respective aorta data. In 2 other canines (canines 3 and 4) the LV pressure estimates were obtained with the mean calibration factor from canines 1 and 2.

Statistical Analyses: To determine the most sensitive IAO level for pressure estimation, the range of subharmonic amplitudes were compared using a one-way analysis of variance (ANOVA) with Bonferroni corrections for multiple comparisons (148). For each LV pressure estimate, two-tailed paired t-tests were conducted to evaluate if there were statistically significant differences between the estimates obtained using the subharmonic data and the pressure catheter. *P*-values less than 0.05 were considered significant.

3.2.2.4 Developing a Technique to Obtain Clinically Relevant Right Ventricle (RV) Pressures using SHAPE

This study with 5 canines was undertaken to develop an approach for utilizing the subharmonic data acquired from the RV to indicate RV pressures i.e., the motivation was similar to the study in *Section 3.2.2.3*, except that the focus of measuring pressures was in the RV.

Data Acquisition: The data acquisition involved three steps. First, the ultrasound guided pressure catheter was introduced into the aorta. The PW gate for RF data acquisition (accumulated or post pulse inversion) was placed in the aorta. After confirmation of the pressure catheter in the aorta based on grayscale ultrasound images, Sonazoid infusion was initiated. Once the presence of Sonazoid microbubbles in the aorta was confirmed based on grayscale ultrasound images, the data were acquired. The IAO levels on the Sonix RP scanner were varied from -8 dB to 0 dB, and the synchronous RF data and pressure catheter data were acquired; in triplicate at each IAO level.

For the second part, the Sonazoid infusion was stopped. The pressure catheter was removed and re-inserted through the jugular/brachiocephalic vein and advanced into the RV. The confirmation of the pressure catheter in the RV was obtained from grayscale ultrasound images. The PW gate for RF data acquisition (accumulated or post pulse inversion) was placed in the RV. Sonazoid infusion was resumed and the presence of Sonazoid microbubbles in the RV was again confirmed on ultrasound. Then, the IAO levels on the Sonix RP scanner were varied from -8 dB to 0 dB, and the synchronous RF data and pressure catheter data were acquired; in triplicate at each IAO level.

In the third part, the Sonazoid infusion was stopped and the pressure catheter was advanced in the RA. The RA pressures were recorded after confirming the presence of the pressure catheter in the RA on ultrasound images and by studying the shape of the pressure profile measured.

*Data Processin*g: The RF data for each accumulated pulse (Figs. 3.8A and 3.8B) were transformed to the Fourier domain (Figs. 3.8C and 3.8D) and the subharmonic signal amplitude (in dB) was extracted as the average signal in a bandwidth ranging from 1 to 1.5 MHz (40 %). The process was repeated for all the pulses for each acquisition. The extracted data were noise filtered in a similar way as compared to the LV data, for data acquired from the aorta and the RV in these canines, and the IAO levels eliciting maximum growth stage stable subharmonic emissions were selected for pressure estimation (from each site i.e., aorta and RV) for each canine.

Based on the subharmonic data and the pressure catheter data from the aorta, a calibration factor was again calculated in (mmHg/dB) by dividing the systemic pulse pressure values and the selected subharmonic range. This calibration factor and the RA pressure values were used with the subharmonic data from the RV to obtain RV pressure contours. This process was repeated for data from each canine.

From the RV pressure contours obtained using the subharmonic data, the RVD_{min}, RVSP and RV peak –dp/dt values were determined. These estimates were also obtained from the pressure catheter data and comparisons were performed.

Statistical Analyses: To determine the most sensitive IAO level for pressure estimation, the range of subharmonic amplitude were compared using a one-way analysis of variance (ANOVA) with Bonferroni corrections for multiple comparisons (147). For each RV pressure estimate, two-tailed paired t-tests were conducted to evaluate if there were statistically significant differences between the estimates obtained using the subharmonic data and the pressure catheter. *P*-values less than 0.05 were considered significant.

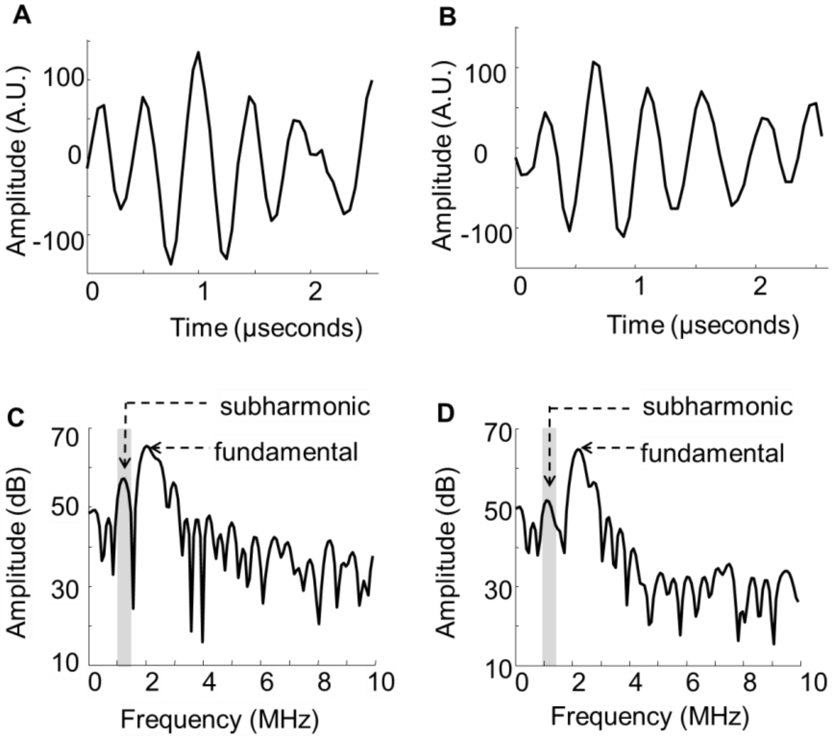

Figure 3.8: Ultrasound RF data acquired from the PW Doppler gate from the RV. The pulses correspond to time points of minimum diastolic (A) and peak systolic (B) RV pressure phases. The Fourier domain representation of the pulses in (A) and (B) are shown in (C) and (D) with the bandwidth selected for extracting the subharmonic amplitude shaded in gray. Note, that the subharmonic signal amplitude decreases from about 56 dB (C) to about 51 dB (D) as the pressure increases during systole, consistent with an inverse relationship between subharmonic signals and ambient pressure values (3, 23, 135, 138, 144). During this systolic pressure rise there is no change in the fundamental amplitude.

Overall experimental approach summarizing *in vivo* cardiac SHAPE studies is shown in Fig. 3.9. The list of canines used for cardiac SHAPE studies is given in Appendix 5.

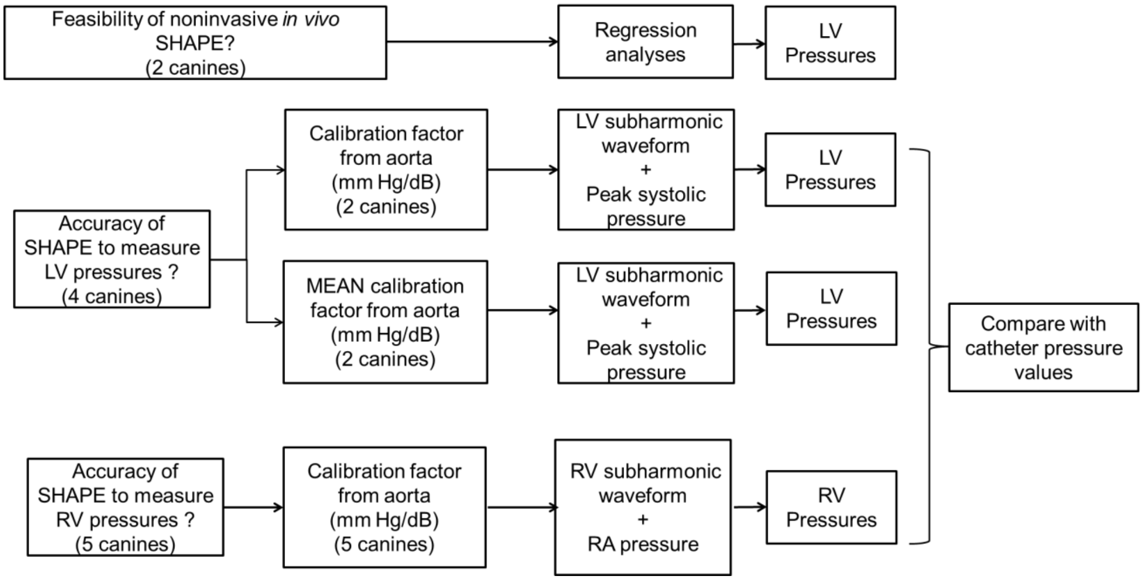
Feasibility of noninvasive *in vivo* SHAPE? (2 canines)
Regression analyses
LV Pressures
Accuracy of SHAPE to measure LV pressures ? (4 canines)
Calibration factor from aorta (mm Hg/dB) (2 canines)
LV subharmonic waveform + Peak systolic pressure
LV Pressures
MEAN calibration factor from aorta (mm Hg/dB) (2 canines)
LV subharmonic waveform + Peak systolic pressure
LV Pressures
Compare with catheter pressure values
Accuracy of SHAPE to measure RV pressures ? (5 canines)
Calibration factor from aorta (mm Hg/dB) (5 canines)
RV subharmonic waveform + RA pressure
RV Pressures

Figure 3.9: Summary of experimental approach for *in vivo* cardiac SHAPE studies

A summary of data acquisition parameters for the cardiac SHAPE studies is provided in Table 3.4

Table 3.4: Data acquisition parameters for cardiac SHAPE studies

Scanner; Probe:	Sonix RP; PA4-2
Scanning mode:	Pulse inversion imaging; 2 transmit cycles
$f_{transmit}$; $f_{receive}$:	2.5 MHz; 1.25 MHz
Contrast agent; Administration:	Sonazoid; Continuous infusion (0.15 μl/kg/min) with 0.9% NaCl (saline) via forelimb vein
Synchronous pressure monitoring:	5F solid state catheter tip manometer
IAO:	-8 dB to 0 dB (0 dB maximum output; 76 kPa to 897.04 $kPa_{pk\text{-}pk}$; mechanical index < 0.38)
Pulse repetition frequency:	4 kHz to 6.7 kHz
Scanning depth:	2 cm to 7 cm
Scanned anatomy:	Aorta, LV, RV and right atrium (11 canines total)
Gate size (PW Doppler):	2 mm
Acquisitions:	5 second runs (n = 3 per IAO level)

3.2.3 *In Vivo* Portal Hypertension (PH) SHAPE Studies

The study was approved by the Institutional Animal Care and Use Committee of Thomas Jefferson University and conducted in accordance with the recommendations of the Panel on Euthanasia of the American Veterinary Medical Association. The PH SHAPE studies were divided into two separate studies: in 17 canines the efficacy of SHAPE to track PV pressures under both, low- and high- flow conditions was investigated (also the efficacy of the SHAPE processing technique was tested); then before conducting PH SHAPE studies in 5 other canines, an automated IAO optimization algorithm was implemented on Logiq 9 scanner and the efficacy of the algorithm was tested in 5 canines (with PH).

3.2.3.1 IAO Measurements for Logiq 9 Scanner with the 4C Array

The subharmonic emissions from the UCAs may be in the occurrence stage, the growth stage, or the saturation stage (3) – this depends on the IAO; about 100-200 kPa for the occurrence stage, 300-600 kPa for the growth stage and higher IAO levels for the saturation (or bubble destruction) stage. The growth phase subharmonic emissions are sensitive to ambient pressures (3). Thus, it is necessary to select the IAO levels that elicit growth phase subharmonic emissions. Consequently, it is important to have an estimate of the IAO levels given the need for growth phase subharmonic emissions to measure ambient pressures. For the Logiq 9 scanner, the acoustic output is encoded as 28 discreet percent levels ranging from 0 % to 100 % (maximum). The IAO levels corresponding to these encoded percent levels were measured using a standard water bath approach.

The IAO at the focus of the transducer were measured using calibrated 0.2 mm needle hydrophone (Precision Acoustics, Dorchester, Dorset, UK; sensitivity of 57.1 mV/MPa at 2.5 MHz). The focal point was determined by finding the point of maximum acoustic pressure using a semi-automated electronic x-y-z- positioning system. The measurements at each encoded percent level were performed in triplicate.

3.2.3.3 Selection of PH Models

These *in vivo* PH studies involved inducing PH in canines; thus a review of PH models published in the literature was conducted.

Model Selection: Various PH models for mice, rats, pigs, rabbits and canines have been described (75, 152-160). The guidelines for selection of a particular animal PH model (or for other hepatic abnormalities) have also been published (161). Note, that canines more closely approximate human physiology – at least for PH studies (156) and thus, allow transducers and settings for human studies to be investigated. Based on the animal models and clinical studies, it is known that pathophysiologically an increase in intrahepatic vascular resistance ultimately leads to PH (73, 74), while etiologically the origin of PH may be pre-, intra- or post- sinusoidal (43). Overall, a modified form of Ohm's law for fluid flow (equation 2.1) explains increases in PV pressures (75), either by an increase in PV flow or an increase in resistance to PV flow or a combination of these two. Thus, two acute PH models were considered, one based on an increase in resistance to PV flow representing a low-flow model of PH and another one with an increase in PV flow representing a high-flow volume PH model.

For the acute low-flow model of PH, increasing intra-sinusoidal resistance in the liver parenchyma by using Gelfoam (Ethicon, Somerville, NJ) injections via the PV was considered. Gelfoam has been used in canines before (162) and has shown no foreign body reactions or inflammatory developments (163). Here the hypotheses were that PV pressures would increase and the pulsatility of PV flow would decrease (due to low-flow) after Gelfoam administration. For the acute high-flow PH model, the use of an arterial-venous (A-V) shunt by connecting the splenic or femoral artery to the PV was considered. In this case, the hypotheses were that PV pressures would increase and the pulsatility of PV flow would also increase (due to the superimposition of arterial flow) after initiating the high-flow conditions in the PV.

3.2.3.3 Animal Preparation

For both PH studies, the animal preparation part of the study was similar and thus, has been summarized together.

The canines were fasted for a period of 24 hours prior to the experiments, to reduce post-prandial effects on PV pressures (164). Initially, an intravenous injection of Propofol (Abbott Laboratories, Chicago, IL; dose of 7 ml/kg) was used as the anesthetic. The canines were placed in supine position on the operating table. During the course of the experiments, the animals were intubated and anesthesia maintained with 0.5 to 2 % Isoflurane (Iso-thesia; Abbott Laboratories, Chicago, IL) via an endotracheal tube. Also a warming blanket was used to maintain normal body temperature. An 18-gauge catheter was placed in the cephalic vein for infusion of Sonazoid microbubbles (GE Healthcare, Oslo, Norway) at a concentration of 0.015 μl/kg/min.

For obtaining data from the IVC, a calibrated 5F pressure catheter (SPR 350S or SPR 350, Millar Instruments, Inc., Houston, TX) was introduced in the canines' IVC through the femoral vein. The catheter was advanced from the femoral vein to the IVC under ultrasound guidance. The presence and localization of the pressure catheter in the IVC was confirmed using color Doppler ultrasound (Fig. 3.10).

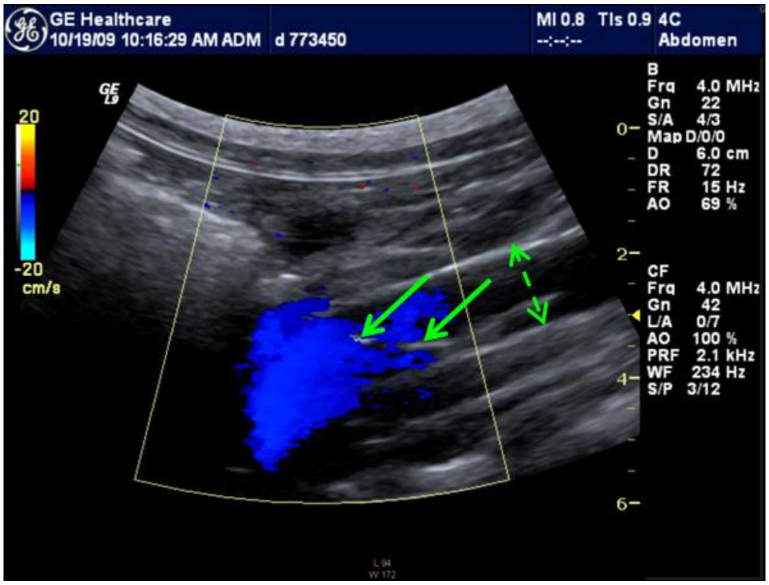
GE Healthcare
10/19/09 10:16:29 AM ADM d 773450
MI 0.8 TIs 0.9 4C
--:--:--
Abdomen
20
-20
cm/s
0–
2–
4–
6–
B
Frq 4.0 MHz
Gn 22
S/A 4/3
Map D/0/0
D 6.0 cm
DR 72
FR 15 Hz
AO 69 %
CF
Frq 4.0 MHz
Gn 42
L/A 0/7
AO 100 %
PRF 2.1 kHz
WF 234 Hz
S/P 3/12

Figure 3.10: A color Doppler image depicting flow (blue) in the IVC. Solid arrows indicate the pressure catheter in the IVC whereas the dotted arrow indicates the diameter of the IVC.

For obtaining data from the PV, a midline abdominal incision was created to provide access to the main PV or one of its branches using a sterile technique (Fig. 3.11A). A PV branch 15 cm distal to the main PV was identified and a calibrated 5 French pressure catheter (SPR 350S or SPR 350) was introduced into the PV branch (Fig. 3.11A), and then advanced into the main PV trunk under ultrasound guidance (Fig.

3.11B). The pressure catheter was fixed with a 2-0 silk suture at the entry point of the PV branch (Fig. 3.11A) to maintain the catheter position during baseline and PH data acquisition. The pressure values were observed on the oscilloscope.

At the end of the experiments the canines were sacrificed by an intravenous injection of Beuthanasia (0.25 mg/kg).

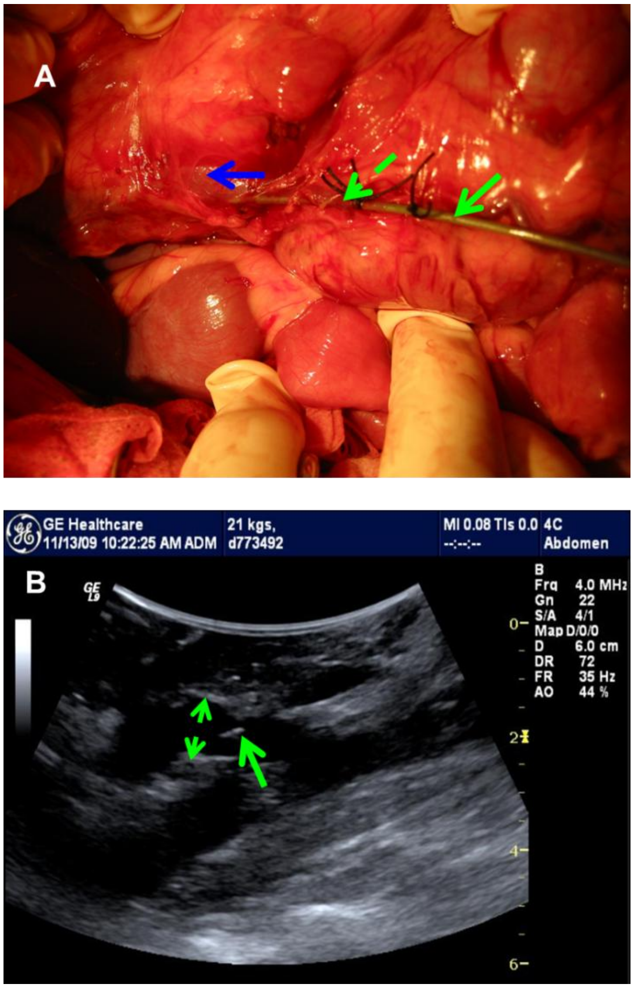
A
GE Healthcare
11/13/09 10:22:25 AM ADM
21 kgs,
d773492
MI 0.08 TIs 0.0
--:--:--
4C
Abdomen
B
B
Frq 4.0 MHz
Gn 22
S/A 4/1
Map D/0/0
D 6.0 cm
DR 72
FR 35 Hz
AO 44 %
0
2
4
6

Figure 3.11: Animal preparation for PH studies. (A) Surgical intervention to introduce pressure catheter (green arrows) into the main PV; the blue arrow indicates the direction towards the liver. (B) Grayscale ultrasound image while scanning PV of the canine; the solid arrow points to the pressure catheter while the dotted arrow indicates the diameter of the PV.

3.2.3.4 Implementation of PH Models

A 5 French catheter was inserted into another branch of PV to access the main PV for Gelfoam injection or A-V shunt connection when needed. The patency of the PV was confirmed by ultrasound imaging after these surgical procedures.

Gelfoam Model or Low-Flow Model: The acute low-flow model of PH was induced by embolization of the liver circulation using Gelfoam (Ethicon, Somerville, NJ) injection. The sterile sheet(s) of Gelfoam (100 cm^2) was (were) cut into small pieces (approximately less than 5 mm in each dimension) and immersed into sterile saline solution. The resulting mixed solution was introduced into the PV through the 5 French catheter.

A-V Shunt Model or High-Flow Model: The acute high-flow PH model was surgically induced by connecting the femoral artery to the PV using a 3-way stopcock with extension tube thereby creating an A-V shunt (Fig. 3.12). A high pressure saline infusion generated by an inflatable pressure cuff was used to supplement the flow volume when needed.

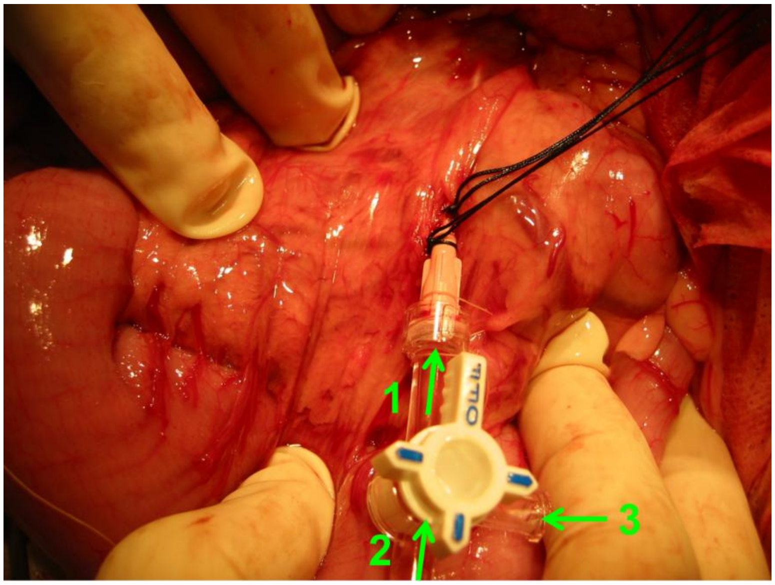

Figure 3.12: Implementation of the A-V shunt model. The numbers indicate the ports of the 3-way stopcock with the arrows indicating the direction of flow used in this experimental setup. Port 1 serves as the outlet through which blood (and extra saline, if required) is diverted to the PV, port 2 serves as the inlet for blood through the femoral vein whereas port 3 is used for high pressure saline infusion, if required.

Model Endpoints: For both PH models, the PV pressures were continuously monitored with the pressure catheter and the patency of the main PV was re-verified with ultrasound. The normal PV pressures in canines vary from 7 to 11 mmHg, whereas the mean IVC pressures vary from 5.6 to 6.6 mmHg (152, 156, 158-160, 165). Thus, the PH endpoint for this study was defined as a stabilized elevation (tracked for > 2 minutes) in PV pressures of 5 mmHg above the baseline value. The IVC pressures obtained from the canines were used for cross-verification of induced PH because PH is also present if the gradient between IVC and PV pressures exceeds 5 mmHg (15).

Model Validation: Baseline pressures were monitored for 15 to 45 minutes and pressure signals were recorded on the computer for 27 – 36 acquisitions with each acquisition containing 5 s of data. The PV diameters were obtained from the ultrasound images. Then PH was induced in canines, using either the Gelfoam model or the A-V shunt model. Pressures after inducing PH were again measured for 15 to 45 minutes and PV pressure and diameter data were acquired as before. The IVC and PV pressure data were analyzed using Matlab. The mean pressure signals from each acquisition were averaged to obtain IVC and PV pressures for the canines. The pulsatility index was calculated as the ratio of the difference between maximum and minimum pressures to the mean pressure value for each canine (similar to its initial use for characterizing velocities (166); but here this index was modified to characterize pressures).

Statistical Analyses: The pressures, pulsatility index and diameter of the PV before and after inducing PH were compared using two-tailed paired t-tests. *P*-values below 0.05 were considered significant.

3.2.3.5 Efficacy of SHAPE to Investigate PH (PH Study 1)

The motivation for this study was to evaluate the efficacy of SHAPE to track PV pressures under both, low- and high- flow conditions. Another goal was to investigate the efficacy of the SHAPE processing technique and to determine the effect of number of transmit cycles on the performance of SHAPE.

Fourteen canines were used in this study, the animal preparation for the experiments and the PH models were already explained (*sections 3.2.3.3 and 3.2.3.4*). The Gelfoam model was used to induce PH in 8 canines and in the remaining 6 canines A-V shunt model was used to induce PH.

Data Acquisition: The experimental setup for data acquisition is illustrated in Fig. 3.13.

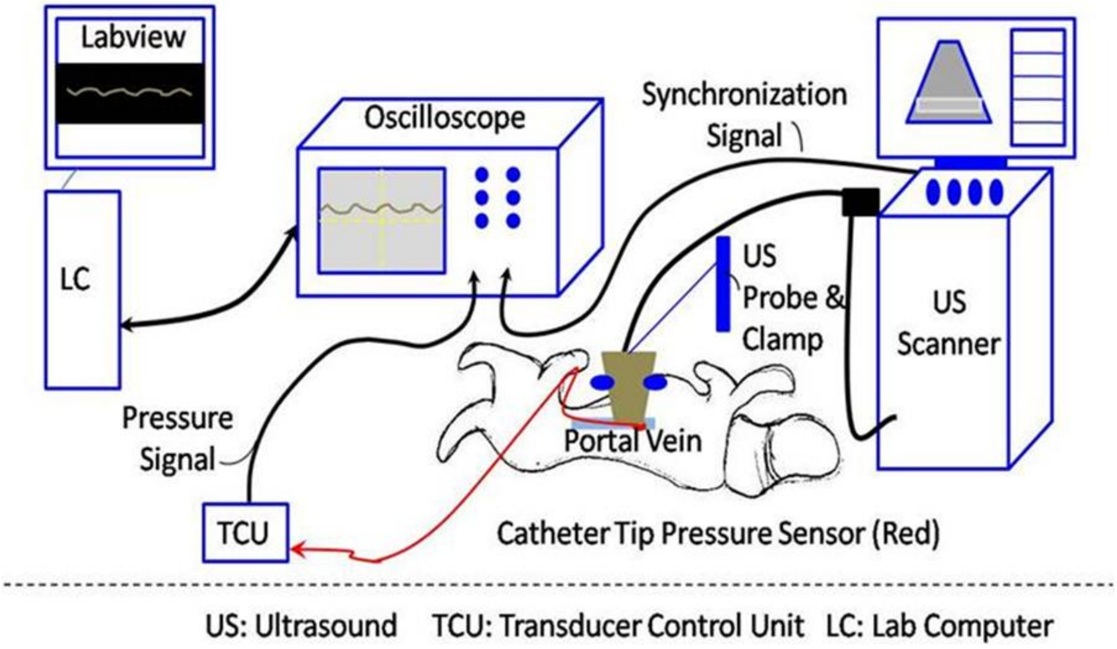
Labview
Oscilloscope
Synchronization Signal
LC
US Probe & Clamp
US Scanner
Pressure Signal
Portal Vein
TCU
Catheter Tip Pressure Sensor (Red)
US: Ultrasound
TCU: Transducer Control Unit
LC: Lab Computer

Figure 3.13: Experimental setup for PH study 1

A Logiq 9 scanner with a curvi-linear array 4C probe was modified to operate either in the standard imaging mode or in pulse inversion subharmonic imaging mode ($f_{transmit}$ = 2.5 MHz, $f_{receive}$ = 1.25 MHz). The 4C transducer was positioned directly over the PV and placed in the abdominal cavity with a support stand as illustrated in Fig. 3.14 to provide a constant scanning plane during the experiment. A sonographer and a physician confirmed the presence of the pressure catheter in the PV and the patency of the PV using standard grayscale and/or color Doppler imaging (Fig. 3.15). The pressures signals from the pressure catheter were recorded on an oscilloscope and digitized and captured on the computer using LabVIEW. A synchronization signal between the Logiq 9 scanner and the oscilloscope enabled simultaneous acquisition of the pressure catheter data and the RF data on the Logiq 9 scanner (Fig. 3.13). Note, the sonographer and the physician monitored the ultrasound scanning plane and data acquisition with the clamped probe throughout the experiment.

Using the ultrasound image as a guide, a region of interest (ROI) including the PV near the site of the pressure catheter was selected (Fig. 3.16A). The Logiq 9 scanner was then switched to RF data acquisition mode to acquire beamformed unfiltered RF data from the ROI (Fig. 3.16B).

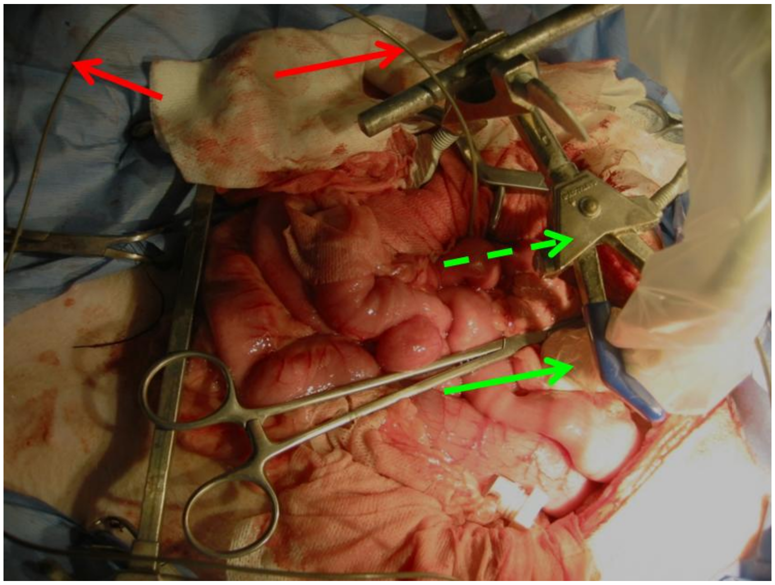

Figure 3.14: Snapshot showing the setup to acquire the data. The green solid arrow indicates the 4C transducer; note, the sterile cover over the 4C transducer used to maintain the sterile environment during data acquisition. The green dotted arrow indicates the clamp to hold the transducer. The red arrows show the pressure catheter whose tip is present in the PV.

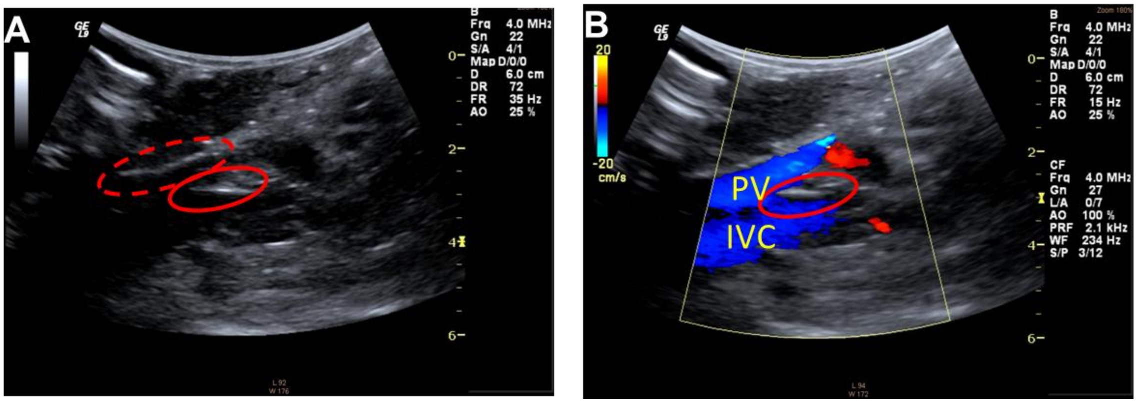
A
GE L9
B
Frq 4.0 MHz
Gn 22
S/A 4/1
Map D/0/0
D 6.0 cm
DR 72
FR 35 Hz
AO 25 %
0
2
4
6
L 92
W 176
B
GE L9
20
-20
cm/s
PV
IVC
B
Zoom 180%
Frq 4.0 MHz
Gn 22
S/A 4/1
Map D/0/0
D 6.0 cm
DR 72
FR 15 Hz
AO 25 %
CF
Frq 4.0 MHz
Gn 27
L/A 0/7
AO 100 %
PRF 2.1 kHz
WF 234 Hz
S/P 3/12
0
2
4
6
L 94
W 172

Figure 3.15: Images confirming the presence of the pressure catheter in the PV and showing the surgical inlet for inducing PH. (A) The surgical inlet for introducing PH is shown as dotted red ring and the pressure catheter is shown as solid red ring. (B). A color Doppler image showing flow in the PV and in the IVC, with the pressure catheter in the PV (solid red ring).

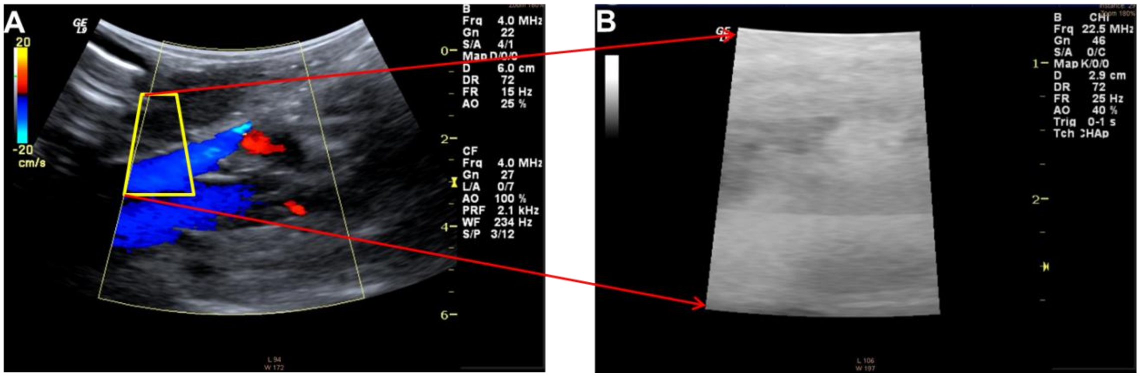
A
GE L9
20
-20
cm/s
B
Frq 4.0 MHz
Gn 22
S/A 4/1
Map D/0/0
D 6.0 cm
DR 72
FR 15 Hz
AO 25 %
0
2
4
6
CF
Frq 4.0 MHz
Gn 27
L/A 0/7
AO 100 %
PRF 2.1 kHz
WF 234 Hz
S/P 3/12
L 94
W 172
B
B CHI
Frq 22.5 MHz
Gn 46
S/A 0/C
Map K/0/0
D 2.9 cm
DR 72
FR 25 Hz
AO 40 %
Trig 0-1 s
Tch CHAp
1
2
L 106
W 197

Figure 3.16: RF data acquisition mode on Logiq 9 scanner. (A) Conventional color Doppler image to identify the region including the PV (yellow outlined area). (B) Logiq 9 scanner operated in RF data acquisition mode. Note, that the data corresponding to the yellow outlined area in (A) is shown in (B). Only the RF data only corresponding to the depth outlined in (A) is acquired.

The performance of the SHAPE technique is dependent on the growth-stage subharmonic emissions, which in turn are dependent on the IAOs. The range of peak negative IAOs spanned 0 to 0.58 MPa as the IAO output on the scanner was stepped from 0 to 100 % (*section 3.2.3.1*). Based on this data and previous *in vitro* and *in vivo* studies showing "optimum" performance of SHAPE with Sonazoid to be in the range of 0.2 to 0.6 MPa (3, 144, 167), three IAO levels corresponding to 10 % (0.14 MPa; peak negative), 20 % (0.23 MPa; peak negative) and 40 % (0.36 MPa; peak negative) were selected. Minimal attenuation was expected *in vivo* due to intra-abdominal scanning. Higher IAOs (> 40 %) were avoided to prevent the destruction of microbubbles. The confirmation that destruction of microbubbles did not occur below 40 % IAO was obtained using an *in vitro* flow phantom setup similar to the experimental setup used in previous studies (167). Lower IAOs (< 10 %) that elicit relatively low energy in the scattered beam profile at the subharmonic frequency were not used. Additionally, because the performance of SHAPE will vary with the number of transmit cycles used, 2, 3 and 4 transmit cycle pulses were considered, each at 10 %, 20 % and 40 % IAO levels. Under baseline conditions (i.e., with normal PV pressures) after Sonazoid infusion and visual confirmation of Sonazoid microbubbles in the PV, the RF data and the pressure catheter data were acquired synchronously with each combination of transmit cycles and IAO levels cumulating in 27 acquisitions (three acquisitions for every combination). Since the visibility of the ROI was compromised in the RF data acquisition mode (Fig. 3.16B), after every 3 acquisitions visual verification of the scanning plane and ROI were performed by the sonographer and the physician after switching the unit into imaging mode (Fig. 3.16A) and the ROI was relocated if required. After baseline conditions, the Sonazoid infusion was stopped and PH states were established using either Gelfoam or A-V shunt for the respective group of canines. Data acquisition in the PH states were again performed after initiating Sonazoid infusion for all transmit cycles and IAOs as described above. Note, that again 27 acquisitions were made (three acquisitions for each combination). The data were transferred to a computer for offline analyses in Matlab.

Data Processing: The data from each acquisition were saved as a DICOM (Digital Imaging and Communications in Medicine) file and the RF data extracted using a proprietary software ‘GE Raw RF data extraction facility’ (GE Global Research, Niskayuna NY). This RF data were DC filtered and then a filter centered at 1.25 MHz with 0.25 MHz bandwidth was applied to extract the subharmonic data (these filter parameters were selected based on previous *in vitro* results (167)). The subharmonic data were log-compressed to generate maximum intensity image (MIP) (Fig. 3.17).

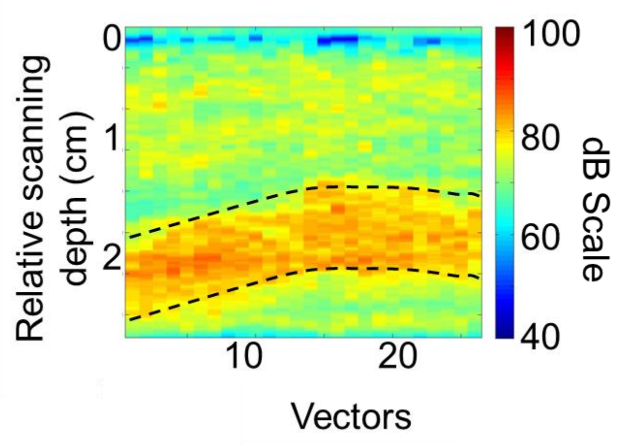

Figure 3.17: MIP subharmonic image. Here the vectors span a region of about 2.5 cm in the lateral dimension as observed with the curvi-linear 4C probe.

An ROI_{PV} (to distinguish it from the ROI used to acquire the complete RF data) was used to select the region within the PV. The PV exhibited maximum subharmonic signal intensity from the presence of Sonazoid microbubbles, whereas there was suppression of tissue signals (because of no subharmonic generation in tissue) and cancellation of other linear signals in the field of view that result from the use of pulse inversion technique (as depicted in Fig. 3.17). These ROI_{PV} selections were made in consultation with the sonographer present during data acquisition stage. Based on the selected ROI_{PV}, the subharmonic signals were extracted as the mean subharmonic amplitude value obtained from the data corresponding to the MIP image (SH_{MIP}) as well as the mean subharmonic signal obtained from the ROI_{PV} data from all frames (SH_{All_Frames}). The data corresponding to the MIP images was included in the analyses, because the MIP images are useful in providing a snapshot of vasculature and thus, whether the data corresponding to the MIP images alone, could be directly used for pressure estimation (or not), would also be verified.

Statistical Analyses: The subharmonic signal amplitudes were used to determine if there was a statistically significant difference between the number of transmit cycles and the subharmonic signal amplitude using a factorial repeated measures ANOVA. Post-hoc comparisons were performed after correcting for multiple comparisons based on the Bonferroni method (148). Linear correlation analyses were performed to identify the relationship between change in the mean PV pressures and change in the subharmonic signal amplitude, and between absolute mean PV pressures and absolute subharmonic signal amplitudes. The correlation coefficients were compared based on calculated t-statistics (168). Paired t-tests were used to analyze the difference between baseline and PH conditions for subharmonic signal amplitudes.

A cross-validation study was also performed to estimate the errors obtained with the SHAPE technique. For the cross-validation study, data from one canine under baseline and PH was eliminated and, a linear model between subharmonic amplitude and the PV pressures was obtained using data from the remaining canines. Then, based on this linear model the PV pressures at baseline and at PH condition were calculated for the canine not included in the linear model and compared to the pressure catheter data. Also based on the pressures obtained with this cross-validation approach, the sensitivity, specificity and the accuracy of identifying PH in these canines was calculated choosing a threshold value of 16 mmHg, because this represents the clinical scenario of HVPG values corresponding to moderate through severe PH cases. For canines, this value of 16 mmHg was selected based on data presented in the literature (152, 156, 158-160, 165, 169).

P-values below 0.05 were considered significant.

A summary of data acquisition parameters for the PH study (study 1) is provided in Table 3.5.

Table 3.5: Data acquisition parameters for PH study (study 1)

Scanner; Probe:	Logiq 9; 4C
Scanning mode:	Standard / Pulse inversion subharmonic
f_{transmit}; f_{receive}:	2.5 MHz; 1.25 MHz
Contrast agent; Administration:	Sonazoid; 0.015 µl/kg/min with saline via forelimb vein catheter (18 Gauge)
Synchronous pressure monitoring:	5F solid state catheter tip manometer
IAO:	10 % (0.13 to 0.15 $\mathrm{MPa}_{\mathrm{pk\ -ve}}$) 20 % (0.21 to 0.24 $\mathrm{MPa}_{\mathrm{pk\ -ve}}$) 40 % (0.35 to 0.37 $\mathrm{MPa}_{\mathrm{pk\ –ve}}$; mechanical index < 0.24)
Induced PH:	8 canines: Increased resistance: Gelfoam 6 canines: Increased flow: Arterial-Venous (A-V) shunt (femoral artery to PV)
Transmit cycles:	2, 3 and 4
Acquisitions:	5 second runs (n = 3 per combination of IAO levels and transmit cycles)

3.2.3.6 Validation of Automated IAO Optimization Algorithm (Implemented on Logiq 9 Scanner; PH Study 2)

A major limitation in the above studies (cardiac and PH study 1) impeding real-time clinical applications is the lack of knowledge about the in situ IAO levels experienced by the Sonazoid microbubbles *in vivo*. The IAO levels may be known at the transducer focal point based on *in vitro* measurements using a hydrophone, but these IAO levels will differ *in vivo* based on the scanned anatomy and patient body habitus. The IAO levels determine the stage of the subharmonic signals and in the growth stage these are sensitive to ambient pressures. Hence, a failure to elicit subharmonic emissions in the growth phase may result in erroneous pressure tracking when using SHAPE.

Therefore, the goal of this study was to develop, implement and validate an algorithm to automatically determine the optimum IAO for SHAPE applications in a given patient. A secondary goal of this study was to also compare SHAPE's performance with 8 and 16 transmit cycles (note that 2, 3 and 4 transmit cycles were compared in the previous sections). If successful, this approach may help eliminate the problems of acquiring and analyzing the data at all IAO levels as discussed in the previous sections and, thus, pave the way for real-time clinical applications.

Five canines were used in this study, the animal preparation for the experiments and the PH models utilized were already explained (*sections 3.2.3.3 and 3.2.3.4*). The Gelfoam model was used to induce PH in these 5 canines.

Equipment Setup: The experimental setup is shown in Fig. 3.18. A Logiq 9 scanner (GE Healthcare, Milwaukee, WI) with a curvi-linear array 4C probe was modified to operate in a dual imaging mode i.e., grayscale and pulse inversion subharmonic imaging modes (130). The transmit and receive frequencies were 2.5 MHz and 1.25 MHz, respectively. The RF data were acquired with all the available configurations of the transmit cycles. All scanning were performed by a sonographer and/or by a radiologist, and data were collected after Sonazoid infusion and visual verification of Sonazoid microbubbles in the PV. A crossover cable was connected for real-time data transfer between the Logiq 9 scanner and a lab computer running Matlab.

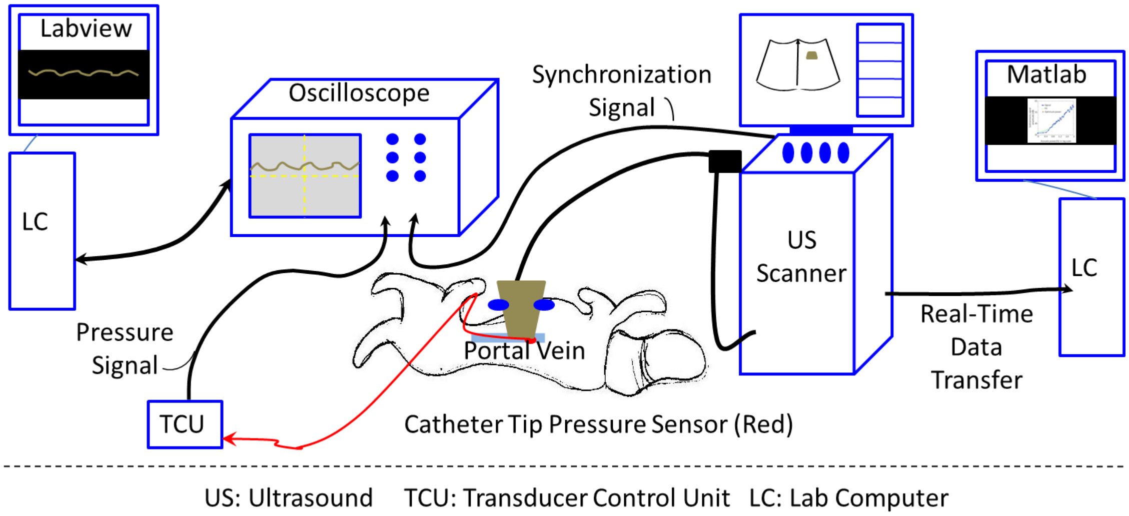
Labview
LC
Oscilloscope
Synchronization Signal
Matlab
US Scanner
LC
Real-Time Data Transfer
Pressure Signal
Portal Vein
TCU
Catheter Tip Pressure Sensor (Red)
US: Ultrasound
TCU: Transducer Control Unit
LC: Lab Computer

Figure 3.18: Experimental setup for PH study 2. Note the difference between this experimental setup and the setup used for PH study 1 (Fig. 3.13) – an additional lab computer is used to interface with the Logiq 9 scanner to enable real time transfer with the Logiq 9 scanner. The automated IAO optimization algorithm was implemented on this lab computer. and it controlled the IAO levels of the Logiq 9 and processed the data captured on Logiq 9 simultaneously. Note, that this algorithm may be ported on the Logiq 9 itself. However to avoid loading the Logiq 9's capability during scanning (especially with the physical available memory size) and to test the capability of the algorithm (first), this configuration was used.

Automatic IAO Optimization: In order to determine the optimum IAO for SHAPE a ROI was placed inside the PV as shown in Fig. 3.19. Note that the left side of Fig. 3.19 depicts the grayscale imaging mode, whereas the right side is configured to show subharmonic data (at 1.25 MHz with 1 MHz bandwidth) in the selected ROI. The automatic IAO control program was initiated based on the flowchart presented in Fig. 3.20. First, the scanner was set to 0 % (0 MPa) IAO level (Fig. 3.19: green arrow) and the corresponding data from the subharmonic ROI over 3 frames were collected. A 50 % threshold mask was applied to the subharmonic data to remove portions of the ROI with relatively low subharmonic signal (i.e., low microbubbles concentration e.g., in the surrounding tissue in Fig. 3.19) and the mean subharmonic amplitude was stored on the PC. This process was repeated for 28 discrete IAO levels up to 100 % IAO corresponding to 3.34 MPa (based on *section 3.2.3.1*). The resulting subharmonic data were plotted as a function of IAO on the PC. A polynomial fitting function was applied to this data set and the slope at each IAO level was calculated using the point-slope equation. The point with the maximum slope was determined and selected as the optimum IAO for SHAPE. The scanner was then configured to acquire SHAPE data at that IAO level.

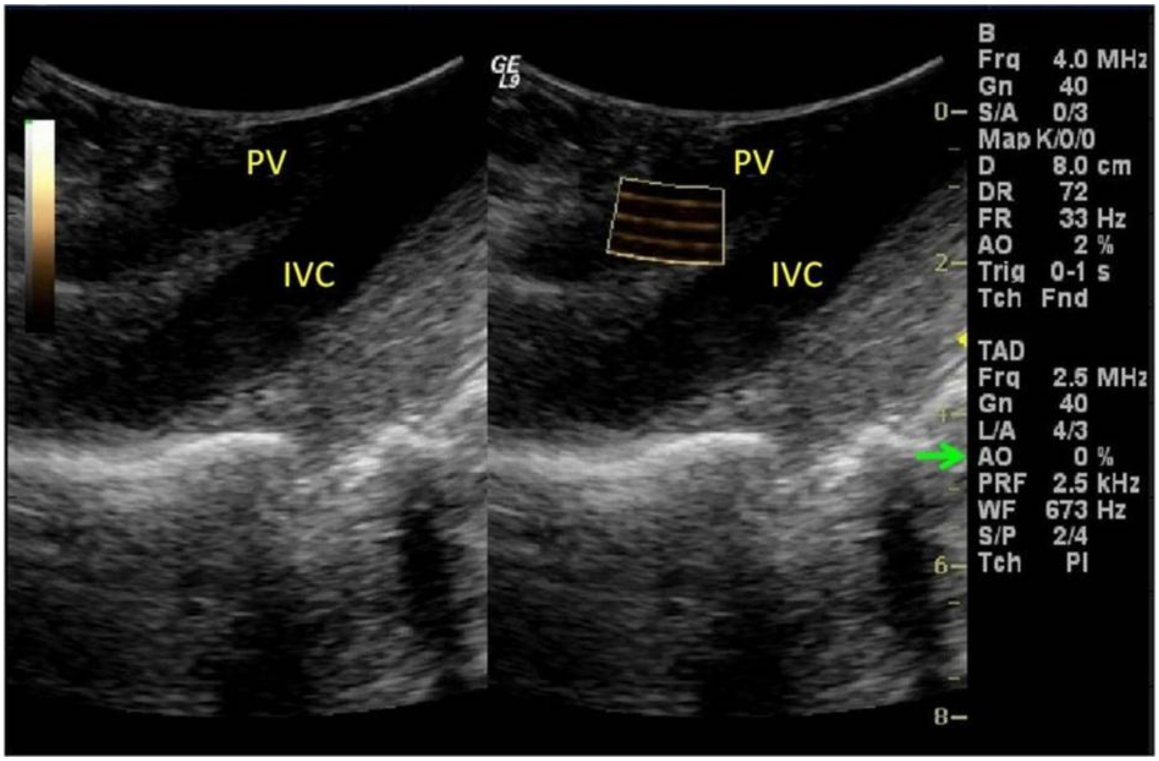
PV
IVC
GE
L9
PV
IVC
0
2
4
6
8
B
Frq 4.0 MHz
Gn 40
S/A 0/3
Map K/0/0
D 8.0 cm
DR 72
FR 33 Hz
AO 2 %
Trig 0-1 s
Tch Fnd
TAD
Frq 2.5 MHz
Gn 40
L/A 4/3
AO 0 %
PRF 2.5 kHz
WF 673 Hz
S/P 2/4
Tch PI

Figure 3.19: The dual grayscale (left) and pulse inversion subharmonic (right: in the ROI) imaging modes. The PV and IVC are marked. Note, that at the start of the IAO optimization function, the acoustic output corresponding to the subharmonic mode is set to 0 % (green arrow); due to no insonation, noise artifacts are seen in the subharmonic ROI.

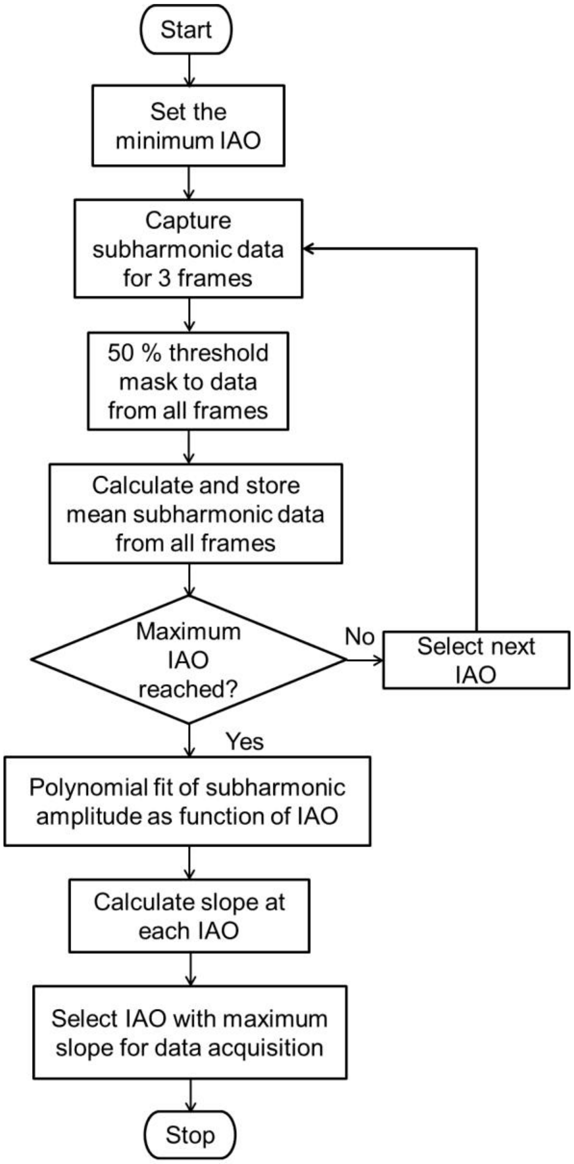
Start
Set the minimum IAO
Capture subharmonic data for 3 frames
50 % threshold mask to data from all frames
Calculate and store mean subharmonic data from all frames
Maximum IAO reached?
No
Select next IAO
Yes
Polynomial fit of subharmonic amplitude as function of IAO
Calculate slope at each IAO
Select IAO with maximum slope for data acquisition
Stop

Figure 3.20: Flowchart of the incident acoustic output (IAO) optimization function.

Data Acquisition: As shown in Fig. 3.18, a synchronization signal from the Logiq 9 scanner was connected to an oscilloscope set to acquire the PV pressures from the pressure catheter and the transducer control unit. The synchronization signal enabled simultaneous and synchronous RF and catheter data acquisition. The oscilloscope transferred the pressure catheter data to a lab computer through LabVIEW.

Under baseline conditions i.e., with normal PV pressures, the RF data and the pressure catheter data were acquired synchronously with 4, 8 and 16 transmit cycles at the optimum IAO level, at an IAO level below the optimum IAO level and then at an IAO level above the optimum IAO level (thus, three consecutive IAO levels were used). Each acquisition was a 5-second run and acquisitions at each IAO level were repeated in triplicate. The order of data acquisition was randomly varied after acquiring 3 data sets at a given configuration. Then, the Sonazoid infusion was stopped and PH states were established (by administering Gelfoam in the PV). Data were again acquired in the portal hypertension states after Sonazoid infusion as mentioned above (in the same order as during baseline conditions). The data were transferred to a computer for offline analyses in Matlab.

Data Processing: Since, the data from each acquisition were saved as a DICOM file, the subharmonic data were extracted using a proprietary software ‘GE Raw RF data extraction facility’ (GE Global Research, Niskayuna NY). This RF data were DC filtered. The subharmonic data for SHAPE from the ROI shown in Fig. 3.19 were extracted using a filter centered at 1.25 MHz with 0.25 MHz bandwidth (167). The mean subharmonic signal amplitude was then calculated from all the frames in the acquired DICOM file. This process was repeated for all acquired data.

Statistical Analyses: The hypothesis was that SHAPE's performance would be best at the optimum IAO level identified by the automatic IAO optimization program and at 4 transmit cycles. The subharmonic signal amplitudes and PV pressures before and after inducing PH were compared using paired t-tests. Linear correlation analyses were performed to identify the relationship between change in the PV pressures and change in the subharmonic signal amplitude, and between absolute PV pressures and absolute subharmonic signal amplitudes. *P*-values below 0.05 were considered significant.

A summary of data acquisition parameters for the PH study (study 2) is provided in Table 3.6.

Table 3.6: Data acquisition parameters for PH study (study 2)

Scanner; Probe:	Logiq 9; 4C
Scanning mode:	Standard / Pulse inversion subharmonic
$f_{transmit}$; $f_{receive}$:	2.5 MHz; 1.25 MHz
Contrast agent; Administration:	Sonazoid; 1.5 μl/kg/min via forelimb vein catheter (18 Gauge)
Synchronous pressure monitoring:	5F solid state catheter tip manometer
A. To determine the most-sensitive IAO for SHAPE	
IAO:	Varied from 0 to 100 % i.e., 0 to 3.34 MPa$_{pk-pk}$
Transmit Cycles:	4, 8 and 16 transmit cycles
B. To determine the efficacy of IAO optimization technique for SHAPE	
IAO:	Most-sensitive IAO and one level above and below the most-sensitive IAO
Transmit Cycles:	4, 8 and 16 transmit cycles
Induced PH:	5 canines: Increased resistance: Gelfoam
Acquisitions:	5 second runs (n = 3 per combination of IAO levels and transmit cycles)

The overall experimental approach, summarizing the *in vivo* PH SHAPE studies, is shown in Fig. 3.21 (analogous to Fig. 3.9 for *in vivo* cardiac SHAPE studies)

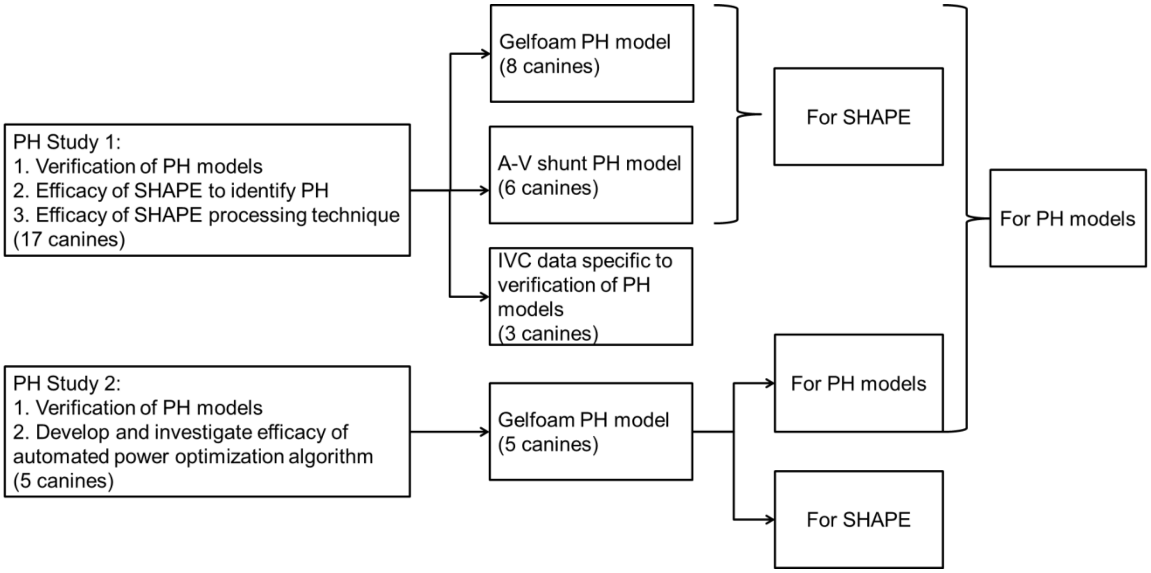
PH Study 1:
1. Verification of PH models
2. Efficacy of SHAPE to identify PH
3. Efficacy of SHAPE processing technique
(17 canines)
Gelfoam PH model
(8 canines)
A-V shunt PH model
(6 canines)
IVC data specific to verification of PH models
(3 canines)
For SHAPE
For PH models
PH Study 2:
1. Verification of PH models
2. Develop and investigate efficacy of automated power optimization algorithm
(5 canines)
Gelfoam PH model
(5 canines)
For PH models
For SHAPE

Figure 3.21: Summary of experimental approach for *in vivo* PH SHAPE studies

Additionally, Appendix 6 is included to provide very specific details about the experimental setup and operating procedures for these SHAPE experiments with Logiq 9 scanner.

Also, Appendix 7 provides a list of all the canines used for the *in vivo* PH studies.

In this chapter the materials used and methods espoused for dynamic *in vitro* SHAPE studies, *in vivo* cardiac SHAPE studies and *in vivo* PH studies were explained. A detailed list of all the statistics used for specific sections is provided as Appendix 8. The next chapter presents the results of the experiments described in this chapter along with the discussions in light of relevant published literature. Conclusions and future recommendations are presented in Chapter 5.

A list of key personnel associated with this project for future reference is provided in Appendix 9. A complete list of software used throughout this project is provided in Appendix 10. A list of grants which supported the work towards this thesis is provided in Appendix 11.

4. RESULTS AND DISCUSSIONS

This chapter includes the results corresponding to each sub-section in the Methods of Chapter 3 along with discussions and summary. A general discussion is also provided towards the end of the chapter. Specific result-statements that evaluate the hypotheses of Specific Aims 1-3 are underlined. All values are mean ± standard deviation unless explicitly stated.

4.1 Dynamic *In Vitro* Studies

4.1.1 Acoustic Output Measurements for Sonix RP scanner with the PA4-2 Array

There were 17 encoded IAO levels on the Sonix RP scanner ranging from -32 dB to 0 dB in steps of 2 dB. IAO levels below –8 dB were too low, even to form a grayscale B-mode image of the lumen of the flow phantom used in the experimental setup. Consequently only IAO levels ranging from -8 dB to 0 dB were used in the *in vitro* and *in vivo* studies. The corresponding range of IAOs was 76 to 897 kPa peak to peak. In order to present the results consistently for different scanners, the IAO levels will be represented as percentage values for plotting such that, -8 dB, -6 dB, -4 dB, -2 dB and 0 dB correspond to 39 %, 50 %, 63 %, 79 % and 100 %, respectively. This approach is also adopted because it was not feasible to know the exact IAO levels (in kPa) at the site of microbubbles *in vitro* and *in vivo*, due to differences in attenuation offered to the ultrasound beam on a case-by-case basis, aggravated by changes in tissue compositions and scanning depth.

4.1.2 Identifying Most Sensitive IAO Level for Dynamic *In Vitro* SHAPE

Fig. 4.1 shows the change in the subharmonic signal amplitude at different IAO as the ambient pressure cycled between 0 mmHg and 120 mmHg. As seen in Fig. 4.1A, the change in subharmonic signal amplitude gradually increased as the IAO was varied from -39 % to 100 %. The maximum range was seen for the incident acoustic pressure of 79 %. Fig. 4.1B is a boxplot of the changes in the subharmonic signal amplitude for each pulse contour in the 3 acquisitions at every IAO level. Video 1 in Ref. (167) demonstrates the change in the range of subharmonic amplitude as the IAO is varied from 39 % to 100 %. A between group comparison (for different IAO levels) revealed significant differences in the changes observed in the received subharmonic signals ($F_{4,51}$ = 558.903; $p < 0.001$).

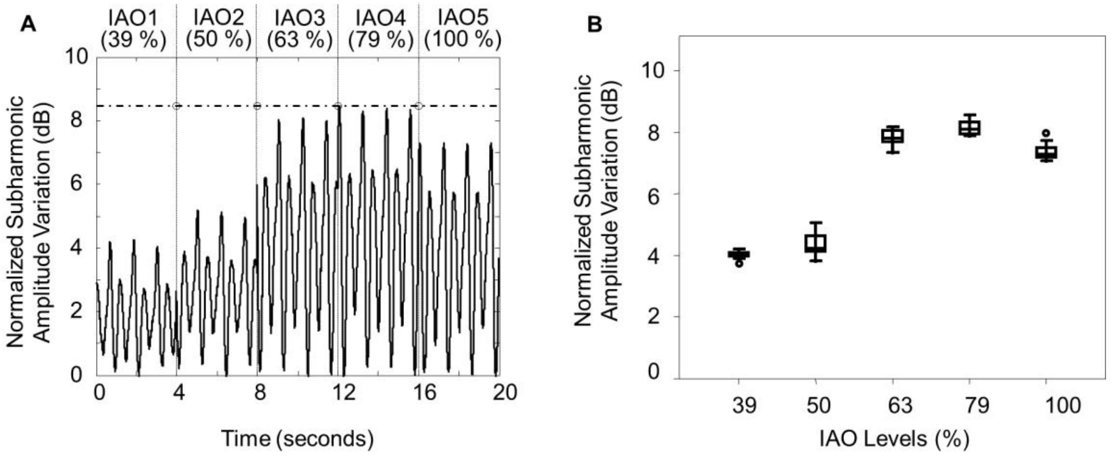

Figure 4.1: Variation in subharmonic signal amplitude as a function of IAO levels. (A) The change in subharmonic signal amplitude was analyzed as IAO levels were varied after 4 seconds (dash-dot line indicates maximum range). (B) Boxplot of subharmonic signal amplitude changes analyzed over several pressure contours as a function of IAO levels.

The range of the subharmonic signal at 79 % IAO level (8.148 dB) was significantly greater ($p < 0.001$) than the range at 39 % (4.014 dB), 50 % (4.338 dB) and 100 % (7.376 dB) (Table 4.1). No significant difference was observed between the range of the subharmonic signal at an IAO level of 63 % and 79 % (mean difference 0.327 dB; 95 % Confidence Interval -0.020 to 0.675 dB; $p = 0.08$). This indicates that at IAO levels corresponding to 63 % and 79 %, the subharmonic response from the microbubbles was in the growth stage (required for pressure tracking). Since the range of the subharmonic signal at 79 % was greater (8.148 dB) than that at 63 % (7.821 dB), 79 % was the IAO selected for ambient pressure tracking (Table 4.1).

Table 4.1: Variation in subharmonic signal amplitude as a function of IAO levels. The range of extracted and processed time varying subharmonic signal at different incident acoustic output levels as the *in vitro* ambient pressures cycled between 0 mmHg and 120 mmHg.

IAO (%)	Range of subharmonic signals (dB; n>10)			
	Mean	Standard Deviation	95% Confidence Interval	
			Lower Bound	Upper Bound
39	4.0	0.1	3.9	4.1
50	4.3	0.4	4.1	4.6
63	7.8	0.3	7.6	8.0
79	8.1	0.2	8.0	8.3
100	7.4	0.3	7.2	7.6

4.1.3 Ability of SHAPE to Estimate Ambient Pressures

Fig. 4.2A shows different components in the spectrum after the microbubbles were insonated with an IAO setting of 79 % (using the PA4-2). The fundamental and the second harmonic component show maximum deviations of 1.6 and 1.9 dB, respectively, whereas the subharmonic component shows a full-scale deflection of 8.5 dB. Based on this observation, it can be concluded that subharmonic response from the microbubbles alone may be used to track ambient pressures. Fig. 4.2B depicts the subharmonic signal amplitude variation with ambient pressure, while Fig. 4.2C demonstrates that the subharmonic response from the microbubbles may be calibrated to yield ambient pressure values as discussed below. Fig. 4.2B shows that the subharmonic signal varies inversely (or exhibits an out-of-phase relationship) with the ambient pressure as documented previously in the literature (3, 23, 135, 136). As shown in Fig. 4.2C, the subharmonic signal amplitude significantly predicted ambient pressure values using regression analysis, with standardized coefficient $\beta = -0.960$, $t\ (13330) = -398.206$, $p < 0.001$. The standardized coefficient reported here indicates the change in the number of standard deviations that will occur in the reported pressure values as a result of one standard deviation change in the subharmonic amplitude (168). A significant t-value indicates that the subharmonic amplitude is significantly contributing to the linear model in predicting the ambient pressure values. Moreover, the unstandardized coefficient representing the gradient of the regression line was -10.881 mmHg/dB (95% Confidence Interval: -10.935 mmHg/dB to -10.828 mmHg/dB). The subharmonic signal amplitude also explained a significant proportion of variance in the ambient pressure signal, $r^2 = 0.922$, F (1, 13330)

= 1.58e5, $p < 0.001$, indicating that 92 % of the change in the subharmonic amplitude was due to the ambient pressure variation.

In Fig. 4.2D a time trace of 20 seconds obtained from SHAPE using the abovementioned regression analysis is shown along with the reference pressure signal (standard error of the estimate: 7.890 mmHg). *(Based on these results Hypothesis 1, which was to evaluate if standard error between catheter pressures and SHAPE results would be below 10 mmHg with an* $r^2 > 0.75$ *for continuous runs of at least 4 seconds, was accepted).* Figs. 4.2E and 4.2F illustrate the agreement between DC-suppressed normalized power spectrum of the pressure catheter data and the subharmonic signal respectively (for the 20 second trace of Fig. 4.2D). From these spectra it is possible to determine different components of the pressure signal such as the heart rate by determining the frequency corresponding to the peak spectral amplitude. As the heart rate can be obtained noninvasively, this data can be used for verification of the SHAPE estimates before tracking cardiac pressures. Note, video 2 in Ref. (167) demonstrates active SHAPE for 20 seconds (the pressure catheter signal i.e., the reference standard is also shown).

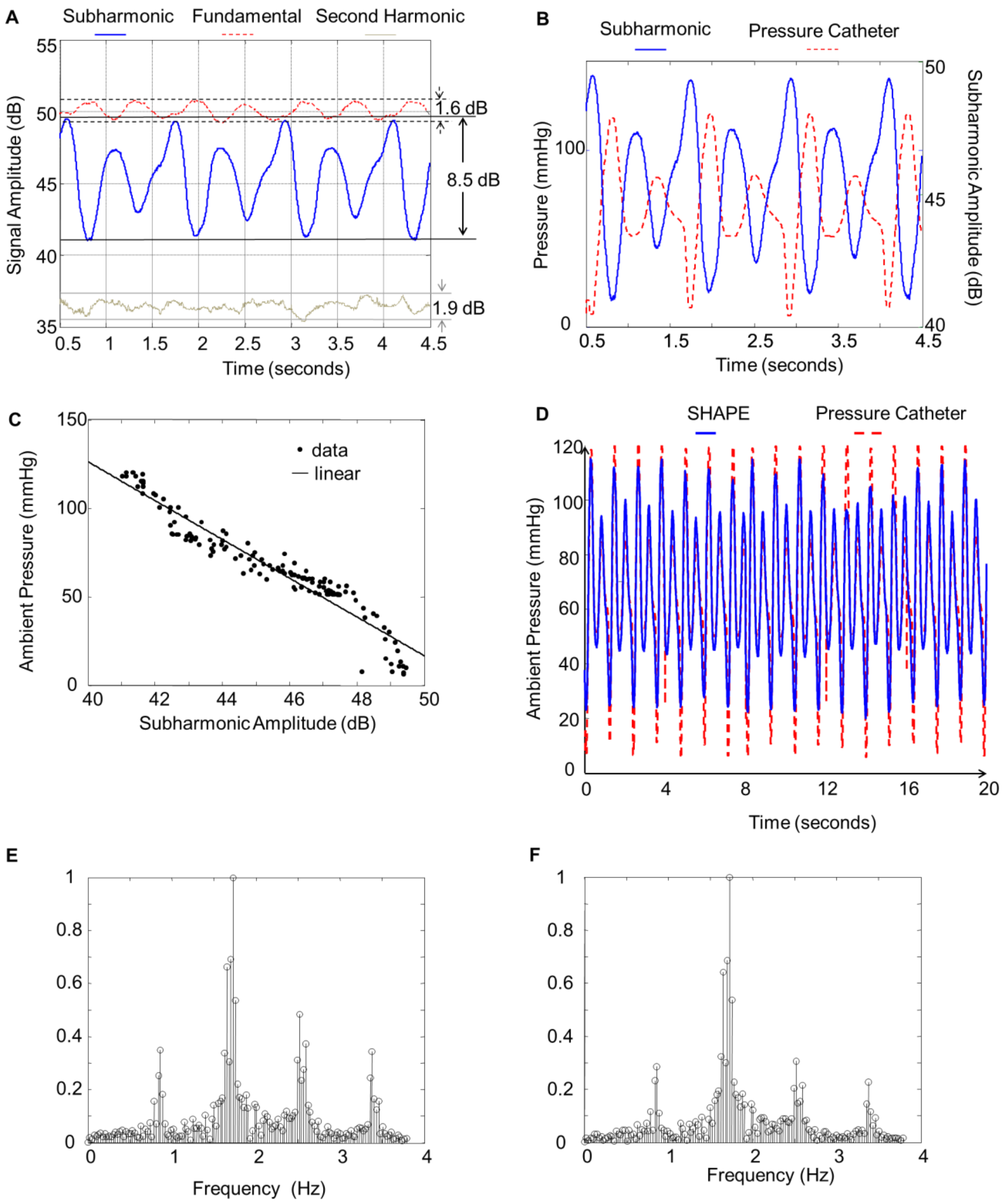

Figure 4.2: *In vitro* SHAPE results. (A) Time varying subharmonic, fundamental and second harmonic components extracted after processing the RF data. (B) The subharmonic component variation with time is plotted with the reference pressure signal from the catheter. (C) Linear regression analyses was performed to determine the relationship between the ambient pressure signal and the subharmonic signal amplitude and the resulting pressure signal (from SHAPE) was plotted with the pressure catheter signal (D). The DC suppressed normalized power spectrum for the pressure catheter data (E) and the SHAPE data (F) are also shown.

4.1.4 Confirmation of Variation of Subharmonic Signals as a Function of Ambient Pressures

Fig. 4.3 shows the SHAPE results after removing the 8 cm tissue mimicking material (tissue mimicking phantom attenuation: 0.5 dB/cm/MHz) and insonating with IAO level of 79 %. With the removal of the attenuation from the beam, the IAO level of 79 % elicited the subharmonic signals from the microbubbles in the saturation stage in which the subharmonic signals are not sensitive to ambient pressures. This resulted in the distorted pressure waveform obtained with the SHAPE technique as seen in Fig. 4.3. These results corroborate findings of the previous section that growth stage subharmonic emissions are best suited for SHAPE.

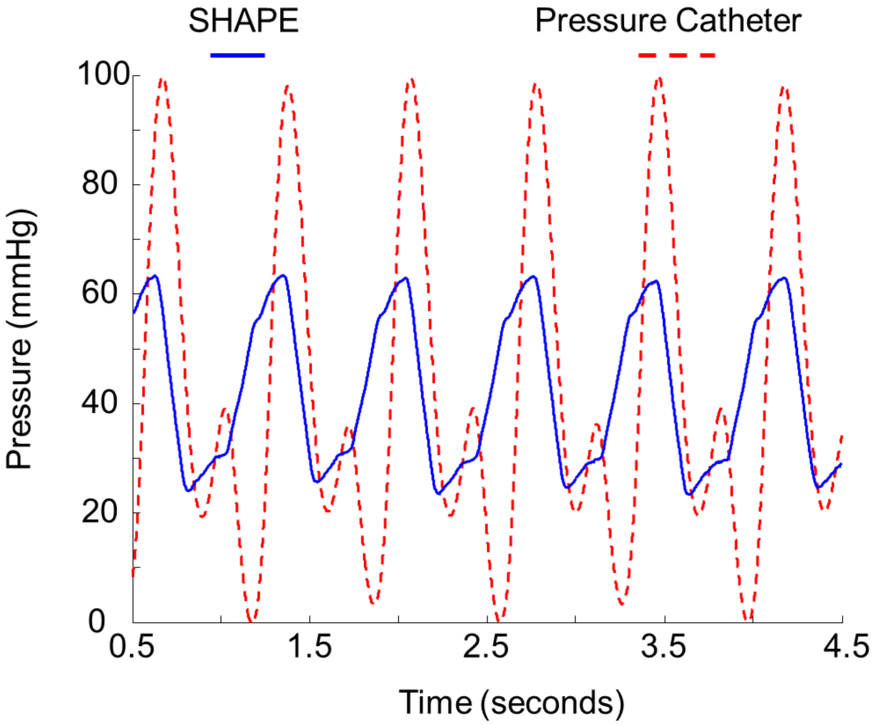

Figure 4.3: *In vitro* SHAPE with IAO levels that resulted in likely bubble destruction.

4.1.5 Developing "Best" Processing Technique for SHAPE

4.1.5.1 Comparing Processing Techniques

Both the median filtering approach and the wavelet based approach eliminated noise (noise seen in Fig. 3.2D) from the subharmonic signals delineating the underlying subharmonic signals, which are modulated by ambient pressures (Figs. 4.4 and 4.5). The wavelet-stage decompositions in Fig. 4.5 also revealed high frequency noise as was expected due to multiple scattering, etc. Moreover, again the subharmonic amplitude variations observed in this study along with the ambient pressure fluctuations confirm the inverse relationship between the ambient pressure and the subharmonic amplitude that was seen in previous data sets and also documented in the literature (e.g., (3)). The RMSEs obtained from the linear regression analysis of the subharmonic data for determining the ambient pressure values using the median and wavelet filters are shown in Fig. 4.6 as a function of the extraction techniques and the filter order.

The repeated measures design involving the median filter revealed a significant main effect of the extraction technique F(1,4) = 16.01, $p = 0.016$, of the filter order F(1,4) = 58.17, $p = 0.002$ and of the interaction effect between the extraction technique and the filter order F(1,4) = 58.46, $p = 0.002$ on the RMSEs obtained after regression analyses. On average, the least RMSEs (8.89 ± 0.27 mmHg) were noted for the extraction technique that utilized a 0.2 MHz bandwidth about the subharmonic frequency. This suggest that utilizing a bandwidth to extract the subharmonic amplitude accounts for the peak shifts that were noted (cf., Fig. 3.3A) and that were not accounted for in the control situation i.e., by extracting the amplitude at the exact theoretical subharmonic frequency. This best approach (least RMSEs) was similar to the technique in section *4.1.3*

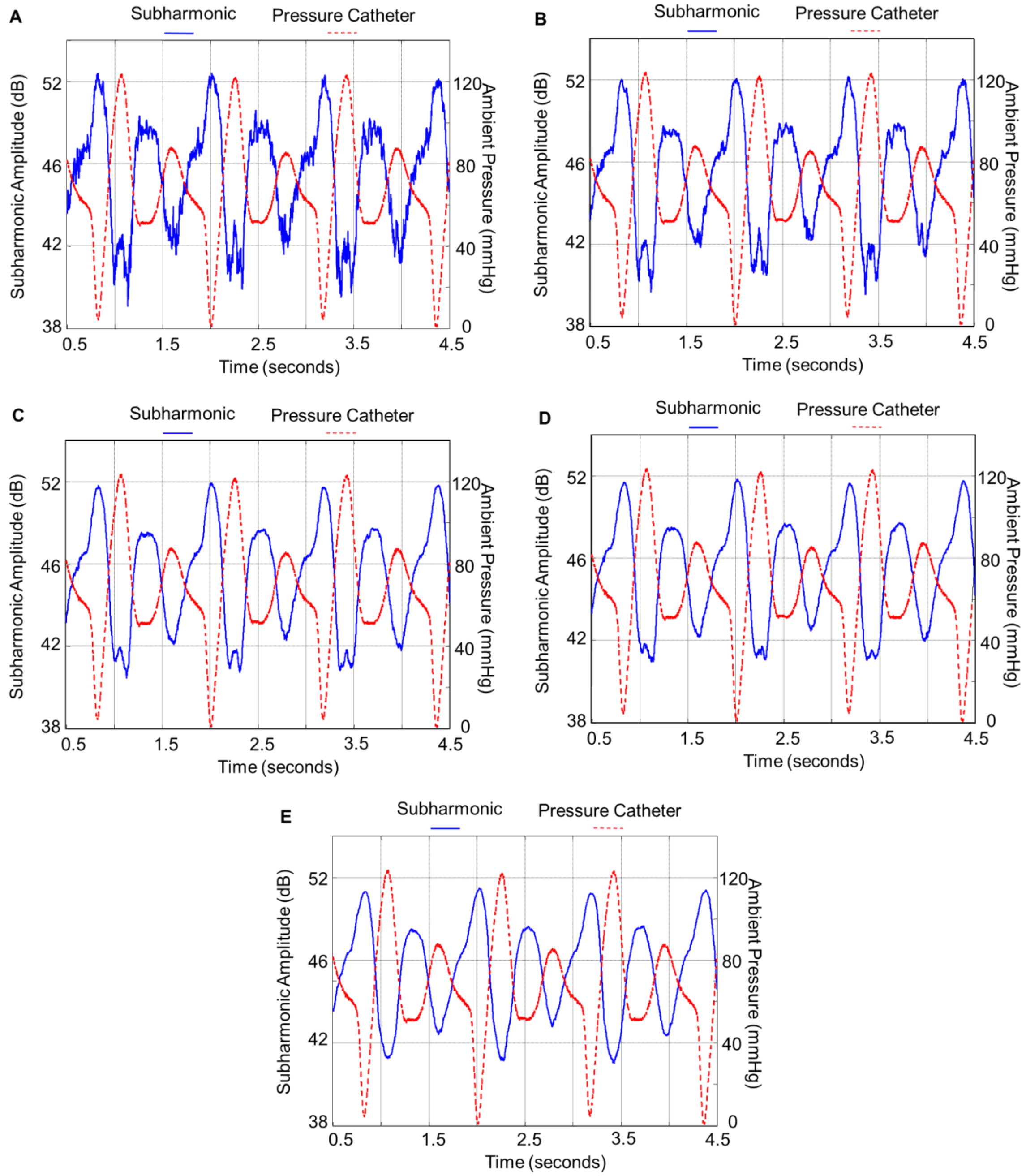

Figure 4.4: Processing of the subharmonic data using median filtering. Processing of the extracted average subharmonic signal in a 0.2 MHz bandwidth (center frequency 1.25 MHz) with a median filter (solid) of order 50 (A), 100 (B), 250 (C), 325 (D) and 500 (E) along with the pressure catheter data (dashed).

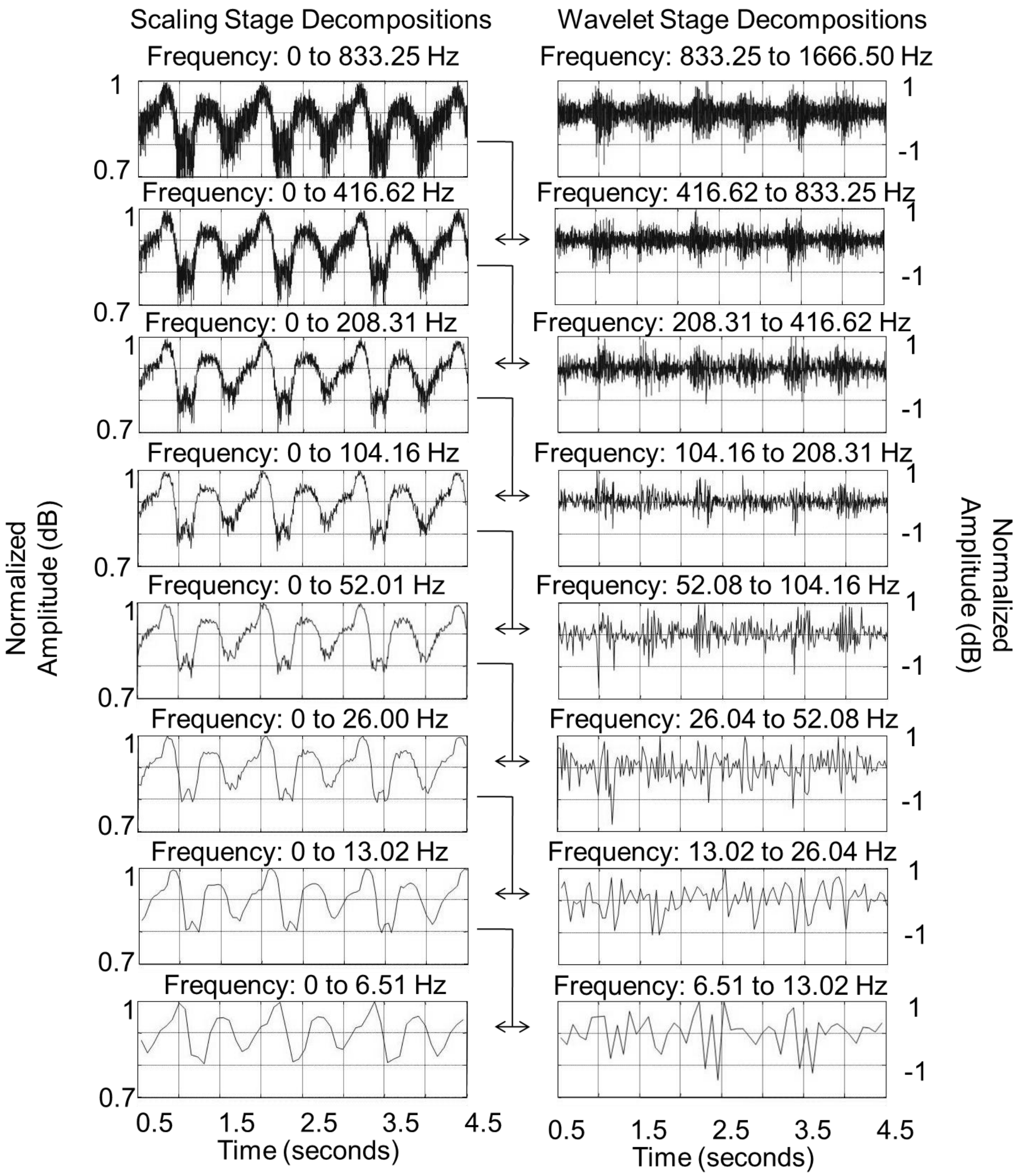

Figure 4.5: Processing of the subharmonic data using wavelet technique. An 8-stage sub-band decomposition of the extracted average subharmonic signal in a 0.2 MHz bandwidth (center frequency 1.25 MHz) into the scaling stage (left) and the wavelet stage (right). Note the high frequency noise components being filtered out at each successive scaling stage. The eight scaling stage (at the bottom) represented frequencies in a band of 0 to 6.51 Hz (spanning a clinical range of 0 to 390 beats per minute) and was used for linear least squares regression analysis.

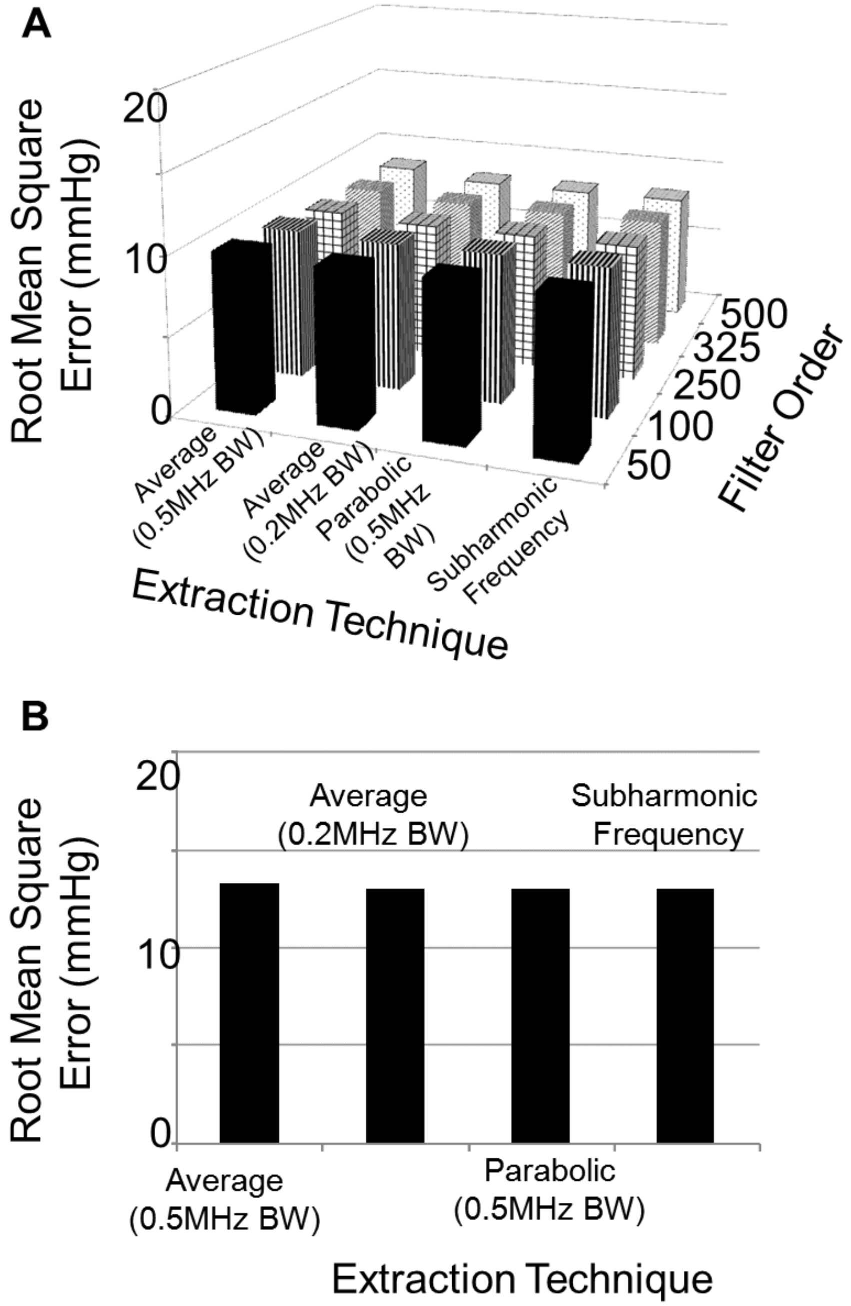

Figure 4.6: Comparing RMSEs obtained with different processing techniques. Comparison of the root mean square errors between the pressure catheter data and the pressure estimated using SHAPE technique for median-filter processing (A) and wavelet based filtering (B) (BW: bandwidth).

For the extraction technique utilizing a bandwidth to extract the subharmonic amplitude, the RMSEs were the least for the filter order of 500 (8.16 ± 0.26 mmHg) which were less than the RMSEs obtained with a filter order of 50 (9.82 ± 0.30 mmHg, $p = 0.003$), of order 100 (9.42 ± 0.30 mmHg, $p = 0.013$), of order 250 (8.72 ± 0.28 mmHg, $p = 0.179$), and of order 325 (8.38 ± 0.26 mmHg, $p = 0.575$); albeit the two later were not statistically significant. This suggests that there may exist a threshold order for median processing of the subharmonic signals and increasing the order of the filter above this level may not necessarily improve the derived pressure estimates. This filter order will be a function of the PRF and may be changed based on the PRF used to acquire the data. A maximum PRF will yield optimal temporal resolution; however, the PRF that can be used *in vivo* is primarily limited by the depth of scanning.

For the wavelet based approach, the repeated measures design indicated no significant difference between the RMSEs obtained using the different extraction techniques ($p = 1$) – the overall error produced by the wavelet based approach was 13.08 ± 0.13 mmHg as compared to an error of 8.98 mmHg ± 0.27 mmHg with the median filtering approach. The wavelet based filtering technique reported higher RMSEs probably due to the associated down-sampling while stepping through the hierarchical filter bank leading to an increasing frequency resolution but decreasing the time resolution. Thus, the pressure contours obtained with the wavelet based approach may be limited in applications like estimating wave reflections, determining the cardiac index, etc. (65, 66), where temporal resolution requirement is relatively high.

4.1.5.2 SHAPE with "Best" Processing Technique

Based on achieving the smallest RMSE, a median filtering approach with a filter order of 500 in conjunction with the extraction technique utilizing a mean signal in a 0.2 MHz bandwidth about the subharmonic center frequency of 1.25 MHz was selected for processing. The temporally varying subharmonic signals thus obtained significantly predicted the ambient pressure values (r^2 = 0.90; $p < 0.001$; Fig. 4.7). The overall RMSEs and the mean absolute errors were 8.16 ± 0.26 mmHg and 6.70 ± 0.17 mmHg, respectively. *(These results confirm the acceptance of Hypothesis 1).*

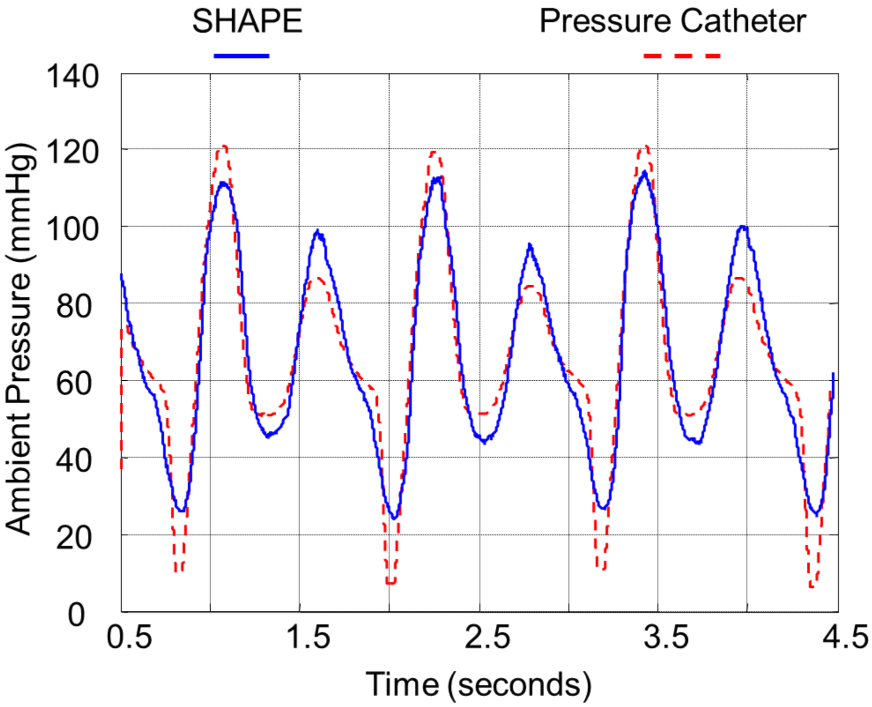

Figure 4.7: Comparing SHAPE results with catheter pressures. Ambient pressure values obtained using the catheter (dashed) and SHAPE (solid) data after least squares linear regression analysis of the extracted average subharmonic data in a 0.5 MHz bandwidth about 1.25 MHz, median-filtered with an order of 500.

The minimal errors obtained with this extraction and processing technique are presumably due to a compromise between utilizing the exact position of the subharmonic frequency i.e., at 1.25 MHz (because slight shifts in the observed subharmonic peaks were noted) and utilizing a much broader bandwidth of 0.5 MHz where the extracted amplitude may suffer from other ambient noise. While Fig. 4.7 represents a compelling result for the SHAPE technique, the pressures obtained using SHAPE did not capture the peak pressures. One reason for this could be the use of the best fit line for obtaining ambient pressures from the subharmonic amplitudes, because the best fit line tries to minimize the RMSE and consequently, may have compromised the peak end-points for a better pressure contour fit (an r^2 value of 0.90 still implies that only 10 % of the variance was not accounted for by the model). Another reason may be the ultrasound data acquisition PRF of 3.3 kHz, whereas for the pressure catheter the acquisition rate was 50 kHz. Thus, the ultrasound data may potentially have missed the peak pressures, which were captured by the pressure catheter.

4.1.6 Discussion Based on *In Vitro* Experiments

Currently different techniques are being developed (and tested) for subharmonic imaging (e.g., (124, 141, 170, 171), however the effort in developing and testing appropriate processing techniques to utilize the subharmonic emissions for ambient pressure estimation is lagging. Since the SHAPE approach may reduce/eliminate the number of catheterizations (and consequently the associated costs and complications) currently required for *in vivo* clinical ambient pressure estimation (4, 5), developing a robust processing technique for SHAPE is required before the clinical applications can be investigated. Therefore, the goal of this study was to develop a signal processing technique to extract and process subharmonic signals from the Sonix RP scanner that may be used for ambient pressure estimation. As the subharmonic emissions and the pressure modulated subharmonic amplitudes from UCAs are dependent on IAO (given that the other transmit parameters were fixed) (1, 3, 109) the SHAPE approach also requires a technique to determine the most sensitive IAO. This approach was presented in *section 4.1.2*.

Sonazoid microbubbles in the *in vitro* studies study showed a sensitivity of -10.881 mmHg/dB *(section 4.1.3)* and -10.655 mmHg/dB *(section 4.1.5).* This similarity is because out of the different extraction and processing techniques considered in *section 4.1.5* for SHAPE, the best processing technique turned out to be the approach previously espoused (*section 4.1.3*: extracting the subharmonic signal in a 0.2 MHz bandwidth about the theoretical subharmonic frequency and then median filtering the signal to reduce high-frequency noise); nonetheless these results corroborate the findings. The negative sign of the sensitivity indicates that the subharmonic signals were 180° out-of-phase with ambient pressure variations. The use of subharmonic microbubble emissions for pressure estimation have previously shown a sensitivity of -13.985 mmHg/dB *in vitro* (144), -6.759 mmHg/dB in simulation studies (135) and approximately -4.444 mmHg/dB *in vivo* (23) (in an invasive proof-of-concept study with single element transducers). This difference of sensitivity in the experimental setup adopted here is attributed to the flow component as the contrast agent concentration may vary spatially and temporally (as in the clinical environment). The time dependent behavior of subharmonic signals from Optison has been described with an in-phase and out-of-phase relationship with ambient pressures (138). However, this setup did not include flow and the transient in-phase relationship was attributed to the gaseous exchanges due to diffusion. Interestingly, some other studies have reported that shell encapsulated microbubbles engineered with “optimized” initial surface tension may exhibit an in-phase relationship (2.12 mmHg/dB) between the ambient pressure and the corresponding modulated subharmonic amplitudes (137) and that this relationship may be exploited for subharmonic imaging (141). However, with Sonazoid such in-phase relationship between ambient pressures and pressure modulated subharmonics has not been observed. In theory, the threshold IAO required for subharmonic generation is the least when the microbubbles are insonated at twice their resonant frequency (109). However, recent simulation studies have shown that the maximum subharmonic generation may also occur for insonation frequencies less than twice the resonant frequency (172). For the studies conducted in this work, an insonation frequency of 2.5 MHz with Sonazoid (resonance frequency is 4.4 MHz) was used because the resulting subharmonic emissions were utilized for SHAPE and the ambient pressure sensitivity of Sonazoid subharmonic emissions was found to be the best when insonated at 2.5 MHz (144).

Currently, there is no accurate theoretical explanation governing the decrease in subharmonic emissions from microbubbles as the ambient pressure increases. This effect was first documented empirically (3) and other independent studies have also reported the same (e.g., (134, 136)). A simulation study using excitation frequencies of 2.06 MHz and 2.46 MHz for Levovist and Sonazoid, respectively, also demonstrated a decrease in the subharmonic signal amplitude as the ambient pressures increased (135). It may be surmised that the volume pulsations of the bubbles give rise to the scattered signal when insonated by IAO and as the amplitude of these pulsations increase (when the IAO is in the growth stage), nonlinear effects dominate giving rise to a strong subharmonic signal. At this stage, an increase in the ambient pressures will then, perhaps, dampen the nonlinear oscillations thus causing a reduction in the subharmonic signal amplitude. Finally, when the incident acoustic pressure is very high, the bubbles oscillate violently before collapsing and thus the sensitivity to ambient pressure is lost (cf., *section 4.1.4*, Fig. 4.3). A more recent simulation study using a range of excitation frequencies again emulating Levovist and Sonazoid, showed that the subharmonic signal amplitude may vary differently if the excitation frequencies are varied (172) i.e., the subharmonic response increases as the excitation frequency increases by 40 % to 60 % above the bubbles' natural resonance frequency, and then, the subharmonic response decreases for increases in excitation frequency above a rise of 60 % beyond the bubbles' natural resonance frequency. Additionally, using single free-bubble (free: un-encapsulated) simulations the authors postulated that the emanated subharmonic response may be a function of the ratio of excitation frequency to the bubbles' natural resonance frequency, the latter being affected by changes in ambient pressure (172). These results with single-free bubble simulation models (without considering gas diffusion) indicate that the properties of a single and then an aggregate population of shell encapsulated microbubble(s) will have to be more thoroughly modeled before a complete understanding of the theory of subharmonic amplitude decrease due to an increase in ambient pressure can be established. Alternately in another study it was shown that the shift of subharmonic optimum driving frequency (i.e., in the frequency eliciting maximum subharmonic response) was maximum when the microbubbles were insonated with an "optimized" IAO (142). The authors further postulate that this may even explain a reduction in the subharmonic amplitude as the ambient pressure is increased if the microbubbles are insonated with that same value of "optimized" IAO (142). However these results should be interpreted with caution given that the results were obtained using simulations alone, and the microbubble and population of microbubbles considered (i.e., SonoVue microbubbles) do not represent the properties (like shell parameters, etc.) of Sonazoid microbubbles.

4.1.7 Summary Based on *In Vitro* Experiments

A practical and accurate technique to determine ambient pressure values in dynamic flow environments using subharmonic emissions from UCAs (i.e., SHAPE) and a commercial ultrasound unit has been developed (*sections 4.1.1-4.1.4*). Subharmonic amplitudes from microbubble emissions were extracted from the RF data and processed using different techniques. A median filter with an order of 500 showed the least RMSEs relative to pressure catheter data after regression analysis for the subharmonic signals extracted as the average amplitude in a 0.2 MHz bandwidth about the theoretical subharmonic frequency (*section 4.1.5*). This processing technique may be implemented for real-time SHAPE applications in the future.

The standard error between catheter pressures and SHAPE results ranged from 7.9 to 8.2 mmHg (i.e., was below 10 mmHg) with an $r^2 \geq 0.9$ for repeatable ($n > 5$) continuous runs of at least 4 second segments. Thus, Hypothesis 1 was accepted. These results indicate the viability of translating the SHAPE technique for *in vivo* noninvasive pressure measuring applications, given that no other technique utilizing UCAs to estimate ambient pressures produced errors below 10 mmHg.

4.2 Cardiac SHAPE Studies

4.2.1 Determination of Optimum IAO Levels for Cardiac SHAPE Studies

The determination of optimum IAO levels i.e., the IAO level eliciting growth phase subharmonic emissions is crucial before the SHAPE technique may be used to estimate ambient pressures. Thus, a separate section with detailed explanation is provided here before the results of SHAPE in predicting LV and RV pressures are shown. Also, since this step was repeated for all the cases (for LV data from 2 canines, then from LV data from 4 canines and for RV data from 5 canines), a representative data set was chosen such that it portrayed, both the occurrence of saturation and possibly bubble destruction, and also the un-occurrence of saturation at 100 % IAO levels. The case selected here is for data from the aorta and the RV of a canine.

The data set of subharmonic amplitudes obtained from the aorta and the RV of a single canine is shown in Fig. 4.8. Fig. 4.8A depicts the subharmonic data acquired from the aorta, specifically with the subharmonic amplitudes corresponding to the peak systolic and minimum diastolic pressures and Fig. 4.8B shows the data acquired from the RV. From the aortic data (Fig. 4.8A), it can be seen that the subharmonic signals are either in the occurrence stage or the growth phase, because the subharmonic amplitudes did not achieve a steady state value (characteristic of the saturation phase) even with 100 % IAO. Statistically, this was confirmed by results obtained from the ANOVA, which showed significant main effect of the IAO level (F (4, 23) = 50.7, and F (4, 28) = 27.8, $p < 0.001$) with subharmonic amplitudes at both 79 % and 100 % greater than at other IAO levels (indicating that saturation was not reached). Thus, based on higher subharmonic signal amplitude in the growth phase, the 100 % IAO level was selected (over 79 % IAO level) based on the aortic data from this canine.

On the other hand, the RV data exhibited subharmonic signals in all three phases – occurrence (up to 50 % IAO level), growth (up to 79 % IAO level) and then saturation followed by bubble destruction (marked by a decreased in subharmonic amplitude at 100 % IAO) (Fig. 4.8B). Statistically, this was confirmed by results obtained from ANOVA, which showed significant main effect of the IAO level (F (4, 31) = 129.2 and F (4, 36) = 98.5, $p < 0.001$). The post-hoc analyses revealed that subharmonic amplitudes at 100 % were less than at 79 % IAO level ($p < 0.001$) indicating saturation at 79 % IAO level and possibly bubble destruction at 100 % IAO level. Thus, 63 % IAO level was selected for the RV data from this canine.

Similarly, data from all other canines were analyzed with ANOVA revealing the optimum IAO levels to be used for SHAPE from the aorta and the LV or the RV and these are presented in the respective sections.

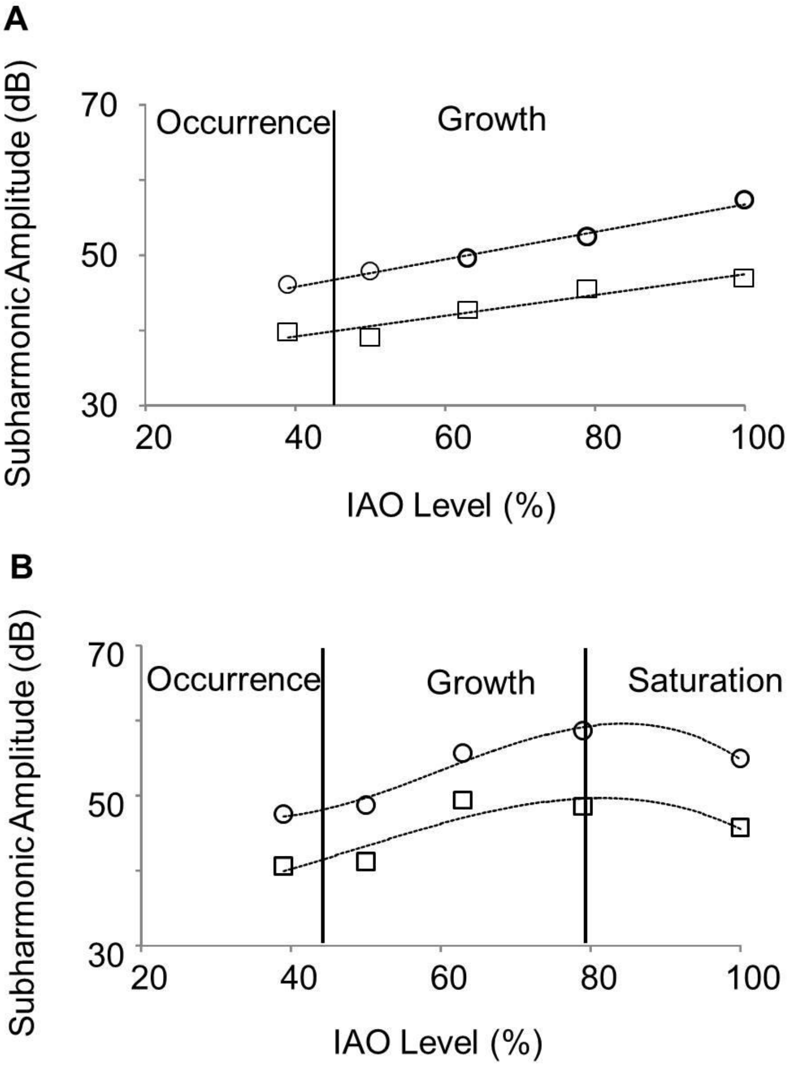

Figure 4.8: Selection of optimum IAO level for *in vivo* cardiac SHAPE. Sample subharmonic signal amplitudes from the aorta and RV of one canine. The mean subharmonic amplitudes corresponding to the peak systolic (squares) and minimum diastolic (circles) pressures in the aorta (A) and the RV (B). The distinct phases of subharmonic emissions from microbubbles identified using ANOVA and post-hoc comparisons are indicated.

4.2.2 Feasibility of Noninvasive *In Vivo* SHAPE

The results of ANOVA and post-hoc comparisons revealed that the most sensitive IAO pressures eliciting growth stage subharmonics in the 2 canines were 50 % and 100 % IAO levels. The depth of placement of the PW Doppler gate was between 5 to 7 cm (cf., Fig. 3.5). This difference in the IAO setting for the 2 canines suggests that this process of selecting the most sensitive IAO level will be required as the attenuation between cases (canines) will vary.

The SHAPE results in the LV of both the canines are shown in Figs. 4.9 and 4.10.

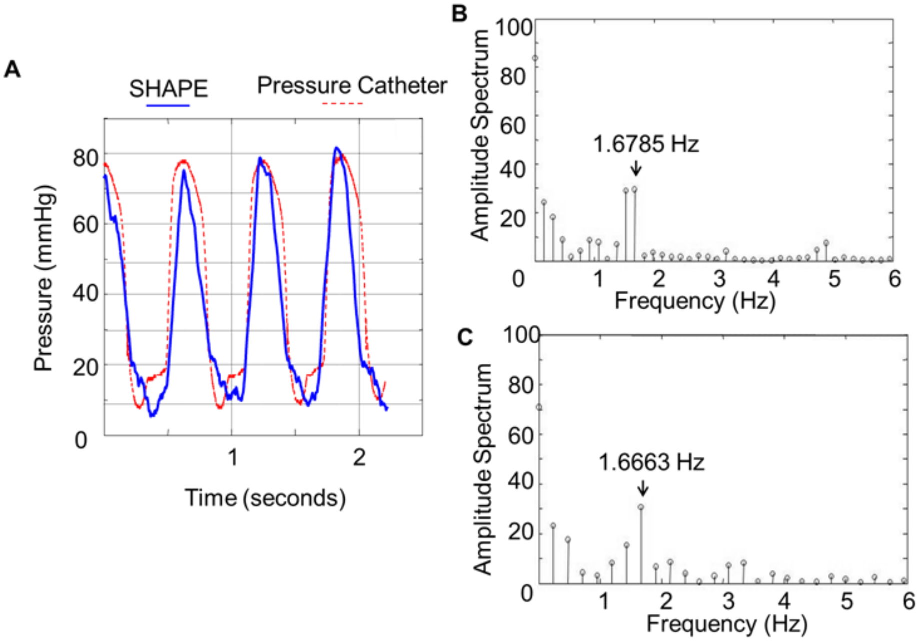

Figure 4.9: SHAPE results for LV pressures obtained from canine 1. (A) The pressure catheter signal and the SHAPE estimates. The amplitude spectrum of the pressure catheter data (B) and the SHAPE data (C) are depicted with the peak frequency in the range of 0.5 to 6.0 Hz (spanning the heart rate from 30 beats per minute to 360 beats per minute).

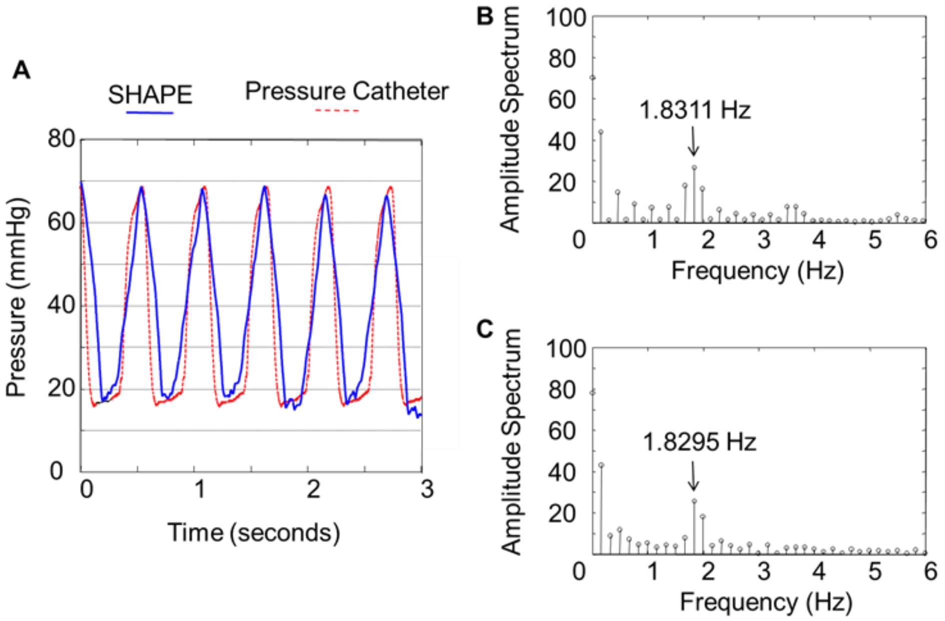

Figure 4.10: SHAPE results for LV pressures obtained from canine 2. (A) The pressure catheter signal and the SHAPE estimates. The amplitude spectrum of the pressure catheter data (B) and the SHAPE data (C) are depicted with the peak frequency in the range of 0.5 to 6.0 Hz (spanning the heart rate from 30 beats per minute to 360 beats per minute).

The subharmonic signal amplitude significantly predicted LV pressure values/waveform in both the canines ($p < 0.001$). The subharmonic signal amplitude also explained a significant proportion of variance in the left ventricle pressure profiles of the 2 canines, ($r^2 = 0.821$ and $r^2 = 0.794$; $p < 0.001$). *(Based on these results Hypothesis 2, that evaluated if the SHAPE data correlated with catheter pressures with an r^2 value greater than 0.75, was accepted)*. The standard errors of the estimate were 10.607 and 12.452 mmHg in the canines. The LVPSP and LVD_{min} were extracted from the SHAPE data and compared to the data obtained from the reference standard (Table 4.2). The maximum error in this comparison was 2.84 mmHg.

Table 4.2: Comparing SHAPE and catheter pressures after regression analyses. Comparison of the peak systolic pressures and the minimum diastolic pressures obtained using the SHAPE approach and the reference pressure catheter in the 2 canines.

Pressure Phases	Canine 1		Canine 2	
	SHAPE (mmHg)	Catheter (mmHg)	SHAPE (mmHg)	Catheter (mmHg)
LVPSP	77.6 ± 3.4	77.8 ± 1.0	68.9 ± 1.3	68.5 ± 0.1
LVD_{min}	8.8 ± 2.2	8.2 ± 0.9	18.6 ± 0.5	15.8 ± 0.1

The heart rate calculated using the peak amplitude in the normalized amplitude spectrum of the SHAPE data matched the true heart rate obtained using the power spectrum of the reference standard data (i.e., the pressure catheter waveform; 1.67 vs. 1.68 Hz for canine 1 and 1.83 Hz vs. 1.83 Hz for canine 2; Figs. 4.9 and 4.10). The peak signal frequency will indicate the heart rate as each pressure cycle corresponds to myocardial contraction followed by LV relaxation. This heart rate match between the SHAPE data and the true heart-rate (that can be obtained noninvasively) may be used as an additional verification criterion before confirming the “optimum” IAO for LV pressure monitoring.

The dynamic *in vitro* experiments were conducted at an ambient temperature of 25° C whereas the temperatures in the canines would be relatively higher (about 38° to 39° C). There are differences between bubble behaviors *in vitro* at 25° C and *in vivo* at 38° to 39° C (173). However, the fact that under both circumstances SHAPE works demonstrates that this is not an important effect for this particular application. Also the bubble concentration may vary somewhat *in vitro*, but will vary more *in vivo* due to mechanisms like phagocytosis. These transient variations in the bubble concentration result in noise in the un-filtered subharmonic signal and this problem was addressed by the use of median filtering to eliminate these resulting transient noise signals. Also, i*n vivo* to compensate for this concentration gradient, a continuous infusion at a steady rate was maintained. Thus, these results demonstrate the feasibility of conducting other *in vivo* SHAPE studies. Also, the pressure contours obtained using the subharmonic data are reproducible and this permits evaluation of parameters based on pressure contours like ventricular relaxation, cardiac output and wave reflection (65, 66). Note, that these experiments were done with a commercial scanner and UCA. Further validation and refinement of this technique are required for clinical application i.e., to estimate cardiac pressures using the subharmonic data alone, and then compare the values with the pressure catheter – this is addressed in the following sections.

4.2.3 Efficacy of SHAPE for Clinically Relevant LV Pressures

4.2.3.1 Optimum IAO levels for SHAPE

A representative data set explaining the criteria governing the selection of optimum IAO levels for SHAPE was shown in *section 4.2.1*. Consequently the optimum IAO levels obtained based on the aortic and the LV data from the canines used to evaluate the efficacy of SHAPE for clinically relevant LV pressures is provided in Table 4.3. The aortic data from canines 3 and 4 were not obtained because a sub-hypothesis to investigate the effect of using a mean calibration factor based on data from other canines was investigated in these canines.

Table 4.3: Optimum IAO levels obtained from the aortic and the LV data

	Optimum IAO Levels			
	For Aortic Data		For LV Data	
Canines	(%)	(as indicated on scanner)	(%)	(as indicated on scanner)
1	100	0 dB	50	-6 dB
2	39	-8 dB	79	-2 dB
3	N/A*	N/A*	100	0 dB
4	N/A*	N/A*	100	0 dB

* N/A: Not applicable

4.2.3.2 Calculation of Calibration Factor (mmHg/dB) in the Aorta

The systemic pulse pressures and the subharmonic amplitudes corresponding to the peak systolic and minimum diastolic pressures are given in Table 4.4. The standard deviations were derived from about 5 to 7 pressure contours per 5 second acquisition and, since data were acquired from three runs, this corresponded to about 15 to 21 values for each canine. The resulting calibration factors for each canine are also shown in Table 4.4. Note, that these values were quite similar. For the two other canines, the mean calibration factor obtained from canines 1 and 2 was used i.e., a value of -4.9245 mmHg/dB.

Table 4.4: Calibration factor calculations from the aorta for LV pressure estimation. Subharmonic signal amplitudes at optimum IAO setting are indicated. Systemic pulse values are calculated as the difference between the systolic and diastolic values. The calibration factor values are calculated by dividing the systemic pulse pressures by the systemic pulse subharmonic amplitudes.

Specific Aortic Pressure Phases	Catheter (mmHg)	Subharmonic Amplitude (dB)	Calibration Factor (mmHg/dB)
Canine 1: Peak Systolic	67.0 ± 0.4	45.3 ± 0.3	
Minimum Diastolic	44.3 ± 0.2	49.9 ± 0.4	
Systemic Pulse	22.7 ± 0.3	-4.6 ± 0.5	-4.93
Canine 2: Peak Systolic	81.1 ± 0.6	49.8 ± 0.7	
Minimum Diastolic	57.0 ± 0.5	54.7 ± 0.5	
Systemic Pulse	24.1 ± 0.7	-4.9 ± 0.8	-4.92

4.2.3.3 Obtaining LV Pressure Profiles in Canines

Fig. 4.11 shows the subharmonic signal variation and SHAPE in the LV compared to the measured pressure, along with the SHAPE generated LV pressure profile from a single canine. Specifically, Fig. 4.11A shows that the subharmonic signals varied inversely with respect to the LV pressures. Fig 4.11B is obtained when the subharmonic data from the LV, the calibration factor from the aorta and the peak systolic aortic pressures were combined.

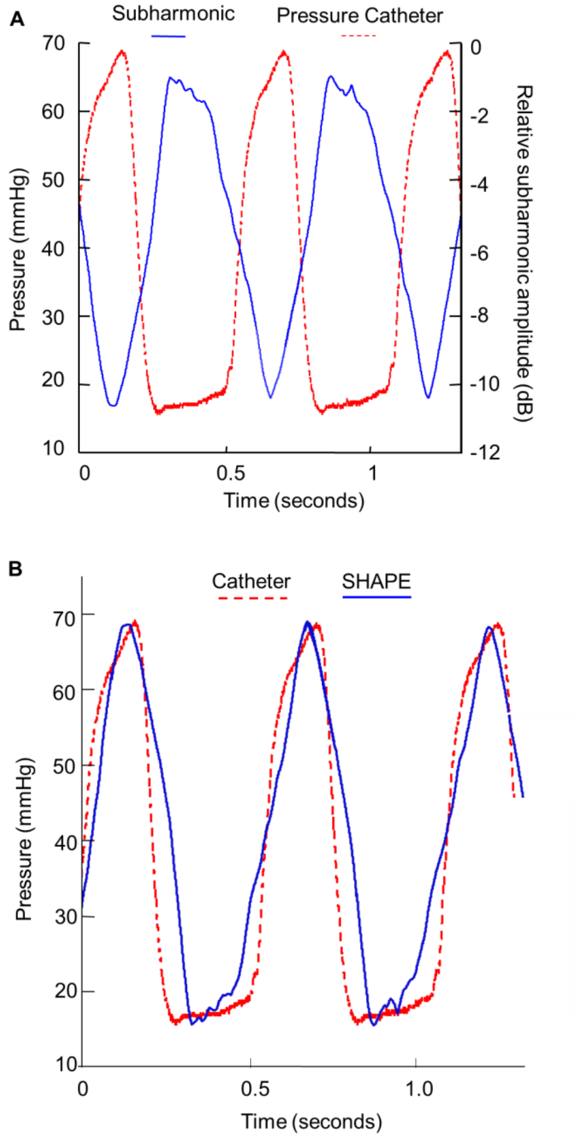

Figure 4.11: SHAPE results in the LV. (A) The subharmonic and the pressure signals are shown – note the inverse relationship which is in agreement with documented literature (3, 23, 135, 136). (B) LV pressure waveform obtained using the pressure catheter and the corresponding SHAPE results.

4.2.3.4 Comparison of SHAPE LV Pressures with Catheter Pressures

For two canines where the calibration factor were obtained from the aorta, the LV pressure estimates were calculated and compared with the pressure catheter (Table 4.5). Overall the errors between the SHAPE approach and the pressure catheter ranged from 0.19 to 2.5 mmHg. For two other canines, the mean calibration factor from the first two canines was used to estimate the LV pressures (Table 4.6). For these canines, relatively higher errors between the SHAPE approach and the pressure catheter were reported ranging from 0.64 to 8.98 mmHg.

None of the differences between the SHAPE and the reference standard for all the estimates of LV pressures were significant (Table 4.7; $p > 0.17$). The mean absolute errors for M-LVDP, LVD_{min}, LVEDP and LVPSP were 1.58 ± 1.01 mmHg, 1.35 ± 0.92 mmHg, 4.90 ± 3.26 mmHg and 1.75 ± 0.98 mmHg, respectively. Heart rate obtained from the frequency domain representation of SHAPE data and pressure catheter data was also in good agreement with maximum absolute error of 4.39 beats per minute (Tables 4.5 and 4.6). These results, based on estimates from all four canines, indicate that SHAPE is able to noninvasively track *in vivo* pressures in the LV, if the pulse pressures in the aorta are known.

The percentage errors when the calibration factors were obtained from respective canines ranged from 1 % to 15 %, but the maximum percentage error i.e., 15 % corresponded to a pressure value error of 1.4 mmHg. Such errors are sufficiently small to explore clinical applications of SHAPE.

Table 4.5: LV pressure measurements with aortic calibration factors.

	Canine 1				Canine 2			
	SHAPE	Catheter	Error		SHAPE	Catheter	Error	
	mmHg	mmHg	mmHg	%	mmHg	mmHg	mmHg	%
M-LVDP[*]	20.1	17.6	2.5	14	14.2	13.4	0.8	6
LVD_{min}[†]	15.9	15.7	0.2	1	7.5	8.9	-1.4	-15
LVEDP[‡]	22.1	19.7	2.3	12	19.1	16.9	2.2	13
LVPSP[§]	70.2	68.8	1.4	2	83.8	82.1	1.7	2
Heart Rate (per min.)	109.8	109.9	N/A	N/A	105.5	109.9	N/A	N/A

[*]mean LV diastolic pressure, [†] minimum LV diastolic pressure, [‡]LV end diastolic pressure, [§]LV peak systolic pressure

Table 4.6: LV pressure measurements without aortic calibration factors.
(abbreviations same as (Table 4.5)

	Canine 3				Canine 4			
	SHAPE	Catheter	Error		SHAPE	Catheter	Error	
	mmHg	mmHg	mmHg	%	mmHg	mmHg	mmHg	%
M-LVDP[*]	13.6	14.2	-0.6	-4	15.4	13.0	2.4	19
LVD_{min}[†]	5.8	7.2	-1.4	-20	12.0	9.6	2.4	26
LVEDP[‡]	12.1	18.1	-6.1	-33	22.0	13.0	9.0	69
LVPSP[§]	82.7	79.6	3.1	4	83.8	84.6	-0.7	1
Heart Rate (per min.)	100.0	100.7	N/A	N/A	94.8	91.5	N/A	N/A

Table 4.7: Paired comparisons of SHAPE in LV and the manometer pressures for all canines.

	Difference (mmHg) (SHAPE – manometer pressure)			95% Confidence Interval of the Difference (mmHg)		Significance (2-tailed)
	Mean	Standard deviation	Standard error of mean	Lower	Upper	
M-LVDP[*]	1.3	1.5	0.7	-1.1	3.6	0.18
LVD_{min}[†]	-0.0	1.8	0.9	-2.9	2.8	0.97
LVEDP[‡]	1.9	6.2	3.1	-7.9	11.7	0.59
LVPSP[§]	1.4	1.6	0.8	-1.2	3.9	0.18

4.2.3.5 Discussion for Cardiac SHAPE - LV

In this study, two hypotheses were tested. First, it was hypothesized that the subharmonic emissions from microbubbles can be utilized to quantify *in vivo* LV pressures noninvasively. The resultant errors in the pressures recorded by SHAPE with respect to the reference catheter measurements did not exceed 2.50 mmHg when the calibration factor from the aorta of the individual canine was used in the pressure derivation stage (cf., Table 4.5). Additionally, there were no statistically significant difference between the pressures recorded by the SHAPE approach and the pressure catheter ($p > 0.17$; cf., Table 4.7). Second, it was hypothesized that a mean calibration factor may be used across all subjects. As seen from results in Table 4.6, the errors increased up to 8.98 mmHg under this hypothesis (cf., Table 4.6). This suggests that the addition of aortic measurements to obtain calibration factor from each individual subject allows LV pressure estimates to be obtained with less error. Thus, the results obtained from SHAPE are in good agreement with the reference standard (maximum mean absolute error: 2.40 ± 2.22 mmHg) based on data from four canines across all pressure estimates.

4.2.4 Efficacy of SHAPE for Clinically Relevant RV Pressures

4.2.4.1 Optimum IAO levels for SHAPE

A representative data set explaining the criteria governing the selection of optimum IAO levels for SHAPE was shown in *section 4.2.1*. Consequently the optimum IAO levels obtained based on the aortic and the RV data from the canines used to evaluate the efficacy of SHAPE for clinically relevant RV pressures is provided in Table 4.8.

Table 4.8: Optimum IAO levels obtained from the aortic and the RV data.

	Optimum IAO Levels			
	For Aortic Data		For RV Data	
Canines	(%)	(as indicated on scanner)	(%)	(as indicated on scanner)
1	79	-2 dB	79	-2 dB
2	63	-4 dB	63	-4 dB
3	63	-4 dB	63	-4 dB
4	63	-4 dB	50	-6 dB
5	100	0 dB	63	-4 dB

4.2.4.2 Calculation of Calibration Factor (mmHg/dB) in the Aorta

The systemic pulse pressures and the subharmonic amplitudes corresponding to the peak systolic and minimum diastolic pressures are given in Table 4.9. The resulting calibration factors for each canine are also shown in Table 4.9. The mean peak systolic and minimum diastolic pressures in the aorta were 86.9 ± 20.1 mmHg and 57.5 ± 14.2 mmHg, respectively. The corresponding mean subharmonic amplitudes were 51.5 ± 6.1 dB and 61.6 ± 7.0 dB with higher subharmonic amplitudes associated with lower ambient pressures (minimum diastolic) and lower subharmonic amplitudes associated with higher ambient pressures (peak systolic), as is reported in the literature (e.g., (3)).

Table 4.9: Calibration factor calculations from the aorta for RV pressure estimation. Subharmonic signal amplitudes at optimum IAO setting are indicated. Systemic pulse values are calculated as the difference between the systolic and diastolic values. The calibration factor values are calculated by dividing the systemic pulse pressures by the systemic pulse subharmonic amplitudes.

Specific Aortic Pressure Phases	Catheter (mmHg)	Subharmonic Amplitude (dB)	Calibration Factor (mmHg/dB)
Canine 1: Peak Systolic	74.8 ± 1.2	53.0 ± 1.1	
Minimum Diastolic	49.6 ± 0.4	65.5 ± 1.3	
Systemic Pulse	25.2 ± 1.0	-12.5 ± 1.0	-2.0
Canine 2: Peak Systolic	81.0 ± 1.1	48.6±0.2	
Minimum Diastolic	59.9 ± 1.0	54.1 ± 0.3	
Systemic Pulse	21.1 ± 0.3	-5.5 ± 0.1	-3.8
Canine 3: Peak Systolic	76.7 ± 1.8	61.6 ± 2.4	
Minimum Diastolic	45.3 ± 3.0	71.6 ± 1.9	
Systemic Pulse	31.4 ± 3.5	-10.0 ± 3.1	-3.1
Canine 4: Peak Systolic	79.3 ± 0.6	47.6 ± 0.9	
Minimum Diastolic	51.7 ± 0.8	59.3 ± 1.3	
Systemic Pulse	27.6 ± 1.0	-11.7 ± 1.6	-2.4
Canine 5: Peak Systolic	122.8 ± 0.8	46.9 ± 1.7	
Minimum Diastolic	81.0 ±1.0	57.3 ± 1.1	
Systemic Pulse	41.8 ± 1.3	-10.4 ± 2.0	-4.0

4.2.4.3 Obtaining RV Pressure Profiles in Canines

Fig. 4.12 shows the subharmonic signal variation and SHAPE in the RV compared to the measured pressure, along with the SHAPE generated RV pressure profile from a single canine. Specifically, Fig. 4.12A shows that the subharmonic signals varied inversely with respect to the RV pressures. Fig 4.12B is obtained when the subharmonic data from the RV, the calibration factor from the aorta and the RA pressures were combined.

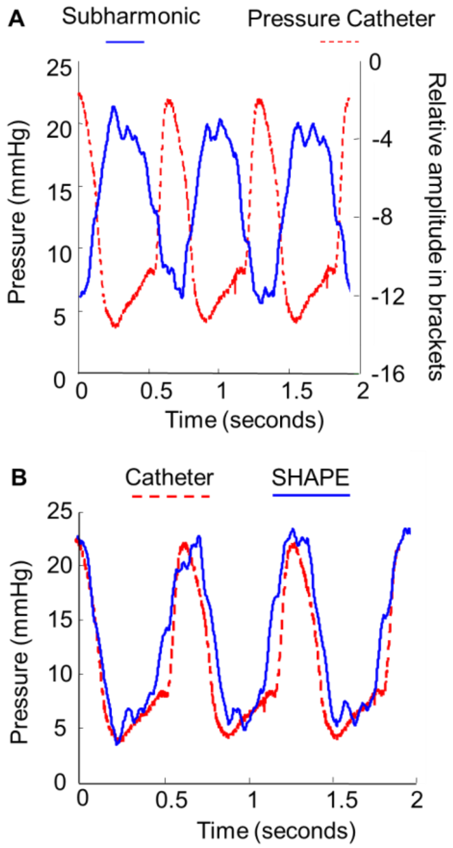

Figure 4.12: SHAPE results in the RV. (A) The subharmonic and the pressure signals are shown – note the inverse relationship which is in agreement with documented literature (3, 23, 135, 136). (B) RV pressure waveform obtained using the pressure catheter and the corresponding SHAPE results.

4.2.4.4 Comparison of SHAPE RV Pressures with Catheter Pressures

Table 4.10 lists the RVSP and RVD_{min} obtained using the SHAPE pressure contours and using the pressure catheter data. For the 5 canines the mean RVSP and RVD_{min} pressures obtained using the pressure catheter were 22.4 ± 4.6 mmHg and 4.7 ± 1.1 mmHg, respectively and obtained using the SHAPE pressures were 24.7 ± 4.8 mmHg and 5.5 ± 1.7 mmHg, respectively. The absolute errors in RVSP and RVD_{min} measurements ranged from 0.0 to 3.4 mmHg and from 0.1 to 1.8 mmHg. Table 4.10 also lists the RV relaxation rate (peak isovolumic –dp/dt) with a mean value of -132.7 ± 39.8 mmHg/s obtained with the pressure catheter data and a mean value of -135.7 ± 38.7 mmHg/s obtained with the SHAPE data; here the maximum error relative to the catheter pressure data was 5.9 mmHg/s.

Finally, the results of paired comparisons for RVSP, RVD_{min}, and RV relaxation rate obtained with the pressure catheter data and the SHAPE data are presented in Table 4.11. Although the RVSP measurements showed a significant difference ($p = 0.02$) between the pressure catheter data and SHAPE data, the absolute difference was less than 4 mmHg (mean 2.3 ± 1.3 mmHg; Table 4.11). The differences in RVD_{min}, and RV relaxation rates were small and not statistically significant (absolute mean differences 0.8 ± 0.7 mmHg and 2.9 ± 3.1 mmHg/s, respectively).

The percentage errors ranged from 1 % to 28 %, but the maximum percentage error i.e., 28 % corresponded to a pressure value error of 1.8 mmHg. Such errors are sufficiently small to explore clinical applications of SHAPE.

Table 4.10: RV pressure measurements with aortic calibration factors. RV relaxation corresponds to the late peak –dp/dt. Errors are indicated as catheter values – SHAPE values.

		Catheter	SHAPE	Error	
				Absolute	%
Canine 1:	RVSP (mmHg)	22.2 ± 1.1	24.5 ± 1.1	-2.3	10.4
	RVD_{min} Pressure (mmHg)	4.5 ± 1.0	5.4 ± 0.9	-0.9	20.0
	RV relaxation (mmHg/s)	-154.1	-155.2	1.2	0.8
Canine 2:	RVSP (mmHg)	21.3 ± 0.6	21.3 ± 1.0	0.0	0.0
	RVD_{min} Pressure (mmHg)	4.2 ± 1.0	5.0 ± 0.7	-0.8	19.0
	RV relaxation (mmHg/s)	-162.5	-161.0	-1.5	0.9
Canine 3:	RVSP (mmHg)	20.2 ± 0.9	23.6 ± 0.6	-3.4	16.8
	RVD_{min} Pressure (mmHg)	5.0 ± 0.1	5.3 ± 1.2	-0.3	6.0
	RV relaxation (mmHg/s)	-113.1	-118.6	5.5	4.9
Canine 4:	RVSP (mmHg)	18.1 ± 0.3	21.2 ± 0.6	-3.1	17.1
	RVD_{min} Pressure (mmHg)	3.5 ± 0.2	3.6 ± 1.2	-0.1	2.9
	RV relaxation (mmHg/s)	-71.5	-75.4	3.9	5.5
Canine 5:	RVSP (mmHg)	30.2 ± 3.6	32.8 ± 2.8	-2.6	8.6
	RVD_{min} Pressure (mmHg)	6.4 ± 0.9	8.2 ± 1.8	-1.8	28.1
	RV relaxation (mmHg/s)	-162.2	-168.1	5.9	3.6

Table 4.11: Paired comparisons of SHAPE in RV and the manometer pressures for all canines.

	Catheter Pressure – SHAPE Pressures		95 % Confidence Interval of the Difference		
	Mean	Standard Deviation	Lower	Upper	Significance (2-tailed)
RVSP (mmHg)	-2.3	1.3	-3.9	-0.6	0.02
RVD_{min} (mmHg)	-0.8	0.7	-1.6	0.0	0.06
RV relaxation (mmHg/s)	2.9	3.1	-0.9	6.9	0.10

4.2.4.5 Discussion for Cardiac SHAPE - RV

The SHAPE technique recorded errors ranging from 0.0 and 3.4 mmHg in measuring RVSPs and provided reproducible RV pressure waveforms for contour based analysis. Also, impairment in RV relaxation (calculated using RV filling pressure difference) is marked by a reduced RV driving force (64). Thus, measuring the RV filling pressures may identify RV diastolic dysfunction. In this regard, the SHAPE measurements yielded errors on the order of 0.1 to 1.8 mmHg in estimating RV diastolic pressures. These errors are sufficiently small to explore clinical applications of SHAPE. Finally, note that the calibration factor varied by as much as a factor of 2, encompassing a range from -2 mmHg/dB to -4 mmHg/dB; underscoring the need to obtain individual calibration factors for each case – this observation matches and supports the conclusion derived from the LV data set regarding the need to obtain individual calibration factors.

4.2.5 Discussion Based on *In Vivo* Cardiac SHAPE Studies

The IAO level required to elicit a subharmonic response sensitive to *in vivo* pressures will vary on a case-by-case basis based on attenuation of the incident beam and the scanning depth. Therefore, IAO levels on the scanner were varied and the IAO level showing maximum stable subharmonic range was selected for pressure monitoring. The data from the aorta, the LV and the RV obtained from all canines show an inverse relationship between the subharmonic signals and the ambient pressure values. A calibration factor from the aorta increases the accuracy of pressures obtained with the SHAPE approach. The calibration factor was successfully obtained for a wide range of systemic pulse pressures i.e., from 21.1 mmHg to 41.8 mmHg.

As already noted, the SHAPE technique is dependent on incident acoustic pressures. In this study, discrete increments (of 2 dB) for the IAO (fixed by the ultrasound scanner) were used. Thus, if the most "sensitive" IAO for SHAPE falls within the range of the increment then the SHAPE pressure sensing will not be "optimum", thereby contributing to the errors attained in the LV and RV pressure estimates here.

Most importantly, the results in these pilot studies for the LV and the RV pressure measurements were obtained from only four and five canines, respectively. This small sample size may obscure any statistically significant difference between SHAPE estimates and the manometer pressures. Also, the hemodynamics in the canines were not altered. However, as evident in Figs. 4.11 and 4.12, relative changes occur in the subharmonic amplitude of the signal in response to changes in the ambient pressures, and thus real-time pressure tracking is feasible (to monitor instantaneous changes as well).

4.2.6 Summary Based on *In Vivo* Cardiac SHAPE Studies

The cardiac studies performed in this work, represent the first ever application of *in vivo* noninvasive cardiac pressure estimation. The correlation between the SHAPE data and pressure catheter values showed values for $r^2 > 0.79$. Thus Hypothesis 2, that SHAPE data would correlate with catheter pressures with an $r^2 > 0.75$, was accepted. The percentage errors for LV pressures, when the calibration factors were obtained from respective canines, ranged from 1 % to 15 %, but notice that the maximum percentage error i.e., 15 % corresponded to a pressure value of 1.4 mmHg. The percentage errors for RV pressures, when the calibration factors were obtained from respective canines, ranged from 0 % to 28 %, but the maximum percentage error i.e., 28 % corresponded to a pressure value of only 1.8 mmHg. Such errors are sufficiently small to explore clinical applications of SHAPE – thus, while Hypothesis 3 should strictly be rejected (because in few cases the percent errors exceeded 10 %), the practical implications of using SHAPE to estimate cardiac pressures can neither be neglected nor be ignored. The favorable results of these pilot studies, showing errors in LV and RV systolic and diastolic pressures below 3.5 mmHg using the SHAPE technique as compared to the pressure catheter, are promising. Subharmonic emissions from UCAs have the potential to track LV and RV pressures noninvasively. These results warrant further studies and validation in clinical populations. As UCA are already approved in the United States for LV opacification, the supplementary pressure values obtained using SHAPE may provide a quantitative parameter for the diagnosis of a myriad of cardiac pathologies**.** Moreover, these pressures can be obtained with the same contrast administration dosage as the subharmonic signal amplitude reduction was negligible even when the concentration of the bubbles was varied by a factor of 3 (3).

4.3 PH SHAPE Studies

4.3.1 Verification of PH Models In Canines

4.3.1.1 PH Induction in Canines

The baseline IVC pressures obtained from the canines were 5.7 ± 1.2 mmHg (range: 4.4 to 6.7 mmHg) whereas the baseline PV pressures from the canines were 10.1 ± 2.7 mmHg (range: 7.1 to 15.8 mmHg). For the canines in the Gelfoam group, the number of Gelfoam sheets administered to reach the PH endpoint ranged from 1/3rd to 4 sheets and the time taken to attain the PH endpoint varied from 2 to 15 minutes (Table 4.12). There was no correlation between the quantity of Gelfoam used and time taken to induce PH (r = 0.22) or the change in PV pressures (r = 0.05). For 10 out of 13 canines, PH endpoint was reached (Table 4.12). For 3 other canines the data acquisition was hampered as explained in Table 4.12.

For the canines in the A-V shunt group, Table 4.13 summarizes the details about the acquired PH status. In 2 canines (Table 4.13: canines 1-2) when an increased flow volume was obtained from the femoral artery alone, the pulsatility index increased, but the defined PH endpoint was not reached. For the 3 other canines (Table 4.13: canines 4-

6) PV flow volume (in addition to the A-V shunt) was augmented by pressure saline infusion into portal circulation via 3-way stopcock connection; in these cases the PH endpoint was reached after 20 minutes.

Table 4.12: PH induction in canines using the Gelfoam technique (low-flow model)

Canine	Sheets of Gelfoam used	Time to induce PH (minutes)[*]	Canine	Sheets of Gelfoam used	Time to induce PH (minutes)[*]
1	8	N/A[†]	8	2	6
2	4	8	9	1/3	5
3	3	4	10	1/2	5
4	2	2	11	1	15
5	2	6	12	N/A[§]	N/A[§]
6[‡]	N/A[‡]	N/A[‡]	13	1/2	10
7	1	8			

[*] This denotes the time taken after Gelfoam injection(s) to reach the PH endpoint

[†] No increase in PV pressures seen and the experiment was terminated (60 minutes after the Gelfoam injections)

[‡] The pressure sensor was physically damaged and thus data from this canine were not considered

[§] Acute embolization was observed on ultrasound images and the experiment was terminated

Table 4.13: PH induction in canines using the A-V shunt technique (high-flow model)

Canine	Flow to the PV obtained from	Time to induce PH (minutes)[*]
1	Femoral artery	N/A[†]
2	Femoral artery	N/A[†,‡]
3	Femoral artery	N/A[§]
4	Femoral artery plus saline bag flushed with a pressure cuff	20
5	Same as for canine 4	20
6	Same as for canine 4	20

[*] This denotes the time taken after starting the flow from the 3-way stopcock in the PV to reach the PH endpoint

[†] No increase in PV pressures were seen; data were still acquired for the post-PH phase

[‡] The pressure signal showed high pulsatility

[§] No rise in PV pressure was observed after 45 minutes and the experiment was terminated; no data were collected for the post-PH phase

4.3.1.2 Inferior Vena Cava (IVC) and PV Data

Fig. 4.13 shows the pressure data obtained from the IVC, and from the PV before and after PH. Fig. 4.13A shows the pressure trace from the IVC, while Figs. 4.13B and 4.13C depict sample PV pressures under baseline and PH conditions from canines in the Gelfoam and the A-V shunt group, respectively. Note that the PH pressure trace in Fig. 4.13C representing the A-V shunt group shows more pulsatility as compared to the baseline pressures and pressures illustrated in Fig. 4.13B, as predicted. The pressures, pulsatility indices and diameters obtained from the IVC and the PV from all the canines are summarized in Table 4.14. From the A-V shunt group, the data from canines where the high flow volume was augmented using an additional pressure saline infusion with the help of a pressure cuff are also presented separately, as the PH endpoint was only reached in these canines (cf., Table 4.13; Table 4.14).

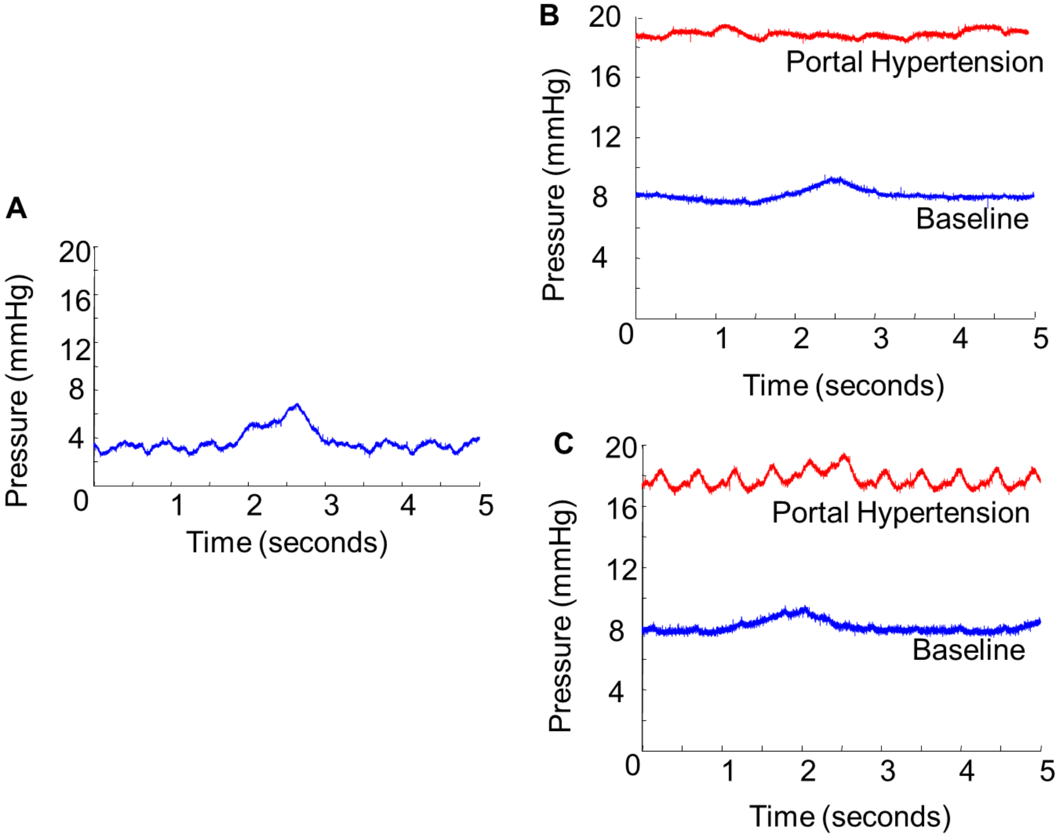

Figure 4.13: IVC and PV pressure waveforms. (A) Pressure trace obtained from the IVC of a canine. (B) Pressure traces obtained from the PV under baseline and PH states in a canine from the Gelfoam group. (C) Pressure traces obtained from the PV under baseline and PH states in a canine from the A-V shunt group. Note, the high pulsatility seen in the PV pressures after PH in the A-V shunt group relative to pressures in (B) and baseline pressures in (C).

Table 4.14: Parameters obtained from the canines before and after inducing PH from the PV and from the IVC

Experimental condition: location	Pressures (mmHg)	Pulsatility Index	Diameter (mm)
Baseline: IVC	5.7 ± 1.2	1.6 ± 0.3	11.4 ± 3.3
Baseline: PV	10.1 ± 2.7	0.6 ± 0.3	9.3 ± 1.7
Gelfoam induced PH: PV	26.5 ± 7.5	0.3 ± 0.2	9.6 ± 1.6
A-V shunt induced PH: PV	19.1 ± 6.5	0.8 ± 0.4	9.7 ± 1.6
A-V shunt induced PH*: PV	23.2 ± 4.3	0.6 ± 0.1	9.8 ± 1.5

[a] Only canines where the flow from femoral artery and saline bag were used

For all the canines where the PV data were acquired before and after PH, the PV pressures, the pulsatility index and diameter values are depicted in Figs 4.14, 4.15 and 4.16, respectively. For the Gelfoam group note the increasing trend of PV pressures and decreasing trend of the pulsatility index after PH induction. For the canines in the A-V shunt group an increasing trend of PV pressures was only seen when the saline was also used to increase the PV flow volume, whereas an overall increasing trend was observed for the pulsatility index values after induced PH. For both groups no appreciable changes in the diameters were seen (Table 4.14).

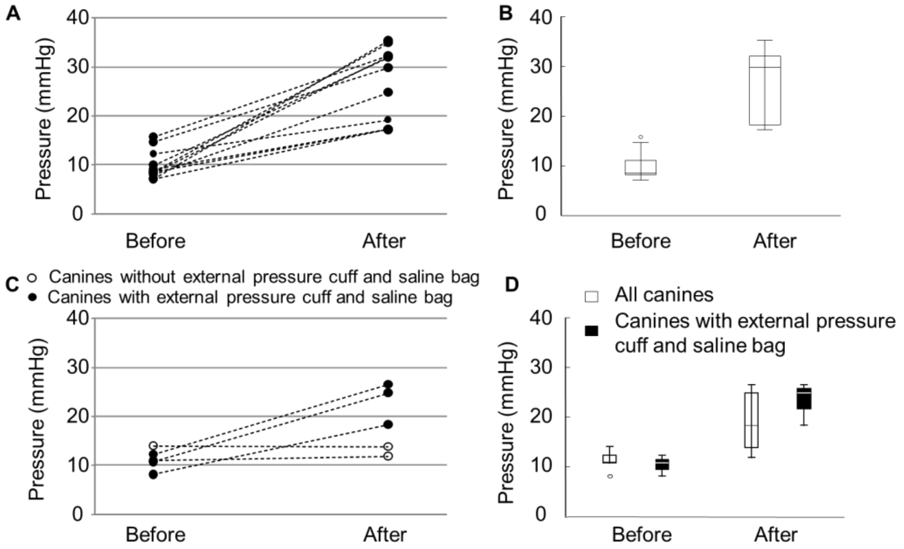

Figure 4.14: PV pressures before and after inducing PH. (A) and (B) illustrate PV pressures (for individual canines) and boxplot of the PV pressures before and after inducing PH using Gelfoam, respectively. (C) and (D) illustrate the data for the A-V shunt model. For panel (C) the unfilled markers indicate 2 canines where changes in PV pressures were not seen. For the boxplot, the vertical span of the box represents the interquartile range, the horizontal line within the box represents the median value, the whiskers represent the range, and minor and major outliers are indicated with circles and asterisks.

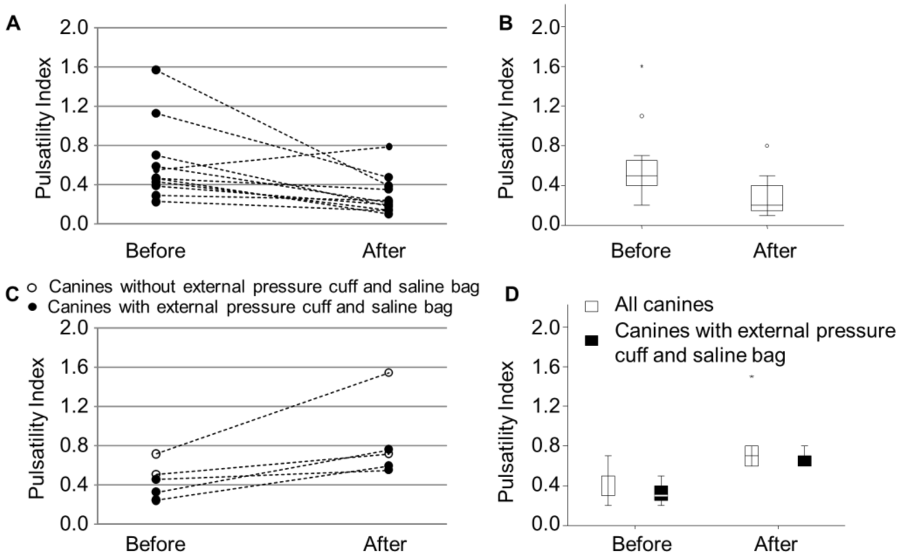

Figure 4.15: Pulsatility index values before and after inducing PH. (A) and (B) illustrate PV pressures (for individual canines) and boxplot of the PV pressures before and after inducing PH using Gelfoam, respectively. (C) and (D) illustrate the data for the A-V shunt model. For panel (C) the unfilled markers indicate 2 canines where changes in PV pressures were not seen. (Boxplot description similar to Fig. 4.14).

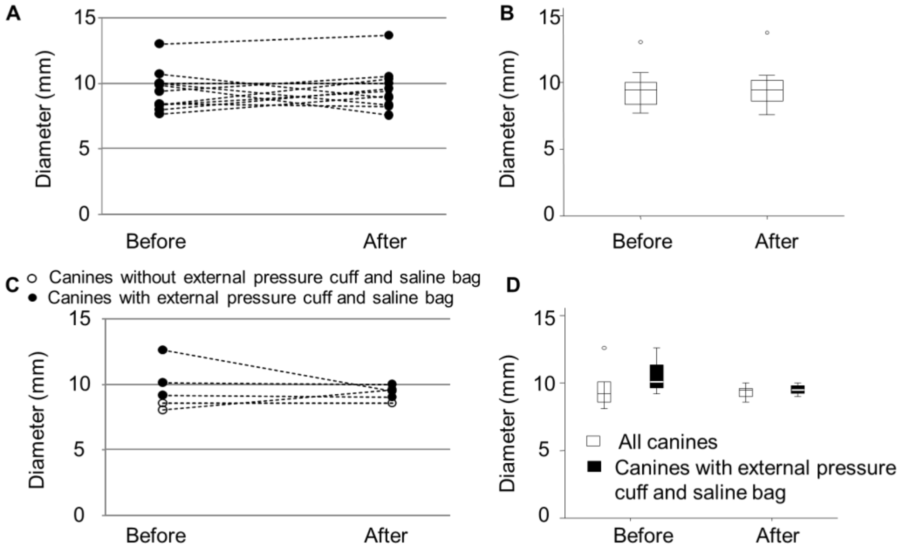

Figure 4.16: Diameter values before and after inducing PH. (A) and (B) illustrate PV pressures (for individual canines) and boxplot of the PV pressures before and after inducing PH using Gelfoam, respectively. (C) and (D) illustrate the data for the A-V shunt model. For panel (C) the unfilled markers indicate 2 canines where changes in PV pressures were not seen. (Boxplot description similar to Fig. 4.14).

4.3.1.3 Statistical Analyses for Comparing Parameters Before and After Inducing PH

For the Gelfoam PH model, there was a statistically significant difference ($p < 0.001$) between PV pressures in the before and after situation implying that PH was successfully induced (Table 4.15). Also the pulsatility index was significantly lower ($p = 0.012$) after PH suggesting a low and damped flow relative to the baseline conditions (Table 4.15). There was no statistically significant difference ($p = 0.89$) between the diameter of the PV at baseline conditions and after PH.

For the A-V shunt model, when all the canines in this group were considered the difference in pressures after inducing PH approached significance ($p = 0.067$); this difference reached significance ($p = 0.010$) for the sub-group of canines where the pressure saline infusion were also used to increase the PV flow volume (Table 4.15). Interestingly, the results for the pulsatility index were inverse. There was a statistically significant difference (*p* = 0.031) between the pulsatility index before and after PH when all the canines were considered, but this difference was not statistically significant (*P* = 0.109) when the sub-group of canines with the pressure saline infusion were considered (Table 4.15). There was no statistically significant difference (*P* > 0.36) between the diameters before and after inducing PH (Table 4.15).

Table 4.15: Comparing baseline and PH parameters in the PV

Parameter	PH model	Paired samples test results			
		Mean Difference	95 % Confidence Interval of Difference		*p*-value
			Lower	Upper	
Pressure (mmHg)	Gelfoam	16.5 ± 7.6	11.5	21.6	< 0.001
	A-V shunt	7.8 ± 7.6	0.9	16.6	0.067
	A-V shunt*	12.8 ± 2.2	7.4	18.3	0.010
Pulsatility Index	Gelfoam	-0.3 ± 0.4	-0.6	-0.1	0.012
	A-V shunt	0.4 ± 0.3	0.1	0.7	0.031
	A-V shunt*	0.3 ± 0.2	-0.2	0.8	0.109
Diameter (mm)	Gelfoam	-0.1 ± 1.6	-1.8	1.6	0.886
	A-V shunt	-0.4 ± 1.7	-2.5	1.7	0.638
	A-V shunt*	-1.1 ± 1.7	-5.4	3.1	0.368

*Only canines where the flow from femoral artery and saline bag were used

4.3.1.4 Discussion

Portal hypertension could be caused by increased resistance to PV flow or by increase in PV flow volume or a combination of these (43, 73-75). Thus, the robustness of the SHAPE technique to evaluate PH was to be investigated under both conditions. Consequently, two acute PH models were developed i.e., the Gelfoam model to represent increased resistance scenario (low-flow) and the A-V shunt model to represent the increased flow volume. The PH endpoint was defined as an increase in PV pressures of at least 5 mmHg above the baseline values. The baseline IVC pressures were 5.7 ± 1.2 mmHg (Table 4.14), which agree with mean values of 5.6 to 6.6 mmHg and the range of 2.7 mmHg to 10 mmHg reported in the literature (169). Baseline PV pressures in the canines were 10.1 ± 2.7 mmHg (Table 4.14) that are consistent with literature reported mean values ranging from 7 to 11 mmHg (152, 156, 158, 160, 165).

For the Gelfoam model, the PH endpoint was reached in 10 out of 11 canines (success rate: 91 %), although in 2 other canines experimental conditions, not associated with the PH model, hampered data acquisition. Thus, Gelfoam administered into the PV increased the resistance to PV flow and induced PH within 2 to 15 minutes. However, there was no correlation between the quantity of Gelfoam used and induced PH or the time taken to induce PH, suggesting that inter-canine response varied considerably, probably due to variability in PV anatomy and liver sizes.

For the A-V shunt group, in 3 canines when the flow from femoral artery was integrated with the PV flow, no rise in PV pressures were seen. The A-V shunt failed to induce PH in all 3 cases. For the remaining 3 canines in the A-V shunt group the flow from the femoral artery was augmented with pressure saline infusion and then PH was successfully induced. These results imply that when the flow from the femoral artery was coupled to the PV the compliance in the PV may be sufficient to compensate for the increased flow volume and thereby, resulted in high pulsatility index (by 0.4 or 40 % higher relative to baseline values; cf. Table 4.15).

The canine PH models have traditionally aimed to elucidate the mechanism of PH development (75, 152, 157, 158, 160) (which is still not well understood (15)) and in all of these studies chronic PH is generally induced to evaluate the associated physiologic changes. For the SHAPE application to identify induced PH, a relatively straightforward and acute low-flow and high-flow PH models were required, wherein the rise in PV pressures occurred within 30 minutes after acquiring baseline data and ultrasound scanning after contrast administration was feasible.

There are various canine PH models that have been proposed in literature (75, 152, 157, 158, 160). A whole liver compression PH model using a polypropylene mesh resulted in death of one canine and, thus, this model was excluded from consideration (160). That approach also involved wrapping the whole liver with mesh or gauze and, thus, was not applicable for evaluation of our ultrasound technique, due to possible scattering of the ultrasound beam by the mesh or gauze. Another approach proposed in the literature was the use of portal and splenic vein stenoses to study the relationship between hypersplenism and hemodynamics in PH (152). But the constriction of portal and splenic veins would affect the amount of ultrasound contrast reaching the PV and thus this model had limited applicability for the SHAPE PH study. In another study, authors used anti-E. coli serum to induce portal fibrosis and tracked PH related changes over 2 weeks (159), but this 2 week time-frame to observe PH changes was not suitable for this work because the baseline PV pressures were obtained after a mid-line abdominal incision to access the PV and then increases in PV pressures needed to be induced acutely for testing the efficacy of SHAPE technique to detect the increase in PV pressures. An approach to use microspheres for inducing PH has been shown to be successful in canines, but the cost associated with these microspheres is relatively high (156). Another approach to develop a multiple portosystemic shunt model using dimethylnitrosamine to study the PH induced portosystemic shunts was also discussed but the time taken to induce these shunts varies between 8 to 14 weeks and can also be as high as 56 weeks and thus not practical for the SHAPE PH study (155). The natural occurrences of canine A-V shunts between the hepatic artery and PV resulting in vascular abnormalities have been reported in the literature (174-176), but none were noted in the canines that were used in the SHAPE PH experiments.

Since Gelfoam was previously used in canines with no reported side effects (162, 163), is known for its hemostatic properties, is inexpensive and is readily available in a hospital or animal laboratory setting, it was used to induce low-flow PH. The success rate in inducing PH was 91 %. However, for chronic PH models the applicability of this Gelfoam PH model is limited, mainly due to recanalization (177). Thus, the choice of the Gelfoam model is application specific. Similarly, it is known that a hyperkinetic syndrome (due to initial increase in resistance to PV flow) ultimately results in increased PV flow and contributes to PH (75). The A-V shunt model was used in the SHAPE PH study because physiologically the hyperkinetic syndrome and the resulting increase in PV flow volume may require considerable time (in weeks) for development after increasing resistance to PV flow. The A-V shunt model used in this study simulated the high-flow condition but did not contribute to rise in PV pressures until the flow from a saline infusion was supplemented. This suggests that A-V shunt alone may not be sufficient to produce a high-flow PH model acutely. This is consistent with findings of a previous study (178) which showed that modest distal vein hypertension may be expected due to an A-V shunt as the high pressure at the arterial end may be dissipated before affecting pressures in a distal vein.

Overall the performance of both models (mainly the Gelfoam model) was acceptable to investigate the efficacy of SHAPE for identifying PH.

4.3.2 Efficacy of SHAPE to Investigate PH (Study 1)

4.3.2.1 Induced PH in Canines

For the canines (14 canines) used in this study, the baseline mean PV pressure was 9.4 ± 2.1 mmHg (Table 4.16). For one canine from the Gelfoam group (8 canines), technical difficulty associated with the pressure catheter impeded data acquisition and thus, the data from this canine were not included in the analyses. From the remaining 7 canines where PH was induced using Gelfoam, one canine did not respond to treatment (determined from the pressure catheter readings), thus post PH data was not acquired for this canine. Post-PH data for the remaining 6 canines in the Gelfoam group are shown in Table 4.16. From the group of 6 canines where PH was induced using A-V shunt, one canine did not respond to the treatment (no rise in PV pressures). No PH data were acquired from this canine and thus, PV data from the remaining 5 canines are shown in Table 4.16. As stated above, two canines (one from the Gelfoam group and one from the A-V shunt group) only provided baseline data. Instead, data from these 2 dogs were subsequently used to test the efficacy of the SHAPE technique in predicting PV pressures along with the cross-validation approach in other canines.

Table 4.16: PV pressures from canines used in PH Study 1

	Minimum Pressure (mmHg)	Mean Pressure (mmHg)	Maximum Pressure (mmHg)
Baseline conditions (13 canines)*	5.6	9.4 ± 2.1	16.0
Gelfoam induced PH (6 canines)†	9.3	26.9 ± 8.3	36.7
A-V shunt induced PH (5 canines)†	8.8	19.1 ± 6.5	28.1

*For one canine technical difficulty associated with the pressure catheter impeded data acquisition; thus baseline data have been reported for 13 canines

†A single canine did not respond to treatment in each case resulting in data acquisition post portal hypertension (PH) from 6 canines in the Gelfoam group and 5 canines in the A-V shunt group

4.3.2.2 Subharmonic Amplitude as a Function of Number of Transmit Cycles and IAO Levels

Fig. 4.17 shows a boxplot of the subharmonic signal amplitudes (SH_{MIP}) obtained from the PVs. Note the relatively low subharmonic signal amplitude obtained with 2 transmit cycles and with 10 % IAO. A factorial repeated measures ANOVA used to compare the subharmonic signal amplitudes (both SH_{MIP} and SH_{All_Frames}) obtained from the PV (for baseline conditions) based on number of transmit cycles and incident acoustic output revealed a significant main effect of the number of transmit cycles (F(1.10, 14.27) = 130.66; $p < 0.001$) and of the IAOs (F(1.15, 14.90) = 325.88; $p < 0.001$). There was also a significant interaction effect between the number of transmit cycles and the IAO levels F(1.35, 17.55) = 78.15 ($p < 0.001$), indicating that the IAO levels had different effects on the subharmonic amplitude depending on the number of transmit cycles. Post hoc tests using Bonferroni adjustment for multiple comparisons showed that the subharmonic amplitude obtained with 2 transmit cycles was significantly less than the subharmonic amplitude with 3 (by 11.5 dB; 95 % Confidence Interval: 8.8 dB to 14.1 dB; $p < 0.001$) and with 4 (by 11.1 dB; 95 % Confidence Interval: 8.4 dB to 13.8 dB; $p < 0.001$) transmit cycles. However, there was no statistically significant difference between the subharmonic amplitudes obtained with 3 and 4 transmit cycles ($p = 0.498$). Thus, 2 transmit cycles may have lacked the ability to elicit a sufficient subharmonic response given the IAO levels considered in this study. Post hoc tests, again using Bonferroni adjustment for multiple comparisons, also showed that the subharmonic amplitude obtained with 10 % IAO was significantly less than the subharmonic amplitudes obtained with 20 % (by 7.7 dB; 95 % Confidence Interval: 6.4 dB to 8.9 dB; $p < 0.001$) and 40 % (by 11.3 dB; 95 % Confidence Interval: 9.7 dB to 13.0 dB; $p < 0.001$) IAOs. Hence, 10 % IAO at 2, 3, and 4 transmit cycles may not have sufficient acoustic pressure amplitude to elicit a subharmonic response detectable by the 4C probe used in this study. Fig. 4.18 depicts subharmonic MIP images as a function of IAO levels and the number of transmit cycles obtained from one canine, before PH was induced. As seen in Fig. 4.18, the subharmonic signal amplitude was relatively low for 2 transmit cycles (Fig. 4.18A-C), with 3 transmit cycles the subharmonic signal amplitude gradually increased with an increase in IAO from 10 % to 40 % (Fig. 4.18D-F), then the subharmonic signal amplitude dropped for 10 % IAO and 4 transmit cycles (Fig. 4.18G), and finally the subharmonic signal amplitude increased for 20 % and 40 % IAO levels with 4 transmit cycles (Fig. 6H-I). Based on similar observations with data from other canines and the statistical analyses, it was concluded that the subharmonic signal at 10 % IAO and with 2 transmit cycles did not elicit the subharmonic signal in the growth-stage required for SHAPE application. Thus, only data obtained with 20 % and 40 % IAO level with 3 and 4 transmit cycles were considered for further analyses.

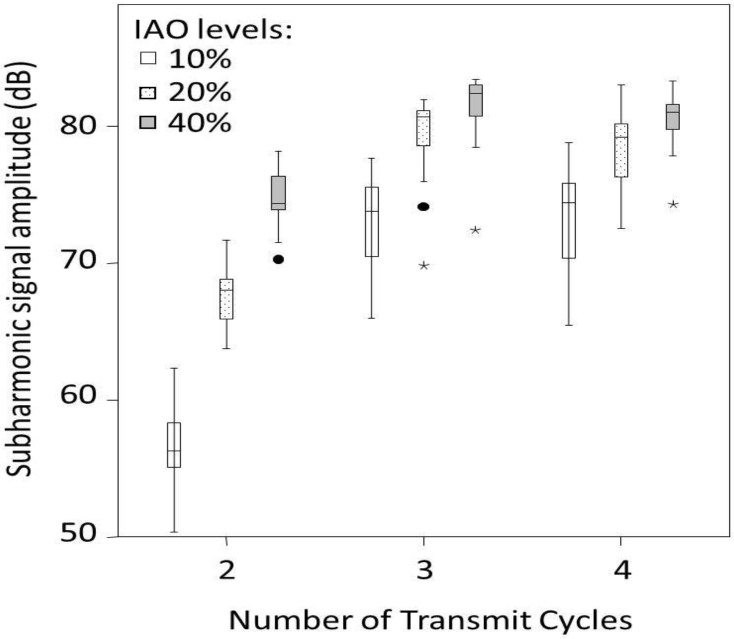

Figure 4.17: Boxplot of the subharmonic signal amplitudes obtained at 10 %, 20 % and 40 % incident acoustic output (IAO) levels with 2, 3 and 4 transmit cycles. Minor and major outliers are indicated with circles and asterisks, respectively. Note, that the subharmonic signal amplitudes obtained with 10 % IAO and with 2 cycles are relatively low as compared to the amplitudes obtained with 20 % and 40 % IAO, for 3 and 4 transmit cycles.

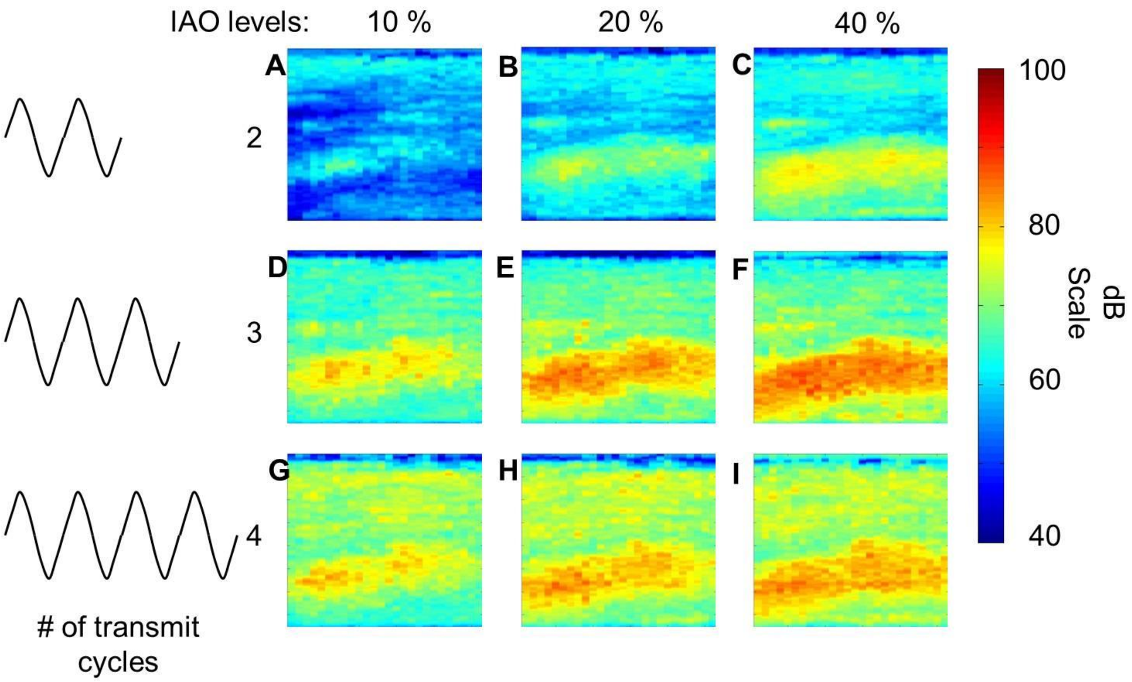

Figure 4.18: MIP subharmonic images of the data obtained from ROI at 10 % (A, D, G), 20 %, (B, E, H) and 40 % (C, F, I) IAO with 2 (A-C), 3 (D-F), and 4 (G-I) transmit cycles. Note, that subharmonic signal amplitude increases with an increase in IAO levels; but is relatively low for 2 transmit cycles.

4.3.2.3 Comparison of 3 and 4 Transmit Cycles for SHAPE Based PH Tracking

Fig. 4.19 (3 cycle pulses) and Fig. 4.20 (4 cycles pulses) illustrate the relationship between the mean change in PV pressures (PH pressures – baseline PV pressures) and the mean change in the subharmonic signal amplitude (at PH state – at baseline conditions). Data obtained using the MIP image alone (SH_{MIP}; panels A and B) and obtained as an average of subharmonic signals from all the frames (SH_{All_Frames}; panels C and D) at 20 % (panels A and C) and at 40 % (panels B and D) IAO levels are shown in Figs. 4.19 and 4.20. As depicted in Fig. 4.19, for both models of PH when 3 transmit cycles were used, there was a reasonably good correlation (ranging from -0.62 to -0.81, n = 6 for the

Gelfoam model and from -0.52 to -0.73, n = 5 for the A-V shunt model) between the change in subharmonic signal amplitude and change in PV pressures, with increased changes in PV pressures associated with increased changes in subharmonic signal. However, as shown in Fig. 4.20, when 4 transmit cycles were used, a relatively stronger correlation (ranging from -0.88 to -0.94, n = 6 for the Gelfoam model and from -0.82 to -0.83, n = 5 for the A-V shunt model) was observed.

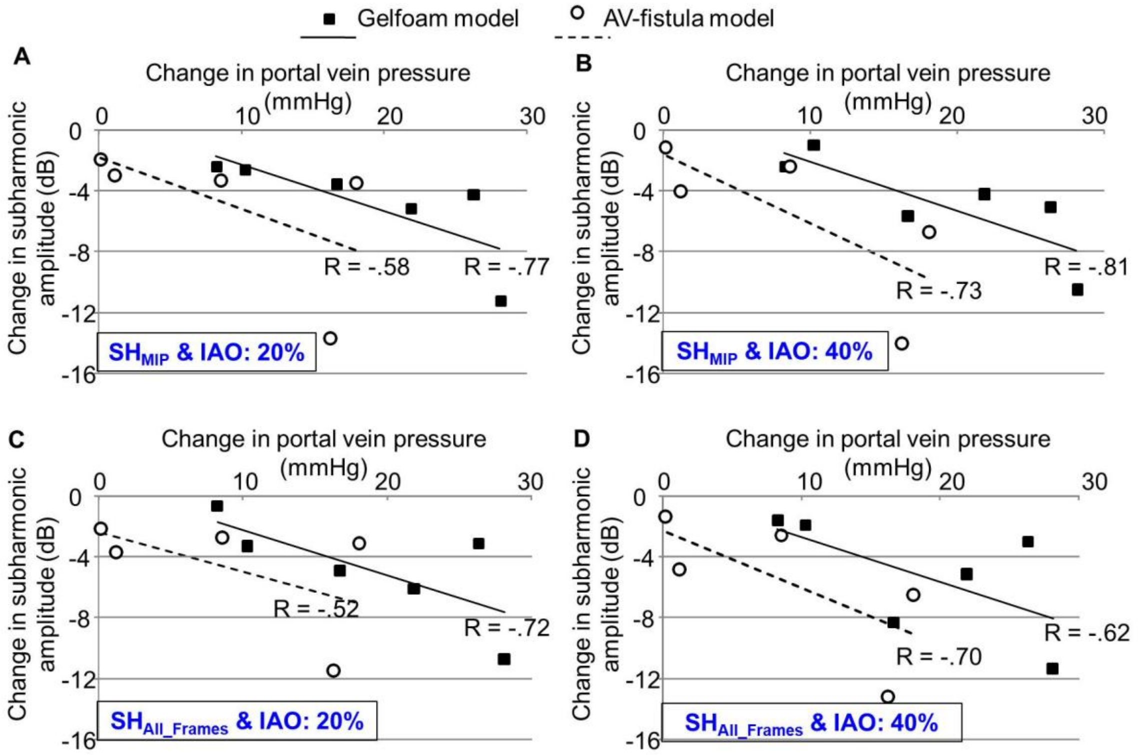

Figure 4.19: Mean changes in the PV pressures are plotted with mean changes in subharmonic signal amplitudes acquired with 3 transmit cycles along with the best-fit line and the correlation coefficient is indicated for both the Gelfoam and A-V shunt PH models. (A) and (C) represent data acquired at 20 % IAO levels for subharmonic signal analyzed from the MIP image (SH_{MIP}) and as the mean value from all the frames (SH_{All_Frames}), respectively. (B) and (D) represent the corresponding data acquired at 40 % IAO.

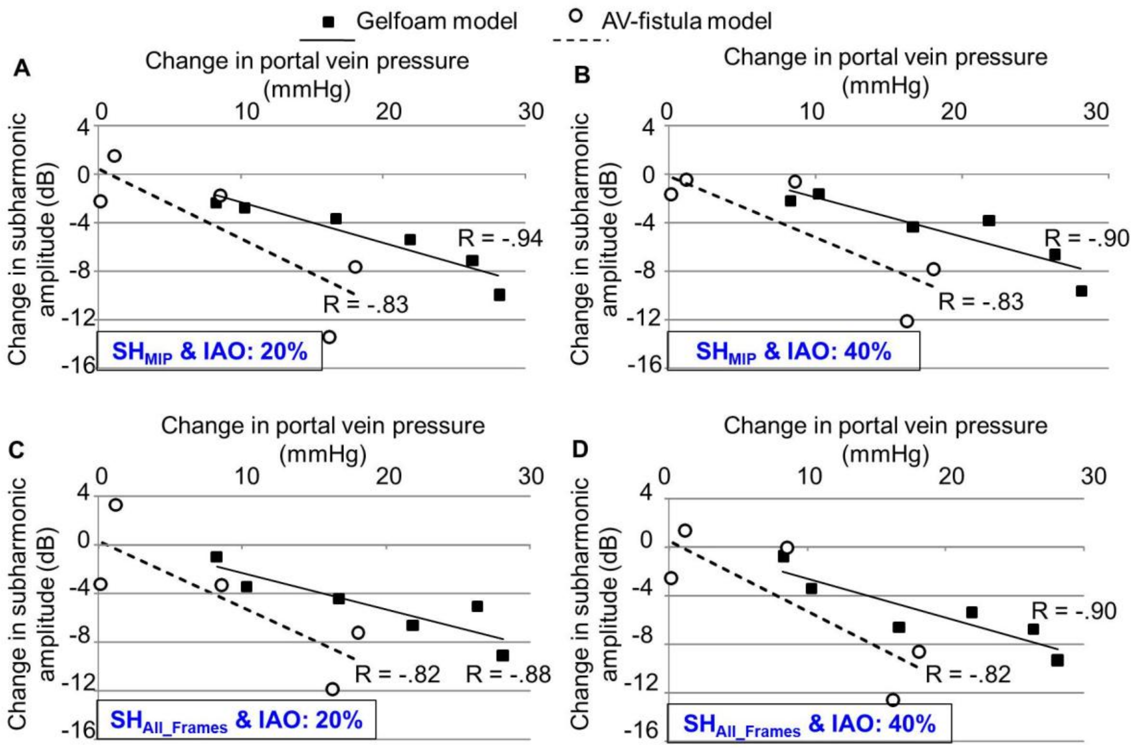

Figure 4.20: Mean changes in the PV pressures are plotted with mean changes in subharmonic signal amplitudes acquired with 4 transmit cycles along with the best-fit line and the correlation coefficient is indicated for both the Gelfoam and A-V shunt PH models. (A) and (C) represent data acquired at 20 % IAO levels for subharmonic signal analyzed from the MIP image (SH_{MIP}) and as the mean value from all the frames (SH_{All_Frames}), respectively. (B) and (D) represent the corresponding data acquired at 40 % IAO.

Table 4.17 presents the correlation coefficients observed with 3 and 4 transmit cycles at 20 % and 40 % IAO levels, when the data from both the PH models were combined (as a more robust indicator of SHAPE's performance). As seen in Table 4.17, significant and higher correlation coefficients were observed for 4 transmit cycles (*p*-values ranging from 0.01 to 0.02) as compared to 3 transmit cycles (*p*-values ranging from 0.07 to 0.1). This suggests that the use of 4 transmit cycles is preferred over 3 transmit cycles for SHAPE applications. *(And based on these results Hypothesis 5, that* *was formulated to determine if significant correlations between changes in PV pressures and the subharmonic amplitude existed, was accepted).*

Table 4.17: Pearson's correlation coefficient (r) between the change in subharmonic signal and change in PV pressures. Data from the Gelfoam and A-V shunt models were combined (n = 11).

Transmit Cycles	IAO (%)	From SH_{MIP}		From SH_{All_Frames}	
		r	*p*-value	r	*p*-value
3	20	-0.53	0.094	-0.54	0.090
3	40	-0.56	0.071	-0.52	0.103
4	20	-0.72	0.013	-0.70	0.017
4	40	-0.70	0.016	-0.73	0.011

4.3.2.4 Comparison of 20 % and 40 % IAO Levels with 4 Transmit Cycles for SHAPE Based PH Tracking

There was no statistically significant difference ($p > 0.4$) between the correlation coefficients obtained with 20 % and 40 % IAO levels for 4 transmit cycles (cf. Table 4.17). This suggests that at both these IAO levels the subharmonic emissions may be in the growth-phase and thus sensitive to ambient PV pressure changes. Additionally there was a strong significant correlation between the mean values of absolute subharmonic amplitudes and mean values of absolute PV pressures as documented in Table 4.18 and Fig. 4.21. This confirms that at both 20 % and 40 % IAO levels the subharmonic signal was in the ambient pressure sensitive phase. This result was consistent with evaluation of subharmonic MIP images (cf. Fig. 4.18). As shown in Fig. 4.21A, the subharmonic signal amplitudes extracted from $\mathrm{ROI}_{\mathrm{PV}}$ of all the frames ($\mathrm{SH}_{\mathrm{All\_Frames}}$) were lower than the subharmonic signal amplitudes extracted from the MIP image ($\mathrm{SH}_{\mathrm{MIP}}$) (mostly due to some Sonazoid concentration fluctuations likely to happen *in vivo*). The gradients of the best-fit lines representing the sensitivity of Sonazoid microbubbles to ambient PV pressures ranged from -1.44 mmHg/dB to -1.69 mmHg/dB (Figs. 4.21A and 4.21C). Interestingly, the gradients for 20 % (Fig. 4.21A) and 40 % (Fig. 4.21C) IAOs were nearly independent of the technique used in analyzing the extracted subharmonic signals (either $\mathrm{SH}_{\mathrm{MIP}}$ or $\mathrm{SH}_{\mathrm{All\_Frames}}$). Also the gradient was lower for 20 % IAO as compared to 40 % IAO, indicating that the ambient pressure sensitivity was relatively more at 20 % IAO, with saturation most likely to occur above 40 % IAO. Figs. 4.21B and 4.21D show boxplots of subharmonic signals obtained before and after inducing PH, at 20 % and 40 % IAO levels with 4 transmit cycles, respectively. Note, that at baseline conditions (pre-PH) the spread in the subharmonic amplitudes is much less than the spread after PH (Figs. 4.21B and 4.21D), primarily because the PV pressures after induced PH also varied considerably between canines (see Table 4.16). A paired t-test comparing these subharmonic amplitudes revealed that there was a statistically significant difference between the subharmonic signal amplitudes obtained under baseline and under PH conditions at 20 % and 40 % IAOs (Table 4.19). Thus, subharmonic signal amplitudes may predict the PV pressures. *(Based on this result Hypothesis 4, that investigated if the SHAPE results would be able to identify induce PH, was accepted).*

Table 4.18: Pearson's correlation coefficient (r) between absolute subharmonic signal amplitudes and absolute PV pressures when data from the Gelfoam and A-V shunt models were combined for 4 transmit cycles (n = 22).

IAO (%)	From SH_{MIP}		From SH_{All_Frames}	
	r	*p*-value	r	*p*-value
20	-0.74	< 0.001	-0.71	< 0.001
40	-0.79	< 0.001	-0.73	< 0.001

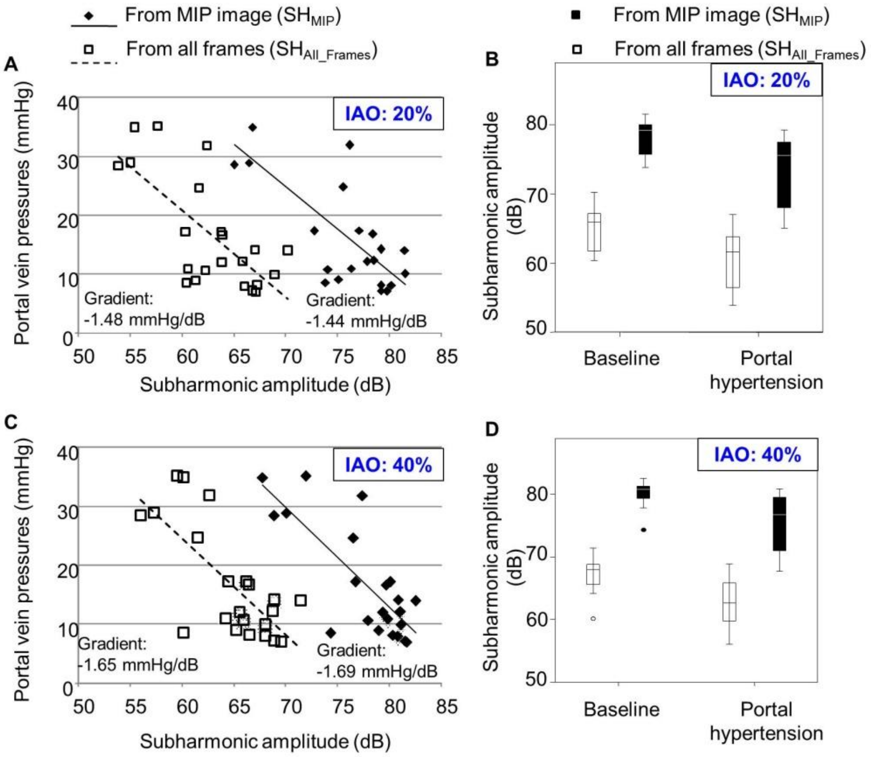

Figure 4.21: Absolute PV pressures are plotted with absolute subharmonic signal amplitudes acquired with 4 transmit cycles (note, these are mean values obtained from each canine). (A-B) and (C-D) represent data acquired at 20 % and 40 % IAO levels, respectively. The subharmonic amplitudes obtained from SH_{MIP} and from SH_{All_Frames})are shown separately in each panel. The best-fit line along with its gradient is indicated in (A) and (C). Boxplots in (B) and (D) indicate the interquartile range (vertical span of the box), the median value (horizontal line within the box), the range (whiskers) and minor outliers (circles) for the subharmonic signal amplitudes. Note that the SH_{All_Frames} is relatively less than the SH_{MIP} (as expected).

Table 4.19: Paired t-test results when comparing subharmonic signal amplitudes obtained at baseline and PH conditions, with 4 transmit cycles (n = 11)

IAO (%)	From SH_{MIP}			From SH_{All_Frames}		
	Mean Difference (dB)	95 % Confidence Interval of Difference (dB)	*p*-value	Mean Difference (dB)	95 % Confidence Interval of Difference (dB)	*p*-value
20	5.0	2.1-7.8	0.003	4.7	2.0-7.4	0.003
40	4.6	2.0-7.2	0.003	4.4	1.3-7.4	0.01

In order to test the viability of using subharmonic signal amplitudes to predict PV pressures, the subharmonic signal amplitudes obtained in 2 canines, where data were only obtained under baseline conditions were first analyzed. The subharmonic signal amplitudes were combined with the equation of the best fit line (shown in Figs. 4.21A and 4.21C) to predict the baseline PV pressures; the values were compared to the catheter pressures. These results are presented in Table 4.20 which demonstrate that the subharmonic signals analyzed from all the frames (SH_{All_Frames}) have relatively less error (error range: 0.2 to 1.9 mmHg) as compared to subharmonic signals analyzed only from the MIP image (SH_{MIP}; error range: 1.8 to 6.9 mmHg) in predicting PV pressures. This suggests that the subharmonic signal amplitude analyzed from all the frames (SH_{All_Frames}) is a more robust indicator (in comparison to SH_{MIP}) of PV pressures and should be the most appropriate means to predict PV pressures; albeit based on analyses in 2 canines.

Table 4.20: Predicting PV pressures and comparing with true pressures (true pressures were obtained with the Millar catheter)

	From SH_{MIP}		From SH_{All_Frames}	
IAO (%)	Calculated Pressure (mmHg)	True Pressure (mmHg)	Calculated Pressure (mmHg)	True Pressure (mmHg)
Canine 1				
20	10.1	8.0	8.2	8.0
40	9.8	8.0	8.5	8.0
Canine 2				
20	2.6	7.8	9.7	7.8
40	0.9	7.8	9.0	7.8

Next, the results of the cross-validation study are summarized in Table 4.21 for the baseline and PH data compared together and also, independently. None of the differences between the pressures obtained using the catheter, and using the cross-validation approach and the SHAPE data were statistically significant ($p > 0.05$; Table 4.21). Finally, the results of the binary classification and the resulting sensitivity, specificity and accuracy of predicting PH are presented in Table 4.22.

Table 4.21: Comparing errors between manometer pressures and SHAPE results using cross-validation approach

IAO (%)	From SH_{MIP} SHAPE vs. catheter pressures			From SH_{All_Frames} SHAPE vs. catheter pressures		
	Mean Difference (mmHg)	95 % Confidence Interval of Difference (mmHg)	*p*-value	Mean Difference (mmHg)	95 % Confidence Interval of Difference (mmHg)	*p*-value
a) For all data						
20	0.0	-3.0 to 3.0	0.982	-0.1	-3.4 to 3.1	0.924
40	0.1	-2.7 to 2.9	0.951	-0.1	-3.3 to 3.1	0.952
b) For baseline data only (before PH)						
20	3.5	-0.1 to 7.0	0.053	3.5	-0.9 to 7.9	0.110
40	3.2	-0.3 to 6.8	0.070	3.6	-0.9 to 8.2	0.103
c) For PH data only						
20	-3.5	-8.0 to 0.9	0.109	-3.8	-8.0 to 0.4	0.072
40	-3.1	-7.0 to 0.9	0.113	-3.8	-7.9 to 0.2	0.062

Table 4.22: Sensitivity, specificity and accuracy for detecting moderate through severe PH. A cut-off threshold for PV pressures of 16 mmHg (13 instances with PV pressures below 16 mmHg and 9 instances with PV pressures above 16 mmHg).

IAO	With SHAPE using SH_{MIP}			With SHAPE using SH_{All_Frames}		
(%)	Sensitivity (%)	Specificity (%)	*Accuracy* (%)	Sensitivity (%)	Specificity (%)	*Accuracy* (%)
20	67	69	68	78	69	73
40	78	85	82	78	77	77

4.3.2.5 Discussion based on PH Study 1

The goal of this study was to analyze if subharmonic emissions from Sonazoid microbubbles (i.e., SHAPE) were useful in predicting PV pressures in canines. Results showed that SHAPE performance in tracking PH was best with 4 transmit cycles for 20 % and 40 % IAO levels; the changes in PV pressures correlated with the changes in the subharmonic signal amplitudes for both cases, when the two PH models were evaluated separately (r ranging from -0.82 to -0.94; Fig. 4.20) and when evaluated together (r ranging from -0.70 to -0.73; Table 4.17). The subharmonic signal amplitude decreased with an increase in ambient pressure, which is consistent with previously published reports (e.g., (3)) and with previous results obtained in this work. Based on this result, the relationship between the absolute PV pressures and absolute subharmonic signal amplitudes were evaluated for data combined from both PH models and obtained with 4 transmit cycles. The correlation coefficient in this case ranged from -0.71 to -0.79 (Table 4.18) and a statistically significant difference was seen between the subharmonic signal amplitudes obtained before and after inducing PH (Table 4.19). Finally, the relationship between absolute subharmonic signal amplitudes and PV pressures were used to track PV pressures in 2 other canines. The errors were lower when the SH_{All_Frames} were used as against the use of SH_{MIP} (0.2 to 1.9 mmHg vs. 1.8 to 6.9 mmHg) for 2 canines (Table 4.20); similar to the errors reported in the cardiac SHAPE study conducted in canines (range: 0.0 to 3.5 mmHg; (179, 180)). Results from the cross-validation study indicate that the robustness of approximating the PV pressures using SHAPE (Table 4.21). The sensitivity, specificity and accuracy values for identifying clinically relevant PH (in canines) ranged from 67 to 85 % (Table 4.22). Thus, PV pressure monitoring using SHAPE appears to be feasible for testing clinical applications.

A major limitation of this study involves the use of fixed IAO levels (10 %, 20 % and 40 %) for eliciting subharmonic emissions for SHAPE. This is reflected in the values presented in Table 4.22. For clinical applications, the optimization of IAO will be required on a case-by-case basis depending on body habitus, PV location and visualization, and other practical factors. Specifically, in a variable clinical population differences due to the attenuation, reverberation and aberration in the abdominal wall may make the promising results obtained in canines difficult to reproduce or the results could be better with the optimal IAO levels. However, these results do warrant a preliminary investigation in a clinical population to evaluate the usefulness of SHAPE in identifying PH.

A real-time display of the subharmonic signal amplitude as a function of IAO will allow the selection of optimum IAO levels (eliciting subharmonic emissions in the growth stage) for clinical SHAPE applications as well as future animal investigations –

this was the purpose for implementing incident acoustic output optimization program (as discussed in *section 3.2.3.6*) for which the results are presented in *section 4.3.3*. Further, the inability to operate in grayscale imaging mode during RF data acquisition may be addressed by the use of newly available dual and simultaneous B-mode and subharmonic imaging mode ((130, 181)).

For the purpose of subharmonic imaging, it was shown that relatively low threshold values (0.02 - 0.15 MPa; ≤ levels corresponding to 10 % incident acoustic output considered in this study) are required to elicit subharmonic emissions from microbubbles closest to their buckling state (137). This buckling state is characterized by zero (minimal) initial surface tension and, thus, specific bubbles engineered with zero initial surface tension may be useful to extract this relationship for subharmonic imaging (137). Alternately, a different approach was proposed in another study where low ambient pressure modulations in the microbubbles' vicinity may be established, that possibly drive the microbubbles to their buckling state by altering the surface tension values and consequently lead to emission of a relatively higher subharmonic signal at relatively lower IAO (141). These studies indicate that the subharmonic emissions may be tailored for subharmonic imaging, but *in vivo* applications were not implemented (137, 141). Besides, in the study presented here the subharmonic emissions at 10 % IAO were too low to be separated from the ambient noise level. Thus, the *in vivo* application of using even lower IAO values to elicit a stronger subharmonic signal *in vivo* remains technically challenging.

4.3.3 Efficacy of SHAPE to Investigate PH (Study 2)

4.3.3.1 Induced PH in Canines

The baseline PV pressures were 11.9 ± 3.9 mmHg. For one canine, the surgical procedure to induce PH resulted in acute embolization and thus, data from this canine were not considered in the analyses. For the remaining 4 canines there was a statistically significant difference of 15.93 ± 6.15 mmHg between the PV pressures before and after inducing PH (95 % Confidence Interval: 6.15 to 25.71 mmHg; $p = 0.014$; Table 4.23).

Table 4.23: PV pressures from canines used in PH Study 2

	Minimum Pressure (mmHg)	Mean Pressure (mmHg)	Maximum Pressure (mmHg)
Baseline conditions	8.4	11.9 ± 3.9	15.8
Induced PH	17.2	27.8 ± 7.1	32.2

4.3.3.2 Analyses of IAO Optimization Function

Fig. 4.22 represents the output of the IAO optimization function. The optimum IAO selected for the case shown in Fig. 3.19 was 20 % (0.56 MPa peak to peak) (Fig. 4.22). Fig. 4.23 illustrates the subharmonic ROI signal at 5 % (0.18 MPa peak to peak; beginning of the growth phase; Fig. 4.23A), 20 % (0.56 MPa peak to peak; at the center of the growth phase; Fig. 4.23B), 60 % (1.19 MPa peak to peak; the end of the growth phase; Fig. 4.23C) and 100 % (3.34 MPa peak to peak; saturation of the subharmonic signal; Fig. 4.23D) IAO levels. The occurrence, growth and saturation phases were also seen in the output obtained from the IAO optimization program for the other canines and the optimum IAO levels computed by the automatic IAO optimization were 6 %, 28 %, 40 % and 32 % (range: 0.2 to 0.9 MPa), respectively.

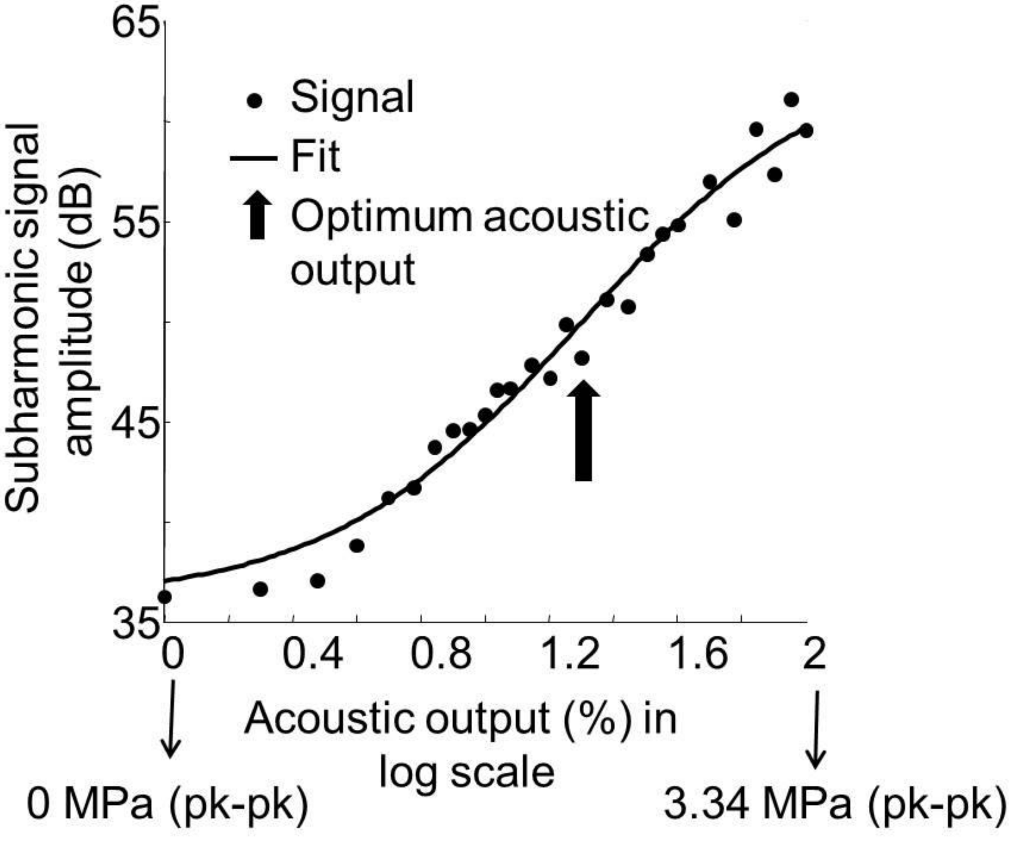

Figure 4.22: Output of the IAO optimization function. The abscissa corresponds to log transformation of the IAO indicated on the scanner in percentage. The fitting function compensates for motion artifacts during IAO optimization, mostly observed due to respiration. The optimum IAO was calculated as the IAO level with the maximum slope. In this case, the optimum IAO (arrow) was 20 % which corresponds to 1.30 on the abscissa.

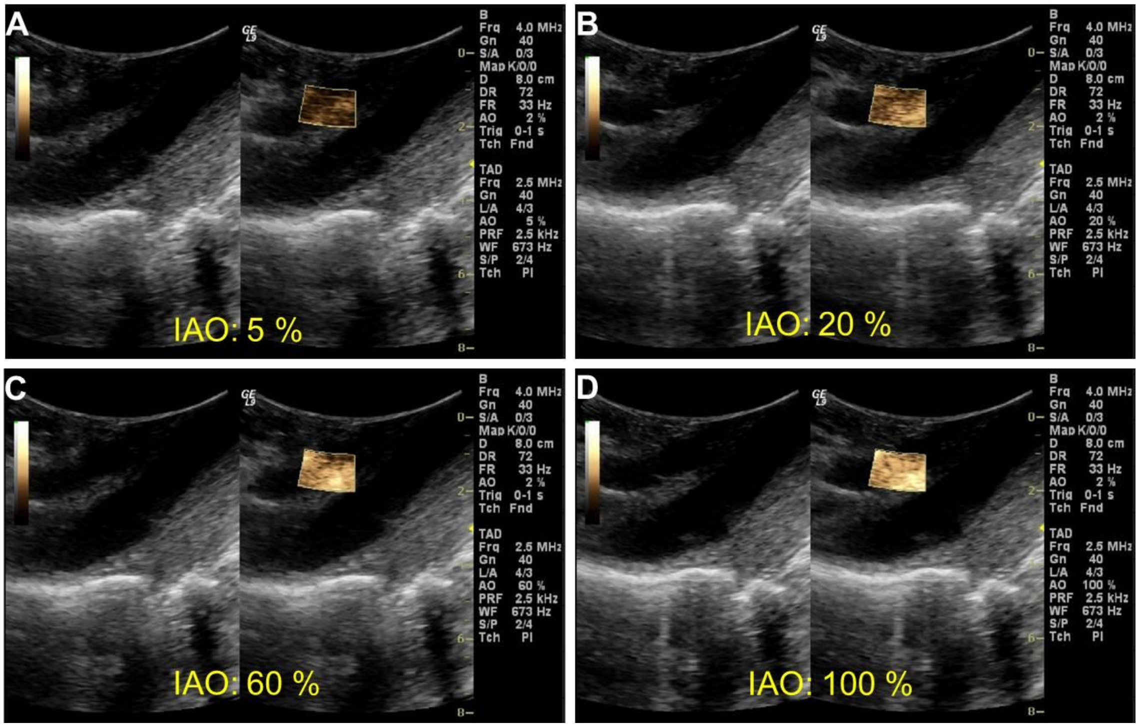
A
B
Frq 4.0 MHz
Gn 40
S/A 0/3
Map K/0/0
D 8.0 cm
DR 72
FR 33 Hz
AO 2 %
Trig 0-1 s
Tch Fnd
TAD
Frq 2.5 MHz
Gn 40
L/A 4/3
AO 5 %
PRF 2.5 kHz
WF 673 Hz
S/P 2/4
Tch PI
IAO: 5 %
B
B
Frq 4.0 MHz
Gn 40
S/A 0/3
Map K/0/0
D 8.0 cm
DR 72
FR 33 Hz
AO 2 %
Trig 0-1 s
Tch Fnd
TAD
Frq 2.5 MHz
Gn 40
L/A 4/3
AO 20 %
PRF 2.5 kHz
WF 673 Hz
S/P 2/4
Tch PI
IAO: 20 %
C
B
Frq 4.0 MHz
Gn 40
S/A 0/3
Map K/0/0
D 8.0 cm
DR 72
FR 33 Hz
AO 2 %
Trig 0-1 s
Tch Fnd
TAD
Frq 2.5 MHz
Gn 40
L/A 4/3
AO 60 %
PRF 2.5 kHz
WF 673 Hz
S/P 2/4
Tch PI
IAO: 60 %
D
B
Frq 4.0 MHz
Gn 40
S/A 0/3
Map K/0/0
D 8.0 cm
DR 72
FR 33 Hz
AO 2 %
Trig 0-1 s
Tch Fnd
TAD
Frq 2.5 MHz
Gn 40
L/A 4/3
AO 100 %
PRF 2.5 kHz
WF 673 Hz
S/P 2/4
Tch PI
IAO: 100 %

Figure 4.23: Representation of the subharmonic signal at varying IAO levels (green arrows) used in the optimization function. (A) At 5 % IAO level the subharmonic signal begins to appear and resides at the beginning of the growth phase. (B) At 20 % IAO level the subharmonic signal resides in the linear portion of growth phase (ambient pressure sensitive phase). (C) At 60 % IAO level the subharmonic saturation begins, possible with the occurrence of bubble destruction. (D) At 100 % IAO level the subharmonic signal is not that different from (C) indicating saturation.

4.3.3.3 SHAPE's Performance for PV pressures and PH Tracking

The correlation coefficient relating the change in PV pressures to the change in subharmonic signal amplitude, before and after inducing PH, and the absolute values of PV pressures and subharmonic signal amplitudes are presented in Table 4.24. For 2 canines the subharmonic data were not acquired in the post PH stage at IAO levels that were higher than the optimized IAO levels due to timing constraints.

Table 4.24: Pearson's correlation coefficient between subharmonic signals and PV pressures. Correlation coefficient relating change in subharmonic signal amplitude to change in PV pressures (r_{change}) and relating absolute subharmonic signal amplitude to absolute PV pressures ($r_{absolute}$) are presented.

IAO Level	Number of transmit cycles	Correlation coefficient					
		n	r_{change}	*p*-value	n	$r_{absolute}$	*p*-value
Optimized	4	4	-.76	0.24	8	-.89	< 0.01
	8	4	.30	0.70	8	-.54	0.16
	16	4	.10	0.90	8	-.59	0.12
Below optimized	4	4	.04	0.95	8	-.72	0.04
	8	4	.15	0.85	8	-.29	0.49
	16	4	.31	0.69	8	-.65	0.08
Above optimized	4	2	N/A*	N/A*	4	-.73	0.27
	8	2	N/A*	N/A*	4	-.61	0.39
	16	2	N/A*	N/A*	4	-.18	0.82

*N/A: not applicable as the number of data points was insufficient, because data from 2 canines were not acquired at higher acoustic IAO level

Fig. 4.24A-C represent the data obtained with 4, 8 and 16 transmit cycles at the optimized IAO level. The best correlation (r = -0.76) for changes in PV pressures and the subharmonic signal amplitude was obtained at the optimized IAO level with 4 transmit cycles (Table 4.24 and Fig. 4.24A-C). These results imply that the optimized IAO level selected by the IAO optimization algorithm worked and 4 transmit cycles (out of 2, 3, 4, 8, and 16 transmit cycles; 2 and 3 transmit cycles were compared to 4 transmit cycles in *sections 4.3.2.2 and 4.3.2.3*) is best suited for SHAPE application. Also the data acquired with optimized IAO and 4 transmit cycles shows that the increases in PV pressures were associated with a greater reduction in subharmonic signal amplitude consistent with previously published reports (e.g., (3)) and other results presented in thesis.

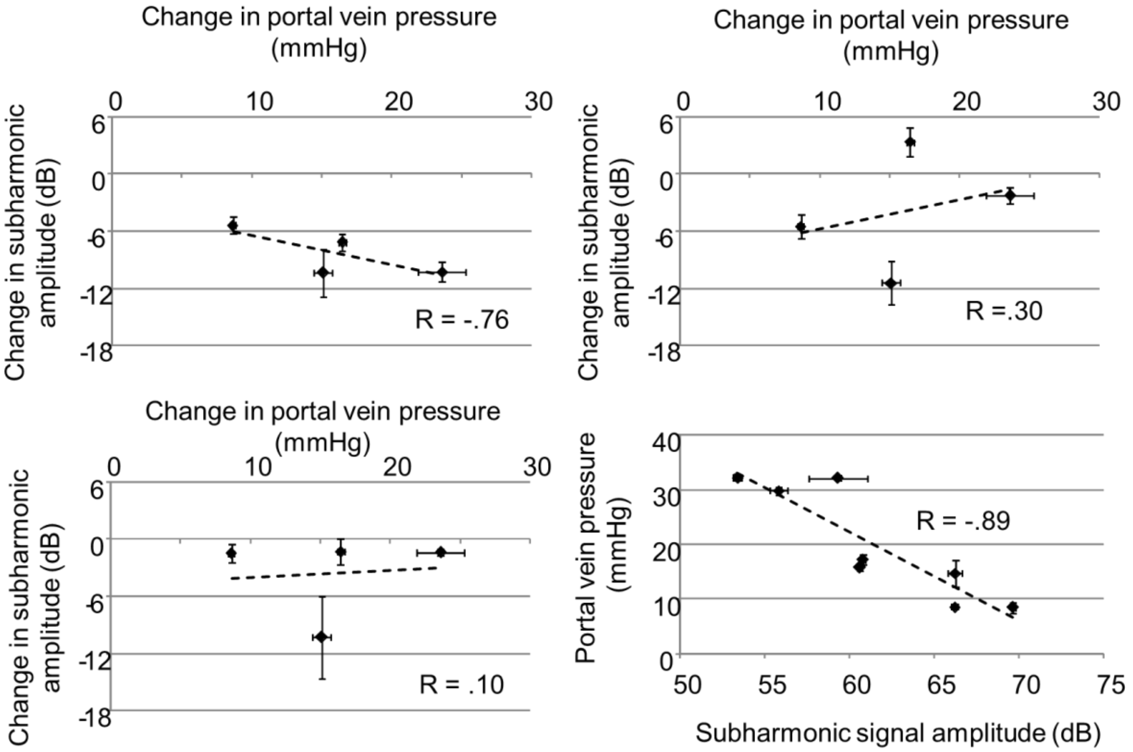

Figure 4.24: (A), (B) and (C) depict the relationship between change in PV pressures and change in subharmonic signal amplitude at optimized IAO levels with 4, 8 and 16 transmit cycles – the best fit line is shown (dashed) with correlation coefficient. Note the best correlation was obtained with 4 transmit cycles and optimized IAO level (A). (D) The relationship between absolute PV pressures and subharmonic signal amplitude is shown with the best fit line (dashed) and the correlation coefficient is indicated.

For other combinations of transmit parameters the correlations between changes in subharmonic signal amplitude and changes in PV pressures were low i.e., ranged from 0.04 to 0.31 (Table 4.24). Table 4.24 also presents the correlation coefficient between absolute values of the subharmonic signal amplitudes and PV pressures. Again, the best and significant correlation coefficient ($r = -0.89$, $p < 0.01$) was obtained when the subharmonic signals were acquired with optimized IAO level and 4 transmit cycles (Fig. 6D). *(Based on this result Hypothesis 6, that evaluated if the SHAPE data correlated with catheter pressures, was accepted.)* For the other sets of transmit parameters, the absolute correlation between subharmonic signal amplitudes and PV pressures ranged from -0.18 to -0.65, with the exception of 4 transmit cycles where correlations of -0.72 and -0.73 at IAO below and above the optimized IAO were observed, respectively (Table 4.24). These correlation coefficients of -0.72 and -0.73 may stem from the fact that the subharmonic signals were in the growth phase of subharmonic emissions even above and below the optimum IAO; but these correlations were still less than -0.89 observed at optimum IAO and were not statistically significant. Also the correlation of -0.73 was obtained with 4 data points only. The results obtained here also agree with results obtained previously where the sensitivity of Sonazoid microbubbles to ambient pressures was maintained throughout the growth phase of subharmonic emissions, but peaked at optimum insonification (144). The decrease in axial resolution and/or using relatively longer duration pulses by using higher transmit cycles (8 and 16) may have resulted in the relatively lower observed correlation coefficient for the changes in PV pressures and subharmonic signal amplitudes, and the absolute PV pressures and subharmonic signal amplitudes with 8 and 16 transmit cycle pulses.

The data in Table 4.25 represent the results of paired comparisons for subharmonic signal amplitudes before and after inducing PH. A statistically significant difference between subharmonic signal amplitudes, before and after inducing PH, was only noted for data acquired with 4 transmit cycles and at optimized IAO level. Thus, based on data presented in Tables 4.24 and 4.25, and Fig. 4.24, the hypothesis that SHAPE's performance would be best at optimum IAO level identified by the IAO optimization program and at 4 transmit cycles was accepted. These results further demonstrate the need to optimize IAO levels for SHAPE applications.

Table 4.25: Paired t-test results when comparing subharmonic signal amplitudes obtained at baseline and PH conditions

IAO level	Number of transmit cycles	Results of paired differences test				
		n	Mean Difference (dB)	95 % Confidence Interval (dB)		*p*-value
				Lower	Upper	
Optimized	4	4	-8.35 ± 2.45	-12.26	-4.44	< 0.01
	8	4	-3.99 ± 6.19	-13.85	5.86	0.29
	16	4	-3.61 ± 4.48	-10.74	3.51	0.21
Below optimized	4	4	-4.51 ± 3.81	-10.57	-1.55	0.10
	8	4	-1.67 ± 6.01	-11.23	7.89	0.62
	16	4	-5.02 ± 4.42	-12.04	-2.01	0.11
Above optimized	4	2*	-7.57 ± 5.57	N/A†	N/A†	0.31
	8	2*	-6.85 ± 7.12	N/A†	N/A†	0.40
	16	2*	-2.52 ± 5.01	N/A†	N/A†	0.61

*Should be interpreted with caution as data from 2 canines at higher IAO level were not acquired due to timing constraints (data provided here for reference);

†N/A: not applicable

4.3.3.4 Discussion based on PH Study 2

As seen in Fig. 4.22, the subharmonic signal documents a sigmoidal relationship with IAO as documented previously (3, 114, 133, 144); the initial occurrence stage, the growth stage and the gradual saturation at acoustic output above 60 % (1.19 MPa) are seen. The fitting function shown in Fig. 4.22 compensates for motion artifacts, mainly due to respiration, during the data collection phase for determining the optimum IAO levels.

This study builds on previous *in vitro* and *in vivo* SHAPE applications (3, 133, 144, 167, 179, 180, 182) and solves the problem of determining optimum IAO levels to insonate the UCAs for SHAPE applications; the feasibility and reliability of this approach to track PV pressures was demonstrated. A small sample size used in this study remains a limitation along with the acute embolization that was developed in one out of the five canines due to the surgical procedure for introducing the pressure catheter in the PV. Since ultrasound scanning and data acquisition were performed by placing the transducer through the open abdominal cavity created to gain access to the PV, the backscattered signals had less attenuation relative to an intact abdomen – this difference in attenuation varies on a case by case basis depending on inter-subject variability.

4.3.4 Discussion Based on PH SHAPE Studies

For PH evaluation using SHAPE, 2 different studies were performed. In PH Study 1, the efficacy of SHAPE to detect PV pressure rises was studied. Since, the results of PH Study 1 were promising with respect to the utility of the SHAPE technique to identify PH, in PH Study 2 the goal was to develop a technique to identify optimum

IAO for SHAPE. This is an important step because the attenuation in clinical cases will vary on a case-by-case basis; without this IAO optimization algorithm the IAO level may have to be selected arbitrarily or data at all IAO levels may have to be captured – this last possibility is computationally expensive and more importantly limits real-time capability.

Similar to the Sonix RP scanner used for cardiac studies, the Logiq 9 scanner used in PH studies also showed discreet IAO levels. Thus, if the 'most-sensitive' IAO level for SHAPE falls between two consecutive discrete levels, then SHAPE's performance may not be optimum. Another practical problem before translating this technique into clinical applications arises from the fact that the subharmonic response depends on both the insonification IAO levels and ambient pressures. By displaying in real-time the subharmonic emissions as a function of acoustic pressure, the optimal IAO level can be identified. However, the associated subharmonic amplitude is still arbitrary due to variable attenuation and unknown ambient pressure. In other words, the same subharmonic amplitude measured in different subjects at an optimal IAO level (eliciting ambient pressure sensitive subharmonic emissions) may correspond to different ambient pressures. One approach to circumvent this problem may require obtaining the subharmonic gradient between the PV and the hepatic vein, which is analogous to the HVPG measurements used clinically (183, 184).

Another factor in the PH studies was the mid-line abdominal incision created for accessing the main PV to obtain reference PV pressures; but absolute PV pressures cannot be obtained by another approach i.e., without accessing the PV.

4.3.5 Summary Based on PH SHAPE Studies

In conclusion, two acute PH models were developed. A low-flow PH model using Gelfoam was repeatable and successful in increasing PV pressures within 15 minutes by 16.5 mmHg on average. A high-flow PH model using A-V shunt (between the femoral artery and the PV vein) was not successful in increasing PV pressures. However, if the flow from the femoral artery was supplemented by additional saline infusion, mean increases in PV pressures of 12.8 mmHg were noted.

The efficacy of SHAPE to determine PV pressures and monitor changes in PV pressures in the canine PH models considered here has been proven. For "optimum" insonification, the changes in subharmonic signal amplitude correlated significantly ($p < 0.05$) with changes in PV pressures; correlation coefficient ranged from -0.82 to -0.94 and from -0.70 to -0.73 for PH models considered separately or together, respectively Thus, Hypothesis 5 was accepted. The subharmonic signal amplitudes correlated with absolute PV pressures (r: -0.71 to -0.79).

There was a statistically significant difference between subharmonic amplitudes before and after inducing PH ($p \leq 0.01$). PV pressures estimated using SHAPE did not reveal significant differences ($p > 0.05$) with respect to the pressures obtained using the Millar pressure catheter. Thus, Hypothesis 4 was accepted.

A novel automated IAO optimization program was developed to determine optimum IAO levels to insonate the UCAs for SHAPE applications. The approach was validated to track PV pressures in canines using SHAPE. The results demonstrated that SHAPE functions best when 4 transmit cycles were used to insonate the UCAs at the optimum IAO determined by the IAO optimization program. SHAPE performance was sub-optimal when IAO levels below- or above- the optimum IAO levels were used. Thus, the need to identify the optimum IAO level for SHAPE applications stands justified. Also, the correlation coefficient between subharmonic amplitude (SHAPE data) and the PV pressures before and after inducing PH was -0.89 (i.e., an $r^2 = 0.79$). Thus Hypothesis 6 was accepted.

Above all, the current standard of direct hepatic venous catheterization should be substituted by a noninvasive, accurate and reliable method to estimate HVPG or PV pressures (15). Such a method would allow screening, diagnosis, monitoring and prognosis of chronic liver diseases or cirrhosis and would limit the number of endoscopies performed (especially for screening populations or patients without clinical signs of PH). The work presented here documents that the SHAPE technique may be used to track PV pressures and thus, may be useful as a screening tool for PV pressure monitoring. In the future, SHAPE may be a viable clinical tool for measuring PV pressures and monitoring treatment in symptomatic or critically ill cirrhotic patients, and identifying nascent PH in asymptomatic patients as well.

4.4 General Discussion Based on SHAPE Studies

4.4.1 Cross Platform Compatibility

In this thesis Sonazoid, which is not yet approved for human use by the USA FDA was selected as the UCA for ambient pressure estimation *in vitro* and *in vivo*. However, another preliminary study showed that subharmonic emissions from Definity (clinically approved to opacify the left ventricle for improved delineation of the left ventricular endocardial border) may also be used for *in vivo* pressure estimation (185); thus the SHAPE technique is not solely limited to the use of Sonazoid. Also, the fact that SHAPE technique worked with scanners from two different manufacturers confirms the reliability of pressure estimation using SHAPE and that the workings of SHAPE are not specific to a given combination of UCA and any particular ultrasound scanner.

4.4.2 Specific Aims and Hypotheses

All specific aims were accomplished. All hypotheses were accepted except Hypothesis 3 which was framed to investigate if “the SHAPE results in the LV and RV will be in agreement with catheter pressures and show a maximum error of less than 10 %”. The SHAPE results in the LV and RV were in agreement with the catheter pressures – this was confirmed because the clinically relevant LV and RV pressures did not differ significantly with respect to the values recorded by the pressure catheter which was the reference standard. However, the percent error overall was as high as 28 %, but this 28 % corresponds to an absolute pressure error of 1.8 mmHg. This suggests that the percent criteria may not have been an appropriate choice to frame the hypothesis, incipiently. But the errors obtained with SHAPE in the LV and RV were all within 3.5 mmHg after using a calibration factor (mmHg/dB) from the aorta data – i.e., the errors were within the 5 mmHg error criteria recommended for noninvasive blood pressure measurement techniques (22). This suggests that SHAPE technique may now be evaluated in a clinical setting – at least in a pilot study.

4.4.3 Sensitivity of Sonazoid and other UCAs for SHAPE

The table below (Table 4.26) lists the sensitivity of Sonazoid microbubbles to changes in ambient pressure expressed as mmHg/dB based on literature and the results presented in this thesis.

Table 4.26: Sensitivity of Sonazoid to ambient pressure changes

*Sensitivity in mmHg/dB	Experiment Description
-6.6 (135)	Simulation studies
-14.0 (144)	Static tank experiments with single element transducers
-10.6 to -10.9 (167, 182)	*In vitro* flow phantom studies with a commercial ultrasound scanner†
-4.4 (23)	*In vivo* (from aorta) with single element transducers
-4.9 (180)	*In vivo* (cardiac LV studies) with a commercial ultrasound scanner†
-2.0 to-4.0 (179)	*In vivo* (cardiac RV studies) with a commercial ultrasound scanner†
-1.4 to -1.7	*In vivo* PH studies with a commercial ultrasound scanner‡

*References are indicated in brackets where applicable; †Sonix RP scanner; ‡Logiq 9 scanner

A general trend appears from Table 4.26. The studies report a decrease in subharmonic signal amplitude with an increase in ambient pressure (marked by a negative sign). The simulation studies that were done at about the same transmit frequency (2.46 MHz) to the one used in this study (2.5 MHz), suggests that the behavior of the Sonazoid microbubbles *in vitro* and *in vivo* may not have been adequately captured in those simulation studies. *In vitro* sensitivity values were much less (indicating that the change in subharmonic signal was relatively less) than *in vivo* sensitivity values. A possible explanation for this may be the constantly changing environment that the microbubbles were exposed to *in vivo* as compared to *in vitro* – the interactions with other blood constituents may influence the bubble towards nonlinear oscillatory mode which is required for subharmonic emissions. When examining the subset of *in vivo* experiments, the variability in sensitivity may be due to a combination of features, including, but not limited to, differences in the transfer function of the input/output systems on the scanner, the difference between the experimental setup i.e., PH studies were performed with an open abdominal cavity (relatively less attenuation as compared to an intact abdomen or the cardiac SHAPE studies), etc.

In contrast to these findings, studies with phospholipid-shell microbubbles engineered with optimized initial surface tension have reported a sensitivity of 2.12 mmHg/dB (137). Also, in the studies mentioned in Table 4.26, the IAO level was chosen with maximum probability of the subharmonic emissions to reside in the growth phase (out of occurrence phase, growth phase and saturation phase) where the subharmonic emissions show a dependency on ambient pressures. In two separate *in vitro* studies (137, 140) using in-house manufactured microbubbles and also SonoVue, it was shown that subharmonic emissions may be characterized by five stages, namely, occurrence, growth, stabilization, regrowth and saturation. Comparing the IAO levels considered in the studies in this thesis with the levels used *in vitro* (137, 140), it may be surmised that the subharmonic emissions in this study may correspond to the regrowth phase. However, major differences exist between these two referenced studies and the studies in this thesis. The microbubbles used here were different (Sonazoid) and the cardiac and PH SHAPE studies were conducted *in vivo*, whereas the two other studies (137, 140) were based on behavior of the microbubbles *in vitro* where an idealized setup permits known peak negative acoustic pressures on the microbubbles and control over ambient pressures. *In vivo*, conditions depart markedly from this idealized *in vitro* setup; in the cardiac and PH studies only ambient noise was observed at IAO levels corresponding to the occurrence stage in Ref. (3), whereas a reasonable subharmonic at IAO levels corresponding to the growth stage in Ref. (3). Also, explicit analysis with Sonazoid microbubbles (which were used in this study) *in vitro* using a test setup mentioned elsewhere (144) revealed only the occurrence, growth and saturation phases as described previously (3). This may indicate that the 5 stages of subharmonic emissions may be a characteristic of the in-house manufactured microbubbles (as in (137)), or of SonoVue microbubbles which are different in composition with respect to Sonazoid microbubbles used in this study – also there have been no observations (to the best of our knowledge) reported on these 5 stages of subharmonic emissions from microbubbles *in vivo*, whereas implications of the 3 stages of subharmonic emissions have been seen and utilized for *in vivo* ambient pressure estimation here.

4.4.4 Algorithm for Future SHAPE Applications

Towards the work put forward for this thesis, an approach to use SHAPE for pressure estimation was developed *in vitro* and then tested *in vivo* under two different conditions – cardiac SHAPE studies involving dynamic pressure variations and PH SHAPE studies involving static pressures (less amplitude of pressure excursions as compared to those encountered in the LV or the RV). A technique to identify optimum IAO level for SHAPE was validated.

In Fig. 4.25, based on the results and discussions of the SHAPE studies, an "on-demand" approach is proposed to identify the optimum IAO level for SHAPE based on the application – pressures that do not oscillate rapidly (like those encountered in the PV) or pressures that do oscillate rapidly (like those encountered in the heart).

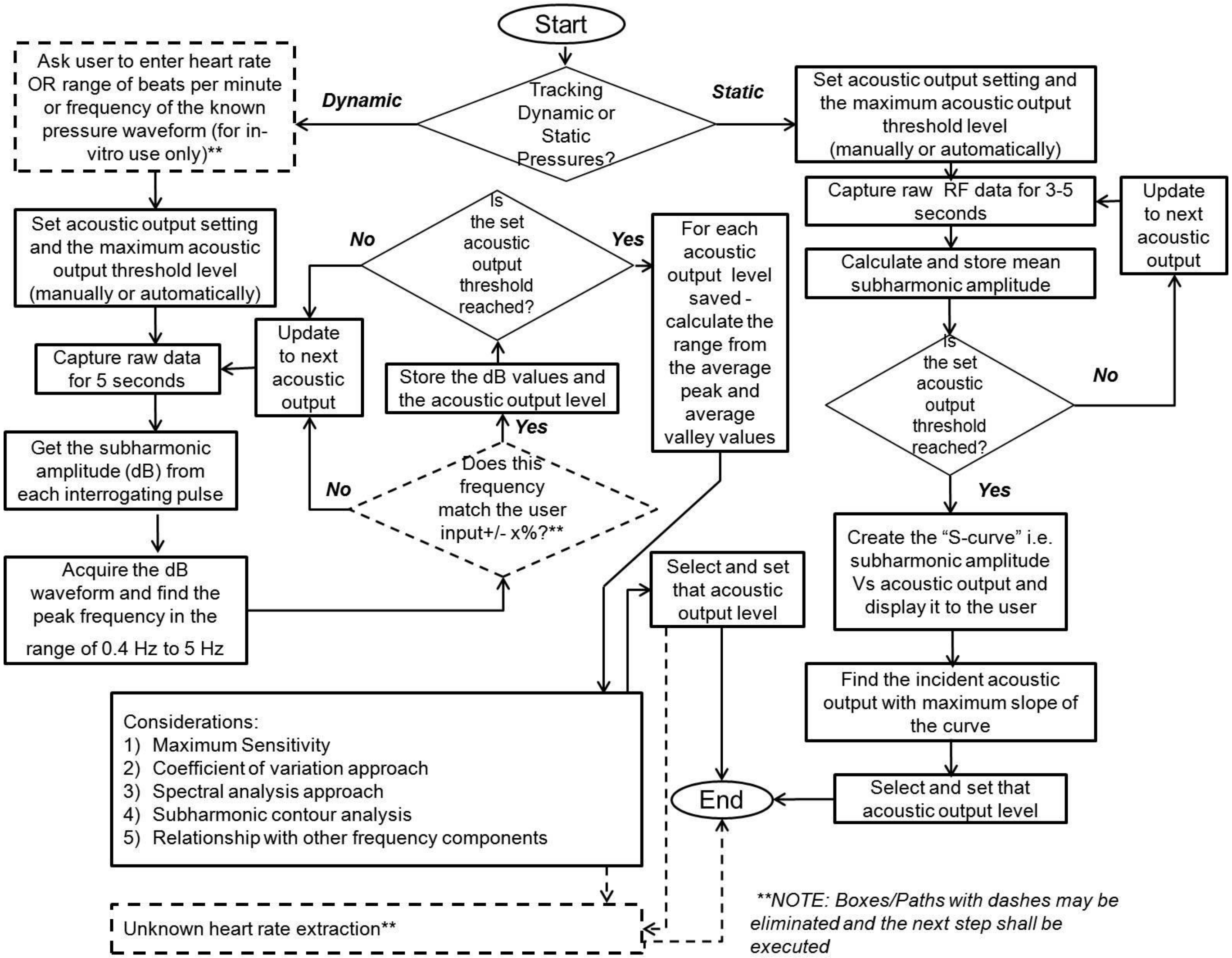
Start
Tracking Dynamic or Static Pressures?
Dynamic
Static
Ask user to enter heart rate OR range of beats per minute or frequency of the known pressure waveform (for in-vitro use only)**
Set acoustic output setting and the maximum acoustic output threshold level (manually or automatically)
Capture raw data for 5 seconds
Get the subharmonic amplitude (dB) from each interrogating pulse
Acquire the dB waveform and find the peak frequency in the range of 0.4 Hz to 5 Hz
Does this frequency match the user input+/- x%?**
Yes
No
Store the dB values and the acoustic output level
Is the set acoustic output threshold reached?
No
Yes
Update to next acoustic output
For each acoustic output level saved - calculate the range from the average peak and average valley values
Considerations:
1) Maximum Sensitivity
2) Coefficient of variation approach
3) Spectral analysis approach
4) Subharmonic contour analysis
5) Relationship with other frequency components
Select and set that acoustic output level
Unknown heart rate extraction**
End
Set acoustic output setting and the maximum acoustic output threshold level (manually or automatically)
Capture raw RF data for 3-5 seconds
Update to next acoustic output
Calculate and store mean subharmonic amplitude
Is the set acoustic output threshold reached?
No
Yes
Create the “S-curve” i.e. subharmonic amplitude Vs acoustic output and display it to the user
Find the incident acoustic output with maximum slope of the curve
Select and set that acoustic output level

***NOTE: Boxes/Paths with dashes may be eliminated and the next step shall be executed*

Figure 4.25: Proposed flow chart for selection of optimum IAO levels for *in vivo* SHAPE

5. CONCLUSIONS AND FUTURE RECOMMENDATIONS

5.1 Conclusions and Contributions to Science

The overall goal of this thesis was to develop and evaluate the efficacy of SHAPE for investigating *in vivo* pressures noninvasively. The immediate clinical applications of noninvasive pressure estimation were recognized in monitoring central cardiac pressures and pressures in blood vessels feeding vital organs like liver, etc. where invasive pressure measurements are the clinical standard (4, 5). Consequently the *in vivo* efficacy of SHAPE to evaluate pressures noninvasively in the heart and in the PV (to investigate PH) was to be determined. All prior studies (before the start of this thesis work) were mostly performed *in vitro* and/or with idealized equipment setup; too remote from the situations encountered clinically. This led to the entire project being divided into 3 specific aims.

In *specific aim 1*, the ability of SHAPE to estimate dynamic pressures including a circulating flow component through a flow-phantom was investigated. Also, an attempt to compare different processing techniques to process the received UCA signals was undertaken. These experiments were performed using a commercially available ultrasound scanner and UCA to readily adopt the technique for *in vivo* evaluations. A signal processing technique was developed and the results showed that the standard error between catheter pressures (used as reference pressures) and SHAPE results were below 10 mmHg – this estimate with commercially available equipment was better than other reported techniques of measuring ambient pressures using UCAs that showed errors above 10 mmHg (even with idealized *in vitro* setup, e.g., isolating single bubble, etc.) (17-21). The results of this work were published (167, 182).

In *specific aim 2*, the feasibility of noninvasive SHAPE was investigated and then the accuracy of SHAPE in obtaining clinically relevant LV and RV pressures was studied. The feasibility of noninvasive SHAPE using commercially available ultrasound scanner and UCA was demonstrated, and this was the first noninvasive *in vivo* SHAPE study to be documented. Also the LV and the RV pressure estimates using SHAPE and the pressure catheter were within 3.5 mmHg for both, systolic and diastolic pressures. The robust results of these pilot studies are promising and should pave the way for validation in clinical populations, given that if these errors are translatable to the clinical population they would drastically reduce the number of cardiac catheterizations performed to obtain central cardiac pressures. These results were published (179, 180).

In *specific aim 3*, the ability of SHAPE to detect and identify induced PH in canines was tested. A secondary outcome of this study was the development of two acute models of PH and the results thus, obtained are “in press” (186). The results obtained through SHAPE demonstrated that the subharmonic emissions from microbubbles have the potential to discriminate PH cases. This is clinically beneficial given that symptoms associated with PH manifest only after severe liver dysfunction develop and are often associated with relatively high mortality – since the clinical standard is invasive measurements and the liver can compensate for mild PH, asymptomatic patients are at greater risk from PH. Thus this noninvasive technique developed here may, ultimately, be useful for PH screening. The SHAPE results obtained from PH studies are “in press” (187).

Also, given that UCA studies are cheaper than other imaging counterparts like nuclear medicine, MRI, CT or fluoroscopy, the SHAPE technique will provide functional status of the organ (in addition to the anatomic imaging) and thus, may potentially be a cost-saver. Overall this thesis germinated from a potential idea of measuring *in vivo* pressures noninvasively using UCAs (3, 23) and led to the development of a processing technique and approach to quantify *in vivo* pressures noninvasively, albeit in canines. Thus, this thesis shall serve as a link between past *in vitr*o tank studies and future clinical studies – probably, justifying the editors' choice of acknowledging the manuscripts resulting from this thesis as "Innovative Methodology", "Concepts on the verge of translation", and reviewers' classifying the studies as "professionally conducted". In that regard, recently, preliminary findings of a similar approach to identify PH in a clinical population were presented and the results revealed a correlation of 0.81 between the HVPG and the subharmonic gradient, when based on data from 27 patients and, this correlation improved to 0.86 when the study included data from 37 patients (183, 184). These preliminary results in a very limited patient population corroborate the findings of the results presented in this thesis. The complete results of the patient study will be published in the future.

Above all, the SHAPE approach has been refined and validated *in vivo* using commercial equipment which is expected to offer a safer and more cost effective alternative to current invasive pressure measurement techniques.

In total, the work presented in this thesis has resulted in 6 peer reviewed first-author publications (or in press articles), 2 first–author published conference proceedings and several conference presentations at the Annual Conventions of the AIUM, the IEEE International Ultrasonic Symposia and the Annual Scientific Meetings of the Radiological Society of North America. A complete list of abstracts, conference proceedings and publications while specifically working towards this project is presented in Appendix 12.

5.2 Future Recommendations

For all the work presented in this thesis, data was processed off-line. Thus, the extraction and processing techniques developed for SHAPE should be ported on commercial ultrasound scanners and the real-time pressure estimation should be evaluated. Also the approach presented in Fig. 4.25 requires *in vivo* validation.

In the canine cardiac studies, the need to obtain a calibration factor from the systemic pulse pressures was realized. The calibration factor was calculated based on the pressure catheter data present in the aorta. The efficacy of using cuff-sphygmomanometer values for calculating the calibration factor remain to be investigated. Also hemodynamic alterations should be introduced to study the effect of increase or decrease in pulse rate, vasodilation, vasoconstriction, etc. on SHAPE results.

Currently work is also underway in the lab to develop the SHAPE technique for investigating interstitial fluid pressure in tumors to monitor treatment response following neoadjuvant chemotherapy.

Finally, pilot studies for cardiac SHAPE and a larger clinical study to evaluate the usefulness of screening asymptomatic or symptomatic patients to identify nascent PH should follow. The application of SHAPE may be extended for any other *in vivo* pressure measuring applications where noninvasive techniques are not available.

Lastly the use of subharmonic emissions from microbubbles to detect ambient pressures has been shown – the technique may be useful for ambient pressure measuring applications away from the field of biomedical engineering as well; in that sense the project has potential applications → ∞!

LIST OF REFERENCES

1. Goldberg B, Raichlen JS, Forsberg F. Ultrasound Contrast Agents: Basic Principles and Clinical Applications. United Kingdom: Martin Dunitz; 2001.

2. Shi WT, Forsberg F, Goldberg BB, Raichlen JS, inventors; Thomas Jefferson University, assignee. Method and system for pressure estimation using subharmonic signals from microbubble-based ultrasound contrast agents. Patent 6302845 United States of America 2001, Filed: Mar 19, 1999.

3. Shi WT, Forsberg F, Raichlen JS, Needleman L, Goldberg BB. Pressure dependence of subharmonic signals from contrast microbubbles. Ultrasound Med Biol. 1999;25(2):275-83.

4. Chatterjee K. The Swan-Ganz catheters: past, present, and future. A viewpoint. Circulation. 2009;119(1):147-52.

5. Lebrec D, Sogni P, Vilgrain V. Evaluation of patients with portal hypertension. Baillieres Clin Gastroenterol. 1997;11(2):221-41.

6. Connors AF, Jr., Speroff T, Dawson NV, Thomas C, Harrell FE, Jr., Wagner D, et al. The effectiveness of right heart catheterization in the initial care of critically ill patients. SUPPORT Investigators. JAMA. 1996;276(11):889-97.

7. Dalen JE. The pulmonary artery catheter-friend, foe, or accomplice? JAMA. 2001;286(3):348-50.

8. Dalen JE, Bone RC. Is it time to pull the pulmonary artery catheter? JAMA. 1996;276(11):916-8.

9. Gore JM, Goldberg RJ, Spodick DH, Alpert JS, Dalen JE. A community-wide assessment of the use of pulmonary artery catheters in patients with acute myocardial infarction. Chest. 1987;92(4):721-7.

10. Robin ED. Death by pulmonary artery flow-directed catheter. Time for a moratorium? Chest. 1987;92(4):727-31.

11. Rose H, Venn R. Recently published papers: dying Swans and other stories. Crit Care. 2006;10(4):152.

12. Shah MR, Hasselblad V, Stevenson LW, Binanay C, O'Connor CM, Sopko G, et al. Impact of the pulmonary artery catheter in critically ill patients: meta-analysis of randomized clinical trials. JAMA. 2005;294(13):1664-70.

13. U.S. Food and Drug Administration. Mikro-Tip Angiographic Catheter, Model SPC-454D and SPC-454F by Millar Instruments Inc.: Class 1 Recall 2011 [cited 2011 11/11]. Available from: http://www.fda.gov/Safety/MedWatch/SafetyInformation/SafetyAlertsforHumanMedicalProducts/ucm249387.htm.

14. Talwalkar JA, Yin M, Venkatesh S, Rossman PJ, Grimm RC, Manduca A, et al. Feasibility of in vivo MR elastographic splenic stiffness measurements in the assessment of portal hypertension. AJR Am J Roentgenol. 2009;193(1):122-7.

15. Thabut D, Moreau R, Lebrec D. Noninvasive assessment of portal hypertension in patients with cirrhosis. Hepatology. 2011;53(2):683-94.

16. Centers for Medicare & Medicaid Services. Pub 100-03 Medicare National Coverage Determinations 2009 [cited 2012 07/15/2012]. Available from: https://www.cms.gov/Regulations-and-Guidance/Guidance/Transmittals/Downloads/R101NCD.pdf.

17. Bouakaz A, Frinking PJ, de Jong N, Bom N. Noninvasive measurement of the hydrostatic pressure in a fluid-filled cavity based on the disappearance time of micrometer-sized free gas bubbles. Ultrasound Med Biol. 1999;25(9):1407-15.

18. Fairbank WM, Jr., Scully MO. A new noninvasive technique for cardiac pressure measurement: resonant scattering of ultrasound from bubbles. IEEE Trans Biomed Eng. 1977;24(2):107-10.

19. Hök B. A new approach to noninvasive manometry: interaction between ultrasound and bubbles. Med Biol Eng Comput. 1981;19(1):35-9.

20. Miwa H, inventor; Fujitsu Limited, assignee. Pressure measuring system with ultrasonic wave. Patent 4483345 United states of America 1984, Filed: August 4, 1982.

21. Shankar PM, Chapelon JY, Newhouse VL. Fluid pressure measurement using bubbles insonified by two frequencies. Ultrasonics. 1986;24(6):333-6.

22. Pickering TG, Hall JE, Appel LJ, Falkner BE, Graves J, Hill MN, et al. Recommendations for blood pressure measurement in humans and experimental animals: part 1: blood pressure measurement in humans: a statement for professionals from the Subcommittee of Professional and Public Education of the American Heart Association Council on High Blood Pressure Research. Circulation. 2005;111(5):697-716.

23. Forsberg F, Liu JB, Shi WT, Furuse J, Shimizu M, Goldberg BB. In vivo pressure estimation using subharmonic contrast microbubble signals: proof of concept. IEEE Trans Ultrason Ferroelectr Freq Control. 2005;52(4):581-3.

24. Baicu CF, Zile MR, Aurigemma GP, Gaasch WH. Left ventricular systolic performance, function, and contractility in patients with diastolic heart failure. Circulation. 2005;111(18):2306-12.

25. Baik SK, Kim JW, Kim HS, Kwon SO, Kim YJ, Park JW, et al. Recent variceal bleeding: Doppler US hepatic vein waveform in assessment of severity of portal hypertension and vasoactive drug response. Radiology. 2006;240(2):574-80.

26. Diwan A, McCulloch M, Lawrie GM, Reardon MJ, Nagueh SF. Doppler estimation of left ventricular filling pressures in patients with mitral valve disease. Circulation. 2005;111(24):3281-9.

27. Dokainish H, Zoghbi WA, Lakkis NM, Al-Bakshy F, Dhir M, Quinones MA, et al. Optimal noninvasive assessment of left ventricular filling pressures: a comparison of tissue Doppler echocardiography and B-type natriuretic peptide in patients with pulmonary artery catheters. Circulation. 2004;109(20):2432-9.

28. Geske JB, Sorajja P, Nishimura RA, Ommen SR. Evaluation of left ventricular filling pressures by Doppler echocardiography in patients with hypertrophic cardiomyopathy: correlation with direct left atrial pressure measurement at cardiac catheterization. Circulation. 2007;116(23):2702-8.

29. Ho CY, Solomon SD. A clinician's guide to tissue Doppler imaging. Circulation. 2006;113(10):e396-8.

30. Kidawa M, Coignard L, Drobinski G, Krzeminska-Pakula M, Thomas D, Komajda M, et al. Comparative value of tissue Doppler imaging and m-mode color Doppler mitral flow propagation velocity for the evaluation of left ventricular filling pressure. Chest. 2005;128(4):2544-50.

31. Kim MY, Baik SK, Park DH, Lim DW, Kim JW, Kim HS, et al. Damping index of Doppler hepatic vein waveform to assess the severity of portal hypertension and response to propranolol in liver cirrhosis: a prospective nonrandomized study. Liver Int. 2007;27(8):1103-10.

32. Kim SY, Jeong WK, Kim Y, Heo JN, Kim MY, Kim TY, et al. Changing waveform during respiration on hepatic vein Doppler sonography of severe portal hypertension: comparison with the damping index. J Ultrasound Med. 2011;30(4):455-62.

33. Mertens LL, Friedberg MK. Imaging the right ventricle--current state of the art. Nat Rev Cardiol. 2010;7(10):551-63.

34. Mor-Avi V, Sugeng L, Lindner JR. Imaging the forgotten chamber: is the devil in the boundary? J Am Soc Echocardiogr. 2010;23(2):141-3.

35. Tschöpe C, Paulus WJ. Is echocardiographic evaluation of diastolic function useful in determining clinical care? Doppler echocardiography yields dubious estimates of left ventricular diastolic pressures. Circulation. 2009;120(9):810-20.

36. Vizzutti F, Arena U, Romanelli RG, Rega L, Foschi M, Colagrande S, et al. Liver stiffness measurement predicts severe portal hypertension in patients with HCV-related cirrhosis. Hepatology. 2007;45(5):1290-7.

37. Yotti R, Bermejo J, Desco MM, Antoranz JC, Rojo-Alvarez JL, Cortina C, et al. Doppler-derived ejection intraventricular pressure gradients provide a reliable assessment of left ventricular systolic chamber function. Circulation. 2005;112(12):1771-9.

38. Zile MR, Gaasch WH, Carroll JD, Feldman MD, Aurigemma GP, Schaer GL, et al. Heart failure with a normal ejection fraction: is measurement of diastolic function necessary to make the diagnosis of diastolic heart failure? Circulation. 2001;104(7):779-82.

39. Zhang CX, Hu J, Hu KW, Zhang C, Wang L, Xu JM. Noninvasive analysis of portal pressure by contrast-enhanced sonography in patients with cirrhosis. J Ultrasound Med. 2011;30(2):205-11.

40. Guyton AC, Hall JE. Heart muscle; the heart as a pump and function of the heart valves. Textbook of Medical Physiology. 11 ed: Saunders - Elsevier; 2006. p. 103-15.

41. Moan AS. The evaluation of liver dysfunction: when to suspect portal hypertension. JAAPA. 2009;22(4):38-42.

42. Sanyal AJ, Bosch J, Blei A, Arroyo V. Portal hypertension and its complications. Gastroenterology. 2008;134(6):1715-28.

43. Cokkinos DD, Dourakis SP. Ultrasonographic assessment of cirrhosis and portal hypertension. Current Medical Imaging Reviews. 2009;5:62-70.

44. Cohen J. A power primer. Psychological bulletin. 1992;112(1):155-9.

45. Østensen J, Hede R, Myreng Y, Ege T, Holtz E. Intravenous injection of Albunex microspheres causes thromboxane mediated pulmonary hypertension in pigs, but not in monkeys or rabbits. Acta Physiol Scand. 1992;144(3):307-15.

46. Heron M. National Vital Statistics Reports. 2011 08/26/2011. Report No.: Contract No.: 8.

47. Roger VL, Go AS, Lloyd-Jones DM, Benjamin EJ, Berry JD, Borden WB, et al. Heart disease and stroke statistics--2012 update: a report from the American Heart Association. Circulation. 2012;125(1):e2-e220.

48. World Health Organization. Cardiovascular diseases (CVDs) 2011 [cited 2011 November 11]. Available from: http://www.who.int/mediacentre/factsheets/fs317/en/index.html.

49. Papaioannou TG, Protogerou AD, Stamatelopoulos KS, Vavuranakis M, Stefanadis C. Non-invasive methods and techniques for central blood pressure estimation: procedures, validation, reproducibility and limitations. Curr Pharm Des. 2009;15(3):245-53.

50. Sabovic M, Safar ME, Blacher J. Is there any additional prognostic value of central blood pressure wave forms beyond peripheral blood pressure? Curr Pharm Des. 2009;15(3):254-66.

51. Nohria A, Mielniczuk LM, Stevenson LW. Evaluation and monitoring of patients with acute heart failure syndromes. Am J Cardiol. 2005;96(6A):32G-40G.

52. Williams B, Lacy PS, Thom SM, Cruickshank K, Stanton A, Collier D, et al. Differential impact of blood pressure-lowering drugs on central aortic pressure and clinical outcomes: principal results of the Conduit Artery Function Evaluation (CAFE) study. Circulation. 2006;113(9):1213-25.

53. Sciarretta S, Palano F, Tocci G, Baldini R, Volpe M. Antihypertensive treatment and development of heart failure in hypertension: a Bayesian network meta-analysis of studies in patients with hypertension and high cardiovascular risk. Arch Intern Med. 2011;171(5):384-94.

54. Webb AJ, Fischer U, Mehta Z, Rothwell PM. Effects of antihypertensive-drug class on interindividual variation in blood pressure and risk of stroke: a systematic review and meta-analysis. Lancet. 2010;375(9718):906-15.

55. Cushman WC, Evans GW, Byington RP, Goff DC, Jr., Grimm RH, Jr., Cutler JA, et al. Effects of intensive blood-pressure control in type 2 diabetes mellitus. N Engl J Med. 2010;362(17):1575-85.

56. Solomon SD, Stevenson LW. Recalibrating the barometer: is it time to take a critical look at noninvasive approaches to measuring filling pressures? Circulation. 2009;119(1):13-5.

57. Aurigemma GP, Zile MR, Gaasch WH. Contractile behavior of the left ventricle in diastolic heart failure: with emphasis on regional systolic function. Circulation. 2006;113(2):296-304.

58. Fishbein MC, Kobashigawa J. Biopsy-negative cardiac transplant rejection: etiology, diagnosis, and therapy. Curr Opin Cardiol. 2004;19(2):166-9.

59. Haddad F, Doyle R, Murphy DJ, Hunt SA. Right ventricular function in cardiovascular disease, part II: pathophysiology, clinical importance, and management of right ventricular failure. Circulation. 2008;117(13):1717-31.

60. Voelkel NF, Quaife RA, Leinwand LA, Barst RJ, McGoon MD, Meldrum DR, et al. Right ventricular function and failure: report of a National Heart, Lung, and Blood Institute working group on cellular and molecular mechanisms of right heart failure. Circulation. 2006;114(17):1883-91.

61. Kasimir MT, Seebacher G, Jaksch P, Winkler G, Schmid K, Marta GM, et al. Reverse cardiac remodelling in patients with primary pulmonary hypertension after isolated lung transplantation. Eur J Cardiothorac Surg. 2004;26(4):776-81.

62. Marino TA, Kent RL, Uboh CE, Fernandez E, Thompson EW, Cooper Gt. Structural analysis of pressure versus volume overload hypertrophy of cat right ventricle. Am J Physiol. 1985;249(2 Pt 2):H371-9.

63. Tedrow UB, Kramer DB, Stevenson LW, Stevenson WG, Baughman KL, Epstein LM, et al. Relation of right ventricular peak systolic pressure to major adverse events in patients undergoing cardiac resynchronization therapy. Am J Cardiol. 2006;97(12):1737-40.

64. Cortina C, Bermejo J, Yotti R, Desco MM, Rodriguez-Perez D, Antoranz JC, et al. Noninvasive assessment of the right ventricular filling pressure gradient. Circulation. 2007;116(9):1015-23.

65. Karamanoglu M, Bennett TD. A right ventricular pressure waveform based pulse contour cardiac output algorithm in canines. Cardiovasc Eng. 2006;6(3):83-92.

66. Karamanoglu M, McGoon M, Frantz RP, Benza RL, Bourge RC, Barst RJ, et al. Right ventricular pressure waveform and wave reflection analysis in patients with pulmonary arterial hypertension. Chest. 2007;132(1):37-43.

67. Hoeks AP, Brands PJ, Smeets FA, Reneman RS. Assessment of the distensibility of superficial arteries. Ultrasound Med Biol. 1990;16(2):121-8.

68. Ishii M, Kato H, Inoue O, Takagi J, Akagi T, Miyake T, et al. Noninvasive evaluation of systolic pressures of pulmonary artery and right ventricle using contrast-

enhanced doppler echocardiography: comparative study using sonicated albumin or glucose solution. Pediatr Cardiol. 1996;17(3):175-80.

69. Reddy AK, Taffet GE, Madala S, Michael LH, Entman ML, Hartley CJ. Noninvasive blood pressure measurement in mice using pulsed Doppler ultrasound. Ultrasound Med Biol. 2003;29(3):379-85.

70. Strauss AL, Roth FJ, Rieger H. Noninvasive assessment of pressure gradients across iliac artery stenoses: duplex and catheter correlative study. J Ultrasound Med. 1993;12(1):17-22.

71. Beulen BW, Bijnens N, Koutsouridis GG, Brands PJ, Rutten MC, van de Vosse FN. Toward noninvasive blood pressure assessment in arteries by using ultrasound. Ultrasound Med Biol. 2011;37(5):788-97.

72. Okuda K, Mitchell DG, Itai Y, Ariyama J. Vascular Disease. Hepatobiliary Diseases Pathophysiology and Imaging. 1 ed: Blackwell Science, Inc. Malden MA 02148; 2001. p. 213-340.

73. de Franchis R, Primignani M. Natural history of portal hypertension in patients with cirrhosis. Clin Liver Dis. 2001;5(3):645-63.

74. Navarro VJ, Rossi S, Herrine SK. Hepatic Cirrhosis. Pharmacology and Therapeutics: Principles to Practice. 1 ed: Saunders- Elsevier; 2008. p. 505-26.

75. Abraldes JG, Pasarin M, Garcia-Pagan JC. Animal models of portal hypertension. World J Gastroenterol. 2006;12(41):6577-84.

76. Calès P, Desmorat H, Vinel JP, Caucanas JP, Ravaud A, Gerin P, et al. Incidence of large oesophageal varices in patients with cirrhosis: application to prophylaxis of first bleeding. Gut. 1990;31(11):1298-302.

77. Christensen E, Fauerholdt L, Schlichting P, Juhl E, Poulsen H, Tygstrup N. Aspects of the natural history of gastrointestinal bleeding in cirrhosis and the effect of prednisone. Gastroenterology. 1981;81(5):944-52.

78. Primignani M, Albe R, Preatoni P, Carnevale P, Bianchi MB, Parravicini ML, et al. 'De novo' development of esophagela varices in patients iwth a recent histologic

diagnosis of liver cirrhosis. The American Gastroenterological Association and Digestive Disease Week; Gastroenterology; April 1998. p. A1324.

79. D'Amico G, Garcia-Tsao G, Pagliaro L. Natural history and prognostic indicators of survival in cirrhosis: a systematic review of 118 studies. J Hepatol. 2006;44(1):217-31

80. Halpern EJ. Noninvasive assessment of portal hypertension - can US aid in the prediction of portal pressure and monitoring of therapy? Radiology. 2006;240:309-10.

81. Kalambokis G, Manousou P, Vibhakorn S, Marelli L, Cholongitas E, Senzolo M, et al. Transjugular liver biopsy--indications, adequacy, quality of specimens, and complications--a systematic review. J Hepatol. 2007;47(2):284-94.

82. Bruix J, Castells A, Bosch J, Feu F, Fuster J, Garcia-Pagan JC, et al. Surgical resection of hepatocellular carcinoma in cirrhotic patients: prognostic value of preoperative portal pressure. Gastroenterology. 1996;111(4):1018-22.

83. Picchiotti R, Mingazzini PL, Scucchi L, Bressan M, Di Stefano D, Donnetti M, et al. Correlations between sinusoidal pressure and liver morphology in cirrhosis. J Hepatol. 1994;20(3):364-9.

84. Samonakis DN, Cholongitas E, Thalheimer U, Kalambokis G, Quaglia A, Triantos CK, et al. Hepatic venous pressure gradient to assess fibrosis and its progression after liver transplantation for HCV cirrhosis. Liver transplantation : official publication of the American Association for the Study of Liver Diseases and the International Liver Transplantation Society. 2007;13(9):1305-11.

85. Roberts S, Gordon A, McLean C, Pedersen J, Bowden S, Thomson K, et al. Effect of sustained viral response on hepatic venous pressure gradient in hepatitis C-related cirrhosis. Clinical gastroenterology and hepatology : the official clinical practice journal of the American Gastroenterological Association. 2007;5(8):932-7.

86. Echosens. Echosens: Information for Fibroscan [November 14, 2011]. Available from: http://www.echosens.com/.

87. Rye K, Mortimore G, Austin A, Freeman J. Non-invasive assessment and prediction of clinically significant portal hypertension. British Society of Gastroenterology Annual General Meeting; Gut; 14-17 March 2011. p. A245-6.

88. Abdelmoneim SS, Talwalkar J, Sethi S, Kamath P, Fathalla MM, Kipp BR, et al. A prospective pilot study of circulating endothelial cells as a potential new biomarker in portal hypertension. Liver Int. 2010;30(2):191-7.

89. Hartleb M, Kirstetter P, Moreau R, Soupison T, Pussard E, Hadengue A, et al. Relationships between plasma concentrations of endothelin and the severity of liver cirrhosis. Gastroentérologie Clinique et Biologique. 1994;18(5):407-12.

90. Durand F, Valla D. Assessment of the prognosis of cirrhosis: Child-Pugh versus MELD. J Hepatol. 2005;42 Suppl(1):S100-7.

91. Lafortune M, Marleau D, Breton G, Viallet A, Lavoie P, Huet PM. Portal venous system measurements in portal hypertension. Radiology. 1984;151(1):27-30.

92. Giday SA, Clarke JO, Buscaglia JM, Shin EJ, Ko CW, Magno P, et al. EUS-guided portal vein catheterization: a promising novel approach for portal angiography and portal vein pressure measurements. Gastrointest Endosc. 2008;67(2):338-42.

93. Bushberg JT. The essential physics of medical imaging. 2nd ed. Philadelphia: Lippincott Williams & Wilkins; 2002. xvi, 933 p.

94. Curry TS, Dowdey JE, Murry RC, Christensen EE. Christensen's physics of diagnostic radiology. 4th ed. Philadelphia: Lea & Febiger; 1990. xi, 522 p.

95. Szabo TL, Lewin PA. Piezoelectric materials for imaging. J Ultrasound Med. 2007;26(3):283-8.

96. Lewin PA. Quo vadis medical ultrasound? Ultrasonics. 2004;42(1-9):1-7.

97. Levin DC, Rao VM, Maitino AJ, Parker L, Sunshine JH. Comparative increases in utilization rates of ultrasound examinations among radiologists, cardiologists, and other physicians from 1993 to 2001. Journal of the American College of Radiology : JACR. 2004;1(8):549-52.

98. Levin DC, Rao VM, Parker L, Frangos AJ. Noncardiac point-of-care ultrasound by nonradiologist physicians: how widespread is it? Journal of the American College of Radiology : JACR. 2011;8(11):772-5.

99. Maitino AJ, Levin DC, Rao VM, Parker L, Sunshine JH. Do emergency medicine physicians perform ultrasound and conventional radiography in the emergency department? Recent trends from 1993 to 2001. Journal of the American College of Radiology : JACR. 2005;2(3):274-8.

100. Gramiak R, Shah PM. Echocardiography of the aortic root. Invest Radiol. 1968;3(5):356-66.

101. Gramiak R, Shah PM, Kramer DH. Ultrasound cardiography: contrast studies in anatomy and function. Radiology. 1969;92(5):939-48.

102. Leighton L. The Acoustic Bubble. United Kingdom: Academic Press Limited; 1994. 613 p.

103. Hoff L. Acoustic Characterization of Contrast Agents for Medical Imaging. The Netherlands: Kluwer Academic Publishers; 2001. 207 p.

104. Rayleigh L. On the pressure developed in a liquid during the collapse of a spherical cavity. Philosophical Magazine Series 6. 1917;34(200):94-8.

105. Plesset M, Prosperetti A. Bubble dynamics and cavitation. The Annual Review of Fluid Mechanics. 1977;9:145-85.

106. Strasberg M. The pulsation frequency of nonspherical gas bubbles in liquids. J Acoust Soc Am. 1953;25(3):536-7.

107. Strasberg M. Gas bubbles as sources of sound in liquids. J Acoust Soc Am. 1956;28(1):20-6.

108. Neppiras E. Subharmonic and other low frequency emission from bubbles in sound field. J Acoust Soc Am. 1969;46(3):587-601.

109. Eller A, Flynn H. Generation of subharmonics of order one-half by bubbles in sound field. J Acoust Soc Am. 1969;46(3):722-7.

110. de Jong N, Hoff L, Skotland T, Bom N. Absorption and scatter of encapsulated gas filled microspheres: theoretical considerations and some measurements. Ultrasonics. 1992;30(2):95-103.

111. Church C. The effects of an elastic solid surface layer on the radial pulsations of gas bubbles. J Acoust Soc Am. 1995;97(3):1510-21.

112. Hoff L, Sontum PC, Hovem JM. Oscillations of polymeric microbubbles: effect of the encapsulating shell. J Acoust Soc Am. 2000;107(4):2272-80.

113. Chatterjee D, Sarkar K. A Newtonian rheological model for the interface of microbubble contrast agents. Ultrasound Med Biol. 2003;29(12):1749-57.

114. Sarkar K, Shi WT, Chatterjee D, Forsberg F. Characterization of ultrasound contrast microbubbles using in vitro experiments and viscous and viscoelastic interface models for encapsulation. J Acoust Soc Am. 2005;118(1):539-50.

115. Marmottant P, van der Meer S, Emmer M, Versluis M, de Jong N, Hilgenfeldt S, et al. A model for large amplitude oscillations of coated bubbles accounting for buckling and rupture. J Acoust Soc Am. 2005;118(6):3499-505.

116. Minnaert M. On musical air-bubbles and the sound of running water. Philosophical Magazine. 1933;16(104):235-48.

117. Hogg JC. Neutrophil kinetics and lung injury. Physiol Rev. 1987;67(4):1249-95.

118. Main ML, Goldman JH, Grayburn PA. Thinking outside the "box"-the ultrasound contrast controversy. Journal of the American College of Cardiology. 2007;50(25):2434-7.

119. Patil H, Main ML. The history of product label changes for Definity in the US. US Cardiology. 2012;9(1):35-9.

120. Abdelmoneim SS, Mulvagh SL. Perflutren lipid microsphere injectable suspension for cardiac ultrasound. Imaging in Medicine. 2012;4(2):171-91.

121. Piscaglia F, Nolsoe C, Dietrich CF, Cosgrove DO, Gilja OH, Bachmann Nielsen M, et al. The EFSUMB Guidelines and Recommendations on the Clinical Practice of Contrast Enhanced Ultrasound (CEUS): update 2011 on non-hepatic applications. Ultraschall Med. 2012;33(1):33-59.

122. Bouakaz A, de Jong N. WFUMB Safety Symposium on Echo-Contrast Agents: nature and types of ultrasound contrast agents. Ultrasound Med Biol. 2007;33(2):187-96.

123. Landmark KE, Johansen PW, Johnson JA, Johansen B, Uran S, Skotland T. Pharmacokinetics of perfluorobutane following intravenous bolus injection and continuous infusion of sonazoid in healthy volunteers and in patients with reduced pulmonary diffusing capacity. Ultrasound Med Biol. 2008;34(3):494-501.

124. Dave JK, Forsberg F, Fernandes S, Piccoli CW, Fox TB, Merton DA, et al. Static and dynamic cumulative maximum intensity display mode for subharmonic breast imaging: a comparative study with mammographic and conventional ultrasound techniques. J Ultrasound Med. 2010;29(8):1177-85.

125. Eisenbrey JR, Sridharan A, Machado P, Zhao H, Halldorsdottir VG, Dave JK, et al. Three-dimensional subharmonic ultrasound imaging in vitro and in vivo. Acad Radiol. 2012;19(6):732-9.

126. Ferrara KW, Merritt CR, Burns PN, Foster FS, Mattrey RF, Wickline SA. Evaluation of tumor angiogenesis with US: imaging, Doppler, and contrast agents. Acad Radiol. 2000;7(10):824-39.

127. Forsberg F, Piccoli CW, Merton DA, Palazzo JJ, Hall AL. Breast lesions: imaging with contrast-enhanced subharmonic US--initial experience. Radiology. 2007;244(3):718-26.

128. Frinking PJ, Bouakaz A, Kirkhorn J, Ten Cate FJ, de Jong N. Ultrasound contrast imaging: current and new potential methods. Ultrasound Med Biol. 2000;26(6):965-75.

129. Iezzi R, Basilico R, Giancristofaro D, Pascali D, Cotroneo AR, Storto ML. Contrast-enhanced ultrasound versus color duplex ultrasound imaging in the follow-up of patients after endovascular abdominal aortic aneurysm repair. J Vasc Surg. 2009;49(3):552-60.

130. Eisenbrey JR, Dave JK, Halldorsdottir VG, Merton DA, Machado P, Liu JB, et al. Simultaneous grayscale and subharmonic ultrasound imaging on a modified commercial scanner. Ultrasonics. 2011;51(8):890-7.

131. Postema M, Bouakaz A, de Jong N. Noninvasive microbubble-based pressure measurements: a simulation study. Ultrasonics. 2004;42(1-9):759-62.

132. Paul S, Katiyar A, Sarkar K, Chatterjee D, Shi WT, Forsberg F. Material characterization of the encapsulation of an ultrasound contrast microbubble and its subharmonic response: strain-softening interfacial elasticity model. J Acoust Soc Am. 2010;127(6):3846-57.

133. Shi WT, Hoff L, Forsberg F. Subharmonic performance of contrast microbubbles: an experimental and numerical investigation. Proc of IEEE Ultrasonics Symposium. 2002;2:1957-60.

134. Adam D, Sapunar M, Burla E. On the relationship between encapsulated ultrasound contrast agent and pressure. Ultrasound Med Biol. 2005;31(5):673-86.

135. Andersen KS, Jensen JA. Ambient pressure sensitivity of microbubbles investigated through a parameter study. J Acoust Soc Am. 2009;126(6):3350-8.

136. Andersen KS, Jensen JA. Impact of acoustic pressure on ambient pressure estimation using ultrasound contrast agent. Ultrasonics. 2010;50(2):294-9.

137. Frinking PJ, Brochot J, Arditi M. Subharmonic scattering of phospholipid-shell microbubbles at low acoustic pressure amplitudes. IEEE Trans Ultrason Ferroelectr Freq Control. 2010;57(8):1762-71.

138. Ganor Y, Adam D, Kimmel E. Time and pressure dependence of acoustic signals radiated from microbubbles. Ultrasound Med Biol. 2005;31(10):1367-74.

139. Frinking PJ, Gaud E, Casqueiro G, Arditi M. Subharmonic scattering of phospholipid-shell microbubbles as a function of hydrostatic pressure. J Acoust Soc Am. 2012;131(4):3322.

140. Biagi E, Breschi L, Vannacci E, Masotti L. Stable and transient subharmonic emissions from isolated contrast agent microbubbles. IEEE Trans Ultrason Ferroelectr Freq Control. 2007;54(3):480-97.

141. Faez T, Renaud G, Defontaine M, Calle S, de Jong N. Dynamic manipulation of the subharmonic scattering of phospholipid-coated microbubbles. Physics in medicine and biology. 2011;56(19):6459-73.

142. Li F, Wang L, Fan Y, Li D. Simulation of noninvasive blood pressure estimation using ultrasound contrast agent microbubbles. IEEE Trans Ultrason Ferroelectr Freq Control. 2012;59(4):715-26.

143. Gorce JM, Arditi M, Schneider M. Influence of bubble size distribution on the echogenicity of ultrasound contrast agents: a study of SonoVue. Invest Radiol. 2000;35(11):661-71.

144. Halldorsdottir VG, Dave JK, Leodore LM, Eisenbrey JR, Park S, Hall AL, et al. Subharmonic contrast microbubble signals for noninvasive pressure estimation under static and dynamic flow conditions. Ultrason Imaging. 2011;33(3):153-64.

145. Sontum PC. Physicochemical characteristics of Sonazoid, a new contrast agent for ultrasound imaging. Ultrasound Med Biol. 2008;34(5):824-33.

146. Ultrasonix. Ultrasonix Research Forum [May 29, 2012]. Available from: http://research.ultrasonix.com/ucp.php?mode=login.

147. Forsberg F, Dave J, Halldorsdottir V, Leodore L, Lin F, Hall A, et al., editors. Applying real-time noninvasive pressure estimation obtained from subharmonic contrast microbubble signals. Proc of IEEE Ultrasonics Symposium. 2008;1694-97.

148. Bland JM, Altman DG. Multiple significance tests: the Bonferroni method. BMJ. 1995;310(6973):170.

149. Yanagisawa K, Moriyasu F, Miyahara T, Yuki M, Iijima H. Phagocytosis of ultrasound contrast agent microbubbles by Kupffer cells. Ultrasound Med Biol. 2007;33(2):318-25.

150. Daubechies I. Ten Lectures on Wavelets. Philadelphia: Pennsylvania: Society for industrial and applied mathematics; 1992.

151. Ogden R. Essential Wavelets for statistical Application and Data Analysis. Boston: Birkhäuser; 1997.

152. Chen Y, Zhang Q, Liao Y, Guo F, Zhang Y, Zeng Q, et al. A modified canine model of portal hypertension with hypersplenism. Scandinavian journal of gastroenterology. 2009;44(4):478-85.

153. de Baere T, Denys A, Paradis V. Comparison of four embolic materials for portal vein embolization: experimental study in pigs. European radiology. 2009;19(6):1435-42.

154. de Graaf W, van den Esschert JW, van Lienden KP, Roelofs JJ, van Gulik TM. A rabbit model for selective portal vein embolization. The Journal of surgical research. 2011;171(2):486-94.

155. Howe LM, Boothe HW, Jr., Miller MW, Boothe DM. A canine model of multiple portosystemic shunting. Journal of investigative surgery : the official journal of the Academy of Surgical Research. 2000;13(1):45-57.

156. Jin W, Deng L, Zhang Q, Lin D, Zhu J, Chen Y, et al. A canine portal hypertension model induced by intra-portal administration of Sephadex microsphere. Journal of gastroenterology and hepatology. 2010;25(4):778-85.

157. Lin D, Wu X, Ji X, Zhang Q, Lin Y, Chen W, et al. A novel canine model of portal vein stenosis plus thioacetamide administration-induced cirrhotic portal hypertension with hypersplenism. Cell biochemistry and biophysics. 2012;62(1):245-55.

158. Palmaz JC, Garcia F, Sibbitt RR, Tio FO, Kopp DT, Schwesinger W, et al. Expandable intrahepatic portacaval shunt stents in dogs with chronic portal hypertension. AJR Am J Roentgenol. 1986;147(6):1251-4.

159. Sugita S, Ohnishi K, Saito M, Okuda K. Splanchnic hemodynamics in portal hypertensive dogs with portal fibrosis. Am J Physiol. 1987;252(6 Pt 1):G748-54.

160. Yamana H, Yatsuka K, Kakegawa T. Experimental production of portal hypertension in dogs by a whole liver compression. Gastroenterologia Japonica. 1983;18(2):119-27.

161. Mullen KD, McCullough AJ. Problems with animal models of chronic liver disease: suggestions for improvement in standardization. Hepatology. 1989;9(3):500-3.

162. Mac DS, Matthews WH. Fibrin foam and gelfoam in experimental kidney wounds. The Journal of urology. 1947;57(5):802-11.

163. Jenkins HP, Janda R. Studies on the use of gelatin sponge or foam as an hemostatic agent in experimental liver resections and injuries to large veins. Annals of surgery. 1946;124:952-61.

164. Fisher AJ, Paulson EK, Kliewer MA, DeLong DM, Nelson RC. Doppler sonography of the portal vein and hepatic artery: measurement of a prandial effect in healthy subjects. Radiology. 1998;207(3):711-5.

165. Buob S, Johnston AN, Webster CR. Portal hypertension: pathophysiology, diagnosis, and treatment. Journal of veterinary internal medicine / American College of Veterinary Internal Medicine. 2011;25(2):169-86.

166. Gosling RG, Dunbar G, King DH, Newman DL, Side CD, Woodcock JP, et al. The quantitative analysis of occlusive peripheral arterial disease by a non-intrusive ultrasonic technique. Angiology. 1971;22(1):52-5.

167. Dave J, Halldorsdottir V, Eisenbrey J, Liu JB, McDonald M, Dickie K, et al. Noninvasive estimation of dynamic pressures in vitro and in vivo using the subharmonic response from microbubbles. IEEE Trans Ultrason Ferroelectr Freq Control. 2011;58(10):2056-66.

168. Field A. Discovering Statistics using SPSS. 3 ed. CA, USA: SAGE Publications Ltd.; 2009. 822 p.

169. Seitchik MW, Poll M, Rosenthal W, Baronofsky ID. Studies in the hemodynamics following supradiaphragmatic constriction of the inferior vena cava. Annals of surgery. 1961;153:71-80.

170. Eisenbrey JR, Joshi N, Dave JK, Forsberg F. Assessing algorithms for defining vascular architecture in subharmonic images of breast lesions. Physics in medicine and biology. 2011;56(4):919-30.

171. Shen CC, Cheng CH, Yeh CK. Phase-dependent dual-frequency contrast imaging at sub-harmonic frequency. IEEE Trans Ultrason Ferroelectr Freq Control. 2011;58(2):379-88.

172. Katiyar A, Sarkar K, Forsberg F. Modeling subharmonic response from contrast microbubbles as a function of ambient static pressure. J Acoust Soc Am. 2011;129(4):2325-35.

173. Wheatley MA, Forsberg F, Oum K, Ro R, El-Sherif D. Comparison of in vitro and in vivo acoustic response of a novel 50:50 PLGA contrast agent. Ultrasonics. 2006;44(4):360-7.

174. Koide K, Koide Y, Wada Y, Nakaniwa S, Yamane Y. Congenital hepatic arteriovenous fistula with intrahepatic portosystemic shunt and aortic stenosis in a dog. The Journal of veterinary medical science / the Japanese Society of Veterinary Science. 2004;66(3):299-302.

175. Moore PF, Whiting PG. Hepatic lesions associated with intrahepatic arterioportal fistulae in dogs. Veterinary pathology. 1986;23(1):57-62.

176. Schaeffer IG, Kirpensteijn J, Wolvekamp WT, Van den Ingh TS, Rothuizen J. Hepatic arteriovenous fistulae and portal vein hypoplasia in a Labrador retriever. The Journal of small animal practice. 2001;42(3):146-50.

177. Denys A, Bize P, Demartines N, Deschamps F, De Baere T. Quality improvement for portal vein embolization. Cardiovascular and interventional radiology. 2010;33(3):452-6.

178. Lavinge J, Brown C, Fewel J, Swan K. Hemodynamics within a canine femoral aeteriovenous fistula. Surgery. 1975;77(3):439-43.

179. Dave JK, Halldorsdottir VG, Eisenbrey JR, Raichlen JS, Liu JB, McDonald ME, et al. Subharmonic microbubble emissions for noninvasively tracking right ventricular pressures. Am J Physiol Heart Circ Physiol. 2012 303:H126-32.

180. Dave JK, Halldorsdottir VG, Eisenbrey JR, Raichlen JS, Liu JB, McDonald ME, et al. Noninvasive LV pressure estimation using subharmonic emissions from microbubbles. JACC Cardiovascular imaging. 2012;5(1):87-92.

181. Dave J, Halldorsdottir V, Eisenbrey J, Park S, Dianis S, Chalek CL, et al. Automated power optimization for subharmonic aided pressure estimation. 2012 AIUM Annual Convention; Phoenix, AZ, USA: J Ultrasound Med 2012. p. S44.

182. Dave J, Halldorsdottir V, Eisenbrey J, Forsberg F. Processing of subharmonic signals from ultrasound contrast agents to determine ambient pressures. Ultrason Imaging. 2012;34:65-75.

183. Eisenbrey J, Dave J, Halldorsdottir V, Merton D, Machado P, Miller C, et al. Subharmonic aided pressure estimation in patients with suspected portal hypertension. Proc of IEEE Ultrasonics Symposium. 2011;620-3.

184. Eisenbrey J, Gonzalez J, Dave J, Halldorsdottir V, Merton D, Machado P, et al. Noninvasive subharmonic aided pressures estimation (SHAPE) of portal hypertension: Initial Clinical Results. The Liver Meeting San Francisco, CA, USA 2011.

185. Halldorsdottir V, Eisenbrey J, Dave J, Forsberg F, Machado P, Cavanaugh B, et al. Subharmonic-aided pressure estimation for monitoring interstitial fluid pressure in swine melanomas: initial in vitro and in vivo results. 97th Scientific Assembly and Annual Meeting of the Radiological Society of North America; Chicago, IL, USA 2011.

186. Dave J, Liu J, Halldorsdottir V, Eisenbrey J, Merton D, Machado P, et al. Acute portal hypertension models in canines: low- & high- flow approaches. Comparative Medicine. 2012; In Press.

187. Dave JK, Halldorsdottir VG, Eisenberg JR, Merton DA, Liu JB, Zhou JH, et al. Investigating the efficacy of subharmonic aided pressure estimation for portal vein pressures and portal hypertension monitoring. Ultrasound Med Biol. 2012; In Press.

188. American Association For Laboratoy Animal Science. Humane Care and Use of Laboratory Animals. Secondary Humane Care and Use of Laboratory Animals [April 01, 2012]. Available from: http://www.aalas.org/pdfUtility.aspx?pdf=humane_care_and_use_of_laboratory_animals.pdf.

189. Vetinfo. The stages of anesthesia [April 01, 2012]. Available from: http://www.vetinfo.com/danesth.html/.

190. American Veterinary Medical Association. AVMA Guidelines on Euthanasia. Secondary AVMA Guidelines on Euthanasia [April 01, 2012]. Available from: http://www.avma.org/issues/animal_welfare/euthanasia.pdf.

Appendix 1: Detailed List of Equipment and Materials Used

I. Ultrasound scanners and UCA

1. Sonix RP scanner (S/N: SX 1.0-0606.0389) and PA4-2 transducer (S/N: TRA 1.0-SP00.194): Ultrasonix (Richmond, British Columbia, Canada). Software version:3.2.2.

2. GE Logiq 9 (System ID: L988822): GE Healthcare (Milwaukee, WI, USA).

3. UCA – Sonazoid: GE Healthcare (Oslo, Norway).

II. For measuring acoustic output of the transducers

1. Hydrophone: Used to determine the acoustic output in MPa at a transmit frequency of 2.5 MHz for both, the PA4-2 transducer and the 4C transducer:
0.2 mm needle hydrophone: Precision Acoustics (UK); sensitivity: 57.1 mV/MPa.

2. X-Y-Z Positioning System: Newport Corporation (Irvine, CA) – This positioning system is used to determine the focal point of the transducer by finding the point of maximum acoustic pressure.

III. For closed loop flow system (for dynamic *in vitro* SHAPE studies)

1. Acrylic Chamber (volume: 4071.5 cm^3): Constructed In-House – This chamber was used as a reservoir for the isotonic diluent with reconstituted Sonazoid microbubbles.

2. Magnetic Stirrer (Model 4657; S/N: 805970823021) and Stirring Bars (Kit # 4772-15): Cole Parmer Instrument Company (Vernon Hills, IL) – These were used to ensure uniform concentration of the Sonazoid microbubbles in the acrylic chamber as the isotonic diluent circulated through the closed-loop flow system.

3. Isotonic Diluent: Val Tech Diagnostics (Pittsburgh, PA) – This was used for *in vitro* experiments.

4. Blood Pump (Model: Sarns S10K II): Sarns Inc. (Ann Arbor, MI) – The pump was used to induce pulsatile flow and control pressures in the closed-loop flow system.

5. Flexible polyvinyl chloride tubes (inner diameter: 8 mm): In-House – The tubes were used to complete the closed-loop flow system.

6. Doppler Flow Phantom and Tissue Mimicking Phantom (15 x 9.5 x 8 cm^3): ATS Laboratories, Inc. (Bridgeport, CT) – The lumen within the Doppler flow phantom was used to simulate a blood vessel within the closed-loop flow system and the tissue mimicking phantom was used to alter the depth of scanning.

7. Acoustic Gel: MediChoice (Distributed by Owens & Minor, Richmond, VA) – For acoustic coupling between the tissue mimicking phantom / Doppler flow phantom and the ultrasound transducer.

IV. For pressure recording (both, *in vitro* and *in vivo*)

1. Oscilloscope (S/N: 9350-8088): LeCroy Corporation (Chestnut Ridge, NY) – The oscilloscope was used to observe and record the pressure catheter data.

2. Pressure Catheter System: This was used to measure ambient pressures around the microbubbles.

2.a. Solid State Pressure Catheter: SPR 350 (S/Ns 415521 & 485859) and SPR 350S (S/N: 492105; 'S' after 350 denotes straight tip otherwise the catheter has a curved tip): Millar Instruments, Inc. (Houston, TX). The SPR 350 catheter (S/N: 415521) has a broken sensor and is not functional (at the time of this writing).

2.b. Pressure Catheter Transducer Control Unit (Model: TCB 500, S/N: 2119): Millar Instruments, Inc. (Houston, TX). The control unit provides the bias voltages to the pressure catheter and was also used for calibrating the pressure catheter sensor.

3. Standard BNC cables (50 Ω): For connection between the pressure catheter transducer control unit and the oscilloscope.

V. For synchronization between the ultrasound scanners and the oscilloscope

1. Sonix RP scanner and oscilloscope: Synchronization signal from the Sonix RP scanner to the oscilloscope was obtained with a standard BNC cable (50 Ω).

2. GE Logiq 9 scanner and oscilloscope: Synchronization signal from the Logiq 9 scanner to the oscilloscope was obtained with a high impedance probe (PP005; 1 MΩ) from LeCroy Corporation (Chestnut Ridge, NY).

VI. *In vivo* experiments (items 2 through 4 were from the Office of Animal Resources, Thomas Jefferson University)

1. Sterile Surgi-Tip Transducer Covers: Civco Medical Solutions (Kaolna, IA) – These were used to maintain a sterile ultrasound scanning environment.

2. Anesthesia Equipment: To maintain anesthesia during experiments.

2.a. Anesthesia Ventilator (Model 2000) from Hallowell EMC (Pittsfield, MA)

2.b. Anesthesia Unit (Quatiflex VMC) from Matrx Medical Inc. (Orchard Park, NY)

3. Canine Monitoring Equipment:

3.a. Capnomac Ultima from Datex Ohmeda (Finland) – This was used to monitor canines' anesthesia, respiration and ventilation.

3.b. Vet/OX Plus 4700 from Sensor Devices Inc. (Lancaster, PA) – This was used to monitor canines' electrocardiogram, temperature and respiration, and for pulse-oximetry.

4. Heat Therapy Pump (Model: TP 400) from Gaymar Industries, Inc. (Orchard Park, NY) – This was connected to a warming blanket to maintain canines' body temperature.

VII. Computers used (for usernames and passwords contact Dr. Flemming Forsberg)

1. Computer 1: PCSO229 (Thomas Jefferson University):
Microsoft Windows XP Professional Ver. 2002 SP3
(3.6 GHz, 1 GB RAM, MAC: 001143B30159)
Used for running LabVIEW to interface with the oscilloscope

2. Computer 2: PCSP800 (Thomas Jefferson University):
(2.83 GHz, 3.25 GB RAM, MAC: 0026B97FEE05)
Used for processing and also, for interfacing with the GE Logiq 9 Scanner

3. Computer 3: PCSL663 (Thomas Jefferson University Hospital):
Microsoft Windows XP Professional Ver. 2002 SP3
(3.0 GHz, 4 GB RAM, MAC: 0017A41F0B7B)
Used for processing and publishing

4. Computer 4: Personal Laptop
MAC OS X Ver. 10.5.8
(2.4 GHz, 2 GB RAM)
Used for processing and publishing

Appendix 2: Use of Vertebrate Animals in the Experiments

Genus and Species: Canis Familiaris

Strain: Mongrel

Sex: Both male and female

Age: Between 6 months and 1 year

Number: 11 (for cardiac SHAPE; this being a pilot study for noninvasive SHAPE, no power analysis was performed)

Number: 22 (to develop SHAPE processing technique and to evaluate the feasibility and application of SHAPE to identify portal hypertension in canines; with 3 repetitions in each canine, the data obtained will have sufficient power (i.e., > 0.8) to detect the relationship of decrease in the subharmonic signals with an increase in PV pressures if a large effect (r > 0.5) genuinely exists (44))

Justification: Techniques for utilizing microbubbles to estimate ambient pressures have persisted over the last 4 decades (2, 3, 17-21, 23). However, none of these techniques have been translated to clinical use due to idealized *in vitro* experimental setups (like the use of single element transducers, isolation of single bubble for pressure estimation, etc.) or due to large errors associated with the proposed techniques. The proof-of-concept for SHAPE technique *in vitro* (3, 134-138) and *in vivo* has been provided (23), but again the experimental setup with single element transducers lacking imaging capability and/or open-thoracic cavity (*in vivo* studies) for obtaining subharmonic data preclude clinical use.

The overall purpose of this thesis was to investigate the application of SHAPE for cardiac and hepatic applications and provide a tool for clinical applications. The initial studies for developing SHAPE algorithm using commercially available ultrasound scanners and UCAs were performed *in vitro* using standard water-bath technique and flow phantoms. However, before clinical testing the efficacy and accuracy of this technique must be investigated *in vivo*. Canines were selected for these studies, because smaller animals, such as rabbits, have blood vessels too small to catheterize and because some species, such as swine, may have marked pulmonary hypertension during contrast microbubble experiments (45). The initial proof-of-concept *in vivo* study was also performed in canines. Also the team at Thomas Jefferson University has had extensive experience in UCA studies in canines.

Veterinary care: The canines were obtained from Marshall BioResources (North Rose, NY). The canines were vaccinated at Marshall BioResources for bordetella, parainfluenza, adenovirus, leptospirosis, distemper, parvovirus and rabies; and these vaccinations were updated as needed while the canines resided at Thomas Jefferson University. Before arrival at Thomas Jefferson University, the canines were dewormed with pyrantel pamoate anthelmintic (Med-Pharmex, Inc., Pomona, CA) and ivermectin (Merck, Whitehouse Station, NJ). When the canines arrived at Thomas Jefferson University, their general appearance was recorded as well as a detailed physical examination was performed including temperature, pulse rate and respiratory rate recordings. The canines were then kept in the AAALAC (Association for Assessment and Accreditation of Laboratory Animal Care International) accredited facilities of Thomas Jefferson University and were cared for and monitored using practices that comply with the principles for the utilization and care of vertebrate animals used in testing, research and training (188). The canines were housed in large and appropriately ventilated animal pens, and acclimated for at least 72 hours before they were allowed to be used in the research study. Since at Thomas Jefferson University the canines were housed inside at all times, parasite infections were not an issue. While Thomas Jefferson University requires treatment for all parasite infections and other illnesses as per the veterinarian's instructions, the canines in this project did not have any problems and thus no treatments were issued. They were fed a mix of canned science diet dog food and a laboratory canine diet produced by Purina Mills (Gray Summit, MO).

Experimental procedures alleviating animal discomfort: An intravenous injection of Propofol (Abbott Laboratories, Chicago, IL; dose 7 mg/kg) was used for initial sedation. The animals were intubated and anesthesia maintained with 0.5 to 2 % of Isoflurane (Iso-thesia; Abbott Laboratories, Chicago, IL) via an endotracheal tube throughout the experiment. For this purpose, a calibrated anesthesia ventilator (Model 2000, Hallowell EMC, Pittsfield, MA) was used with the anesthesia unit (Quatiflex VMC, Matrx Medical

Inc., Orchard Park, NY). Throughout the experiment the canines' anesthesia, respiration and ventilation were monitored (Capnomac Ultima, Datex Ohmeda, Finland) by certified veterinary technicians. During the course of the experiments, the canines were placed on a warming blanket connected to a heated water pump (TP 400, Gaymar Industries, Inc., Orchard Park, NY) to maintain body temperature. The canines' electrocardiogram, temperature and respiration along with pulse-oximeter data were also monitored (Vet/OX Plus 4700, Sensors Devices, Inc., Lancaster, PA). All procedures were performed when the canines were fully anesthetized (Stage 3, Plane 2) (189).

Euthanasia: The canines were sacrificed by intravenous injection of Beuthanasia (0.25 mg/kg). These experiments were conducted in accordance with guidelines provided by the Institutional Animal Care and Use Committee of Thomas Jefferson University. These guidelines are consistent with the recommendations of the Panel on Euthanasia of the American Veterinary Medical Association (190).

Appendix 3: Detailed Operating Procedures

I. Pressure catheter setup

1. Soak the pressure catheter tip in sterile water or sterile saline for 30 minutes before the experiment(s) for stabilization.

2. Connect the Millar transducer control unit to one of the channels on the oscilloscope.

3. The verification of the pressure control unit performance is performed as follows:

- Turn on the power switch on the transducer control unit
- Set the knob on transducer control unit to 'Standby' position and center the trace on the oscilloscope monitor
- Verify the conversion factor from mV to mmHg by setting the transducer control unit to 20 mmHg, and noting a DC offset of 40 mV on the oscilloscope
- Again verify the conversion factor from mV to mmHg by setting the transducer control unit knob to 100 mmHg, and noting a DC offset of 200 mV on the oscilloscope

(Note, that if the observed DC offset for 20 and 100 mmHg are different from the values mentioned above, then check the BNC cable used to connect the transducer control unit to the oscilloscope; if the problem persist then contact Millar Instruments)

4. Adjust the oscilloscope 'Volts/div' setting to cover the range of pressures that may be present during the experiment – this is required because only the visible portion of the trace will be captured by LabVIEW. Thus if the trace is partially clipped on the monitor, then, the digitized data output of LabVIEW will also be clipped.

5. Connect the pressure catheter to the transducer control unit (either directly or using an extension cable) and switch the knob on the transducer control unit to ‘Transducer’.

6. Shield the pressure catheter tip from the ambient light and then adjust the ‘Transducer Balance Control’ on the transducer control unit so that the trace remains centered on the oscilloscope display at the same position as in Step 3 (baseline position). Once the trace is returned to its baseline position, ‘Lock’ the transducer balance control.

7. Troubleshooting tips for the pressure catheter:

    - A continuous drift seen in the signal on the oscilloscope implies the presence of some bias voltage. In order to remove this bias voltage insert a conducting wire (example, a solder wire) near the pressure catheter tip and ground it (to oscilloscope outer panel/phantom outer covering/transducer control unit housing). This step removes any static charge that may be picked up by the catheter.
    - If the above step does not work, then remove the catheter and use a water jet (from a syringe) to clean the tip. Note, that the pressure sensor located at the tip is extremely fragile and thus delicate handling is required.
    - For additional details regarding troubleshooting, cleaning the pressure catheter and for sterilization of the pressure catheter before *in vivo* experiments refer to the ‘Millar Mikro-Tip catheter pressure transducer Animal use Only Instructions for Use’ manual in the lab. Alternately, the technical sales and support engineer Blayne P. Fleck (bfleck@millarmail.com; (832) 667-7165) at Millar Instruments may be contacted.

II. Experimental setup:

1. Take known quantity of isotonic diluent in an acrylic water bath. Typically for the flow phantom experiments 750 ml of isotonic diluent was used.

2. Place the acrylic water bath on the magnetic stirrer and insert a magnetic stirring bar in the acrylic water bath.

3. Obtain a close loop flow system between the acrylic water bath and the Doppler flow phantom using flexible PVC (polyvinyl chloride) tubes and the roller pump.

4. After the pressure catheter has been setup as explained in this Appendix – Part I (Appendix – 3I), insert it carefully (because the pressure sensor tip is fragile) through the PVC tubes till the pressure catheter tip resides in the selected lumen within the Doppler flow phantom.

5. Turn the roller pump 'RPM' setting to the desired level to initiate the flow and obtain the desired level of pressure in the flow phantom. Let the pump run for up to 3 to 4 minutes to remove the resident air cavities in the lumen of the flow phantom and the tubes.

III. LabVIEW setup (Note, that this setup was first developed by Flemming Forsberg and William T. Shi)

1. Start LabVIEW on the lab computer (Computer 1: Appendix 1(VII)).

2. Select 'Basic Waveform' from –

(C:\Documents and Settings\fxf105\My Documents\William\LabViewBill)

3. Enter a filename.

4. Select the channel source (this should be same as the channel where the output of the transducer control unit is connected).

5. Click ‘Run’ - to start capturing and click into file name field and save by clicking the 'tick' symbol.
6. The text files gets saved in - *(C:\Documents and Settings\fxf105\My Documents\Ray).*

IV. Synchronization Settings for Triggering the Oscilloscope Capture with Sonix RP scanner and Data Acquisition:

1. Connect ‘Ext’ on the oscilloscope to the ‘Print’ button on the Sonix RP located on the “Back Panel Control System Board”.
2. Set the ‘Sync Output (1)’ to ‘1’ on the Sonix RP software (this option appears on the left hand side panel when the unit is operated in ‘Research’ mode).
3. The settings on the oscilloscope should be as follows:
    - Trigger Setup: ‘Edge’ trigger, with trigger on ‘Ext’ with coupling set to ‘DC’, slope set to ‘Pos’ and external setting selected as ‘DC 50 Ω’
    - Time-Base Setup: Time per division set to ‘0.5 sec’ (to collect data corresponding to 5 seconds), with recording set to 50000 samples at 10 kS/sec for 5 seconds. Sampling is set to ‘Single Shot’, sequence set to “Off” and the ‘Peak Detect’ option selected. Recording setting should be set to ‘Record up to 50K samples’. Obviously select the channel (either 1 or 2) depending on the channel where the output of the transducer control unit is connected.
    - The update mode should be set to ‘Normal’
4. Verification of the synchronization may be performed as follows:
    - While the ‘Freeze’ button is engaged, the pressure trace on the oscilloscope display should not update (and the Sonix RP scanner should not be scanning).

- When the ‘Freeze’ button is dis-engaged, the pressure trace on the oscilloscope should update every 5 seconds (and the Sonix RP scanner should be scanning).

5. The data acquisition steps are detailed below:
   - User releases (or disengages) the ‘Freeze’ on the Ultrasonix Unit and waits for 5 seconds
   - After 5 seconds, engage the ‘Freeze’ button on the Ultrasonix Unit
   - Simultaneously, the ‘Run’ command on LabView should be clicked to collect the digitized pressure data visible on the oscilloscope monitor. Note, that if the ultrasound data is captured for more than 5 seconds, then there may be a second trigger signal from the Sonix RP sent to the oscilloscope which may refresh the data displayed on the oscilloscope monitor and consequently the pressure data may not correspond to the acquired RF data. Thus, care should be taken to capture the pressure data before a second update of pressure data initiates (corresponding to pressure data from 5 to 10 seconds).
   - Verify the text file is saved on the hard-drive at location specified in Appendix 3 III-3
6. The data on the Sonix RP is stored ‘*D:\PatientInf*o’ in the folder with the same name as the ‘patient name’ entered before starting the scanning. The RF data can be accessed using the Matlab code provided by Ultrasonix at: http://research.ultrasonix.com/ucp.php?mode=login (will require registration and login) – Program used was: ‘RPread.m’.
7. For additional details on RF data capture options refer the Ultrasonix Research Forum (at: http://research.ultrasonix.com/ucp.php?mode=login).

Appendix 4: Matlab Functions Developed for Processing

For reading encoded data files captured using the Sonix RP unit, a proprietary function ‘RPead.m’ was obtained from Kris Dickie and Corina Leung (Ultrasonix; available on the Research Users Forum:
http://research.ultrasonix.com/ucp.php?mode=login)
This function loads the encoded data in the Matlab workspace as a variable. Then, the under mentioned functions and subroutines may be used. ‘RPread.m’ function is thus not presented here.

I. Inbuilt Matlab Functions Used

fft & fftshift: to obtain the Fast Fourier Transform (FFT) of the data

squeeze: to adjust the dimensions of the array

uigetfile: to open a file dialog box from Matlab; for pointing to the location on the hard-drive where the data is stored

xlswrite: to write values into Microsoft Excel directly

II. Function: To Extract Signal Within a Bandwidth of 1 to 1.5 MHz

Input: FFT of the vectors such that first column represents frequency values, the second column represents the FFT amplitude and the third column represents the number of vectors

Output: Array of FFT values with the size dependent on the number of vectors

```
function [output]=shape101_averageauto(rfdata)
```

```
sz=size(rfdata);
for i=1:sz(3)
    data=rfdata(:,:,i);
    loc=find(data(:,1)>1 & data(:,1)<1.5);
    red_data=data(loc,:);
    output(i)=mean(red_data(:,2));
end

output=20*log10(output);
```

III. Function: To Extract Signal Within a Bandwidth of 1.15 to 1.35 MHz

Input: FFT of the vectors such that first column represents frequency values, the second column represents the FFT amplitude and the third column represents the number of vectors

Output: Array of FFT values with the size dependent on the number of vectors

```
function [output]=shape101_averageauto_red(rfdata)

sz=size(rfdata);
for i=1:sz(3)
    data=rfdata(:,:,i);
    loc=find(data(:,1)>1.15 & data(:,1)<1.35);
    red_data=data(loc,:);
    output(i)=mean(red_data(:,2));
end

output=20*log10(output);
```

IV. Function: To Extract Signal at 1.25 MHz after a Parabolic Fit Within a Bandwidth of 1.0 to 1.5 MHz

Input: FFT of the vectors such that first column represents frequency values, the second column represents the FFT amplitude and the third column represents the number of vectors

Output: Array of FFT values with the size dependent on the number of vectors

```
function [output]=shape101_parabolafit125(rfdata)

sz=size(rfdata);
for i=1:sz(3)
   data=rfdata(:,:,i);
   loc=find(data(:,1)>1 & data(:,1)<1.5);
   red_data=data(loc,:);
   pcoeff2=polyfit(red_data(:,1),red_data(:,2),2);
   yfitted =polyval(pcoeff2,red_data(:,1));
   n=max(size(yfitted));
   E2=sqrt( sum(abs(yfitted-red_data(:,2) ).^2 )/n );
   output(i,1)=polyval(pcoeff2,1.25);
   output(i,2)=E2;
end
parabolafiterror=output(:,2);
output=20*log10(output(:,1));
output=output';
```

V. Function: To Extract Signal at 1.25 MHz

Input: FFT of the vectors such that first column represents frequency values, the second column represents the FFT amplitude and the third column represents the number of vectors

Output: Array of FFT values with the size dependent on the number of vectors

```
function [output]=shape101_125(rfdata);

sz=size(rfdata);
for i=1:sz(3)
   data=rfdata(:,:,i);
   loc=find(data(:,1)==1.25);
   output(i)=data(loc,2);
end

output=20*log10(output);
```

VI. Subroutine: To Operate with Pressure Catheter Data (in batch mode) i.e., text files obtained from LabVIEW

Purpose: To read all data from the text files, convert the catheter data (in mV) to pressure data (in mmHg) and then store the values in variables *time_cat* and *pres_cat* in an array format; each column in *time_cat* corresponds to the time points for the corresponding column in *pres_cat* with the number of columns depending on number of text files present.

```
files1=dir('*.txt');
number_txt_files1=max(size(files1));
for i=1:(number_txt_files1)
    txt_files(i)={files1(i).name};
end
txt_files=txt_files';

for i=1:number_txt_files1
    temp_info=importdata(char(txt_files(i)));
    pres=(temp_info(:,2)*1000)/2;
    loc1=find(temp_info(:,1)>0.5 & temp_info(:,1)<4.5);
    time_cat(:,i)=temp_info(loc1,1);
    pres_cat(:,i)=pres(loc1);
    clearvars temp_info pres temp_info loc1
end
```

VII. Subroutine: To Operate with Data Captured with Sonix RP Scanner (in batch mode)

Purpose: To read all data from the '.drf' files, and for the given file obtain the subharmonic amplitude. Note that the '*fft_signal*' utilizes the standard Matlab functions to obtain the FFT.

```
files2=dir('*.drf');
number_drf_files2=max(size(files2));
for i=1:(number_drf_files2)
    drf_files(i)={files2(i).name};
end
drf_files=drf_files';
i =  %enter the file number to work with
[image,header] = RPread(char(drf_files(i)));
sampling_freq = header.sf/1000000; %in MHz
```

```
rfdata=image;
sz=size(rfdata);
for j=1:sz(3)
    rfdata_fft(:,:,j)=fft_signal(rfdata(:,:,j));
end
shape_average = shape101_averageauto(rfdata_fft); % OR any other function to extract
the RF data (from functions I through IV listed above)
s1=medfilt1(shape_average,order); %enter the order of the filter as required
```

Appendix 5: Canines Used for Cardiac SHAPE Studies

Table A5.1: List of canines used for cardiac SHAPE studies

Experiment Date	Canine ID	Weight (kg)
12/10/2008	720763	24.0
12/11/2008	729493	24.0
12/15/2008	718815	25.0
12/18/2008	712361	24.0
07/20/2009	766119	23.0
07/21/2009	762750	21.0
09/15/2009	771333	22.6
09/18/2009	763489	23.2
01/31/2012	830241	20.0
03/08/2012	826944	22.3
03/13/2012	826235	22.0

Appendix 6: Equipment Setup and Matlab Functions Specific to Logiq 9 Scanner

I. Synchronization Settings for Triggering the Oscilloscope Capture with GE Logiq 9 Unit and Data Acquisition:

(this was used to acquire data before the optimized incident acoustic output control algorithm was implemented on the Logiq 9 scanner)

1. Obtain the password from GE personnel to operate the unit in the maintenance mode; the password is updated periodically so the latest password should be obtained to do the experiments. Also be sure that the RF data capture ‘option keys’ are current and have not expired; else contact GE to obtain the updated ‘option keys’.
2. Before powering on the GE Log 9 unit, remove the side panel to access the Scan Control Board.
3. Insert the USB ‘Hasp’ key in the USB slot and power on the unit.
4. Enter the maintenance password and then let the unit start-up.
5. Make a folder: ‘Projects‘ and within it create a folder ‘mke07_shi’.
6. Copy ‘vars.bat’ file in this folder and extract ‘target’ in this folder (‘target’ contains the RF data capture software).
7. Copy files for the required frequency in the folder ‘target/RO/Probe’.
8. Then, on the command prompt execute the following commands:
    - *E:*
    - *cd Projects*
    - *cd mke07_shi*

- *vars.bat*
- *echoloader/reg*

9. Wait for the software to initiate.

10. If the unit shows streak like artifacts while scanning:

    - push the turn off button located on the top-left hand side of the keyboard
    - click on exit
    - at the command prompt – type ‘rackpower’ – press ‘enter’
    - after about 10 seconds click ‘escape’ on the keyboard
    - again execute ‘vars.bat’ and ‘echoloader/reg’ on the command prompt

11. Unplug the 4C probe and wait for the probe icon in the touch panel to be grayed out and then plug the probe back in.

12. Enter in the ‘Contrast’ mode and the new settings will be in effect.

13. Verify that the ‘Investigational Device’ notification appears on Logiq 9 monitor.

14. Confirm that the RF data capture button is available under ‘*Utility-> Admin-> System Admin*’. The ‘installed option keys’ should be current and should not have expired. If the keys have expired then contact GE and obtain the new software keys.

15. Under contrast select the desired option ‘Coded PI 1/2’ or ‘Res’ or ‘Pen’, then select the RF capture button.

16. Adjust the depth and incident acoustic output as required.

17. Then place the sampling volume so that it lies in the area of interest.

18. Connect the ‘txsync’ signal from the scan control board on the GE unit to the available channel (e.g., channel 2) on the oscilloscope using a high impedance cable. If

at this point the unit shows streak like artifacts then follow directions indicated in Step 10 in this section.

19. The settings on the oscilloscope should be as follows:
    - Trigger Setup: 'Smart-Qualified' trigger, with setup for 'Smart' trigger configured by 'State' to trigger on 'channel as per step 18' only after that 'channel' goes and stays above '0.18 V'. The 'wait' should be set to 'Off'.
    - Time-Base Setup: Time per division set to '0.5 sec' (to collect data corresponding to 5 seconds), with recording set to 50000 samples at 10 kS/sec for 5 seconds. Sampling is set to 'Single Shot', sample clock set to 'Internal' with the 'Peak Detect' option selected. Recording setting should be set to 'Record up to 50K samples'. Obviously select the channel depending on the channel where the output of the transducer control unit is connected.
    - The update mode should be set to 'Normal'
20. The data acquisition steps are detailed below:
    - User releases (or disengages) the 'Freeze' on the GE Unit and waits for 5 seconds
    - After 5 seconds, engage the 'Freeze' button on the GE Unit
    - Simultaneously, the 'Run' command on LabView should be clicked to collect the digitized pressure data visible on the monitor. Note, that if the ultrasound data is captured for more than 5 seconds, then there may be a second trigger signal from the GE Logiq 9 sent to the oscilloscope which may refresh the data displayed on the oscilloscope monitor and consequently the pressure data may not correspond to the acquired RF data. Thus, care should be taken to capture the pressure data

before a second update of pressure data initiates (corresponding to pressure data from 5 to 10 seconds).

21. To save the file on the GE unit perform the following steps:
    - Move the mouse controller to top right slightly
    - Cine Option should appear on the display panel above the keyboard
    - Press – ‘Cine Capture on’ – on the display unit
    - Press – ‘Run/Stop’ – on the display unit
    - On the keyboard – Press ‘DICOM Store’
22. Verify the text file is saved on the hard-drive at location specified in Appendix 3 III3.
23. The dicom data is stored under ‘*E:\Image Buffer*’ in the form of ‘.dcm’ files. The RF data may be extracted in Matlab using the *proprietary* ‘extractRFFromDicom’ software made available by GE.

II. Sample Output of the ‘GE Raw RF data extraction facility’ Software: (the example below is from a ‘.dcm’ file acquired during an experiment, before the optimized incident acoustic output control algorithm was implemented on the Logiq 9 scanner)

```
Microsoft Windows XP [Version 5.1.2600]
(C) Copyright 1985-2001 Microsoft Corp.
C:\Documents and Settings\jxd026.TJUH-MST\Desktop\Extract_RF_10262010>
extractRFFromDicom Image29.dcm
GE Raw RF data extraction facility V2.2.
```

```
Copyright GE 2010, all rights reserved.
Processing .\\Image29.dcm...
Data acquired with 4C probe on Logic.Musashi at 2009/11/25-10:26:04.
Processing simplex movie type 2D with sampleType Tissue(8)
Processing simplex movie type 2D with sampleType Complex(n*32)
This data set contains raw RF data.  The data matrix is dimensioned as
(377 samples X 4 firingsperzone X 1 zones X 1 packets X 27 vectors X 126 frames)
Reading public image data...the public image data is dimensioned:
  3 bytes/pixel x 480 rows x 640 columns x 1 frames
Done
Saving the 2D RF data and timestamps to .\Image29_2DRF.mat
Saving the public image pixel data to .\Image29_2DImage.mat
Done.
```

Note, in the output, the data matrix contains 377 samples that correspond to a span of 2.9 cm in the axial direction which is the size of the region of interest seen in Fig. 3.16B.

III. Subroutine: To Operate with Data Captured on the Logiq 9 Scanner

Note, functions ‘dc_filter.m’ and ‘eq_filter.m’ were obtained from Feng Lin (GE Global Research) for pre-processing the RF data obtained after using their proprietary software for extracting RF data from the acquired DICOM files (Appendix 6 II). These functions are not presented here. Also other functions and subroutines presented in

Appendix 4 are applicable here, once the data is present in the Matlab workspace as a variable. Thus, these functions and subroutines are not repeated here; but a subroutine created to operate in batch mode and load all the workspaces obtained after extracting the data from '.dcm' files (output of Appendix 6 II) in Matlab is given below:

Purpose: To create an array with file names for batch mode processing; then the filter functions mentioned above i.e., 'dc_filter.m' and 'eq_filter.m' and processing functions mentioned in Appendix 4 were used.

```
files=dir('*.mat');
sprintf('Determining number of workspaces # :  ...')
number_ws_files=max(size(files));
for i=1:(number_ws_files)
   ws_files(i)={files(i).name};
end
ws_files=flipud(ws_files');
% ws_files=ws_files';
sprintf('The total number of ws files in the folder: %d',max(size(ws_files)))
```

Appendix 7: Canines Used for PH SHAPE studies

Table A7.1: List of canines used for PH SHAPE studies **before** the optimized incident acoustic output control algorithm was implemented on the Logiq 9 scanner

Experiment Date	Canine ID	Weight (kg)
10/19/2009	773450	21.5
10/27/2009	768774	22.7
10/27/2009	772372	20.8
10/30/2009	773026	22.0
11/13/2009	773492	21.0
11/17/2009	769593	23.0
11/17/2009	774651	22.0
11/19/2009	768138	21.0
11/19/2009	774791	21.0
11/25/2009	770621	22.0
12/09/2009	774634	24.0
12/11/2009	774839	25.0
12/15/2009	772917	25.0
12/15/2009	777510	24.0
12/17/2009	779512	21.0
12/17/2009	777277	22.0
12/21/2009	7811193	22.0

Table A7.2: List of canines used for PH SHAPE studies **after** the optimized incident acoustic output control algorithm was implemented on the Logiq 9 scanner

Experiment Date	Canine ID	Weight (kg)
10/19/2010	809781	20.8
10/25/2010	809161	21.0
01/13/2011	809322	22.0
01/18/2011	808971	25.0
01/20/2011	811696	23.0

Appendix 8: List of Statistical Tests Used

ANOVA: ANOVA was used when mean values acquired with multiple settings were to be compared in contrast to the t-test used when values acquired with two settings were to be compared – ANOVA was used to maintain the probability of making type I error to 5 % (i.e., a *p*-value of 0.05). Multiple t-tests for such comparisons would increase the probability of type I error e.g., 2 t-tests on the same data set would increase the probability of type I error to 9.75 % (calculation: $1-0.95^2$).

1. One-Way: *In vitro* and *in vivo* studies to identify the most sensitive IAO level.
2. Repeated: *In vitro* studies to compare the extraction and filtering techniques for SHAPE.
3. Factorial Repeated: *In vivo* PH studies to determine differences in subharmonic signal amplitude for the number of transmit cycles and the IAO levels

Bonferroni Corrections:

1. Adopted for post-hoc multiple comparisons to control for Type-I error rate, by dividing the desired significance level by the number of comparisons performed.

Linear Regression Analyses:

1. *In vitro* and *in vivo* studies to predict the ability of the processed subharmonic signal to estimate ambient pressure values.

Paired t-test: Paired t-test was used for obtained from the same subject (in this case, canines) and when comparisons were required before and after some form of treatment (e.g., inducing PH) or when comparisons were required between two techniques (e.g., pressures obtained with SHAPE and with the pressure catheter)

1. *In vivo* studies to investigate if there were significant differences between the pressures obtained using the subharmonic data and the pressure catheter.
2. *In vivo* PH studies to investigate differences in pressures, pulsatility index and diameter of the PV before and after inducing PH.
3. *In vivo* PH studies to investigate difference between baseline and PH conditions for subharmonic signal amplitudes.

Correlation Analyses:

1. *In vivo* PH studies to identify the relationship between change in the mean PV pressures and change in the subharmonic signal amplitude, and between absolute mean PV pressures and absolute subharmonic signal amplitudes.

Correlation Comparisons using T-Test:

1. *In vivo* PH studies to compare correlation coefficients obtained with different transmit parameters.

Cross-Validation Study:

1. *In vivo* PH Studies to investigate robustness of the predictive capability of the results of correlation analyses for identifying PH.

Appendix 9: List of Key Personnel

The work towards this thesis required communication between various manufacturers and between colleagues at Thomas Jefferson University. Thus, a list of key personnel is compiled here for future reference. This list is not exhaustive but it at least provides a first point-of-reference for communication (at the time of this writing); it is intended to provide a guidance if laboratory team members or Dr. Flemming Forsberg are not available. Dr. Flemming Forsberg should be otherwise contacted for all practical purposes.

I. Thomas Jefferson University:

a. For scheduling and coordinating *in vivo* experiments:

- Ji-Bin Liu: Ji-Bin.Liu@jefferson.edu
- Joseph Altemus: Joseph.altemus@jefferson.edu

b. For scanning during *in vivo* experiments:

- Daniel Merton: Daniel.A.Merton@jeffersonhospital.org
- Maureen E McDonald: maureen.e.mcdonald@jefferson.edu

c. For ensuring catheter sterilization before *in vivo* experiments:

- Crystal: (7th Floor, Thomson Building, Department of Ultrasound)

II. Millar Instruments, Inc.

For technical information on Millar pressure catheters:

- Blayne P Fleck: bfleck@millarmail.com

III. GE Global Research

For assistance in configuring the software implemented on the GE ultrasound scanner and for providing the utility function to extract acquired RF data from the DICOM files:

- Kai E. Thomenius: thomeniu@ge.com
- Feng Lin: linf@research.ge.com
- Suhyun Park: tumbler77@gmail.com
- Scott Dianis: dianis@ge.com (now with Philips: scott.dianis@philips.com)
- Carl L. Chalek: chalekcl@ge.com
- Kirk Wallace: wallacek@ge.com

IV. Ultrasonix

For technical information and troubleshooting during data acquisition with the Sonix RP scanner and for the Matlab program to decode the acquired RF data:

- Kris Dickie: Kris.Dickie@ultrasonix.com
- Corina Leung: Corina.Leung@ultrasonix.com

Appendix 10: List of Software Used

Note, that specific software versions are not provided because the software were upgraded between 2008-2012.

1. **Matlab** (The Mathworks Inc., Natick, WA)

License: Thomas Jefferson University & Drexel University

Purpose: For programming and, acquiring and processing RF data

2. **LabVIEW** (National Instruments Corporation, Austin, TX)

License: Thomas Jefferson University

Purpose: For capturing oscilloscope data (interface between oscilloscope and a lab computer)

3. **IBM SPSS** (IBM Corporation, Armonk, NY)

License: Drexel University

Purpose: For statistical analyses

4. **G*Power** *(http://www.psycho.uni-duesseldorf.de/aap/projects/gpower/)*

Link last verified: May 31, 2012

License: Freely Available

Purpose: For power analyses

5. **Virtual Dub** (*http://www.virtualdub.org/index.html*)

Link last verified: May 31, 2012

License: GNU General Public License

Purpose: For creating animations and processing video files

6. **Endnote** (Thomas Reuters, New York, NY)

License: Drexel University

Purpose: For managing and publishing bibliographies

7. **Microsoft Office** (Microsoft Corporation, Redmond, WA)

License: Thomas Jefferson University & Drexel University

Purpose: For record keeping, publishing and presentations

Appendix 11: Grants

1. The American Heart Association (Dallas, Texas): Grant 0655441U
2. The National Institutes of Health (Bethesda, Maryland): Grant R21 HL081892
3. The National Institutes of Health (Bethesda, Maryland): Grant RC1 DK087365
4. The USA Army Medical Research and Material Command (Fort Detrick, Maryland): Grant W81XWH-08-1-0503

Appendix 12: List of Professional Contributions

A complete list of abstracts, conference proceedings and publications while working towards this project is presented**.**

I. Peer Reviewed Publications:

1) Dave JK, Halldorsdottir VG, Eisenbrey JR, Raichlen JS, Liu JB, McDonald ME, Dickie K, Wang S, Leung C and Forsberg F. *Subharmonic microbubble emissions for noninvasively tracking right ventricular pressures.* Am J Physiol Heart Circ Physiol. 2012 303:H126-32.

2) Dave JK, Halldorsdottir VG, Eisenbrey JR and Forsberg F. *On the processing of subharmonic signals from ultrasound contrast agents to determine ambient pressures*. Ultrason Imaging. 2012 34:65-75.

3) Dave JK, Halldorsdottir VG, Eisenbrey JR, Raichlen JS, Liu, JB, McDonald ME, Dickie K, Wang S, Leung C and Forsberg F. *Noninvasive left ventricular pressure estimation using subharmonic emissions from microbubbles – an in vivo pilot study*. J Am Coll Cardiol. Img. 2012 5:87-92.

4) Halldorsdottir VG, Dave JK, Leodore LM, Eisenbrey JR, Park S, Hall AL, Thomenius KE and Forsberg F. *Subharmonic contrast microbubble signals for noninvasive pressure estimation under static and dynamic flow conditions*. Ultrason Imaging. 2011 33: 153-64.

5) Eisenbrey JR, Dave JK, Halldorsdottir VG, Merton DA, Machado P, Liu JB, Miller C, Gonzalez JM, Park S, Dianis S, Chalek CL, Thomenius KE, Brown DB, Navarro V and Forsberg F. *Dual grayscale and subharmonic imaging on a modified commercial ultrasound scanner*. Ultrasonics. 2011 51: 890-7.

6) Dave JK, Halldorsdottir VG, Eisenbrey JR, Liu JB, McDonald ME, Dickie K, Leung C and Forsberg F. *Noninvasive estimation of dynamic pressures in vitro and in vivo using the subharmonic response from microbubbles*. IEEE Trans. Ultrason. Ferroelectr. Freq. Control. 2011 58: 2056-66.

II. Accepted Manuscripts (pending publication):

1) Dave JK, Liu JB, Halldorsdottir VG, Eisenbrey JR, Merton DA, Machado P, Zhao H, Needleman L, Brown DB and Forsberg F. *Acute portal hypertension models in canines: low- & high- flow approaches.* Comp Med. (Jan 2012).

2) Dave JK, Halldorsdottir VG, Eisenbrey JR, Merton DA, Liu JB, Zhou JH, Wang HK, Park S, Dianis S, Chalek CL, Lin F, Thomenius KE, Brown DB and Forsberg F. *Investigating the efficacy of subharmonic aided pressures estimation for portal vein pressures and portal hypertension monitoring.* Ultrasound in Med. & Biol. (Jan 2012).

III. Submitted Manuscripts (pending review):

1) Eisenbrey JR, Dave JK, Halldorsdottir VG, Merton DA, Miller C, Gonzalez JM, Machado P, Park S, Dianis S, Chalek CL, Kim C, Thomenius KE, Brown DB, Navarro V and Forsberg F. *Noninvasive subharmonic aided pressure estimation of portal vein pressures in patients with chronic liver disease.* Radiology. (August 2012).

2) Halldorsdottir VG, Dave JK, Eisenbrey JR, Machado P, Liu JB, Merton DA and Forsberg F. *Subharmonic aided pressure estimation for monitoring interstitial fluid pressure in tumors – in vitro and in vivo proof of concept.* To be submitted.

IV. Conference Proceedings:

1) Dave JK, Halldorsdottir VG, Eisenbrey JR, Liu JB, McDonald ME, Dickie K, Leung C and Forsberg F. *Noninvasive estimation of dynamic pressures in vitro and in vivo using the subharmonic response from microbubbles.* Proc. IEEE Ultrason. Symp. 2011, Pg 176-9.

2) Eisenbrey JR, Dave JK, Halldorsdottir VG, Merton DA, Gonzalez JM, Miller C, Machado P, Park S, Dianis S, Chalek CL, Thomenius KE, Brown DB, Navarro V and Forsberg F. *Subharmonic aided pressure estimation in patients with suspected portal hypertension.* Proc. IEEE Ultrason. Symp. 2011, Pg 620-3.

3) Eisenbrey JR, Dave JK, Halldorsdottir VG, Park S, Dianis S, Merton DA, Machado P, Liu JB, Gonzalez JM, Miller C, Thomenius KE, Brown DB, Navarro V and Forsberg F. *Dual grayscale and subharmonic ultrasound imaging on modified ultrasound scanner in 2 and 3D.* Proc. IEEE Ultrason. Symp. 2011, Pg 624-7.

4) Dave JK, Halldorsdottir VG, Eisenbrey JR, Liu JB, Lin F, Zhou JH, Wang HK, Thomenius KE, and Forsberg F. *In vivo subharmonic pressure estimation of portal hypertension in canines.* Proc. IEEE Ultrason. Symp. 2010, Pg 778-81.

5) Forsberg F, Dave JK, Halldorsdottir VG, Leodore LM, Lin F, Hall AL and Thomenius KE. *Applying real-time noninvasive pressure estimation obtained from subharmonic contrast microbubble signals.* Proc. IEEE Ultrason. Symp. 2008, Pg 1694.

V. Conference Presentations: * represents presenting author

1) Eisenbrey JR*, Dave JK, Halldorsdottir VG, Merton DA, Gonzalez JM, Miller C, Machado P, Park S, Dianis S, Chalek CL, Thomenius KE, Brown DB, Navarro V and

Forsberg F. *Noninvasive measurement of portal hypertension using subharmonic emissions from ultrasound contrast agents in patients with suspected portal hypertension.*

- March 2012: The American Institute of Ultrasound in Medicine, Oral Presentation
- J. Ultrasound Med. vol. 31 pp. S11, 2012

2) Dave JK*, Halldorsdottir VG, Eisenbrey JR, Suhyun P, Scott D, Chalek CL, Merton DA, Liu JB, Machado P, Thomenius KE, Brown DB and Forsberg F. *Automated optimized power determination for subharmonic aided pressure estimation – implementation on a commercial scanner.*

- March 2012: The American Institute of Ultrasound in Medicine, Oral Presentation
- J. Ultrasound Med. vol. 31 pp. S44, 2012

3) Dave JK*, Halldorsdottir VG, Eisenbrey JR, Merton DA, Liu JB, Zhou JH, Wang HK, Suhyun P, Scott D, Chalek C, Feng L, Thomenius KE, Brown DB and Forsberg F. *Quantitative contrast enhanced subharmonic ultrasound reveals portal vein pressures and tracks portal hypertension in canines.* (Shortlisted for *New Investigator Award*)

- March 2012: The American Institute of Ultrasound in Medicine, Oral Presentation
- J. Ultrasound Med. vol. 31 pp. S28, 2012

4) Eisenbrey JR, Dave JK, Halldorsdottir VG, Merton DA, Gonzalez JM, Miller C, Machado P, Suhyun P, Dianis S, Chalek CL, Thomenius KE, Brown DB*, Navarro V and Forsberg F. *Noninvasive measurement of portal hypertension using a novel contrast-enhanced ultrasound technique.*

- March 2012: SIR Annual Scientific Meeting, Oral Presentation

5) Halldorsdottir VG, Eisenbrey JR, Dave JK, Forsberg F*, Machado P, Cavanaugh B, Merton DA, Liu JB. *Subharmonic-aided Pressure Estimation for Monitoring Interstitial Fluid Pressure in Swine Melanomas: Initial in Vitro and in Vivo Results.*

- November 2011: The Radiological Society of North America, Oral Presentation

6) Forsberg F*, Dave JK, Halldorsdottir VG, Eisenbrey JR, Raichlen J,Liu, JB, McDonald ME Wang S, Leung C and Dickie K. *Noninvasive Cardiac Pressure Estimation Using Subharmonic Microbubble Signals.*

- November 2011: The Radiological Society of North America, Poster Presentation

7) Forsberg F*, Eisenbrey JR, Dave JK, Halldorsdottir VG, Gonzalez JM, Miller C, Merton DA, Machado P, Park S, Dianis S, Chalek CL, Thomenius KE, Brown DB and Navarro V. *Noninvasive Subharmonic-aided Pressure Estimation in Patients with Suspected Portal Hypertension: Preliminary Results.*

- November 2011: The Radiological Society of North America, Poster Presentation

8) Forsberg F*, Eisenbrey JR, Dave JK, Halldorsdottir VG, Liu JB, Gonzalez JM, Miller C, Machado P, Merton DA, Park S, Dianis S, Chalek CL, Thomenius KE, Brown DB and Navarro V. *Dual Grayscale and Subharmonic US Imaging on a Modified Commercial Scanner.*

- November 2011: The Radiological Society of North America, Poster Presentation

9) Dave JK, Halldorsdottir VG, Eisenbrey JR and Forsberg F*. *Processing Acoustic Data from US Contrast Agents for Ambient Pressure Estimation*.
- November 2011: The Radiological Society of North America, Poster Presentation

10) Eisenbrey JR, Gonzalez JM, Dave JK, Halldorsdottir VG, Merton DA, Machado P, Miller C, Park S, Dianis S, Chalek CL, Thomenius KE, Brown DB, Forsberg F and Navarro V*. *Subharmonic Aided Pressure Estimation (SHAPE): A Noninvasive Technique for the Estimation of Portal Hypertension.*
- November 2011, The Liver Meeting, Poster Presentation

11) Dave JK*, Halldorsdottir VG, Eisenbrey JR, Liu JB, McDonald ME, Dickie K, Leung C and Forsberg F. *Noninvasive estimation of dynamic pressures in vitro and in vivo using the subharmonic response from microbubbles.*
- October 2011, IEEE International Ultrasonics Symposium, Oral Presentation

12) Eisenbrey JR, Dave JK, Halldorsdottir VG, Merton DA, Gonzalez JM, Miller C, Machado P, Park S, Dianis S, Chalek CL, Thomenius KE, Brown DB, Navarro V and Forsberg F*. *Subharmonic aided pressure estimation in patients with suspected portal hypertension.*
- October 2011, IEEE International Ultrasonics Symposium, Poster Presentation

13) Eisenbrey JR*, Dave JK, Halldorsdottir VG, Park S, Dianis S, Merton DA, Machado P, Liu JB, Gonzalez JM, Miller C, Thomenius KE, Brown DB, Navarro V and Forsberg F. *Dual grayscale and subharmonic ultrasound imaging on modified ultrasound scanner in 2 and 3D.*
- October 2011, IEEE International Ultrasonics Symposium, Poster Presentation

14) Forsberg F*, Halldorsdottir VG, Cavanaugh BC, Machado P, Liu JB, Eisenbrey JR, Dave JK, Merton DA. *Subharmonic aided pressure estimation for monitoring neoadjuvant chemotherapy of locally advanced breast cancer*.
- August 2011, Proc. Era of Hope, pp. 595

15) Forsberg F*, Dave JK, Halldorsdottir VG, Eisenbrey JR, Raichlen JS, Liu JB, Miller C, Gonzalez JM, McDonald ME, Merton DA, Brown DB and Navarro V. *On the utility of subharmonic contrast microbubble signals*.
- June 2011: Ultrasonic Imaging and Tissue Characterization Symposium, Oral Presentation

16) Dave JK*, Halldorsdottir VG, Eisenbrey JR, McDonald ME, Liu JB, Raichlen JR, Leung C, Dickie K and Forsberg F. *Subharmonic signals for noninvasive cardiac pressure estimation – initial in vivo experience.*
- April 2011: The American Institute of Ultrasound in Medicine, Oral Presentation
- J. Ultrasound Med. vol. 30 pp. S71, 2011

17) Halldorsdottir VG*, Dave JK, Eisenbrey JR, Machado P, Liu J, Merton DA and Forsberg F. *Subharmonic aided pressure estimation for monitoring interstitial fluid pressure in tumors: in vitro and in vivo proof of concept*. (Awarded the *New Investigator Award)*

- April 2011: The American Institute of Ultrasound in Medicine, Oral Presentation
- J. Ultrasound Med. vol. 30 pp. S28, 2011

18) Dave JK*, Halldorsdottir VG, Eisenbrey JR, Liu JB, Lin F, Zhou JH, Wang HK, Thomenius KE, and Forsberg F. *In vivo subharmonic pressure estimation of portal hypertension in canines.*

- October 2010: IEEE International Ultrasonics Symposium Proceedings, Oral Presentation

19) Forsberg F*, Dave JK, Halldorsdottir VG, McDonald ME, Liu JB, Leung C and Dickie K. *Noninvasive cardiac subharmonic pressure estimation in vivo*

- March 2010: The American Institute of Ultrasound in Medicine, Oral Presentation
- J. Ultrasound Med., vol 29, pp. S13, 2010

20) Forsberg F*, Halldorsdottir V, Dave JK, McDonald ME, Liu JB, Leung CL and Dickie K. *In vivo noninvasive cardiac subharmonic pressure estimation.*

- June 2009*:* Ultrasonic Imaging and Tissue Characterization Symposium, Oral Presentation

21) Forsberg F*, Dave JK, Halldorsdottir VG, Leodore LM, Lin F, Hall AL and Thomenius KE. *Implementing Real-Time Noninvasive Subharmonic Pressure Estimation.*

- December 2008: The Radiological Society of North America, Poster

22) Forsberg F*, Dave JK, Halldorsdottir VG, Leodore LM, Lin F, Hall AL and Thomenius KE. *Applying Real-time Noninvasive Pressure Estimation Obtained from Subharmonic Contrast Microbubble Signals.*

- November 2008: IEEE International Ultrasonics Symposium Proceedings, Poster

23) Forsberg F*, Dave JK, Halldorsdottir VG, Leodore Lm, Leung C and Pelissier L. *Implementation of Noninvasive Subharmonic Pressure Estimation on a Commercial Ultrasound Scanner.*

- November 2008: American Heart Association, Oral Presentation

Appendix 13: Ambigram for SHAPE

Taking a cue from Dan Brown’s fictional character Robert Langdon and from an adjunct professor John Langdon associated with Drexel University, in “some” “free” time, an attempt was made to develop an ambigram for SHAPE!

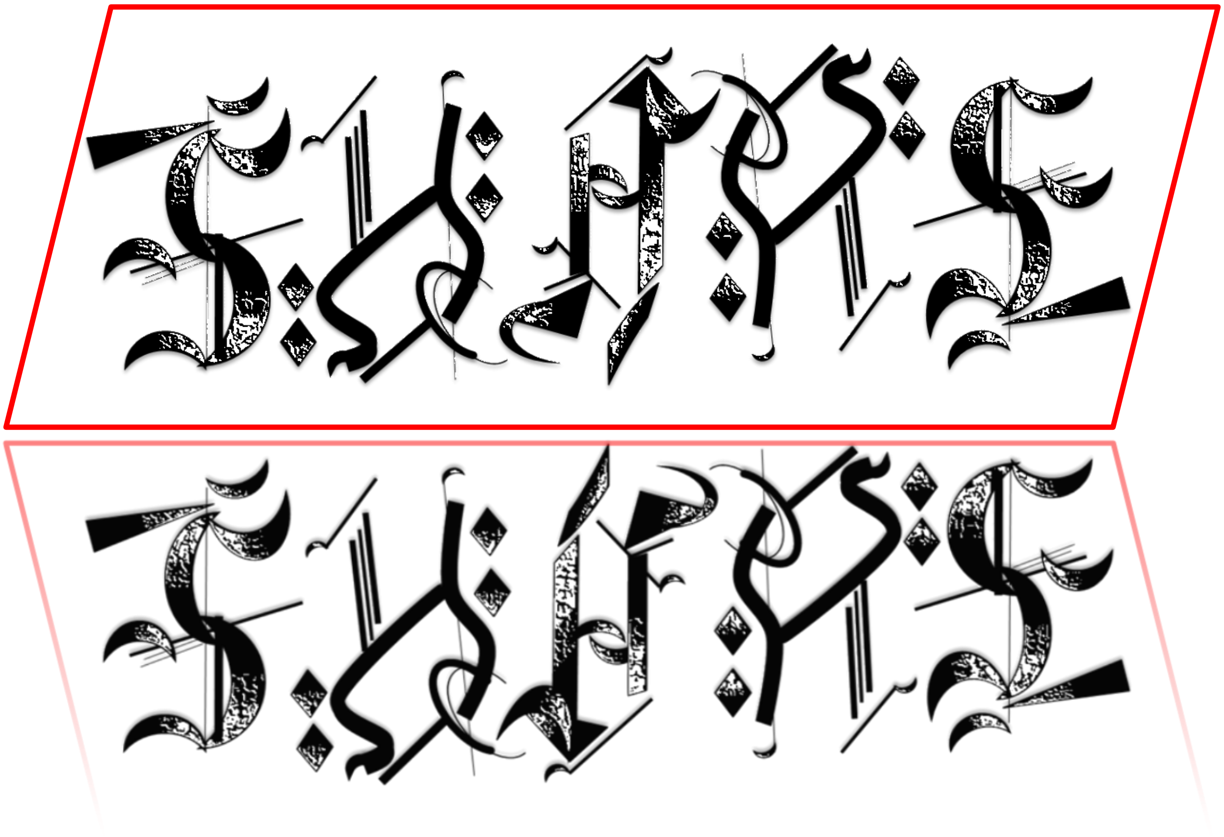

VITA

Jaydev Dave is a citizen of the Republic of India. He completed his Bachelors in Biomedical Engineering (B.E.) from the D. J. Sanghvi College of Engineering (University of Mumbai) in May-2006 with distinction. During his internship, he was awarded as the 'Best Trainee Engineer' for personal dedication during MRI installation by GE Healthcare (Mumbai).

Immediately following his undergraduate studies, Jaydev pursued his M.S. in Biomedical Engineering from Drexel University (Philadelphia, PA) and graduated in June-2008 with a 4.0 GPA. For his M.S. thesis, Jaydev worked under the supervision of Dr. Flemming Forsberg (Thomas Jefferson University) and was involved in developing an imaging technique to enhance visualization of breast tumor vasculature using subharmonic ultrasound.

For his doctoral degree, Jaydev continued his research with Dr. Flemming Forsberg, but worked on developing subharmonic aided pressure estimation technique to enable monitoring *in vivo* pressures noninvasively. Concurrently, Jaydev also received a prestigious certification in Radiological Physics (Diagnostic) from the American Board of Radiology – he is currently working as a Medical Physicist in the Department of Radiology of the Thomas Jefferson University Hospital. He has served as an Adjunct Faculty member at the Holy Family University.

Jaydev has received travel awards for both national and international conferences. Consequently he has presented at various conferences (15 - 1st author abstracts) and has authored 8 publications (excluding conference proceedings) in engineering as well as clinical journals – his work has also been highlighted on AuntMinnie, amongst the imaging industry professionals.

Jaydev is a Scientific Reviewer for 'Medical Physics' and 'Radiology' - two premier radiology journals for physicists and clinicians. He has recently been invited to write physics questions for the American Board of Radiology. He receives annual invitations from the Bayard Rustin High School (West Chester, PA) to lecture on scopes and advances of Biomedical Engineering. In his free time, he enjoys long distance swimming events.